ITERATIVE ANALYTICAL TECHNIQUES FOR THE DESIGN OF TRANSFER TRAJECTORIES FOR DIRECT INTERPLANETARY ORBITER MISSION

A thesis submitted

in partial fulfillment for the award of the degree of

Doctor of Philosophy

by

Parvathi S.P

Department of Aerospace Engineering

Indian Institute of Space Science and Technology

Thiruvananthapuram, India

May 2019

CERTIFICATE

This is to certify that the thesis entitled **Iterative Analytical Techniques for the Design of Transfer Trajectories for Direct Interplanetary Orbiter Mission**, submitted by **Parvathi S.P.,** to the **Indian Institute of Space Science and Technology, Thiruvananthapuram**, in partial fulfillment for the award of the degree of **Doctor of Philosophy**, is a bonafide record of the research work done by her under my supervision. The contents of this thesis, in full or in parts, have not been submitted to any other institute or university for the award of any degree or diploma.

Dr. R. V. Ramanan,
Research Supervisor,
Department of Aerospace Engineering,
IIST.

Counter signature
The Head-of-Department,
Department of Aerospace Engineering,
IIST.

Seal

Place: Thiruvananthapuram
Date: 22 May 2019

DECLARATION

I declare that this thesis entitled **"Iterative Analytical Techniques for the Design of Transfer Trajectories for Direct Interplanetary Orbiter Mission"**, submitted in partial fulfillment for the award of the degree of **Doctor of Philosophy**, is a bonafide record of the original research that I have carried out under the supervision of **Dr. R. V. Ramanan**, and that this work has not formed the basis for the award of any degree or diploma, in this or any other institute or university. In keeping with the ethical practice in reporting scientific information, due acknowledgements have been made wherever the finding of others have been cited.

Parvathi S.P.

Place: Thiruvananthapuram
Date: 22 May 2019

ACKNOWLEDGEMENTS

Adding a thank you note is the finishing touch on my PhD thesis. I would like to reflect on the people who have supported me throughout this period.

"Guru Brahma Guru Vishnu
Guru Devo Maheshwara
Guru Sakshat Param Brahma
Tasmai Shri Gurave Namah"

Prima facie, I would like to express my sincere gratitude to my research supervisor, Dr. R. V. Ramanan, who has the attitude and the substance of a genius. Without his valuable guidance and infinite patience, I would be hard-pressed to say this PhD would not have been possible. It has been a great learning experience, not only in the technical arena, but also on a personal level. I would also like to thank Mrs. Radha Ramanan for her utmost care and support.

I would like to thank my doctoral committee members, Dr. Manoj T. Nair, Prof. K. Kurien Issac, Dr. K. S. S. Moosath, Dr. P. Raveendranath, Dr. Hari B. Hablani and Dr. P. V. Subbaraju for their critical reviews and suggestions. A very special thanks to Dr. Aravind Vaidyanathan for his invaluable suggestions on presentation and documentation works. I would like to express my heartfelt thanks to all my teachers who laid the foundation of my knowledge and interest in science. My deepest thanks to my friends in IIST who fuelled me to think and speculate in various aspects.

I am thankful to the fraternity of Aerospace engineering and also, to my beloved teachers of the Humanities department for being a support always. I also thank the library officer and the staffs for their timely help in fishing out research publications which dated way back.

I am highly grateful to my parents, Suresh Kumar P. and Preetha K. S., and my sibling Lekshmi S.P, for their unconditional love and support. They are my pillars and source of strength. I can't thank them enough, especially my mother for her unassuming support and selfless love. I am thankful to my grandmother, Smt. Sulochana Amma who has been a math teacher and has always praised the student that was me. I extend my deepest gratitude to my husband, Syam Mohan, who has

been very tolerant and understanding. Also, my sincere gratitude goes to my extended family who helped me in all possible ways during this challenging period. Finally and above all, I am most indebted to my baby boy, Vasudev Syam, who turned one a few months back. He has been most supportive and has showed me enough love that lasts for a lifetime. I thank The God Almighty for all the wonder people around me.

Parvathi S.P.

PREFACE

Born in a traditional Hindu family, the subtle link between science and religion has always fascinated me. I was much enthused to read the religious scripts that detail the scientific facts in an explicit manner. From such books and also some science fiction movies, I had developed a sense of love for the stars and the universe. As years passed by, some of my circumstances made me opt to become an Electrical engineer. Soon after, I proceeded in the same route and took up the job as an assistant professor in Control systems. However, like Paulo Coelho said, "When you want something, all the universe conspires in helping you to achieve it", the destiny took my steering and routed me to become a research scholar in space flight mechanics. Today, I'm in love with the cosmos even more. I thank The God Almighty for making my dream come true. I sincerely hope that this research work would qualify as a good contribution in the field of astrodynamics.

ABSTRACT

In an interplanetary transfer, the spacecraft experiences the gravitational pull of many celestial bodies. The motion of the spacecraft is studied by solving the n-body equations of motion using numerical techniques. As the interplanetary transfer is a two-point boundary value problem, there is no complete information on the initial or departure states. To find the initial states, exorbitantly large number of trajectory propagations under high fidelity force models are required making the process computationally intensive. Usually analytic techniques that are based on simple force models are used to generate an initial guess of the transfer trajectory design. The current research focuses on developing ***efficient analytical techniques*** that generate improved trajectory designs for an interplanetary orbiter mission.

The analytical techniques proposed are based on the patched conic and pseudostate concepts. These techniques are iterative in nature and identify the four distinct trajectory design options for an opportunity which the conventional design techniques fail to do. The gravity perturbations of the non-spherical Earth and third body effects of the Moon and the Sun are included in the analytical design process. The numerical propagation of the proposed analytical designs, under a force model that includes major perturbations, achieves the arrival target parameters with good accuracies. The numerical refinement of these analytical designs require very less computation time as compared to that of the conventional designs. An analysis of the MOM and MAVEN mission designs generated using the proposed technique is presented. Also, trajectory designs are generated for direct transfers from Earth to Venus and Earth to Jupiter for the minimum energy opportunities of 2023 and 2022 respectively. The use of the proposed analytical techniques as a quick mission design and analysis is demonstrated using an Earth to Mars orbiter mission for Type I (2018) and Type II (2022) minimum energy transfers. Fortran 95 codes have been developed based on the proposed analytical techniques and used to analyze realistic mission scenarios.

TABLE OF CONTENTS

LIST OF FIGURES

LIST OF TABLES

ABBREVIATIONS

AoP	argument of periapsis
APO	arrival parking orbit
B-ITRPC	biased iterative patched conic technique
BFM	B-ITRPC force model
CAA	closest approach altitude
DE	differential evolution
DPO	departure parking orbit
EPO	Earth parking orbit
HTO	Hohmann transfer orbit
ITR-PC	iterative patched conic technique
ITR-PS	iterative pseudostate technique
MCDE	multiconic differential-evolution technique
MJD	modified Julian date
PC	patched conic technique
PCFM	patched conic force model
PSFM	Pseudostate force model
POI	parking orbit insertion
RAAN	right ascension of ascending node
SOI	sphere of influence
STM	state transition matrix
TCM	trajectory correction maneuver
TDB	barycentric dynamical time
TPI	transplanetary injection
UTC	universal coordinated time
VPC	V-infinity tuned patched conic technique

NOMENCLATURE

a	semi-major axis, km
e	eccentricity
h_P	periapsis altitude, km
i	inclination, deg
J_2 *to* J_6	non-spherical Earth gravity zonal harmonic coefficients
$\{x, y, z\}$	position coordinates, km
$\{\dot{x}, \dot{y}, \dot{z}\}$	velocity coordinates, km/s
J	objective function
$\boldsymbol{R}$	heliocentric position vector, km
$\boldsymbol{r}$	planetocentric position vector, km
Δr	magnitude of difference in position vector, km
T_P	time of arrival periapsis (UTC)
t_i	initial time in Lambert problem
t_f	final time in Lambert problem
t_A	sweep-back/SOI duration of arrival planet, days
t_D	sweep-forward/SOI duration of departure planet, days
t_{FD}	flight duration, days
Δt	difference in time between the desired and achieved values, chapter 3
u_∞	argument of latitude in the hyperbolic orbit, deg
$\boldsymbol{V}$	heliocentric velocity vector, km/s
$\boldsymbol{v}$	planetocentric velocity vector, km/s
$\boldsymbol{v}_\infty$	asymptotic velocity vector, km/s
$\Delta \boldsymbol{v}$	magnitude of difference in velocity vector, km/s
ΔV	velocity impulse, km/s
Ψ	angle between desired and achieved velocity vector, deg
Ω	right ascension of ascending node, deg
α_∞	right ascension of asymptotic velocity vector, deg
δ_∞	declination of asymptotic velocity vector, deg
ϵ	threshold/tolerance limit
θ_∞	asymptotic true anomaly, deg
μ	gravitational constant, km^3/s^2
ν	true anomaly, deg
ω	argument of periapsis, deg

Subscripts

A	arrival planet
a	high point of rectilinear hyperbola
D	departure planet
FD	flight duration
h	pseudosphere point

∞	hyperbolic orbit
p	periapsis
PC	patch point
PO	parking orbit
PS	pseudostate point
S	Sun
TO	transfer orbit
0	initial point
1	departure planet
2	arrival planet

CHAPTER 1
INTRODUCTION

"The infinite! No other question has ever moved so profoundly the spirit of man."
-David Hilbert

1.1 Introduction

From time immemorial, the vast expanse of the universe and the stars have been a source of wonder. Ancient men have worked tirelessly to decipher the mysteries of the universe and to understand the patterns of the stars. Starting from Newton's formulation of the law of gravity, scientists sought continuously to develop analytical theories to describe the motion of the Earth's only natural satellite, the Moon. October 4, 1957, marked the beginning of space age when the Soviet Union successfully launched Sputnik I, the world's first artificial satellite. Several spacecraft have been launched beyond Earth orbit since 1959. On July 20, 1969, the Apollo 11 crew landed on the Moon and returned safely to Earth. NASA's Galileo mission (launch date: 0ctober 18, 1989) became notable for discoveries during its journey to the gas giant Jupiter. It was the first spacecraft to visit two asteroids, Gaspra and Ida. India's first mission to Moon, Chandrayaan-1, was launched successfully on October 22, 2008 (Chandrayaan-1, 2008). On November 5, 2013, the Indian Space Research Organization launched the Mars Orbiter Mission (MOM) which was its first venture into the interplanetary space (Mars Orbiter Mission, 2018). Historians marked 2014 as a pivotal year in the space age when the scientists and engineers of the European Space Agency landed a tiny probe onto a 4 km wide comet traveling at 37.5 km/s at a distance of 500 million km. The Rosetta mission didn't end when the Philae probe landed on Comet 67P/Churyumov-Gerasimenko, sent back volumes of data and went dormant. The spacecraft is functioning optimally and has settled into the 'comet escort phase' of the operation. It will continue returning images and data of the comet as it approaches the Sun (Clark, 2016). In Earth orbit, the International Space Station continues to soar around the planet with a continually staffed crew of astronauts. There

are spacecraft currently on the way to Venus, Mars, asteroids, Jupiter, Saturn, the Kuiper Belt and even exploring the interstellar space (NASA Solar system exploration, n.d.).

Today, modern spacecraft continue to explore the nature of the solar system and return invaluable data from exotic satellites of gas giants, drifting asteroids and other untapped sources of knowledge to the universe. For all these scientific missions, scientists endeavor to investigate as much about a celestial body as possible with a single spacecraft. However, the limitations on mass restrict the number of instruments that can be carried across the solar system. Though launch vehicles are ever improving, the most efficient way of sending more useful mass outside the influence of Earth's gravity is to reduce the fuel mass of the spacecraft and accommodate more scientific instruments. Most interplanetary missions require a large quantity of fuel for the spacecraft to achieve the required heliocentric trajectory and arrive at the destination celestial body. The amount of propellant required to complete the mission objectives can be significantly reduced by utilizing efficient trajectory designs. Thus, designing a preliminary trajectory is an important step in the mission design process. **In general, the design process involves two steps, (i) identifying the launch opportunity and (ii) designing the optimal transfer trajectory that minimizes the V-infinity vector**. An interplanetary mission requires selection of suitable launch opportunity, parking orbit characteristics etc. which are decided based on an extensive mission analysis. Therefore, a mission design and analysis tool that is quick and capable of handling a wide range of mission scenarios is essential.

In an interplanetary transfer, the spacecraft experiences the gravitational pull of many celestial bodies and hence, to obtain an accurate trajectory design, it is essential that the mission design and analysis tool includes a realistic force model in the design process. Also, the interplanetary transfer is a two-point boundary value problem and so, there is no complete information on the initial or starting conditions. In general, an accurate trajectory design is generated using numerical techniques. The numerical technique includes numerical search for the initial condition and numerical integration of the n-body equations of motion. Therefore, executing the two steps of the design process using a numerical technique is computationally intensive and takes exorbitantly large time. Thus, for design analysis purposes, numerical technique is not suitable. Usually, the numerical design process uses the launch opportunity which is identified using some quick alternative methods (Escobal, 1965; Cornelisse, 1978). The number of numerical propagations of the n-body equations of motion in the numerical technique can be reduced

with a reasonably good guess of the trajectory parameters at the initial condition i.e., the initial guess. The complexity of finding the initial guess increases when the objective is to obtain the trajectory design for a minimum-energy interplanetary transfer. Usually, analytic techniques that generate quick solutions that are close to the numerical solutions are used for finding the initial guess. The current research focusses on developing ***efficient analytical techniques*** that provide improved transfer trajectory design for an interplanetary orbiter mission and can be used as a quick mission design and analysis tool.

This chapter is organized as follows. In section 1.2, the literature review that includes an exhaustive list of the currently available trajectory design and optimization techniques is presented. This section encompasses various numerical, and analytical trajectory design techniques and also optimization techniques used for finding the launch opportunity for interplanetary and lunar missions. Section 1.3 outlines the limitations of the conventional analytical trajectory design techniques which is the motivation for the current research. The objectives of the research are presented in section 1.4. Section 1.5 provides a summary of the research. Section 1.6 provides the thesis architecture.

1.2 Literature Review

The preliminary design of interplanetary trajectory is obtained by exploring numerous sets of transfer trajectories. Each set is numerically propagated under the n-body force model to verify the accuracy in achieving the target parameters. With the advent of high speed computers, several numerical techniques are used for optimal trajectory design under the n-body force model. Betts (1998) presented a survey of the numerical methods used for trajectory optimization. The application of optimal control theory to space flight has led to the development of several useful computer programs. One such program is Mission Design and Analysis Software (MIDAS) which is designed to obtain complex ballistic heliocentric transfer trajectories for interplanetary space flight missions [Sauer, 1989]. Laura M. B., et al. (2010) used MIDAS to generate Earth to Mars transfer trajectories for the years of 2026 through 2045. Another tool that has been widely used is COPERNICUS [Ocampo, 2003]. A recent tool that has been developed by NASA is the Generalized Mission Analysis Tool (GMAT) [Hughes, 2008]. A commercial tool kit STK (currently known as Systems Tool Kit) also provides numerical solution [STK user's manual, 1997]. All these high accuracy trajectory optimization tools account for realistic force models. These trajectory optimization softwares use gradient methods and so, they can find an optimal trajectory design only if the initial guess/design is close to the optimal

design. As pointed out earlier, even when the launch opportunity is known apriori, the numerical design requires good initial guess to obtain the other unknown design parameters. In the context of interplanetary transfer, studies on the numerical trajectory design under the full force model is scarce. In the context of lunar transfer, Ramanan et al. (2005) generated a numerical trajectory design under the full force model. A random search method, genetic algorithm, was used to obtain the initial guess of the transfer trajectory.

As we know, the numerical process is computationally intensive and so, alternative analytical techniques have been explored to substitute the numerical integration process. These techniques have been conceived independently by several investigators [Stumpff and Weiss, 1968; Wilson, 1970; Byrnes and Hooper, 1970] and are closely related. Because these analytical techniques use a larger step size, the computation time required for propagation is less. The analytical design techniques are used to obtain the initial guess of the transfer trajectory quickly. Unlike the numerical integration formulas which depend on polynomials, these analytical techniques are based on two-body conics. The general design approach is to solve the simplified two-body or three-body problems analytically and obtain the initial trajectory set. These initial or coarse set is numerically refined under the full-body force model to obtain the realistic transfer trajectory design. The equations of motion are numerically integrated using the initial design under the n-body framework.

The research on the trajectory design for interplanetary mission started with the simple two-body models. Gobetz and Doll (1969) gives a survey of the design methods of two-body impulsive trajectories. These techniques operate under simplified force models by introducing suitable assumptions. The analytical computation of interplanetary trajectory design was triggered by Walter Hohmann through his publication "The Accessibility of Celestial Bodies" in 1925. Though the technique gives a rough idea of the launch opportunity, flight duration and the velocity impulses for the interplanetary transfer, the transfer trajectory was a two-dimensional heliocentric ellipse. Thus, the Hohmann technique is not directly applicable for actual mission planning. With the introduction of patched conic concept [Clarke et al., 1963], a three-dimensional transfer trajectory design applicable for actual mission planning became possible as this technique considers the actual positions of the target planets. NASA's spectacular multiple flyby missions such as Voyager and Galileo are based on patched conic designs [Marsden and Ross, 2006]. Unlike the Hohmann transfer, this technique takes into account the

gravitational forces of the target planets using the concept of the sphere of influence (SOI). The patched conic approximations offer an efficient and easy means for generating interplanetary trajectories for direct and gravity-assist transfers [Carlson K. M., 1970; Bate et al., 1971; Battin, 1987; Brown, 1992; Prussing and Conway, 1993; Bell et al., 1995; Chobotov, 2002; Heaton et al., 2002; Bessette C. R. and Spencer D. B., 2007; Conway, 2010; Armellin R., 2011; Spreen et al., 2011; Englander, 2012; Campagnola et al., 2014] and is the most commonly used trajectory design technique. Brennan (2011) developed a tool for the design of interplanetary transfer trajectories using the patched conic approach. However, because of the patched conic assumptions, there are discontinuities in the position and velocity vectors at the boundary of the SOI. Many numerical techniques are used to patch these discontinuities. Clarke et al. (1966) described an analytical model based on the conventional patched conic concept to generate one-way transfer trajectories from a circular Earth parking orbit to both Mercury and Jupiter. Here, the differential correction technique is used to modify the departure V-infinity vectors such that the desired arrival B-plane coordinates (Jah M., n.d.) are achieved. Note that B-plane is a plane passing through the center of the arrival planet and normal to the V-infinity vector. Many variants of the patched conic technique are available in the literature [Cornelisse, 1978]. A hybrid patched conic technique is discussed for lunar transfer by Escobal (1965) wherein the perturbing accelerations in the equations of motion are averaged over a larger time step. Here, the velocity discontinuity is removed by using the differential correction technique. Another variant of the patched conic technique is the Linked conic technique [Olds et al., 2007], where the planetocentric and heliocentric trajectories are patched at the SOI through iterations using different strategies to ensure continuity. Bayliss (1970) described the perturbed conic technique taking into account the perturbing effects of the Sun on the planetocentric legs, and of the planets on the heliocentric legs. Lancaster (1973) developed the matched asymptotic technique for lunar and interplanetary transfers. Cornelisse (1978) synchronized the velocity vector at the SOI using the Newton-Raphson method. Park and Wright (2007) presented a comparison of the patched conic trajectory code to the commercially available softwares - STK and swing-by calculator and concluded that STK took the largest computation time (about a day) as compared to the swing-by calculator and the patched conic trajectory code. Bradley and Russell (2014) proposed a method to convert the patched conic trajectories for gravity assist and rendezvous missions from low fidelity patched conics models to full-ephemeris n-body dynamics. Jin Li (2018) developed an

iterative technique based on the patched conic concept which reduces the discontinuities at the SOI using the assumption that the direction of the asymptote and the velocity vector at SOI are the same.

In 1970, an improved analytical technique known as the overlapped approximation technique was proposed by Wilson S. W for lunar transfer cases. The deviations in the achieved arrival parameters were largely reduced for the pseudostate design as compared to the conventional patched conic design. The improvement in the trajectory design is due to the inclusion of Earth (primary body) even in the neighborhood of Moon (secondary body) using the concept of Moon's sphere of action. Wilson presented this technique for analytical trajectory simulation and also demonstrated its use as a state vector propagation technique with step size larger than that used in the numerical technique. He observed that, when the step size is reasonably small, the pseudostate technique can be used as an alternative to the numerical propagation technique. The discontinuities at the arbitrary boundaries of the target planets are removed under iterative schemes using Regula-Falsi method. Byrnes and Hooper (1970) formulated a multi-step pseudostate technique, named as multiconic technique, for lunar transfer considering the gravity perturbations due to the non-spherical Earth and the third body effect of the Sun. Byrnes (1989) modified the multi-step pseudostate technique into a one-step pseudostate technique for gravity-assist missions. The modified pseudostate technique has been applied for trajectory determination between two massive bodies, which he named as the **three-body Lambert problem**. He reported good improvement in the design as compared to the conventional patched conic design. To achieve the time of periapsis of the flyby trajectory, Byrnes used the State Transition Matrix (STM) introduced by Goodyear (1966). Sergeyevsky et al. (1983) applied the one-step pseudostate technique to design a direct Earth to Jupiter transfer trajectory with additional assumptions on the departure and arrival trajectories. He assumed rectilinear hyperbolas for the planetocentric conics of the departure and arrival legs which removed the complicated computations involving STM. Since for a rectilinear hyperbola, the position and velocity vectors are parallel, there arises difficulty in fixing the orientation of the hyperbolic orbital plane. This design results in vertical impact with the target planets which is not desirable in actual mission scenario. Sergeyevsky (1983) consolidated the design charts for Earth to Mars transfers using the one-step impact pseudostate technique. Sweetser (1989) compiled the analytical techniques for the transfer trajectory design with special emphasis on the importance of size of the pseudostate transformation

sphere/pseudosphere. He derived an empirical relation to find the size of the pseudosphere. Kledron and Sweetser (1988) compared various techniques based on the pseudostate concept for the transfer trajectory design. Ramanan (2002) used the one-step impact pseudostate technique in the arrival phase of the lunar transfer trajectory. Ramanan and Adimurthy (2005) presented a one-step non-impact pseudostate algorithm to obtain the transfer trajectory for lunar orbiter mission. The arrival V-infinity vector is achieved using an analytical tuning strategy and used to determine the pseudostate/pseudo target aiming point of the Moon. The analytical tuning strategy was an effective and simple alternative to the use of STM. The lunar transfer trajectory design was used as the initial guess for the numerical refinement process and the numerical design thus obtained was close to the one-step non-impact pseudostate design [Adimurthy and Ramanan, 2005]. The numerical search was regulated using an optimization technique. ***It is to be noted that, in an interplanetary transfer context, an analytical technique that can provide the departure parking orbit characteristics is not available in the literature. The departure parking orbit characteristics is very important as the angles, Right Ascension of Ascending Node (RAAN) and Argument of Periapsis (AoP) of the departure parking orbit decides the direction of the departure V-infinity vector which in turn forms a crucial parameter to help arrive at the desired target planet.***

For all the analytical trajectory design techniques, the Lambert problem is the lifeline. Gauss (1857) developed an orbit determination method using the observations on three different time instances, instead of two which is used in a classical Lambert problem. With his method, Gauss was able to correctly determine the orbit of the newly-discovered Ceres. Many great mathematicians like Euler and Lagrange solved the classical orbit determination problem [Escobal, 1965]. As there is no closed form solution of Lambert's problem, iterative methods and series expansions became the accepted approaches of solutions. Escobal (1965) consolidated six methodologies for orbit determination and discussed the merits and demerits of each method. Prussing (2000) presents the classical Lambert solution by iterating on the semi-major axis. Other Lambert solutions are based on iterations on the orbital elements such as the semi-latus rectum [Boltz, 1984], true anomaly [Bate, 1971], and eccentricity [Avanzini, 2008]. Each of these solutions has different advantages and disadvantages. Mainly, these methods have different formulations for different type of conics: circular, elliptic, parabolic or hyperbolic. They also encounter mathematical singularities. Thorne (1995) derived a series solution to Lambert's problem that works for hyperbolic and elliptic orbits. Battin

and Vaughan (1984) developed a technique for solving the Lambert's problem in terms of the universal variables [Bate, 1971] wherein all types of conics can be handled. This technique is widely used because of its elegance and robustness. Later, the universal variables solution have been developed by several authors independently [Lancaster, 1969; Gooding, 1990; Luo et al., 2011; Thompson, 2011; Izzo, 2015]. The universal variables methodology discussed by Vallado (1997) is computationally simple and it is a secant method that iterates on the universal variable until the desired flight duration is achieved.

The analytical design techniques generate the transfer trajectory for a given transfer opportunity viz. departure epoch and flight duration. Generally the minimum-energy opportunity is computed using some gradient-based optimization technique under the patched conic force model. For Galileo mission, the trajectory optimization was carried out using the Newton algorithm and the trajectory propagation was carried out using the multiconic (pseudostate) technique [D'Amario et al., 1982]. D'Amario (1989) gives the details of the softwares, MOSES and PLATO, which generate the optimal trajectory design. Many authors have used the differential correction technique for various purposes in the interplanetary mission design. Byrnes (1970) used the differential correction, as pointed out earlier, to match the incoming and outgoing V-infinity vectors in the context of gravity assist transfers. D'Amario et al. (1981) used this technique for multiple flyby trajectories. As already mentioned, Clarke et al. (1966) used the differential correction process to refine the outgoing V-infinity vector to achieve the target B-plane coordinates for direct interplanetary missions. For direct interplanetary transfers, in general, the minimum energy opportunity is found using a simple grid search [Sergeyevsky, 1953]. A large number of global search methods have also been employed for the selection of minimum-energy opportunity. For the direct interplanetary mission, genetic algorithm [Gage et. al., 1995] was used for trajectory optimization under the patched conic framework. An ant colony algorithm was applied to design the trajectory for a simple, two-impulse Earth–Mars transfer [Radice and Olmo, 2006]. Many authors have used optimization techniques to explore solutions for several space trajectory problems such as low-thrust and impulsive transfers **[**Pamadi, 1995; Rauwolf et al., 1996; Rauwolf and Coverstone-Caroll, 1996; Hartmann et al., 1998; Coverstone-Caroll et al., 2000; Hughes and McInnes, 2001; Gurfil and Kasdin, 2002; Betts and Orb, 2003; Dachwald, 2004; Becerra et al., 2005; Izzo, 2006; Woo et al., 2006; Izzo et al., 2006; Addis et al., 2011; Vasile and DePascale, 2006; Vasile et al., 2006; Sentinella and

Casalino, 2009; Vasile et al., 2010; Vasile and Zuiani, 2010**]**. Vasile et al. (2005) used an evolutionary optimization technique to design the optimal gravity assist transfers based on the Lambert conic force model. Other optimization techniques that are used to find the minimum energy opportunity for gravity-assist missions under the patched conic assumptions are hybrid global-local search (Crain et al., 2000) and differential evolution (Olds et al., 2007) techniques.

The analytical trajectory design obtained using the patched conic model, in general, is used as the initial guess and later refined in the precision mode (numerical design process). It is desirable to obtain an analytical solution that is close to the numerical design under the full-force model. A close initial guess reduces the computational time for numerical refinement and also aids in converging to the precise design which is discussed in section 3.2. In the absence of a good initial guess, there is a possibility that the numerical refinement process does not converge to the desired solution or does not converge at all. The close initial guess is obtained by including the effect of perturbations in the analytical trajectory design process. There are numerous studies on lunisolar perturbations i.e., the third body perturbations of the Sun and the Moon, on an Earth orbiting satellites. Also, there are studies on the perturbing effect of the non-spherical gravity of Earth on an Earth orbiting satellite. King-Hele (1958), the pioneer in this area, developed analytical theories to study the effect of Earth's oblateness on an Earth-orbiting satellite. The closed form solution is obtained using a perturbation technique and is applicable to satellite orbits with eccentricity less than 0.05. Kozai (1959) derived the closed-form expressions to account for the principal secular and long-periodic terms of the lunisolar perturbations by expressing the disturbing function in terms of the orbital elements of the Sun and the Moon. Musen (1961) included the parallactic term in addition to the lunisolar perturbations in the disturbing function and developed the Fourier series expressions. Blitzer (1959) computed the precession of satellite orbits due to the lunisolar perturbations using the closed form expressions obtained with secular terms only. Later, Kozai (1962) derived the closed form expressions to account for the secular perturbations of Jupiter on asteroids with high inclination and eccentricity. Many authors studied the effect of perturbations using the Lagrange planetary equations and numerical approximations. Cook (1962) used the Lagrange's planetary equations to obtain expressions for the variation of the orbital elements averaged over one revolution of the satellite. Kaula (1962) developed the lunar and solar disturbing function for a close satellite and developed a quasi-potential for the radiation pressure effects that were

included in the equations of motion. Kozai (1963) introduced the disturbing function accounting for the Sun and the Moon by including both secular and long periodic terms and formulated the equations of motion. Roy (1969) presented a study on the lunisolar perturbations on an Earth satellite. Giacaglia (1973) derived the disturbing function accounting for the disturbance of the Moon. He derived the closed form expressions for secular, long and short periodic terms separately using the disturbing function. Kozai (1973) developed another method to calculate the effect of lunisolar perturbations by expressing the disturbing function in a novel way. The term that represents the central body (Earth) force in the disturbing function is expressed in terms of the orbital elements and the terms that represent the Sun and the Moon are expressed in terms of polar geocentric coordinates. This representation eliminated the short-periodic terms by averaging over the mean anomaly of the satellite and aided to calculate the secular and long periodic effects with a larger step size for numerical integration. Lane (1989) developed analytical expressions for modeling the effect of lunar perturbations on Earth-orbiting satellites. Montenbruck and Gill (2000) consolidated the expressions for lunisolar and non-spherical Earth gravity perturbations on Earth satellites. Solórzano et al. (2004) studied the effect of the third body perturbation in the spacecraft motion. They developed a semi-analytical study of the perturbation by a single averaged model. One of the most important applications is to calculate the effect of lunar and solar perturbations on high-altitude Earth satellites. Hough (1981) studied the effects of the lunisolar disturbance in orbits. Hough (1981) studied the effects of the lunisolar disturbance in orbits close to the inclinations 63.4 deg and 116.6 deg (critical inclinations with respect to the Geopotential of Earth) and concluded that the effects are significant in high altitudes. Narumi and Hanada (2007) presented new expressions for the rate of change of orbital elements to account for the gravitational forces of the Sun and the Moon. They analyzed the long-term effects of orbital perturbations based on the analytic models of third-body forces and conventional analytical models of atmospheric drag, solar radiation pressure and zonal harmonics. Domingos et al. (2008) presented a semi-analytical and numerical study of the perturbation effected on a spacecraft by a third-body using a double averaged analytical model with the disturbing function expanded in Legendre polynomials up to the second order. All these studies deal with the lunisolar and non-spherical Earth gravity perturbations on Earth orbiting satellites or closed orbits. In the context of lunar transfer, Byrnes and Hooper (1970) discussed an analytical design technique that included the third-body effects of the Sun and the Moon, and also the non-

spherical gravity effect of Earth. They accounted the third-body perturbation effects averaged over a specified time step used for multiconic propagation. The non-spherical gravity of Earth was accounted using the analytical expressions obtained from Penzo (1970). Recently, Zhang et al. (2014) developed a linear approximation (LA) based fast prediction algorithm to generate the transfer trajectory for lunar transfer including the effects of the non-spherical gravity perturbation of the Earth and the third-body effects of the Moon. ***Specifically, there is no study available in the literature to the best of knowledge of the author that deals with perturbations for analytical trajectory design in the context of interplanetary transfers.***

1.3 Motivation of the Research

There are noticeable limitations with the conventional analytical techniques that are used for transfer trajectory design. These techniques generate trajectory designs under certain assumptions on the force models. These assumptions lead to the generation of only notional and approximate designs. The conventional analytical designs result in large deviations in the arrival target parameters on numerical propagation under the design force model. These are mainly due to the following reasons.

1) Discontinuities in position and velocity vectors at the SOI due to certain assumptions.
2) Non-inclusion of the perturbations such as the non-spherical gravity of Earth and the third-body effects of the Moon and the Sun in the analytical trajectory design process.

These factors make the conventional analytical design a poor initial guess for the trajectory design process and as such cannot be used for actual mission planning.

Also, for any opportunity, there are two geometries for the departure/arrival hyperbolic orbit that contains the corresponding V-infinity vector in its plane. These are the ascending and the descending geometries of the hyperbolic orbit with respect to the planet equatorial plane. Connecting these orbits at the departure and the arrival phases result in four distinct design options for transfer trajectories. ***Note that the conventional analytical techniques provide only notional designs of the transfer trajectories and does not identify the four distinct design options for an opportunity (Ramanan and Adimurthy, 2005).*** With the conventional designs as initial guess, the numerical refinement process takes about a day and requires manual intervention for convergence to the desired design option.

Further, the conventional analytical techniques do not provide the parking orbit characteristics accurately. For an interplanetary orbiter mission, such parameters are of great interest. Even a small deviation in the orbit characteristics will lead to missing the target. So, the conventional analytical techniques do not serve as a mission analysis tool. For example, how much the departure design will have to vary, in order to achieve different inclinations of the arrival parking orbit, cannot be assessed using the conventional techniques. So, the current research focuses on developing analytical design techniques for the trajectory design of direct interplanetary orbiter missions removing the limitations of the conventional design techniques.

1.4 Objectives of the Research

The aim of the current research is to develop analytical design techniques that serve the following objectives,

1) ***Remove the position and velocity discontinuities at the boundary of SOI of the target planets***

   In the existing literature, in general, these discontinuities are removed using numerical/brute force methods. There is one analytical technique that already exists in the literature called one-step pseudostate technique (Sergeyevsky, 1983). But it deals with only rectilinear hyperbolas that lead to impact. The current research aims to relax the assumption of rectilinear hyperbola and develop improved analytical techniques.

2) ***Include the gravity perturbations due to the non-spherical Earth and the third body effects of the Moon and the Sun in the analytical trajectory design process***

   In the existing literature, there is no analytical model that considers all the aforementioned perturbations together in the trajectory design process.

3) ***Identify the distinct design options for an opportunity***

   In the current literature, the analytical design techniques generate only one option of the trajectory design for a given opportunity.

4) ***Generate good initial guess for numerical refinement***

   The conventional analytical techniques provide poor initial guess for numerical refinement and the numerical process require additional information on the arrival condition for convergence to the desired design option. So, the current research essentially aims to develop analytical techniques that generate quick

initial guess for the desired design option as close as possible to the numerical design.

5) ***Serve as a quick mission design and analysis tool***

The objective is to develop analytical techniques that can be used to quickly generate accurate designs for the large number of mission scenarios in the design analysis process.

1.5 Research Summary

With the goal of achieving the aforementioned objectives, the current research explores both the ***patched conic*** and ***pseudostate concepts*** for the analytical trajectory design. Initially, the four notional design options for an opportunity are obtained using the conventional patched conic technique which is the most commonly used analytical technique. These design options result in large deviations in the arrival target parameters such as the closest approach altitude, inclination of hyperbolic orbit and time of periapsis, on numerical propagation under the design force model. By 'design force model', we mean the force model that is used to generate the analytical trajectory design. The conventional patched conic design options must be modified/tuned to achieve the V-infinity vector at the SOI. This is carried out using an analytical tuning strategy adopted from Ramanan (2002). The patched conic technique that uses the analytical tuning strategy is named as ***V-infinity tuned patched conic (VPC) technique***. This technique generates design options which on numerical propagation under the design force model result in improved achievable accuracies in the arrival target parameters, but the deviations from the desired values are still large. Moreover, the VPC technique fails to identify the distinct design options for an opportunity.

To improve the design, the research initially focused on developing a trajectory design technique based on the pseudostate concept for direct interplanetary orbiter missions. The inherent advantage of the pseudostate concept is the inclusion of the Sun's gravity even in the vicinity of the target planets (within the pseudosphere/extended SOI). An iterative method based on the one-step pseudostate concept, named as ***iterative pseudostate (ITR-PS) technique,*** is developed. The iterative nature of this technique helps identify the four distinct design options for an opportunity. The analytical tuning strategy is used to tune the departure/arrival hyperbolic orbit characteristics to achieve the departure/arrival V-infinity vectors at the pseudosphere. The ITR-PS technique provides improved design in terms of the achieved target parameters as compared to the

conventional techniques. However, numerical propagation of the ITR-PS design under the design force model results in large deviation in the arrival hyperbolic inclination. This can be reduced by using the multi-step pseudostate technique, instead of the one-step pseudostate technique, in the departure and arrival phases. The analytical tuning strategy is not suitable for the multi-step technique and so an optimization technique, differential evolution, is used to search for the departure/arrival hyperbolic orbit characteristics to achieve the departure/arrival V-infinity vector at the SOI. This technique, named as ***multiconic differential evolution (MCDE) technique*** refines the ITR-PS design. The numerical propagation of the MCDE design under the design force model results in only small deviations in the target parameters. However, in both of these techniques, the trajectory design is heliocentric even in the neighborhood of Earth and so inclusion of gravity perturbations of the non-spherical Earth is not straight forward. These techniques derive the merit in identifying the four design options for an opportunity distinctly.

To overcome the difficulties of the pseudostate technique, the patched conic concept which considers one gravity body at a time is used. An iterative technique based on the patched conic concept, named as ***iterative patched conic (ITR-PC) technique***, is developed. This iterative technique clearly identifies the four distinct design options for an opportunity. The computation time required for numerical refinement of the ITR-PC design is less and so, this technique is efficiently used to analyze various departure and arrival scenarios for the four design options. The numerical propagation of the ITR-PC design options under the design force model results in very small deviations in the target parameters. However, when the ITR-PC design is numerically propagated under a force model that includes perturbations, the achieved arrival target parameters result in large deviations from the desired values. Because of this, if the ITR-PC design is used as the initial guess, the numerical refinement under the force model including perturbations can converge to any of the four possible design options. To arrive at the desired option, additional information on the arrival geometries must be provided. Thus, it is desirable to generate a better initial guess which is attempted by including the perturbations in the analytical design process. The technique thus developed is named as ***biased-iterative patched conic (B-ITRPC) technique***.

The B-ITRPC technique generates the transfer trajectory design close to the numerical design. The computation time required for generating the B-ITRPC design is about 25 s. The numerical refinement process of the B-ITRPC design takes about 5 s to converge to the desired design option without the help of any additional information. Note

that the same process using the numerical technique will require a computation time of about a day and requires manual intervention to converge to the desired design option. Therefore, the B-ITRPC technique can be used as a powerful design analysis tool without resorting to numerical technique. Further advantage of the B-ITRPC technique is that the total velocity impulse (sum of transplanetary injection (TPI) and parking orbit insertion (POI)) required by the B-ITRPC design is less (by about 56 m/s) as compared to that required by the conventional patched conic design.

1.6 Thesis Architecture

The current thesis includes seven chapters, each of which are outlined below.

- **Chapter 1**: This chapter outlines an introduction on the research topic. A brief literature review of the available data on the research topic is presented. The limitations of the existing techniques which motivated the current research is discussed. The objectives of the research and a brief summary is presented. The thesis architecture is explained in this chapter.
- **Chapter 2**: The conventional analytical techniques used for trajectory design are discussed in detail. These include the interplanetary Hohmann transfer, conventional patched conic technique and its variants, and the conventional pseudostate technique. The Lambert problem which is central to all analytical design techniques is also discussed in this chapter.
- **Chapter 3**: This chapter discusses the analytical tuning strategy that generates the hyperbolic orbit characteristics to achieve the V-infinity vector at the planet SOI/pseudosphere. For the transfer to occur with a minimum velocity impulse, the parking orbit (PO) and the hyperbolic orbit must be coplanar. Using this concept, a technique to obtain the parking orbit characteristics is presented. Also, the V-infinity tuned patched conic technique (VPC) is discussed in detail.
- **Chapter 4**: The analytical trajectory design techniques developed based on the pseudostate concept are discussed. The first part of the chapter presents the iterative pseudostate technique (ITR-PS) which results in four distinct design options for an opportunity. The second part of the chapter presents the multiconic differential evolution technique (MCDE) that refines the ITR-PS design.
- **Chapter 5**: In this chapter, the iterative patched conic technique (ITR-PC) is described. This technique exploits the simplicity of the conventional patched conic technique and identifies the four distinct design options in very short span of time.

The use of this technique for quick mission design and analysis of all the four design options is demonstrated using an Earth to Mars orbiter mission (Type I transfer).

- **Chapter 6**: This chapter deals with the biased-iterative patched conic technique (B-ITRPC). This technique generates the analytical design accounting for the non-spherical gravity perturbations of the Earth and the third-body effects of the Moon and the Sun in the departure phase of the interplanetary transfer trajectory. The analytical propagation is carried out using the linear approximation technique and the states are updated using the closed form solution obtained from the generalized spectral decomposition theorem. The B-ITRPC technique yields design very close to the numerical design. The use of this technique as a powerful mission design and analysis tool is demonstrated using an Earth to Mars orbiter mission (Type II transfer). The trends and tradeoffs of various realistic mission scenarios can be understood from this analysis. The B-ITRPC technique is used to analysis the trajectory designs of the MOM and MAVEN missions. Also, the B-ITRPC designs are generated and presented for direct transfers from Earth to Jupiter and Earth to Venus for the minimum energy opportunities of 2022 and 2023 respectively. A comparison of the performance of different analytical trajectory design techniques based on the patched conic concept is provided in this chapter.
- **Chapter 7**: This chapter summarizes the merits of the proposed analytical techniques and consolidates the major inferences drawn from the analysis. The future scope of this research is also presented.

♠♠♠♠♠♠♠♠♠♠♠♠♠♠♠♠♠♠♠

CHAPTER 2
CONVENTIONAL ANALYTICAL TECHNIQUES FOR TRANSFER TRAJECTORY DESIGN

2.1 Chapter Summary

This chapter gives an account of the conventional analytical techniques available in the literature for transfer trajectory design. These techniques provide quick solutions that are used as the initial guess for numerical refinement under high-fidelity force models. First, the Hohmann interplanetary transfer which gives a two-dimensional transfer trajectory is discussed. The central part of all the analytical trajectory design techniques is the Lambert problem. This chapter includes a discussion on the Lambert problem and a comparison of two solution methods that are based on universal variables. Then, the conventional patched conic technique which is the most commonly used analytical design technique is presented. Another conventional design technique based on the pseudostate concept, the one-step pseudostate technique, which provides improved trajectory design is also discussed. These conventional techniques generate the V-infinity vector which is the main design parameter for an interplanetary transfer. This chapter brings out the assumptions, merits and demerits of the conventional analytical techniques.

2.2 Introduction

> "*the probability of finding there (Venus) an atmosphere and consequently conditions for life, similar to those on Earth, is so great, and the difficulties of the one-way trip there - having once established the station on Moon - so small that presumably Venus must be primarily considered as a goal for immigration, Mars on -the other hand a goal for scientific investigation trips*".
>
> -Walter Hohmann

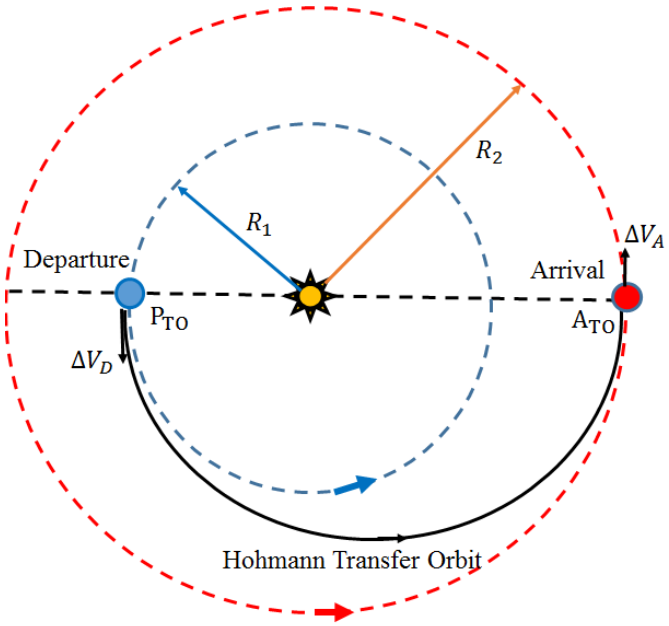

Fig. 2.1a. Geometry of a typical Hohmann (coplanar) transfer

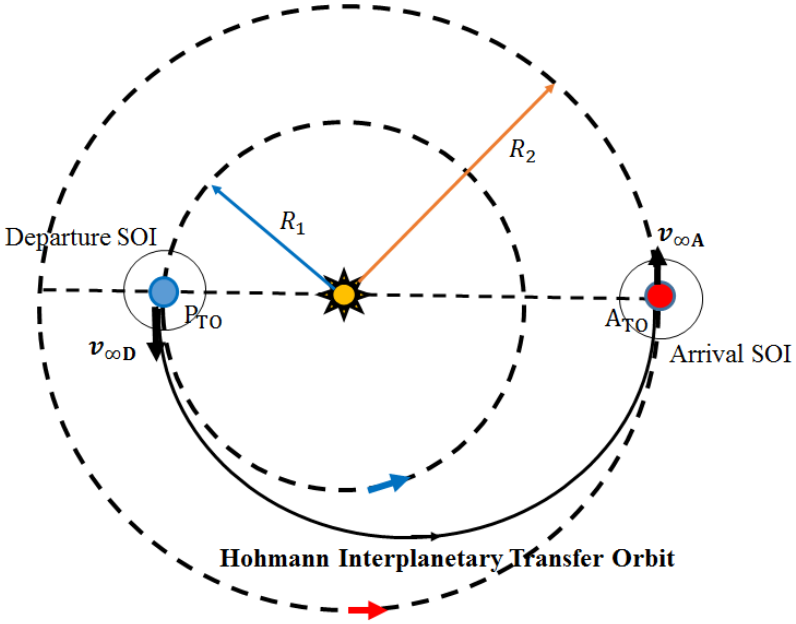

Fig. 2.1b. Geometry of a Hohmann interplanetary transfer

The pioneer in the field of astrodynamics who had serious thoughts for interplanetary travel is Walter Hohmann. In 1925, he introduced the first analytical method for trajectory design in his book "The Accessibility of Celestial Bodies" (NASA technical translation, 1960). The Hohmann transfer is essentially a heliocentric transfer between the orbits of the target planets i.e. the departure and arrival planets. The planetary orbits are assumed as circular and coplanar. Fig. 2.1a shows the typical Hohmann transfer from an inner orbit to an outer orbit. The periapsis (P_{TO}) of the Hohmann transfer orbit is at the initial circular

orbit (radius, R_1) and apoapsis (A_{TO}) is at the final circular orbit (radius, R_2). The Hohmann transfer orbit is tangential to both the inner and outer orbits and elliptic with respect to the Sun. This transfer is a minimum-energy, two-impulse transfer between two coplanar circular orbits.

The Vis-Viva equation yields the magnitude of the heliocentric velocity vectors at the periapsis $(V_{P_{TO}})$ and apoapsis $(V_{A_{TO}})$ of the Hohmann Transfer Orbit,

$$V_{P}^{2}{}_{TO} = \mu_s \left(\frac{2}{R_1} - \frac{1}{a_{TO}}\right) \tag{2.1}$$

$$V_{A}^{2}{}_{TO} = \mu_s \left(\frac{2}{R_2} - \frac{1}{a_{TO}}\right) \tag{2.2}$$

where the subscript 'P/A' denotes periapsis/apoapsis, parameter 'μ_s' is the gravitational constant of the Sun and 'a_{TO}' is the semi-major axis of the elliptic (heliocentric) transfer trajectory which is given by,

$$a_{TO} = \frac{R_1 + R_2}{2} \tag{2.3}$$

The velocity impulses (ΔV) for the two-impulse transfer are easily computed as follows. The departure velocity impulse (ΔV_D) for departure from a circular orbit of radius R_1 is,

$$\Delta V_D = V_{P_{TO}} - \sqrt{\frac{\mu_s}{R_1}} \tag{2.4}$$

The arrival velocity impulse (ΔV_A) upon arrival at the circular orbit of radius R_2 is,

$$\Delta V_A = \sqrt{\frac{\mu_s}{R_2}} - V_{A_{TO}} \tag{2.5}$$

The total velocity impulse required for the transfer is given by,

$$\Delta V_{total} = \Delta V_D + \Delta V_A \tag{2.6}$$

In practice, Hohmann transfers provide an approximate quick estimate of the velocity impulses required for a particular mission.

2.3 Hohmann Interplanetary Transfer

The interplanetary transfer trajectory is obtained by connecting the heliocentric orbits of the target planets. The gravitational influences of the target planets are superimposed over

the Sun's gravity field using the concept of the sphere of influence (SOI). The assumption used here is the patched conic assumption, i.e. the heliocentric velocity vector at the SOI and the departure/arrival are same. Fig. 2.1b shows the Hohmann interplanetary transfer from an inner orbit to an outer orbit. The departure and arrival velocity impulses, given by the Eqs. 2.4 and 2.5, are used as the magnitude of the departure and arrival V-infinity vectors i.e. v_{∞_D} and v_{∞_A} respectively, for the interplanetary transfer.

$$\left.\begin{aligned} v_{\infty_D} &= \Delta V_D \\ v_{\infty_A} &= \Delta V_A \end{aligned}\right\} \tag{2.7}$$

The Hohmann interplanetary transfer provides only the magnitude of the V-infinity vector and not the direction. However, this method is helpful to determine the region in which the minimum-energy opportunity occurs for an interplanetary mission. This is because the actual transfer geometry for an interplanetary mission occurs near the Hohmann geometry.

2.4 Selection of solution method for Lambert problem

The Hohmann transfer does not consider the actual positions of the target planets. This lead to the development of various other analytical trajectory design techniques. When the actual positions are considered, the connecting arc is determined as the solution to the Lambert problem. All the analytical design techniques use the Lambert problem solution as the baseline solution. So, in this section, Lambert problem and two of its solution methods are discussed.

The Lambert problem determines the trajectory connecting two position vectors with a known transfer time. A typical interplanetary transfer involves connecting the departure and arrival planetary positions. This results in an elliptical (heliocentric) trajectory between the target planets. The solution to the Lambert problem is obtained using the Lambert's theorem. The Lambert's theorem states that, in an elliptic orbit, the transfer time between two points depends only on the semi-major axis, sum of the distances from the primary focus to each of the two points, and the chord length between

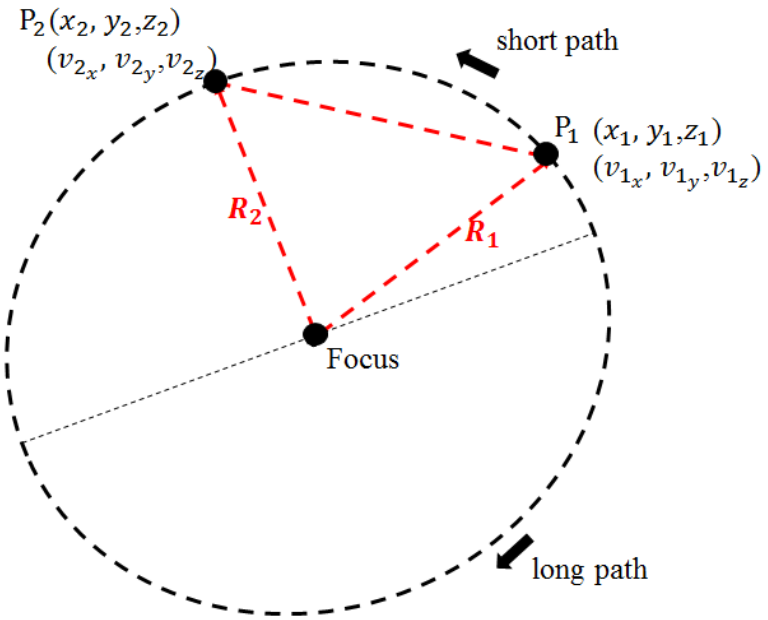

Fig. 2.2. Geometry of Lambert problem

them. The solution of the Lambert problem is the heliocentric departure velocity vector in the transfer orbit. With the initial position and velocity vectors of the spacecraft fully known, the transfer trajectory is obtained.

Several methods are available in the literature to solve the Lambert problem. Some methods iterate on one of the orbital parameters and obtain the solution. While some of these methods have singularities for large transfer angle, some others are applicable only for specific type of conics. The solution methods developed based on the universal variables (Bate et al., 1971) are widely used because of their elegance and robustness. The universal methods developed by Battin (1987) and Vallado (1997) can be applied to all types of conics and have shown robustness to most of the singularity conditions. So, these methods have been implemented in the current research. All these methods fail as the transfer angle between the departure and arrival position vectors of the trajectory segment approaches 180 deg (collinear). This is because an infinite number of transfer planes exist connecting the collinear position vectors.

For performance comparison, some cases have been solved using the universal methods. These cases have been generated using some reference orbits and they cover all types of conics. The geometry for the Lambert problem is shown in Fig. 2.2. The two points considered are P_1 and P_2. The position vectors are given in terms of Cartesian coordinates (x_1, y_1, z_1) and (x_2, y_2, z_2), and the flight duration connecting them is fixed. The solution of the Lambert problem is the velocity vector at P_1. The initial state is

propagated for the transfer time to obtain the velocity vector at P_2. For the reference orbit, a geocentric coordinate frame with Earth equator and Equinox of J2000 is used. From the reference orbit, the points P_1 and P_2 are obtained at two time instances. The inputs to the Lambert problem are the position vectors of these points and the transfer time $(t_f - t_i)$.

Tables 2.1 to 2.4 present the solution of the Lambert problem, for some of the cases, obtained using the two universal methods. These cases include different type of conics: elliptic posigrade, elliptic retrograde, circular and hyperbolic. The difference between the reference and determined velocity vectors at P_1 is presented. Also, the position vector and the determined velocity vector at P_1 are used to obtain the transfer trajectory which is given in the table. The transfer trajectory is represented in terms of the orbital elements $(a, e, i, \Omega, \omega, \nu)$ where a is the semi-major axis, e is the eccentricity, i is the inclination, Ω is the right ascension of ascending node, ω is the argument of periapsis and ν is the true anomaly. It is evident that the transfer trajectory determined using Vallado's method has higher accuracy as compared to Battin's method. It has been observed that, compared to Battin's method, Vallado's method takes very less computation time even though the number of iterations to converge to the solution is more (cf. Table 2.1).

Both the methods perform in a similar fashion for all the cases except for those with transfer angles approaching 180 deg. Some such cases are solved using both the universal methods. An elliptical posigrade orbit is taken as the reference orbit. Table 2.5 shows the determined transfer trajectory for two cases with: (i) transfer angle: 180.001 deg and (ii) transfer angle: 180.0001 deg. It can be noted that the deviations in the orbital elements are large for the solution obtained using Battin's method as compared to that from Vallado's method. Table 2.6 gives the deviation in velocity vector for many cases when the transfer angle approaches180 deg with higher precision. ***Note that for the solution obtained using Battin's universal method, the deviation in the velocity vector increases by one order as the precision of the 180 deg transfer increases. With Vallado's solution, although the deviation increases by two order, the magnitude of deviation is very small.*** Hence, it is concluded that Battin's universal method suffer more in the 180 deg transfer regime as compared to Vallado's universal method. Thus, Vallado's universal method is found to be efficient for all types of conics and also near 180 deg transfer cases. Therefore, this solution method is adopted in the current research.

Table 2.1 Elliptic posigrade orbit (transfer angle = 100 deg, transfer time = 7.342 h)

Orbital elements	Reference orbit	Battin's method	Vallado's method
a (km)	50000.0000	50000.0039	50000.0000
e	0.20000000	0.20000006	0.20000000
i (deg)	40.0000000	39.9999999	39.9999999
Ω (deg)	30.0000000	30.0000000	29.9999999
ω (deg)	140.000000	139.999999	140.000000
ν_{t_i} (deg)	20.0000000	20.0000003	19.9999999
Δv (m/s)	-	1.076654E-04	8.22847E-8
No. of iterations/ computation time (ms)	-	3 / 0.20	32 / 0.05
Initial time t_i: x_1 = -38175.67 km, y_1 = -9816.48 km, z_1 = 8883.13 km Final time t_f: x_2 = 12097.04 km, y_2 = -39475.16 km, z_2 = -33761.18 km			

Table 2.2 Elliptic retrograde orbit (transfer angle = 100 deg, transfer time = 7.342 h)

Orbital elements	Reference orbit	Battin's method	Vallado's method
a (km)	50000.0000	50000.0039	50000.0000
e	0.20000000	0.20000006	0.20000000
i (deg)	100.000000	100.000000	100.000000
Ω (deg)	30.0000000	29.9999999	29.9999999
ω (deg)	140.000000	139.999999	140.000000
ν_{t_i} (deg)	20.0000000	20.0000003	19.9999999
Δv (m/s)	-	1.076654E-04	1.13567E-7
x_1 = -31682.53 km; y_1 = -21062.93 km; z_1 = 13609.75 km at t_i x_2 = -12580.73 km; y_2 = 3267.99 km; z_2 = -51725.13 km at t_f			

Table 2.3 Circular orbit (transfer angle = 100 deg, transfer time = 8.585 h)

Orbital elements	Reference orbit	Battin's method	Vallado's method
a (km)	50000.0000	50000.0026	49999.9999
e	0.00000000	5.67004E-08	2.23727E-11
i (deg)	40.0000000	40.000000	40.000000
Ω (deg)	30.0000000	29.999999	29.999999
ω (deg)	140.000000	140.491316	30.000204
ν_{t_i} (deg)	20.0000000	19.5086834	129.999795
Δv (m/s)	-	9.24719E-5	4.40366E-9
x_1 = -47239.94 km; y_1 = -12147.26 km; z_1 = 10992.31 km at t_i x_2 = 11340.97 km; y_2 = -37007.96 km; z_2 = -31651.11 km at t_f			

Table 2.4 Hyperbolic orbit (transfer angle = 50 deg, transfer time = 0.3940 h)

Orbital elements	Reference orbit	Battin's method	Vallado's method
a (km)	-50000.0000	-49999.9936	-49999.9993
e	1.20000000	1.2000000	1.2000000
i (deg)	40.0000000	40.000000	39.999999
Ω (deg)	30.0000000	29.999999	29.999999
ω (deg)	10.0000000	9.9999993	10.000000
ν_{t_i} (deg)	20.0000000	20.000006	19.999999
Δv (m/s)	-	9.20040E-5	7.78215E-7
x_1 = 5774.85 km; y_1 = 7907.30 km; z_1 = 3323.25 km at t_i x_2 = -3537.96 km; y_2 = 11545.11 km; z_2 = 9873.97 km at t_f			

Table 2.5 Elliptic posigrade orbit for transfer angles approaching180 deg

Orbital elements	Transfer angle = 180.001 deg		Transfer angle = 180.0001 deg	
	Battin's method	Vallado's method	Battin's method	Vallado's method
a (km)	49704.512	49999.994	47264.826	49998.655
e	0.195411	0.199999	0.15586	0.19997
i (deg)	39.9999	39.9999	39.9999	39.9999
Ω (deg)	30.0000	30.0000	30.0000	30.0000
ω (deg)	139.5957	139.9999	135.0606	139.9980
ν_{t_i} (deg)	20.4042	20.0000	24.9393	20.0019
P_2 (km)	x_2 = 55845.81 y_2 = 14361.01 z_2 = -12994.21		x_2 = 55845.94 y_2 = 14360.29 z_2 = -12994.79	
Reference orbit: a = 50000 km; e = 0.2; i = 40 deg; Ω = 30 deg; ω = 140 deg; ν_{t_i} = 20 deg P_1: x_1 = -38175.67, y_1 = -9816.48, z_1 = 8883.13				

Table 2.6 Deviation in velocity vector for transfer angles approaching 180 deg

(Elliptic posigrade orbit, cf. Table 2.5)

Transfer angle (deg)	Δv (m/s)	
	Battin's method	Vallado's method
180.010000	0.69	5.93E-6
180.001000	6.91	1.26E-4
180.000100	67.26	3.12E-2
180.000010	576.55	2.34
180.000001	2294.10	586.30

2.5 Conventional Analytical Techniques

The main aim of these conventional analytical techniques is to determine the V-infinity vector which is the primary design parameter for any interplanetary transfer. Some of the conventional analytical techniques are briefly described below.

1) **Patched conic technique**: In the patched conic technique, the target planet is the primary attracting body within its SOI, elsewhere Sun is the primary attracting body. Thus, the primary bodies act one-at-a-time basis and the interplanetary trajectory is split into three two-body trajectories. The departure/arrival V-infinity vector is computed by using the assumption that the heliocentric velocity vectors at the departure and the SOI are the same. The zero-sphere-of-influence patched conic technique is called the point conic/Lambert conic technique [Battin R.H., 1987] and is discussed in detail in section 2.5.1.
2) **Linked conic technique**: The patched conic technique results in velocity mismatches between the two-body trajectories. In Cornelisse (1978), the linked conic technique is described as an iterative procedure that drives these mismatches to zero. In general, the discontinuities in the velocity vectors are driven to zero using some gradient based methods such as Newton-Raphson method.
3) **Perturbed conic technique**: Bayliss (1970) described this technique taking into account the perturbing effects of the Sun in the planetocentric legs, and of the planets in the heliocentric legs. The reference trajectory is obtained from the linked conic technique. Starting at the mid-point of each trajectory leg, the position and velocity deviations at the end points due to third-body perturbations are calculated by solving quadratures. The requisite mid-point position and velocity offsets are determined analytically such as to nullify the position offsets at end points. The process is repeated to drive the velocity discontinuities to zero.
4) **Pseudostate technique**: Wilson Jr. (1970) introduced this concept wherein the position of the departure and arrival pseudostates are used for Lambert conic determination instead of the actual position of the target planets. The transfer trajectory is considered heliocentric even in the vicinity of the target planet (pseudosphere). This technique superimposes the gravitational force of the target planet over that of the Sun within the pseudosphere and generates the pseudostate. Thus, we have the 3-body force model, Sun-planet-spacecraft, within the pseudosphere. This technique is discussed in detail in section 2.5.2.

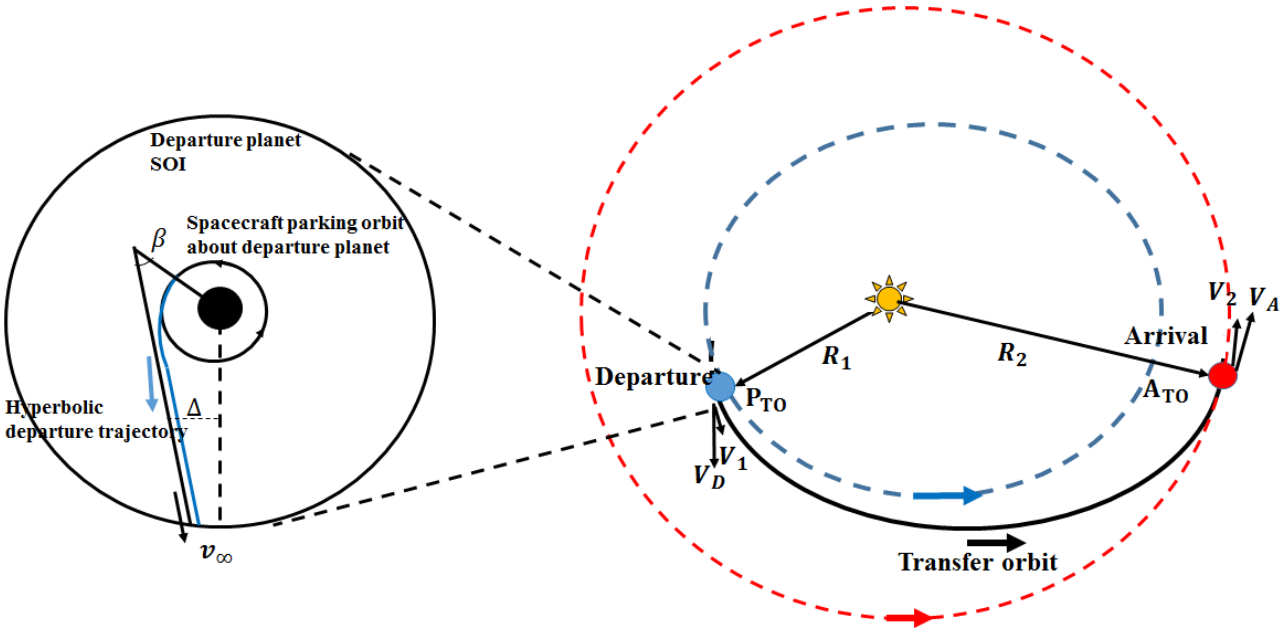

Fig. 2.3. Illustration of Patched conic technique [adopted from Brennan M.J. (2011)]

There are many variants of the patched conic technique like the matched asymptotes [Lancaster, 1973] and the pseudostate technique like the multiconic technique [Byrnes and Hooper, 1970]. These techniques differ mainly on their force models.

2.5.1 Conventional Patched Conic Technique

The conventional patched conic (PC) technique is based on two-body assumptions and generates a reasonably good approximation of the transfer trajectory. The patched conic procedure is used for preliminary mission planning. Brennan (2011) developed a software tool for trajectory design using the patched conic technique. The patched conic approach considers the multiple gravity fields acting on the spacecraft one-at-a-time. Accordingly, the trajectory is divided into heliocentric and planetocentric phases. As stated earlier, these phases are; (i) the geocentric departure hyperbola, (ii) the heliocentric ellipse and, (iii) the planetocentric arrival hyperbola. The region surrounding a planet where its gravity is predominant over the Sun's is defined as the sphere of influence (SOI) of that planet. The patched conic methodology is illustrated in Fig. 2.3.

2.5.1.1 Assumptions

1) Within the SOI, the spacecraft is influenced solely by the planet which is the central body of attraction.
2) Sun influences the spacecraft outside the SOI of the target planets.
3) The heliocentric velocity vector at the departure point and SOI are the same.

2.5.1.2 Methodology

The conventional patched conic (PC) methodology is described as follows. The velocity vectors of the target planets at the departure and arrival epochs are obtained from the ephemeris. Let the heliocentric velocity vector of the departure and arrival planets be $\boldsymbol{V_1}$ and $\boldsymbol{V_2}$ respectively. The heliocentric phase of the transfer trajectory is determined by solving the Lambert problem connecting the position vectors of the target planets at the departure and arrival epochs. The heliocentric velocity vector at the departure epoch is obtained as the solution to the Lambert problem. The departure states are used to find the arrival heliocentric velocity vector. Let the heliocentric velocity vectors be $\boldsymbol{V_{D_{PC}}}$ at the departure and $\boldsymbol{V_{A_{PC}}}$ at the arrival. It is to be noted that the difference between the heliocentric velocity vectors at the departure and the SOI is less than 1 m/s and so, neglected. Thus, from the patched conic assumptions,

$$\left.\begin{aligned} \mathbf{V}_{D_{SOI}} &\cong \boldsymbol{V}_{D_{PC}} \\ \mathbf{V}_{A_{SOI}} &\cong \boldsymbol{V}_{A_{PC}} \end{aligned}\right\} \tag{2.8}$$

The V-infinity vector ($\boldsymbol{v}_\infty$) at the departure and arrival phases are computed as,

$$\left.\begin{aligned} \boldsymbol{v}_{\infty_D} &= \boldsymbol{V}_{D_{SOI}} - \boldsymbol{V}_1 \\ \boldsymbol{v}_{\infty_A} &= \boldsymbol{V}_{A_{SOI}} - \boldsymbol{V}_2 \end{aligned}\right\} \tag{2.9}$$

The heliocentric vector is transformed to the planetocentric reference frame.

2.5.1.3 Illustrative Results

The conventional patched conic technique is applied for an Earth to Mars transfer. The minimum energy opportunity which corresponds to the opportunity having the least value of V-infinity is obtained through grid search. The V-infinity vector is computed using the conventional PC technique. The minimum energy opportunity includes the departure epoch and the flight duration. There are two types of interplanetary transfers, (i) Type I transfer which has a transfer angle less than 180 deg and hence, short flight duration, and (ii) Type II transfer which has a transfer angle greater than 180 deg and hence, long flight duration. For the Earth to Mars transfer, a type I and type II minimum energy opportunity are presented in Table 2.7. The departure and arrival V-infinity vectors for these opportunities obtained using the conventional PC technique are presented in Table 2.8a. The V-infinity vector is represented in terms of its magnitude (v_∞) (km/s) and the orientation angles, right ascension α_∞(deg) and

declination δ_∞(deg). The subscript 'D' or 'A' in these parameters denote the 'departure' or 'arrival' phases. The departure V-infinity is in geocentric coordinate frame with Earth equator and Equinox of J2000. The arrival V-infinity vector is in a Marscentric coordinate frame with Mars equator and IAU vector of J2000. The heliocentric transfer trajectories obtained for the minimum energy opportunities are presented in terms of the heliocentric orbital elements in Table 2.8b.

Table 2.7 Details of minimum energy opportunity for Earth to Mars direct transfer

Departure epoch (TDB) DD/MM/YYYY HH:MM:SS	Flight duration (days)	Transfer angle (deg)	Total velocity impulse (m/s)
12/05/2018 00:00:00 (Type I transfer)	204	152.8	3603.4
30/08/2022 00:00:00 (Type II transfer)	348	212.5	3743.6

Table 2.8a V-infinity vectors from conventional PC technique

Opportunity	Departure V-infinity vector $\{v_{\infty_D}; \alpha_{\infty_D}; \delta_{\infty_D}\}$	Arrival V-infinity vector $\{v_{\infty_A}; \alpha_{\infty_A}; \delta_{\infty_A}\}$
2018	{2.7891; 321.4262; -36.8551}	{2.9621; 245.6645; 9.2562}
2022	{3.8810; 80.3386; 3.2164}	{2.6041; 39.7271; 31.7927}

Table 2.8b Heliocentric transfer trajectory from conventional PC technique

Orbital elements	2018 opportunity	2022 opportunity
a (km)	182,714,816.6	200,701,313.90
e	0.174735	0.249984
i (deg)	24.57	21.36
Ω (deg)	3.27	2.52
ω (deg)	218.24	344.85
ν_{t_i} (deg)	9.74	349.13

For the 2018 opportunity, design charts are obtained based on the data generated using conventional PC technique. The design charts of the magnitude (km/s) and declination (deg) of the departure V-infinity vector are shown in Figs. 2.4 and 2.5. Note that, in Fig. 2.4, the minimum value of the departure V-infinity vector (2.78 km/s) occurs on 17th May 2018 and the corresponding flight duration is 234 days. This opportunity can be chosen for minimum energy flyby or gravity assist missions. Also, the minimum value

of the total V-infinity vector (5.74 km/s) occurs on 12th May 2018 and the corresponding flight duration is 204 days.

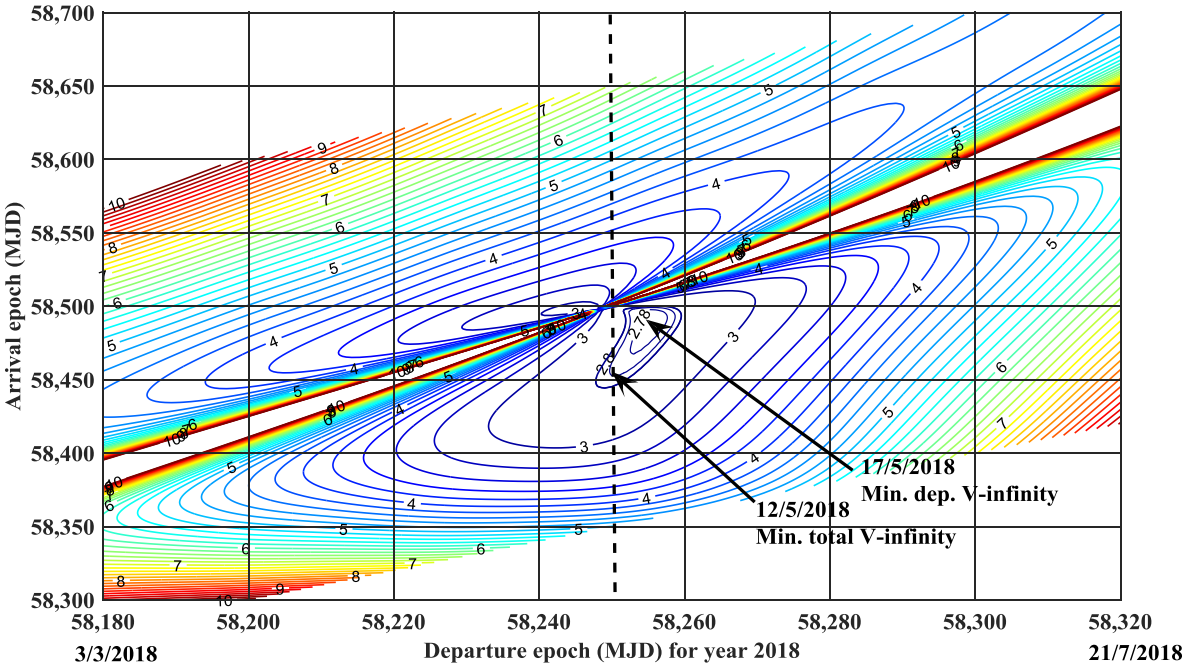

Fig. 2.4. Design chart: Magnitude of departure V-infinity vector (2018)

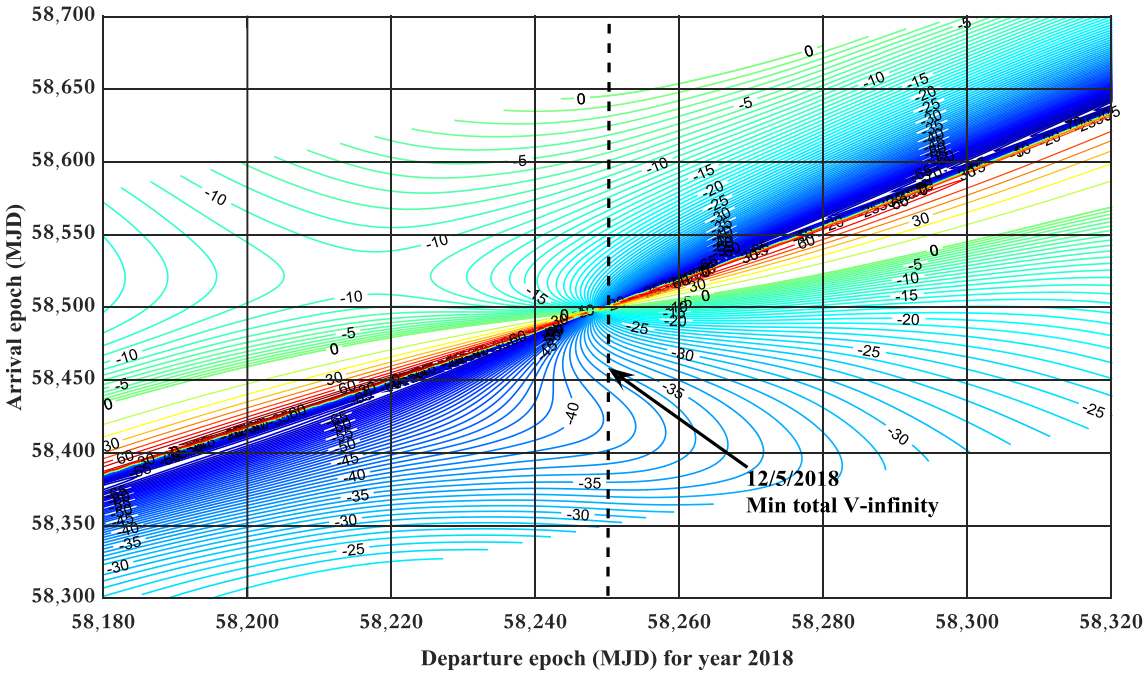

Fig. 2.5. Design chart: Declination of departure V-infinity vector (2018)

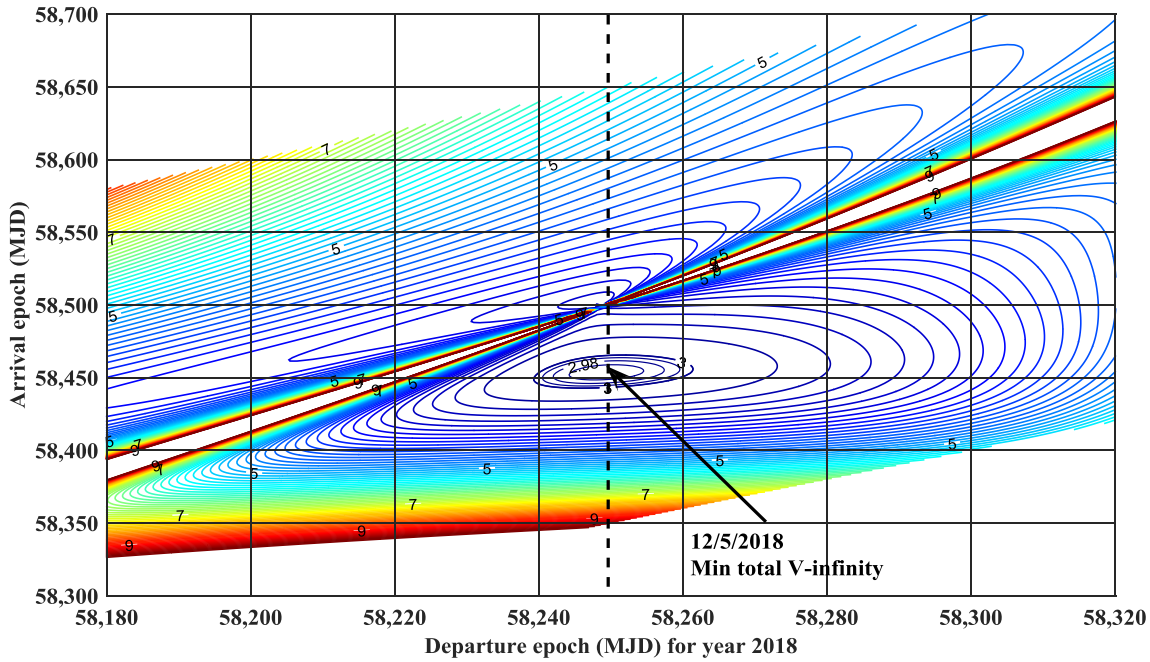

Fig. 2.6. Design chart: Magnitude of arrival V-infinity vector (2018)

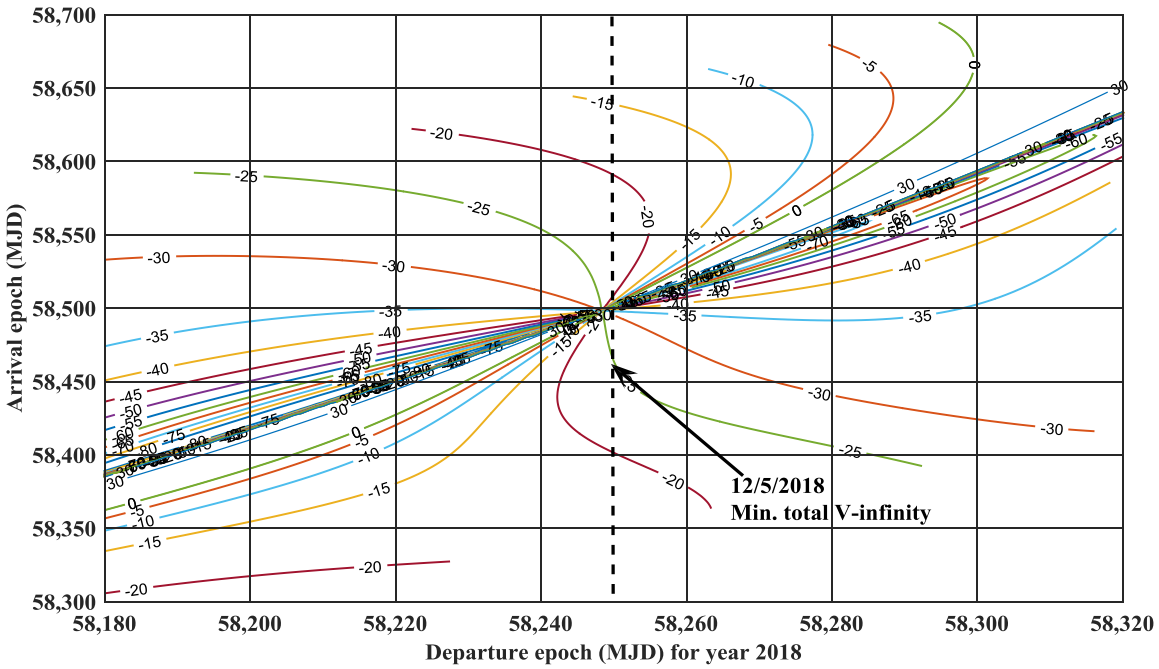

Fig.2.7. Design chart: Declination of arrival V-infinity vector (2018)

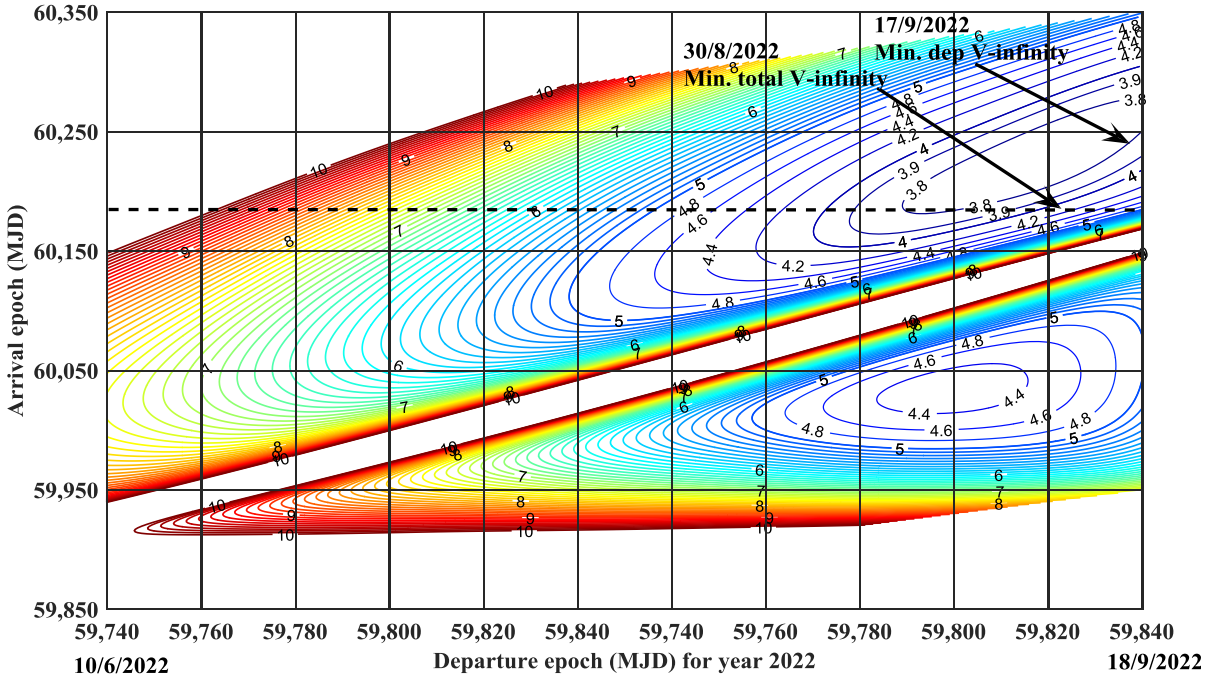

Fig. 2.8. Design chart: Magnitude of departure V-infinity vector (2022)

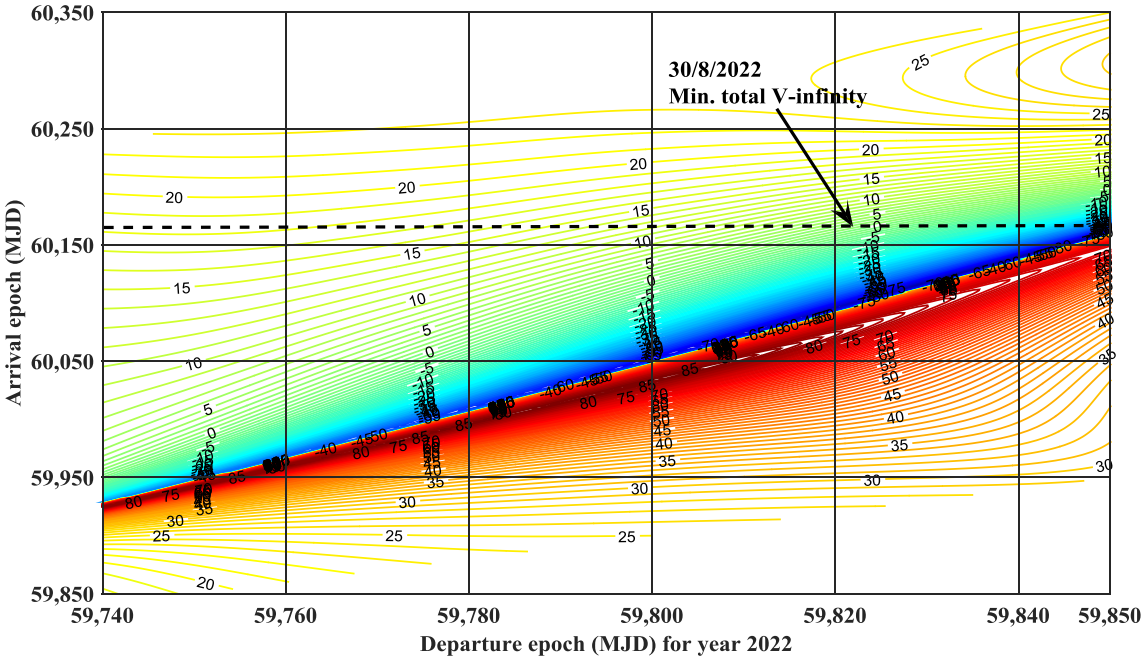

Fig. 2.9. Design chart: Declination of departure V-infinity vector (2022)

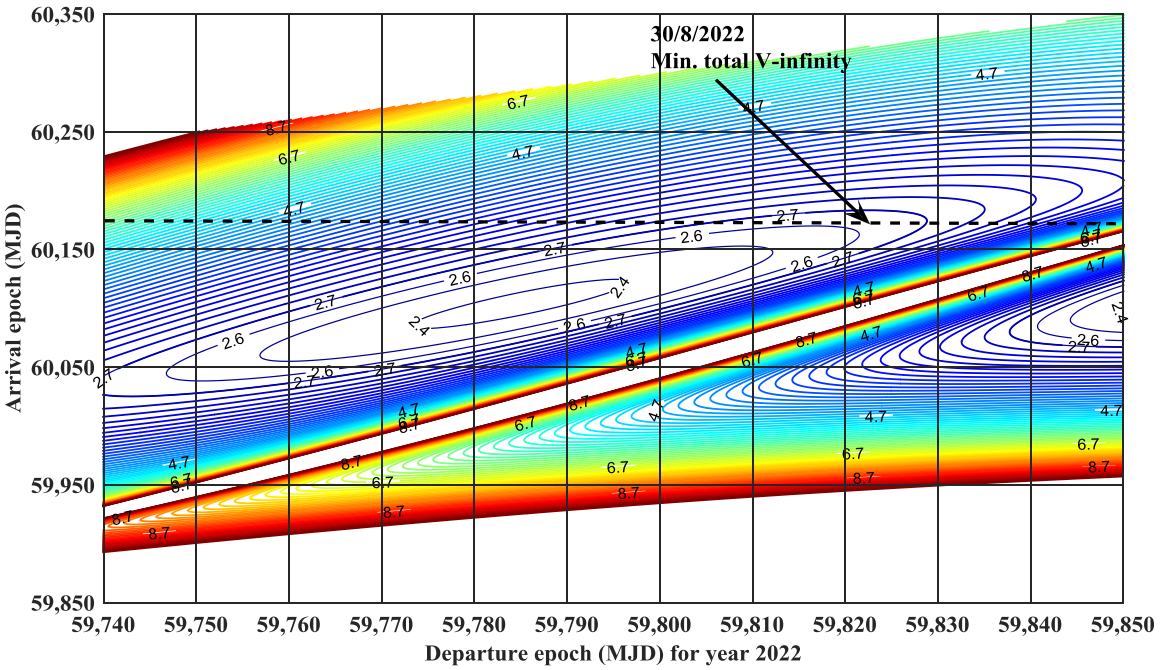

Fig. 2.10. Design chart: Magnitude of arrival V-infinity vector (2022)

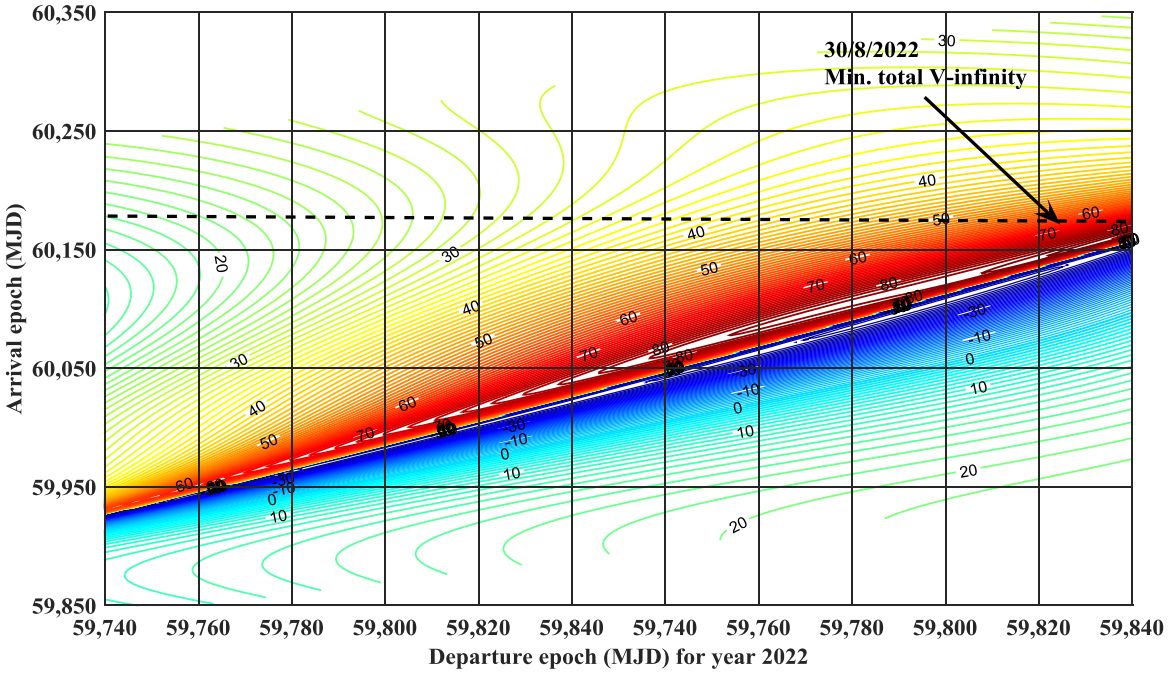

Fig. 2.11. Design chart: Declination of arrival V-infinity vector (2022)

This minimum energy opportunity can be used for direct interplanetary transfer. The declination contours are important for any mission. This is because, the inclination (deg)

of the departure and arrival hyperbolic orbits must be greater than the declination (deg) of the corresponding V-infinity vector. Similarly, the design charts of the magnitude (km/s) and declination (deg) of the arrival V-infinity vector are shown in Figs. 2.6 and 2.7.

The design charts of the magnitude (km/s) and declination (deg) of the departure V-infinity vector for the minimum energy opportunity of 2022 are presented in Figs. 2.8 and 2.9. The design charts of the magnitude (km/s) and declination (deg) of the arrival V-infinity vector for the minimum energy opportunity of the same opportunity are presented in Figs. 2.10 and 2.11. Note that the minimum value of the total V-infinity vector (6.48 km/s) occurs on 30 Aug 2022 and the flight duration is 347 days.

2.5.1.4 Disadvantages

The conventional patched conic design technique considers only one primary gravity field at a time. This results in the following limitations,

1) Position and velocity discontinuities at the exit and entry locations of the SOIs.
2) Approximate design of the transfer trajectory.

If an interplanetary mission is executed using the patched conic design, the trajectory correction maneuvers (TCM) required for the transfer will be large to compensate for the approximate design.

2.5.2 Pseudostate Technique

In the patched conic force model, the gravity field of Sun is not accounted within the SOI of the target planets. This deficiency is overcome in the pseudostate technique. Within the pseudosphere of the departure and arrival planets, this technique is used **to solve the three-body problem analytically**. An underlying assumption in the pseudostate theory is that the mass of the secondary body is sufficiently small relative to the mass of the primary body. As such, within the pseudosphere (extended SOI) of the target planets, the Sun is the primary body and the departure/arrival planets are the secondary bodies.

In the pseudostate technique, the pseudostates are used as target points for determining the Lambert conic instead of the actual positions of the planets. These pseudostates are generated by superimposing the gravity field of the target planet over that of the Sun which forms a three-body problem within the pseudosphere. The analytical

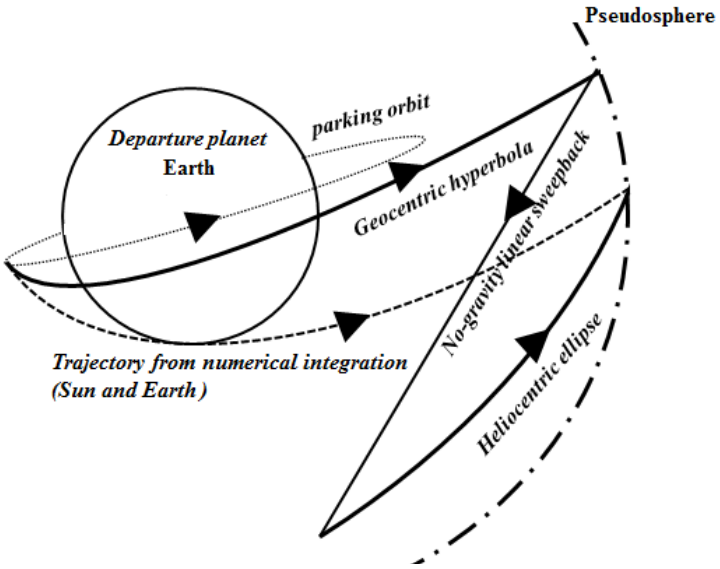

Fig. 2.12. Illustration of pseudostate propagation technique at departure

three-body trajectory within the pseudosphere is obtained using the following two-body trajectory phases,

(i) ***the planetocentric hyperbola,***

(ii) ***the linear/straight line motion and***

(iii) ***the heliocentric ellipse.***

All these conics has the same duration. The straight line represents the zero-gravity linear motion. Outside the pseudosphere, the spacecraft experiences only the Sun's gravity. The pseudostate concept is illustrated in Fig. 2.12 for the departure phase of an Earth-departing spacecraft. Within the pseudosphere, the analytical propagation of the 3-body problem is carried out using the pseudostate concept. The steps of the pseudostate propagation technique for a prefixed duration are discussed here.

1) From the periapsis of the DPO, the trajectory is propagated forward under the Earth's gravity for a small duration. This analytical propagation is carried out by solving the Kepler equation. Clearly, the resultant trajectory is a geocentric hyperbola.
2) The geocentric position vector, thus obtained, is propagated linearly backward along a straight line with the geocentric velocity vector for the same small duration. This is labeled as 'no-gravity linear sweepback' in Fig. 2.12. The geocentric state is transformed to the heliocentric state and is referred to as the **pseudostate**. *The pseudostate represents the state from which the heliocentric transfer trajectory would have started in the absence of Earth gravity*.

3) The heliocentric pseudostate is analytically propagated forward under the Sun's gravity for the same duration.
4) The heliocentric orbital elements obtained from step (3) are transformed to the geocentric frame.

Repeat the steps (1) to (4) for the prefixed duration or until the pseudosphere is reached. *The heliocentric state, thus obtained, is equivalent to the heliocentric state obtained on numerical propagation of the initial state from DPO periapsis under the technique for 3-body force model (Sun, target planet and spacecraft).*Note that the analytical propagation is carried out in small durations and this duration is referred as the sweep-back duration in the departure phase, and sweep-forward duration in the arrival phase.

2.5.2.1 One-step Impact Pseudostate Technique

The one-step impact pseudostate technique was used for the trajectory design of a direct transfer from Earth to Jupiter by Sergeyevsky (1983). He compared this technique with the Lambert/Zero-SOI patched conic technique and concluded that there is significant improvement in accuracy. This one-step algorithm based on pseudostate technique, as developed by Sergeyevsky in the interplanetary context, assumes rectilinear hyperbola for the departure and arrival phases. This assumption eases the computational effort as the eccentricity of the rectilinear hyperbola is one and hence, one of the unknowns is fixed. However, the conic passes through the center of the target planet, thus resulting in impact. The one-step pseudostate technique considers the step size for analytical propagation that spans the entire pseudosphere. That means, the sweep-back/sweep-forward duration, in this case, is the duration to reach the departure/arrival pseudosphere. The representing diagram of the one-step impact pseudostate technique is given in Fig. 2.13. The steps of the one-step impact pseudostate technique [Sergeyevsky, 1983] is briefly described here.

The departure epoch, flight duration (t_{FD}), sweep-back duration (t_D) for departure phase and sweep-forward duration (t_A) for the arrival phase are fixed.

1) Obtain the heliocentric states of the departure planet on the departure epoch $(\boldsymbol{R_1}, \boldsymbol{V_1})$ and the arrival planet on the arrival epoch $(\boldsymbol{R_2}, \boldsymbol{V_2})$. Set $(\boldsymbol{R_1}, \boldsymbol{R_2})$ as the position vectors of the initial pseudostates i.e., $\boldsymbol{R_{DPS}} = \boldsymbol{R_1}$ at the departure phase and $\boldsymbol{R_{APS}} = \boldsymbol{R_2}$ at the arrival phase. These states are in Earth mean equator and Equinox of J2000 frame.

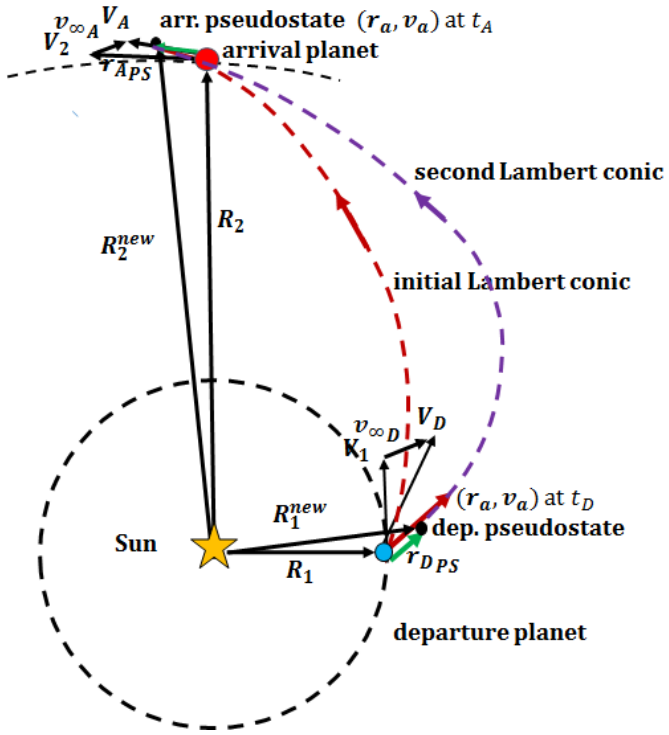

Fig.2.13. Illustration of one-step impact pseudostate technique

2) Determine the heliocentric Lambert conic connecting the pseudostates ($\boldsymbol{R_{D_{PS}}}, \boldsymbol{R_{A_{PS}}}$) for the prefixed flight duration (t_{FD}). Let the heliocentric velocity vector at $\boldsymbol{R_{D_{PS}}}$ be $\boldsymbol{V_{D_{PS}}}$ and $\boldsymbol{R_{A_{PS}}}$ be $\boldsymbol{V_{A_{PS}}}$.
3) Compute the planetocentric V-infinity vectors at the departure and arrival phases i.e. $\boldsymbol{v_{\infty_D}}$ and $\boldsymbol{v_{\infty_A}}$ respectively, by using the assumption that the heliocentric velocity vectors at the departure/arrival and the pseudosphere are the same.

$$\left.\begin{aligned} \boldsymbol{v_{\infty_D}} &= \boldsymbol{V_{D_{PS}}} - \boldsymbol{V_1} \\ \boldsymbol{v_{\infty_A}} &= \boldsymbol{V_{A_{PS}}} - \boldsymbol{V_2} \end{aligned}\right\} \tag{2.10}$$

The heliocentric vector is now transformed to the planetocentric vector.

4) Compute the fictitious planetocentric rectilinear hyperbolic distance (r_a) and velocity (v_a) using the V-infinity vectors. These represent the high point of the rectilinear trajectory at the end of sweep-back and sweep-forward durations.
   i) Compute the semi-major axis from the current V-infinity vector ($v_{\infty_{D\ or\ A}}$), mean motion, mean anomaly and eccentric anomaly at $t_{D\ or\ A}$. Use this eccentric anomaly to find r_a and v_a at $t_{D\ or\ A}$.
5) Compute the corresponding vectors $\boldsymbol{r_a}$ and $\boldsymbol{v_a}$ with respect to the target planets. These vectors are obtained by treating them parallel to the V-infinity vector ($\boldsymbol{v_\infty}$).

6) Propagate the planetocentric position vectors in a gravity-free, straight line motion, backward for the sweep-back duration (t_D) in the departure phase and forward for the sweep-forward duration (t_A) in the arrival phase. The resulting states are the updated pseudostates.

$$\boldsymbol{r}_{\boldsymbol{D\ or\ A_{PS}}} = \boldsymbol{r}_{\boldsymbol{a_{D\ or\ A}}} + q(\boldsymbol{v}_{\boldsymbol{a_{D\ or\ A}}} t_{D\ or\ A}) \tag{2.11}$$

$$q = \begin{cases} \text{-1 for departure (D)} \\ +1 \text{ for arrival (A)} \end{cases}$$

The planetocentric pseudostates are transformed to heliocentric pseudostates,

$$\boldsymbol{R}^{\boldsymbol{new}}_{\boldsymbol{D\ or\ A_{PS}}} = \boldsymbol{r}_{\boldsymbol{D\ or\ A_{PS}}} + \boldsymbol{R}_{\boldsymbol{1\ or\ 2}} \tag{2.12}$$

7) For the first pass, the new heliocentric pseudostates are used to determine the new Lambert conic and the steps (2) to (7) are repeated.
If not, compute the duration to reach the high point ($t_{hP_{D\ or\ A}}$) on the rectilinear conic i.e., from $\boldsymbol{r}_{\boldsymbol{a_{D\ or\ A}}}$ to $\boldsymbol{r}_{\boldsymbol{D\ or\ A_{PS}}}$ [Sergeyevsky, 1983].
   i) Compute the semi-major axis from r_a and v_a. Find the eccentric anomaly, mean anomaly, mean motion and then the duration to reach the high point on the rectilinear conic.

8) If the difference between the prefixed pseudosphere duration and the computed high-point duration ($\Delta t_{D\ or\ A}$) is less than a threshold value, the procedure for finding the V-infinity vector is terminated and the iteration process is considered to be converged.

$$\Delta t_{D\ or\ A} = \left| t_{D\ or\ A} - t_{hP_{D\ or\ A}} \right| \tag{2.13}$$

The transfer trajectory thus obtained is the required design.

9) If not, the iteration is continued by correcting the value of the fictitious planetocentric position at the high point ($r_{a_{D\ or\ A}}$). The iteration is to nullify the differences in durations and it is done using a sensitivity partial, $\text{PARTIAL}_{D\ or\ A}$. For the second pass, the partial is set as:

$$\text{PARTIAL}_{D\ or\ A} = v_{a_{D\ or\ A}}$$

From third pass onwards, $\text{PARTIAL}_{D\ or\ A}$ is found as;

$$\text{PARTIAL}_{D\ or\ A} = \frac{\left(r_{a_{D\ or\ A}} - r_{a0_{D\ or\ A}}\right)}{\left(\Delta t_{D\ or\ A} - \Delta t_{0_{D\ or\ A}}\right)} \tag{2.14}$$

where subscript '0' refers to the value obtained in the previous iteration. The position of the high point $r_{a_{D\ or\ A}}$ is updated as;

$$r_{a_{D\ or\ A}}^{new} = r_{a_{D\ or\ A}} + \Delta t_{D\ or\ A}\text{PARTIAL}_{D\ or\ A} \tag{2.15}$$

The current values are set as old values;

$$r_{a0_{D\ or\ A}} = r_{a_{D\ or\ A}}$$
$$\Delta t_{0_{D\ or\ A}} = \Delta t_{D\ or\ A} \tag{2.16}$$

10) Repeat the steps (5) to (10) till the iterative process converges.

2.5.2.2 Illustrative Results

The one-step impact pseudostate technique is used for a direct Earth to Mars orbiter mission. The minimum energy opportunities presented in Table 2.7 are used. The departure and arrival V-infinity vectors obtained using the one-step impact pseudostate technique for these minimum energy opportunities are presented in the Table 2.9a and the corresponding heliocentric transfer trajectories are presented in Table 2.9b. Note that the parameters are different from those of conventional patched conic technique.

Table 2.9a V-infinity vectors from pseudostate technique

Opportunity	Departure V-infinity vector $\{ v_{\infty_D} ; \alpha_{\infty_D}; \delta_{\infty_D}\}$	Arrival V-infinity vector $\{ v_{\infty_A} ; \alpha_{\infty_A}; \delta_{\infty_A}\}$
2018	{2.7894; 321.892; -37.024}	{2.962; 245.512; 9.409}
2022	{3.8827; 80.478; 3.389}	{2.6030; 39.600; 31.680}

Table 2.9b Heliocentric transfer trajectories obtained using pseudostate technique

Orbital elements	2018 opportunity	2022 opportunity
a (km)	182,717,574.26	200,702,636.07
e	0.174692	0.250052
i (deg)	24.60	21.38
Ω (deg)	3.30	2.52
ω (deg)	218.21	344.85
ν_{t_i} (deg)	9.80	349.17

2.5.2.3 Disadvantages

The limitations of the one-step impact pseudostate technique are,

1) The use of one step for analytical propagation reduces the accuracy of the V-infinity vector obtained.
2) Both the planetocentric trajectories pass through the center of the target planets which results in impact. So, this technique cannot be used for orbiter missions.

2.6 Conclusions

In this chapter, the conventional analytical techniques used for the trajectory design of interplanetary missions are discussed. The Lambert problem and two of its solution methods (Battin and Vallado) using the universal variables formulation are discussed. ***The Universal algorithm developed by Vallado performed better than Battin's method and so this method is adopted for the current research***. ***For a typical Earth to Mars orbiter mission, design charts of the V-infinity vector for a type I and type II interplanetary transfers are presented.*** The steps for computing the V-infinity vector using the conventional patched conic and the one-step pseudostate concepts are explained in detail. The limitations of these techniques for designing the transfer trajectory are brought out in this chapter.

♠♠♠♠♠♠♠♠♠♠♠♠♠♠♠♠♠♠♠

CHAPTER 3
DETERMINATION OF ORBIT CHARACTERISTICS AND THE V-INFINITY TUNED PATCHED CONIC TECHNIQUE

3.1 Chapter Summary

The V-infinity vector using the conventional analytical techniques is asymptotic in nature with respect to the planet. For practical design purposes, the asymptotic distance is generally quantified as the radius of the sphere of influence (SOI). In this chapter, the departure/arrival hyperbolic orbit characteristics are computed from the V-infinity vector using spherical trigonometric relations. The hyperbolic orbit characteristics of the departure and arrival phases must be obtained such that the V-infinity vector is achieved at the boundary of the planet SOI. An analytical tuning strategy adopted from Ramanan (2002) is used to find the suitable hyperbolic orbit characteristics that achieves the V-infinity vector. The trajectory design technique that uses the analytical tuning strategy in the patched conic technique is named as **V-infinity tuned patched conic (VPC) technique**. This technique results in improved trajectory design. Further, the link between the hyperbolic orbit characteristics and the parking orbit characteristics which ensures minimum energy transfer is discussed. Also, the mathematical model to compute the velocity impulses required for the interplanetary transfer is provided.

3.2 Determination of Hyperbolic Orbit Characteristics

For minimum energy transfer, the hyperbolic trajectory must be designed such that its plane contains the V-infinity vector. To ensure this, the inclination of the hyperbolic orbit (i_∞) must be greater than the declination of the V-infinity vector (δ_∞), i.e. $i_\infty \geq |\delta_\infty|$. For coplanar transfer, the inclinations of the hyperbolic orbit (i_∞) and the parking orbit (i_{PO}) must be same.

Let the hyperbolic orbit characteristics be represented in terms of orbital elements $(a_\infty, e_\infty, i_\infty, \Omega_\infty, \omega_\infty)$ and ν. These orbital elements are obtained using the V-infinity vector. The following equations are used to calculate the semi-major axis (a_∞) and eccentiricty (e_∞) of the hyperbolic orbit.

$$a_{\infty} = \frac{-\mu}{{v_{\infty}}^2} \tag{3.1}$$

$$e_{\infty} = 1 - \frac{r_{P_{\infty}}}{a_{\infty}} \tag{3.2}$$

where μ is the gravitational constant of the primary attracting body (target planet) and $r_{P_{\infty}}$ is the periapsis distance of the hyperbolic orbit. The periapsis altitude $\left(h_{\infty_D}\right)$ and inclination (i_{∞_D}) of the hyperbolic orbit are prefixed. The true anomaly of the hyperbolic orbit is assumed to be zero (discussed in the next section). The other two angles (RAAN, Ω_{∞} and AoP, ω_{∞}) at the departure and arrival phases are derived using the geometry of TPI and POI injections respectively.

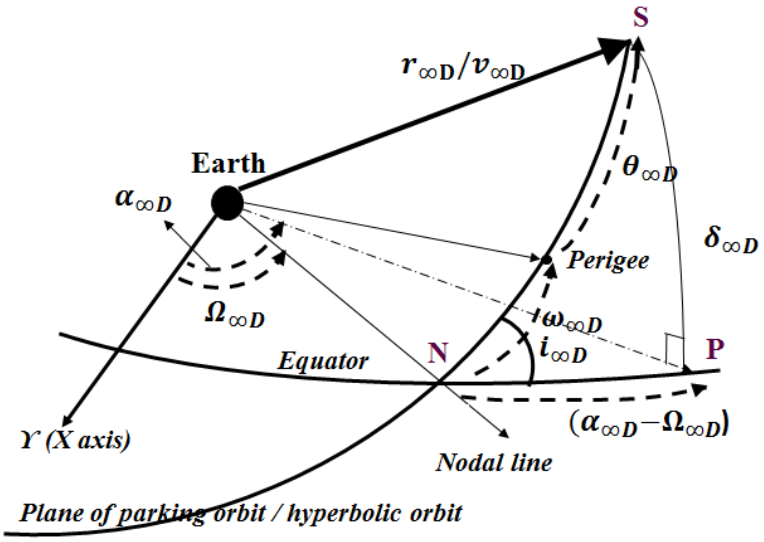

Fig.3.1. Geometry of transplanetary injection (departure phase)

The major assumptions used in the derivation are: (i) the planets are spherical masses, (ii) only the planet's gravity influences the spacecraft within the respective SOI. In a departure hyperbola, the asymptotic radius vector (r_{∞_D}) and the asymptotic V-infinity vector (v_{∞_D}) are in the **same direction** (cf. Fig. 3.1). The geometry of the transplanetary injection (TPI) at the departure phase is given in Fig. 3.1. From the geometry, the departure RAAN and AoP are obtained using the trigonometric relations in the spherical triangle NSP [Tolson, 1963; Ramanan, 2002]. They are,

$$sin\left(\alpha_{\infty_D} - \Omega_{\infty_D}\right) = tan\,\delta_{\infty_D} / tan\,i_{\infty_D} \tag{3.3}$$

$$sin(\omega_{\infty_D} + \theta_{\infty_D}) = sin\,\delta_{\infty_D} / sin\,i_{\infty_D} \tag{3.4}$$

where $\theta_{\infty D}$ is given by,

$$\theta_{\infty_D} = cos^{-1}\left(-1/e_{\infty_D}\right) \tag{3.5}$$

The Eqs. 3.3 and 3.4 give two sets of angles viz.

$$\Omega_{\infty_D}|_1 = \alpha_{\infty_D} - sin^{-1}\left(tan\,\delta_{\infty_D}/tan\,i_{\infty_D}\right) \tag{3.6}$$

$$\Omega_{\infty_D}|_2 = 180 - \alpha_{\infty_D} + sin^{-1}\left(tan\,\delta_{\infty_D}/tan\,i_{\infty_D}\right) \tag{3.7}$$

$$\omega_{\infty_D}|_1 = sin^{-1}\left(sin\,\delta_{\infty_D}/sin\,i_{\infty_D}\right) - \theta_{\infty_D} \tag{3.8}$$

$$\omega_{\infty_D}|_2 = 180 - sin^{-1}\left(sin\,\delta_{\infty_D}/sin\,i_{\infty_D}\right) + \theta_{\infty_D} \tag{3.9}$$

The two sets are $(\Omega_{\infty_D}|_1, \omega_{\infty_D}|_1)$ and $(\Omega_{\infty_D}|_2, \omega_{\infty_D}|_2)$ and these correspond to the two possible geometries of the hyperbolic orbit containing the V-infinity vector, i.e. while ascending and descending. The Eqs. 3.6 to 3.9 have mathematical singularity for inclinations of 0 deg and 90 deg. For $i_{\infty_D} = 0$ deg, the declination of the V-infinity vector $\left(\delta_{\infty_D}\right)$ must be zero because $i_{\infty_D} \geq \delta_{\infty_D}$. For $i_{\infty_D} = 90$ deg, the values of RAAN and AoP are: $\Omega_{\infty} = \alpha_{\infty}$ and $\omega_{\infty} = \delta_{\infty} - \theta_{\infty}$. The above procedure is used to find the arrival hyperbolic orbital elements that achieves the desired arrival V-infinity vector. The arrival hyperbolic orbit also has two possible geometries that correspond to $(\Omega_{\infty_A}|_1, \omega_{\infty_A}|_1)$ and $(\Omega_{\infty_A}|_2, \omega_{\infty_A}|_2)$. In an arrival hyperbola, the asymptotic radius vector and the asymptotic V-infinity vector are in **opposite direction**. So, for the computation of the arrival hyperbolic orbital elements, the parameters of the arrival V-infinity vector are set as,

$$\alpha_{\infty_A} \Longrightarrow \pi + \alpha_{\infty_A} \tag{3.10a}$$

$$\delta_{\infty_A} \Longrightarrow -\delta_{\infty_A} \tag{3.10b}$$

Each of the departure hyperbolic orbit can be mapped to each of the arrival hyperbolic orbit and this results in four transfer trajectory design options (cf. Table 3.1).

Table 3.1 Trajectory design options

Transfer trajectory options	Departure phase	Arrival phase
option 11	$(\Omega_{\infty_D}\|_1, \omega_{\infty_D}\|_1)$	$(\Omega_{\infty_A}\|_1, \omega_{\infty_A}\|_1)$
option 12	$(\Omega_{\infty_D}\|_1, \omega_{\infty_D}\|_1)$	$(\Omega_{\infty_A}\|_2, \omega_{\infty_A}\|_2)$
option 21	$(\Omega_{\infty_D}\|_2, \omega_{\infty_D}\|_2)$	$(\Omega_{\infty_A}\|_1, \omega_{\infty_A}\|_1)$
option 22	$(\Omega_{\infty_D}\|_2, \omega_{\infty_D}\|_2)$	$(\Omega_{\infty_A}\|_2, \omega_{\infty_A}\|_2)$

3.3 Analytical Tuning Strategy

Using the procedure described in the previous section, the initial estimate of the hyperbolic orbital elements are obtained from the asymptotic V-infinity vector. But for a practical design, the hyperbolic orbital elements must be such that the desired V-infinity vector is achieved at the boundary of the SOI. In the current research, the SOI is

represented in terms of the number of days required to reach the boundary of the SOI from the periapsis of the parking orbit. The initial estimate of the hyperbolic orbital elements is propagated under Keplerian force model from the periapsis for the SOI duration. The resulting velocity vector at the SOI is referred to as the propagated V-infinity vector. This need not be the same as the desired V-infinity vector obtained from the Lambert conic. In order to achieve the desired V-infinity vector at the SOI, the hyperbolic orbital elements must be tuned. In this section, an analytical tuning strategy adopted from Ramanan (2002) is presented.

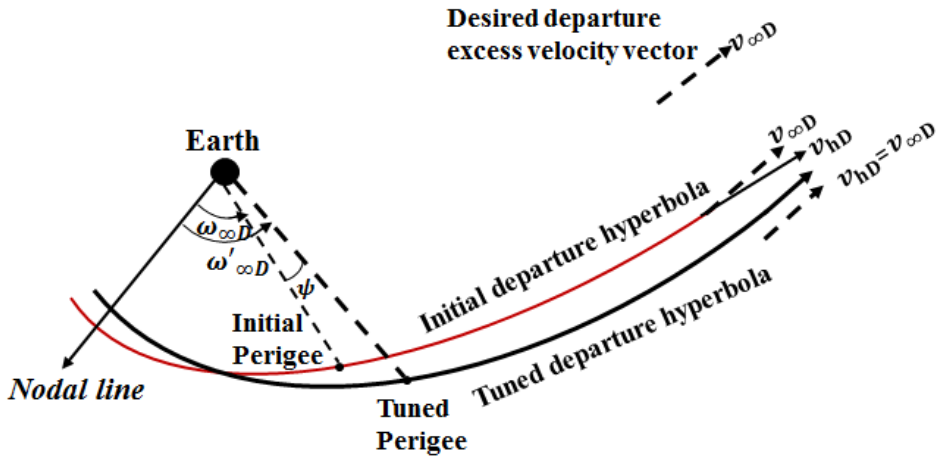

Fig. 3.2. Analytical tuning strategy at the departure phase

The philosophy of the analytical tuning strategy is as follows. The periapsis altitude and the inclination of the hyperbola are prefixed. Let the difference in direction (angle) between the desired and propagated V-infinity vectors be ψ. The propagated V-infinity vector at the SOI is rotated by the angle ψ about the angular momentum vector in the hyperbolic orbital plane to match the direction of the desired V-infinity vector. This rotation causes a shift in the location of periapsis of the hyperbola. Using this concept, a new location for the periapsis is computed. The magnitude of the desired V-infinity vector is achieved by changing the semi-major axis of the hyperbola. This process is repeated till the propagated V-infinity vector matches the desired V-infinity vector.

The analytical tuning strategy for the departure phase is illustrated in Fig. 3.2 and the steps of the procedure are given below.

The periapsis altitude ($h_{\infty P_D}$), *inclination* (i_{∞_D}) *of the departure hyperbola and the SOI-duration at the departure phase are fixed.*

1) Compute the semi-major axis (a_{∞_D}) and the related eccentricity (e_{∞_D}) of the departure hyperbola using Eqs. (3.3) and (3.4) respectively.

2) Compute both the values of RAAN (Ω_{∞_D}) and AOP (ω_{∞_D}) from Eqs. (3.6) to (3.9) respectively and choose one of the transfer trajectory options (cf. Table 3.1).
3) Find the departure hyperbolic orbital elements (a_{∞_D}, $e_{\infty_D}, i_{\infty_D}, \Omega_{\infty_D}, \omega_{\infty_D}, \nu_{\infty_D} = \nu_{P\infty_D} = 0$) at the departure SOI by solving the Kepler equation. Compute the propagated position vector ($\boldsymbol{r_{hD}}$) and V-infinity vector ($\boldsymbol{v_{h_D}}$).
4) Compute the difference between the desired and propagated V-infinity vectors, $\epsilon = \left|\boldsymbol{v_{h_D}} - \boldsymbol{v_{\infty_D}}\right|$. If ϵ is less than a prefixed threshold value, the hyperbolic orbital elements are obtained. Otherwise the following steps are continued.
5) Find the angle (ψ) between the desired V-infinity vector ($\boldsymbol{v_{\infty_D}}$) and the propagated V-infinity vector ($\boldsymbol{v_{h_D}}$).
6) The shift in AOP location is computed as,

$$\Delta\omega = \psi \tag{3.11}$$

Update the new location of the periapsis of the departure hyperbolic orbit as,

$$\omega_{\infty D} = \omega_{\infty D} \pm \Delta\omega \tag{3.12}$$

7) Update the semi-major axis of the rotated departure hyperbolic trajectory,

$$a_{\infty_D} = -\mu_D / \left({v_{\infty_D}}^2 - \frac{2\mu_D}{r_{h_D}} \right) \tag{3.13}$$

and the related eccentricity using Eq. 3.4. Note that in Eq. 3.13, for velocity, the value of v_{∞_D} is used and not v_{h_D}.

8) Repeat the steps (3) to (8) till the threshold value is achieved.

The above steps can be used for tuning the arrival hyperbolic orbit characteristics also by simply replacing the subscript ‘D’ by ‘A’.

3.4 Parking Orbit Characteristics

In the previous section, the hyperbolic orbit that contains the V-infinity vector at the boundary of the SOI is determined. The next step is to achieve this hyperbolic orbit from a parking orbit (PO). To achieve the departure hyperbolic orbit, a velocity impulse is to be imparted from the departure parking orbit (DPO), which is known as the transplanetary injection (TPI). Similarly, a velocity impulse is to be imparted at an appropriate location of the arrival hyperbolic orbit to enter the arrival parking orbit (APO), which is known as the parking orbit insertion (POI). The imparting of the velocity impulse is assumed to be instantaneous. The parking orbit characteristics must be chosen such that the velocity

impulse required for the transfer is minimum. Clarke and Bollman (1966) determined a suitable launch azimuth and coasting time in a circular parking orbit, for a given launch site and inclination of the transfer trajectory, that minimizes the velocity impulse and achieves the desired departure V-infinity vector. A method to find the point of injection on a circular parking orbit that minimizes the departure velocity impulse was presented by Battin (1987). He discussed separate strategies to deal with tangential and non-tangential injections. Bell et al. (1995) described a technique to find a suitable location for injection from an elliptical parking orbit that minimizes the departure velocity impulse by searching along the parking orbit. Jones and Ocampo (2012) used the sequential quadratic programming technique to find the optimal impulsive trajectories that takes a spacecraft from a circular parking orbit to a desired V-infinity vector.

In the current research, the parking orbit characteristics that minimizes the velocity impulse are determined. The velocity impulse is minimum when the addition of velocity impulse is **tangential and horizontal**. Such an addition is possible only when: i) the parking orbit and the hyperbolic orbit are coplanar, ii) the location of the velocity impulse is at the periapsis of the parking orbit, and iii) the argument of periapsis (AOP) of the hyperbolic orbit and the parking orbit are the same. The conditions for horizontal, tangential injection at the periapsis which minimizes the velocity impulse are listed below.

1) For coplanarity, $i_{PO} = i_{\infty}$ and $\Omega_{PO} = \Omega_{\infty}$.
2) For impulsive addition, $\nu_{PO} = \nu_{P_{\infty}} = 0$ and $r_{P_{PO}} = r_{P_{\infty}}$,
   where $\nu_{P_{\infty}}$ is the true anomaly, $r_{P_{\infty}}$ is the position vector at the periapsis of the hyperbolic transfer trajectory and $r_{P_{PO}}$ is the position vector at the periapsis of the parking orbit.
3) $\omega_{PO} = \omega_{\infty}$

The above conditions are valid for both departure and arrival phases.

In an actual mission, the size, shape and inclination of the parking orbit are dictated by the launch vehicle. So, the periapsis altitude and inclination of the hyperbolic orbit are kept same as that of the parking orbit to satisfy the above conditions (1 and 2).

3.5 Computation of Velocity Impulses

To transfer the spacecraft from a DPO to the departure hyperbolic orbit, a transplanetary injection (TPI) is required. Also, to transfer the spacecraft from an arrival hyperbolic orbit

to an APO, a parking orbit insertion (POI) is required. The TPI and POI velocity impulses are computed following the steps given below.

1) From the V-infinity vector (v_∞), compute the velocity vector at the periapsis of the hyperbolic orbit,

$$v_{P_\infty} = \sqrt{{v_\infty}^2 + \frac{2\mu}{r_{P_\infty}}} \tag{3.14}$$

2) Compute the velocity vector at the periapsis of the parking orbit,

$$v_{P_{PO}} = \sqrt{\mu(\frac{2}{r_{P_{PO}}} - \frac{1}{a_{PO}})} \tag{3.15}$$

where a_{PO} is the semi-major axis and $r_{P_{PO}}$ is the periapsis radius of the parking orbit.

3) The velocity impulse is computed as;

$$\Delta V = \left|v_{P_\infty} - v_{PO}\right| \tag{3.16}$$

In the above equations, the parameters at the departure and arrival phases are used to determine the TPI and POI impulses respectively. Note that, only magnitude of the velocity vectors are used because of the assumption that the velocity addition is tangential and horizontal.

3.6 V-infinity Tuned Patched conic Technique

An algorithm which includes the tuning process of the hyperbolic/parking orbit characteristics, named as V-infinity tuned patched conic (VPC) technique, is introduced in this section. The hyperbolic orbit characteristics are tuned to achieve the V-infinity vector using the analytical tuning strategy discussed in section 3.3. The parking orbit characteristics and the velocity impulses required for the transfer are computed using the procedures described in sections 3.4 and 3.5 respectively. The steps of the V-infinity tuned patched conic technique are as follows,

The periapsis distance (r_∞) and inclination (i_∞) of the departure and arrival hyperbolic orbits are fixed. Also, the departure epoch, flight duration (t_{FD}) and the SOI-duration for the departure and arrival phases (t_D and t_A days respectively) are fixed.

1) Obtain the heliocentric states of the departure planet on the departure epoch ($\boldsymbol{R_1}, \boldsymbol{V_1}$) and the arrival planet on the arrival epoch ($\boldsymbol{R_2}, \boldsymbol{V_2}$). These states are in Earth mean equator and Equinox of J2000 frame.

2) Determine the heliocentric Lambert conic connecting the position vectors ($\boldsymbol{R_1}, \boldsymbol{R_2}$) for the given flight duration (t_{FD}). Compute the corresponding heliocentric velocity vectors ($\boldsymbol{V_{D_{PC}}}$ and $\boldsymbol{V_{A_{PC}}}$) in the transfer trajectory.
3) Compute the planetocentric V-infinity vectors at the departure and arrival phases i.e. $\boldsymbol{v_{\infty_D}}$ and $\boldsymbol{v_{\infty_A}}$ respectively.

$$\boldsymbol{v_{\infty_D}} = \boldsymbol{V_{D_{PC}}} - \boldsymbol{V_1} \tag{3.17a}$$

$$\boldsymbol{v_{\infty_A}} = \boldsymbol{V_{A_{PC}}} - \boldsymbol{V_2} \tag{3.17b}$$

Note that the steps (1) to (3) describe the conventional patched conic technique already discussed in chapter 2, section 2.5.1.

4) From the V-infinity vectors, find the orbital elements ($a_\infty, e_\infty, i_\infty, \Omega_\infty, \omega_\infty, \nu_\infty = \nu_{P_\infty} = 0$) of departure and arrival hyperbolic orbits using the procedure described in section 3.2. One of the four design options is chosen for further processing.
5) Find the departure planetocentric velocity vector/propagated departure V-infinity vector ($\boldsymbol{v_{h_D}}$) from the departure hyperbolic orbital elements by solving Kepler equation for the prefixed SOI duration (t_D). Similarly, find the arrival planetocentric velocity vector/propagated arrival V-infinity vector ($\boldsymbol{v_{h_A}}$).
6) The desired and propagated V-infinity vectors, i.e. $\boldsymbol{v_{\infty_D}}$ and $\boldsymbol{v_{h_D}}$, are matched at the SOI of the departure planet using the analytical tuning strategy described in section 3.3. Similarly at the arrival phase also.

The steps (1) to (6) describe the V-infinity tuned patched conic technique. The V-infinity tuned hyperbolic orbit characteristics are used to find the departure and arrival velocity impulses.

3.6.1 Illustrative Results

The V-infinity tuned patched conic technique (VPC) is used to generate the trajectory design for an Earth to Mars orbiter mission. The minimum energy opportunity that occurs on 12th May 2018 0 h TDB with a flight duration of 204 days is chosen for generating the design. The Earth parking orbit (EPO) is 300 x 25,000 km with an inclination of 75 deg with respect to Earth equator and Equinox of J2000. The Mars parking orbit (MPO) is 300 km circular with an inclination of 75 deg with respect to Mars equator and IAU vector of J2000 [Archinal et al., 2009]. The SOI durations of Earth and Mars are 3 and 2 days respectively. The position vector of the target planets are obtained using JPL ephemeris DE 405.

Table 3.2 Conventional patched conic design options (i_{∞_D}=75 deg; i_{∞_A}=75 deg)

Parameters	option 11	option 12	option 21	option 22
a_{∞_D} (km)	-51239.9	-51239.9	-51239.9	-51239.9
e_{∞_D}	1.130332	1.130332	1.130332	1.130332
Ω_{∞_D} (deg)	333.0131	333.0131	129.8392	129.8392
ω_{∞_D}(deg)	169.3999	169.3999	64.5845	64.5845
a_{∞_A}(km)	-4881.1	-4881.1	-4881.1	-4881.1
e_{∞_A}	1.757441	1.757441	1.757441	1.757441
Ω_{∞_A}(deg)	68.1673	243.1616	68.1673	243.1616
ω_{∞_A}(deg)	115.0951	314.2668	115.0951	314.2668

The departure and arrival V-infinity vectors obtained from the conventional PC technique (cf. Table 2.8) are used to the find the initial estimate of the departure and arrival hyperbolic orbital elements (conventional PC design). The conventional PC design for the four design options are given in Table 3.2. Note that, the departure orbital elements for the options 11 and 12 are exactly the same, but they result in different arrival hyperbolic geometries. Similar trend is seen for options 21 and 22 also. ***Clearly, the conventional patched conic technique could generate only four notional design options.*** Each of these design option is tuned to achieve the V-infinity vector using the analytical tuning strategy and the tuning process is illustrated in Table 3.3. The tuned hyperbolic orbital elements which results in the VPC design, are given in Table 3.4. Note that after tuning, there is drastic change in the size and shape of the departure and arrival hyperbolic orbital elements. However, the design options are not distinctly different. This is because the VPC technique could not capture the different V-infinity vectors for the four design options. ***So, it can be concluded that the V-infinity tuned patched conic technique fails to identify the distinct design options for an opportunity***.

The TPI and POI velocity impulses required for the Earth to Mars orbiter mission (opportunity: 2018) are given in Table 3.5. The difference in the total velocity impulse between the Hohmann design and the conventional patched conic design is about 654 m/s which is very large. The difference in the total velocity impulse between the conventional patched conic design and the V-infinity tuned patched conic design is 58 m/s. This

difference, though comparatively smaller, is significant for an actual mission and brings out the necessity of tuning the hyperbolic orbital elements.

Table 3.3 Illustration of analytical tuning strategy

(Threshold values on: velocity direction/angle = 1E-3 deg, magnitude = 1E-6 km/s)

Iteration	Differences between desired and propagated V-infinity vectors			
	Departure phase		Arrival phase	
	angle (ϵ,deg)	magnitude (km/s)	angle (ϵ,deg)	magnitude (km/s)
1	0.04896	0.163435	0.00343	0.027125
2	1.46266	0.071678	0.31051	0.016055
3	0.07181	0.003513	0.00274	0.000140
4	0.00339	0.000165	0.00002	0.000023
5	0.00016	0.000007	0.00016	0.000007

Table 3.4 V-infinity tuned patched conic design options (i_{∞_D}=75 deg; i_{∞_A}=75 deg)

Parameters	option 11	option 12	option 21	option 22
a_{∞_D} (km)	-58640.5	-58640.5	-58640.5	-58640.5
e_{∞_D}	1.113882	1.113882	1.113882	1.113882
Ω_{∞_D} (deg)	333.0131	333.0131	129.8392	129.8392
ω_{∞_D}(deg)	167.8129	167.8129	64.5845	64.5845
a_{∞_A}(km)	-4973.4	-4973.4	-4973.4	-4973.4
e_{∞_A}	1.743391	1.743391	1.743391	1.743391
Ω_{∞_A}(deg)	68.1673	243.1616	68.1673	243.1616
ω_{∞_A}(deg)	115.4118	314.5835	115.4118	314.5835

The analytical designs are numerically propagation under the design force model (Patched Conic Force Model: departure phase/Earth for 3 days, cruise phase/Sun for 199 days and arrival phase/Mars for 2 days) and the resulting arrival target parameters are given in Table 3.6. The desired arrival target parameters are: (i) time of periapsis (T_P), 2nd December 2018 0 h TDB, (ii) closest approach altitude (CAA), 300 km and, (iii) arrival inclination, 75 deg. For the conventional PC design, there are very large deviations in the achieved target parameters (time of periapsis deviates by about 26 days from the desired value; achieved CAA: 3,011,712 km; APO inclination: 156.32 deg). For the VPC design, the deviation in the time of periapsis has significantly reduced to about 1.5 days.

There is an improvement in the achieved CAA (1,107,535 km) and inclination (141.01 deg) also. In summary, the deviations in the arrival target parameters achieved with the VPC design are still large, although it offers significant improvement in the trajectory design over the conventional PC technique. This is because of the discontinuity in the position vector that still exist even after tuning the V-infinity vector. ***It can be concluded that the improvement is not sufficient for actual mission purposes.***

Table 3.5 Velocity impulses from different analytical techniques

Technique	Velocity impulses (m/s)		
	TPI	POI	Total
Hohmann	1367.65	2889.73	4257.38
Conventional PC	1355.22	2248.21	3603.43
VPC	1311.61	2223.38	3545.41

Table 3.6 Achievable accuracies of different designs under PCFM

Design	Arrival CAA (km)	APO inclination (deg)	T_P (UTC) DD/MM/YYYY HH:MM:SS
Desired value	300	75.00	02/12/2018 00:00:00
Conventional PC design	3,011,712	156.32	05/11/2018 22:16:50
VPC design	1,107,535	141.01	29/11/2018 17:22:58

3.7 Conclusions

In this chapter, the procedure for determining the hyperbolic orbit characteristics from the V-infinity vector is discussed. It is observed that there is a drastic change in the size and shape of the hyperbolic orbit and also the argument of periapsis for the V-infinity tuned patched conic design compared to the conventional patched conic design. However, the right ascension of ascending node is the same. ***The V-infinity tuned patched conic technique generates only notional designs of the four options for an opportunity.*** On numerical propagation of the VPC design under the design force model, the deviations in the arrival target parameters are still large, although it offers significant improvement in the trajectory design over the conventional patched conic technique. So, the V-infinity tuned patched conic design needs further improvement.

♠♠♠♠♠♠♠♠♠♠♠♠♠♠♠♠♠♠♠

CHAPTER 4
ITERATIVE PSEUDOSTATE TECHNIQUES FOR TRANSFER TRAJECTORY DESIGN

4.1 Chapter Summary

The trajectory design can further be improved by including perturbations in the analytical trajectory design process. New techniques using the pseudostate concept are presented in this chapter. In the first part of the chapter, an iterative analytical technique based on the pseudostate concept, named as **iterative pseudostate (ITR-PS) technique** is presented. This technique includes the gravity effect of Sun also in the vicinity of the target planets and thereby generates an improved trajectory design. Further, the iterative process connects the departure and arrival phases using the Lambert conic after tuning the V-infinity vector. While the V-infinity tuning reduces the velocity discontinuity at the SOI, the iterative process reduces the position discontinuity at the SOI. Also, this process helps in distinctly identifying the four design options for an opportunity.

However, the ITR-PS technique uses the one-step pseudostate concept for analytical propagation in the departure and arrival phases. This reduces the accuracy of the achieved V-infinity vector. So, the numerical propagation of ITR-PS design under the design force model results in deviations in the arrival target parameters especially the inclination.

To improve the ITR-PS design in terms of achievable accuracies in the target parameters, a new technique named as **multiconic differential-evolution (MCDE) technique** is proposed. In this technique, instead of the one-step pseudostate technique, multiconic technique is used wherein the analytical propagation using the pseudostate concept is carried out in multiple steps using a smaller step size. To obtain the hyperbolic orbit characteristics, the analytical tuning strategy is not suitable for the multiconic technique and so an optimization technique, differential evolution technique, is used. The analytical design obtained using the MCDE technique is very close to the numerical design under the three-body force model.

4.2 One-step Pseudostate Technique

The inherent advantage of the pseudostate concept is the inclusion of Sun's gravity using the concept of pseudosphere. The pseudosphere of a target planet, as already discussed, is a larger SOI within which the gravity of the respective planet is also considered in addition to the gravity of Sun. As pointed out in section 2.5.2, the underlying assumption in the pseudostate theory is that the mass of the secondary body is sufficiently small relative to the mass of the primary body. Another assumption is that the tertiary body has a positive energy w.r.t the secondary body. For an interplanetary transfer, Sun is the primary body throughout the transfer while the gravitational forces of the target planets are superimposed over the heliocentric transfer trajectory within their respective pseudosphere. Thus, **we use the pseudosphere concept to solve a three-body problem analytically**. Outside the pseudosphere of the departure and arrival planets, we have the two-body problem with Sun as the primary body.

For Lambert conic determination, the departure and arrival pseudostates are used instead of the actual position vectors of the target planets. The departure and arrival pseudostates are the fictitious states at the beginning and end of the interplanetary (heliocentric) transfer trajectory, in the absence of the respective target planet's gravity. In the current research, the pseudosphere is represented in terms of the number of days required to reach the boundary of the pseudosphere from the periapsis of the orbit. The steps for using the pseudostate technique for propagation are presented in section 2.5.2.

The one-step pseudostate technique (cf. section 2.5.2) developed by Sergeyevsky et al. (1983) assumed rectilinear hyperbola for the departure and arrival phases of the interplanetary transfer which results in impact. An analytical formulation for the transfer trajectory design of an interplanetary orbiter mission is not readily available in the literature. In this chapter, an integrated method, named as **iterative pseudostate (ITR-PS) technique**, based on pseudostate technique that synchronizes the parking orbit and the heliocentric transfer trajectory characteristics, satisfying the arrival constraints, is presented.

4.2.1 Iterative Pseudostate Technique

The process of determining the V-infinity vector and the pseudostate along with the related hyperbolic orbit characteristics is given below.

The periapsis distance, inclination of the departure and arrival hyperbolic orbits are fixed. Also, the departure epoch, flight duration (t_{FD}), the sweep-back duration (t_D) for the departure phase and the sweep-forward duration (t_A) for the arrival phase are fixed.

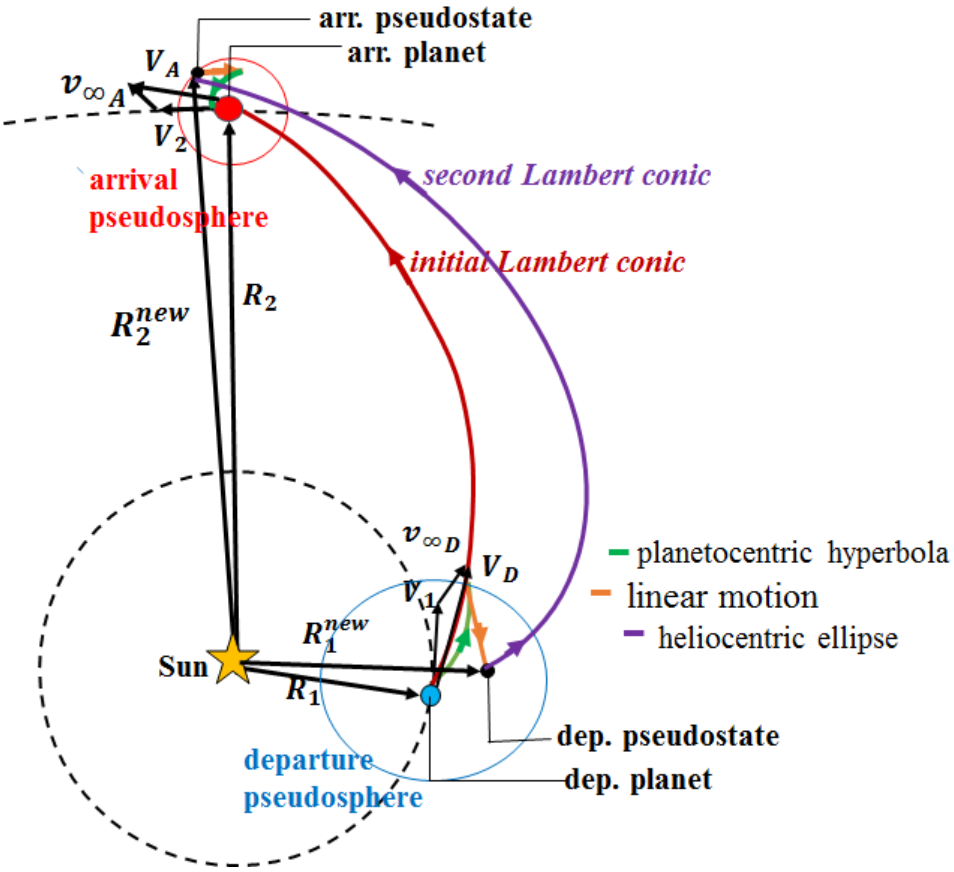

Fig. 4.1a. Illustration of the ITR-PS technique

1) Obtain the heliocentric states of the departure planet on the departure epoch $(\boldsymbol{R_1}, \boldsymbol{V_1})$ and the arrival planet on the arrival epoch $(\boldsymbol{R_2}, \boldsymbol{V_2})$. Set $(\boldsymbol{R_1}, \boldsymbol{R_2})$ as the position vectors of the initial pseudostates i.e., $\boldsymbol{R_{D_{PS}}} = \boldsymbol{R_1}$ at the departure phase and $\boldsymbol{R_{A_{PS}}} = \boldsymbol{R_2}$ at the arrival phase. Note that, $\boldsymbol{R_{D\ or\ A_{PS}}}$ is not the position vector at the pseudosphere.
2) Determine the heliocentric Lambert conic connecting the position vectors of the pseudostate points $(\boldsymbol{R_{D_{PS}}}, \boldsymbol{R_{A_{PS}}})$ for the given flight duration (t_{FD}). Let the determined heliocentric velocity vectors at respective pseudostate points be $\boldsymbol{V_{D_{PS}}}$ and $\boldsymbol{V_{A_{PS}}}$.
3) Compute the planetocentric V-infinity vectors at the departure and arrival phases i.e., $\boldsymbol{v_{\infty D}}$ and $\boldsymbol{v_{\infty A}}$ respectively.

$$\boldsymbol{v_{\infty D}} = \boldsymbol{V_D} - \boldsymbol{V_{D_{PS}}} \tag{4.1a}$$

$$\boldsymbol{v}_{\infty_A} = \boldsymbol{V}_A - \boldsymbol{V}_{A_{PS}} \tag{4.1b}$$

4) From the V-infinity vectors, find the orbital elements ($a_\infty, e_\infty, i_\infty, \Omega_\infty, \omega_\infty, \nu_\infty = \nu_{P_\infty} = 0$) of the departure and arrival hyperbolic orbits using the procedure described in section 3.2. One of the four options is chosen for further processing.
5) Find the departure planetocentric velocity vector ($\boldsymbol{v}_{h_D}$) from the departure hyperbolic orbital elements by solving Kepler equation for t_D days. Similarly, find the arrival planetocentric velocity vector ($\boldsymbol{v}_{h_A}$).
6) The desired and propagated V-infinity vectors i.e., $\boldsymbol{v}_{\infty_D}$ and $\boldsymbol{v}_{h_D}$, are matched at the pseudosphere of the departure planet using the analytical tuning strategy. Similarly at the arrival phase also.
7) Obtain the position vectors at the pseudosphere of the departure ($\boldsymbol{r}_{h_D}$) and arrival ($\boldsymbol{r}_{h_A}$) phases by propagating the respective tuned hyperbolic orbital elements.
8) The planetocentric pseudostates are obtained by a linear sweep back at the departure phase and linear sweep forward at the arrival phase i.e.,

$$\boldsymbol{r}_{D_{PS}} = \boldsymbol{r}_{h_D} - \boldsymbol{v}_{h_D} t_D \tag{4.2}$$

$$\boldsymbol{r}_{A_{PS}} = \boldsymbol{r}_{h_A} + \boldsymbol{v}_{h_A} t_A \tag{4.3}$$

The planetocentric pseudostates are transformed into the heliocentric pseudostates.

$$\boldsymbol{R}_{D_{PS}}^{new} = \boldsymbol{R}_1 + \boldsymbol{r}_{D_{PS}} \tag{4.4a}$$

$$\boldsymbol{R}_{A_{PS}}^{new} = \boldsymbol{R}_2 + \boldsymbol{r}_{A_{PS}} \tag{4.4b}$$

These heliocentric pseudostates form the new terminal points to be used for determining the next Lambert conic.

9) Check the differences between the successive position vectors of the pseudostates both at the departure and arrival phases. If the differences are less than a prefixed threshold value, then the transfer trajectory design is obtained. Otherwise the steps (2) to (9) are repeated.

At the end of these steps, the transfer trajectory design for one of the options is obtained. ***The resulting hyperbolic orbit characteristics can be used to find the TPI and POI velocity impulses*** *(cf. section 3.5)*. We can apply these steps for the other three design options also. The step (6) makes the proposed technique different from the one-step impact technique. Note that there are two loops, (i) an inner loop for tuning the hyperbolic orbit characteristics to achieve the desired V-infinity vector and, (ii) an outer loop that

connects the pseudostates for Lambert conic determination. After updating the pseudostates in the outer loop, the desired V-infinity vectors at the departure and arrival phases are updated from the Lambert conic solutions, and matched at the pseudospheres using the analytical tuning strategy in the inner loop. The diagram depicting the ITR-PS technique is given in Fig. 4.1a and the flowchart is presented in Fig. 4.1b.

4.2.2 Illustrative Results

To illustrate the performance of the ITR-PS technique, the Earth to Mars orbiter mission is considered. The minimum energy opportunity occurring on 12 May 2018 0 h TDB for a flight duration of 204 days is used. The DPO is 300 x 25,000 km with an inclination of 75 deg with respect to Earth Equator and Equinox of J2000. The APO is 300 km circular with an inclination of 75 deg with respect to Mars equator and IAU vector of J2000 [Archinal et al., 2009].

Table 4.1 V-infinity vectors from ITR-PS technique

Parameters	option 11	option 12	option 21	option 22
v_{∞_D}(m/s)	2.7893	2.7906	2.7847	2.7859
α_{∞_D}(deg)	321.9206	321.9437	321.7844	321.8078
δ_{∞_D}(deg)	-37.1345	-37.2146	-36.7642	-36.8449
v_{∞_A}(m/s)	2.9609	2.9605	2.9622	2.9618
α_{∞_A}(deg)	245.5156	245.4841	245.5985	245.5668
δ_{∞_A}(deg)	9.5043	9.5446	9.2203	9.2607

The four distinct V-infinity vectors obtained using the ITR-PS technique are presented in Table 4.1 and the corresponding four distinct design options are given in Table 4.2. Each of the parameters of the four design options are distinctly different except the departure and arrival inclinations which are prefixed. It is observed that even small differences in the departure/TPI angles (RAAN, 0.23 deg; AoP 0.17 deg between the design options 11 and 12) result in completely different arrival geometries. Similar trend is seen for the other two options 21 and 22. ***The high sensitivity of the departure parameters can be understood from this observation.***

Table 4.3 gives a comparison of different analytical trajectory designs for the design option 11. The ITR-PS design, VPC design and the numerical design generated using the design force model (Pseudostate force model: departure phase/Sun-Earth for 3

days, cruise phase/Sun for 199 days, and arrival phase/Mars for 2 days) are given. Note that the VPC technique could not capture the change in RAAN which is possible by the ITR-PS technique. Further, the ITR-PS design is closer to the numerical design as compared to the VPC design.

Table 4.2 Design options from ITR-PS technique

(i_{∞_D} =75 deg; i_{∞_A}=75 deg)

Parameters	option 11	option 12	option 21	option 22
a_{∞_D} (km)	-58625.72	-58564.68	-58859.51	-58799.08
e_{∞_D}	1.113911	1.114030	1.113458	1.113575
Ω_{∞_D} (deg)	333.6273	333.6850	130.2362	130.2252
ω_{∞_D}(deg)	167.5207	167.4482	64.4443	64.5418
a_{∞_A}(km)	-4977.4201	-4978.7431	-4973.0997	-4974.4693
e_{∞_A}	1.742794	1.742597	1.743439	1.743235
Ω_{∞_A}(deg)	68.0867	242.9018	68.0914	243.0627
ω_{∞_A}(deg)	115.1685	314.9005	115.4479	314.5917

Table 4.3 Comparison of design option 11 from different techniques

(i_{∞_D} =75 deg; i_{∞_A}=75 deg)

Parameters	Numerical design	VPC design	ITR-PS design
a_{∞_D} (km)	-58613.9834	-58640.49	-58625.72
e_{∞_D}	1.113911	1.113882	1.113911
Ω_{∞_D} (deg)	333.6176	333.0131	333.6273
ω_{∞_D}(deg)	167.5163	167.8129	167.5207
a_{∞_A}(km)	-4977.4480	-4973.42	-4977.42
e_{∞_A}	1.742577	1.743391	1.742794
Ω_{∞_A}(deg)	68.0835	68.1673	68.0867
ω_{∞_A}(deg)	115.1746	115.4118	115.1685

The ITR-PS design options are numerically propagated under the design force model and the resulting target parameters are presented in Table 4.4. The deviation in the achieved target parameters are significantly reduced as compared to the VPC design. The achieved CAA ranges from 1,916 km to 11,245 km for the four distinct ITR-PS design

options. The deviations in the time of periapsis are also largely reduced to about 1 to 2 hours. This brings out the fact that, even though the differences in the departure/TPI angles between the VPC design and the ITR-PS design (RAAN, 0.85 deg; AoP, 0.36 deg) are very small, there is large improvement in the achieved CAA and the time of periapsis. However, there is large deviation in the achieved APO inclination from the desired value. ***This indicates that further refinement of the ITR-PS design is necessary.***

Table 4.4 Achievable accuracies on numerical propagation under design force model

Parameters		Achieved CAA (km)	Arr. inclination (deg)	T_P (UTC)	TCM (m/s)
Desired value		300	75.00	2 Dec 2018 00:00:00	-
VPC design		1,107,535	141.00	29 Nov 2018 17:22:58	~ 165 m/s
ITR-PS design	option 11	1,916.3	32.32	2 Dec 2018 01:32:04	< 1 m/s
	option 12	4,542.0	50.26	2 Dec 2018 01:38:16	
	option 21	6,956.8	10.63	2 Dec 2018 02:32:55	
	option 22	11,244.9	41.35	2 Dec 2018 02:39:40	

To assess the implication of modelling errors, the trajectory correction maneuvers (TCM) required to achieve the desired target parameters under the design force model are estimated and given in Table 4.4. The TCM is applied after 13 days of departure from the DPO periapsis. The VPC design requires a TCM addition of about 200 m/s whereas the ITR-PS design requires less than 1 m/s. This indicates the refinement taken place in the design level itself. This happened because of the inclusion of Sun's gravity within the pseudosphere. It is understood that the corrections in the departure hyperbolic orbital elements in the numerical refinement process will be minimal. ***Although the TCM requirement is less than 1 m/s, the large deviation in the arrival inclination reflects the high sensitivity of the departure design parameters as pointed out earlier.***

Table 4.5 Comparison of velocity impulses from different analytical techniques

Velocity impulses	VPC design	ITR-PS design			
		option 11	option 12	option 21	option 22
TPI (m/s)	1311.61	1311.68	1311.99	1310.48	1310.79
POI (m/s)	2223.38	2233.94	2233.15	2234.00	2233.80
Total (m/s)	3545.41	3545.62	3545.15	3544.48	3544.59

For completion, the velocity impulses viz. TPI and POI required for the Earth to Mars transfer are computed for the ITR-PS design and compared with those of the VPC

design in Table 4.5. It is seen that the velocity impulses are almost the same for the VPC design and ITR-PS design options.

For all the above analysis, the sweep-back and sweep-forward durations of Earth and Mars are considered as 3 and 2 days respectively, after some trial runs. ***The trial runs indicate that lesser durations result is infeasible scenarios and the larger durations do not significantly improve the design in terms of the achievable accuracies of the arrival target parameters. So, a suitable intermediate value is chosen.*** The FORTRAN 95 code developed based on the ITR-PS technique is used for design analysis. The details are included in **Appendix A**.

4.2.3 Disadvantages

The one-step iterative pseudostate technique has the following disadvantages.

1) In the one-step iterative pseudostate technique, the step size used for analytical propagation is large. The boundary of the pseudosphere is reached from the periapsis in a single step. This causes deviation in the V-infinity vector achieved on numerical propagation.
2) A small deviation in the V-infinity vector results in large deviations in the arrival target parameters. Thus, the APO inclination is not achieved.
3) The transfer trajectory is heliocentric even in the close vicinity of the target planets.

In the next section, the problem of reducing the deviation in the V-infinity vector is addressed.

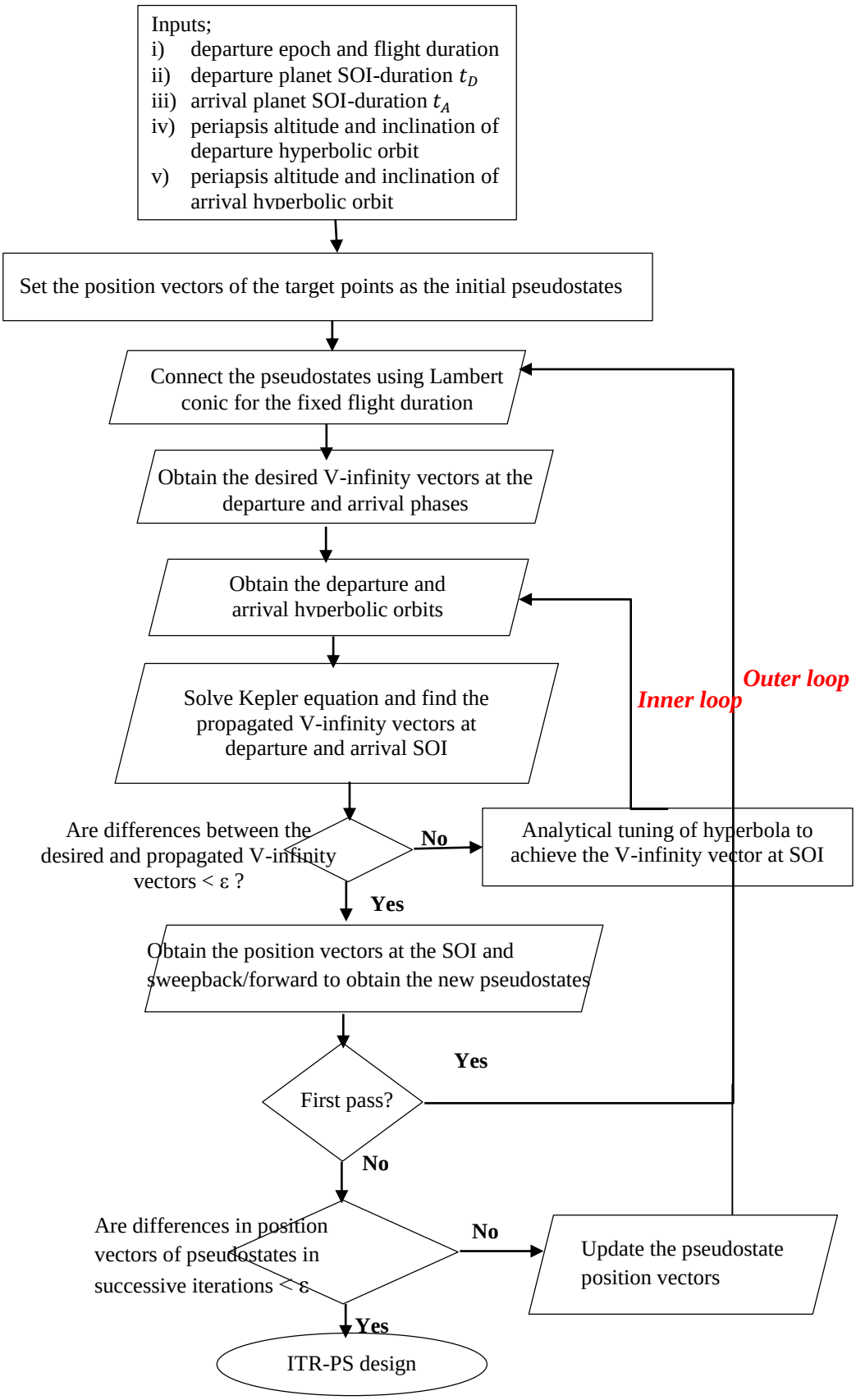

Fig. 4.1b. Flowchart illustrating the ITR-PS technique

4.3 Multiconic Differential Evolution Technique

4.3.1 Motivation

The analytical design generated using the one-step pseudostate technique results in deviations in arrival target parameters on numerical propagation under the design force model. Specifically, the deviation in the arrival inclination (cf. Table 4.4) is significant. As pointed out earlier, these deviations are mainly due to the position and velocity discontinuities at the pseudospheres and these discontinuities need to be minimized. This is possible by applying the pseudostate technique in multiple steps (referred to as multiconic technique in literature). It is known that the choice of departure hyperbolic orbital elements influences the V-infinity vector. The analytical tuning strategy which is used to tune the hyperbolic orbital elements in Keplerian orbit, is not suitable for the multiconic technique. So, the Differential Evolution technique [Storn and Price, 1997] is employed for the tuning purpose. The use of multiconic propagation and differential evolution together generates departure hyperbolic orbital elements that achieves the V-infinity vector at the pseudosphere precisely. When the design thus obtained is numerically propagated, the deviations in the arrival target parameters are largely reduced. The small differences that still exist are due to the discontinuity in the position vector at the pseudosphere. These differences occur because the differential evolution technique targets only the velocity vector at the boundary of the pseudosphere. So, an iterative technique, named as **multiconic differential-evolution (MCDE) technique**, is proposed that iterates on the position vector at the pseudosphere. Thus, the MCDE technique involves two loops, (i) an outer loop that connects the position vector at the departure and arrival pseudospheres using the Lambert conic and (ii) an inner loop to find the hyperbolic orbital elements using differential evolution and multiconic propagation.

In the following sections, first the performance of multiconic technique as a propagation technique is demonstrated and then the use of differential evolution technique for tuning the hyperbolic orbital elements is discussed. Finally, the MCDE technique which generates the interplanetary transfer trajectory is presented.

4.3.2 Multiconic Propagation Technique

As pointed out earlier, when the step size used for analytical propagation of the departure hyperbolic orbital elements is large as in the case of the one-step pseudostate technique, the V-infinity vector obtained at the pseudosphere differs from the desired V-infinity value (obtained by numerically integrating the three-body equations of motion; Sun-

Earth-spacecraft). This deviation can be reduced by applying the pseudostate technique in multiple steps (multiconic propagation). Cook et al. (1962) used the multiconic propagation technique to obtain the trajectory design for lunar transfer. Byrnes and Hooper (1970) used the multiconic technique to solve for the initial conditions of the optimum burn maneuver from Earth orbit for Apollo mission.

For completion, the steps of multiconic propagation (cf. section 2.5.2) in the departure phase are repeated below.

1) From the perigee, the departure hyperbolic orbital elements are propagated forward analytically using the Keplerian force model (Earth and spacecraft) for a short duration. This conic is a geocentric hyperbola.
2) The geocentric state vector of the spacecraft obtained from step (1) is propagated backward for the same duration along a straight line. This represents the zero-gravity linear sweep-back motion.
3) After propagation, the geocentric state vector obtained from step (2) is transformed to the heliocentric frame. The corresponding heliocentric orbital elements are propagated forward analytically under the Keplerian force model (Sun and spacecraft) for the same duration. This conic is a heliocentric ellipse.
4) The state vector corresponding to the heliocentric orbital elements obtained from step (3) is transformed to the geocentric frame.

The steps (1) to (4) are repeated up to the pseudosphere of Earth.

From the pseudosphere of Earth up to the pseudosphere of the arrival planet, the propagation is essentially Keplerian under the influence of Sun only. In the arrival phase of the interplanetary transfer, the aforementioned steps are reversed. The steps for multiconic propagation in the arrival phase are given below.

1) From the pseudosphere of the arrival planet, the heliocentric orbital elements are propagated forward analytically using the Keplerian force model (Sun and spacecraft) for a short duration. This conic is a heliocentric ellipse.
2) The heliocentric orbital elements (after propagation) are transformed to planetocentric state vector and the planetocentric states are propagated backward for the same duration along a straight line.
3) The planetocentric state vector obtained from step (2) is propagated forward analytically under the Keplerian force model (planet and spacecraft) for the same duration. This conic is a planetocentric hyperbola.

4) The state vector corresponding to the planetocentric orbital elements obtained from step (3) is transformed to the heliocentric frame.

Repeat the steps (1) to (4) up to the periapsis of the arrival planet (for the prefixed arrival pseudosphere duration).

Table 4.6 Comparison of pseudostate and numerical propagation techniques

Parameters	*Initial state vector	state vector obtained from		
		One-step pseudostate propagation	Multiconic propagation	Numerical propagation
x(km)	-5675.81	490426.88	490451.97	490453.30
y(km)	3231.00	-396836.83	-396802.43	-396802.34
z(km)	1393.88	-510121.95	-510091.13	-510090.49
$\dot{x}$(km/s)	-3.435537	1.738437	1.738542	1.738544
$\dot{y}$(km/s)	-1.464928	-1.375038	-1.374869	-1.374864
$\dot{z}$(km/s)	-10.593643	-1.682609	-1.682452	-1.682448
Δr (km)	-	**53.64**	**1.47**	-
Δv (m/s)	-	**0.26**	**0.0067**	-
*Initial departure hyperbolic orbital elements a_{∞_D}= -58625.72 km; e_{∞_D}=1.113911; i_{∞_D}= 75 deg; Ω_{∞_D}=333.6273 deg; ω_{∞_D}=167.5207 deg; $\nu_{P\infty_D}$=0 deg				

The multiconic propagation is an effective and quick alternative to the numerical propagation for the three-body problem (cf. Table 4.6). A typical state vector in Earth equator and Equinox of J2000 frame is propagated for 3 days from the DPO periapsis up to the departure pseudosphere under the 3-body force model (Sun, Earth and the spacecraft). In Table 4.6, the state vector obtained using different analytical propagation techniques are presented. The analytical propagation is carried out using the one-step pseudostate and multiconic propagation techniques. The step size used for multiconic propagation is 0.005 days. The state vector obtained on numerical integration (cf. Table 4.6) of the three-body force model is used as the reference for comparison. The deviations in the magnitude of position vector (Δr) and velocity vector (Δv) are presented. It is to be noted that the magnitude of deviation in the position vector obtained using the one-step pseudostate technique is 53.64 km. On multiconic propagation, this deviation reduces to 1.47 km. The magnitude of deviation in the velocity vector obtained using the one-step pseudostate technique is 0.26 m/s. This small deviation is sufficient to cause very large

deviation in the achieved target parameters (cf. Table 4.12). The deviation in the velocity vector reduces to 0.0067 m/s on multiconic propagation (cf. Table 4.6). ***Thus, multiconic propagation technique is a good alternative to numerical integration.***

4.3.3 Differential Evolution for Suitable Hyperbolic Orbital Elements

For a given V-infinity vector at the pseudosphere, the problem is to determine suitable hyperbolic orbital elements that achieve the desired V-infinity vector at the pseudosphere. The differential evolution (DE) technique is used to solve this problem. This technique does not require any initial guess on the unknowns and require only a range of values (bound) within which the unknowns could vary. A population (say, of size NP) of unknowns (say, N) is generated randomly from their respective bounds and the objective function is evaluated for each member of the population. Each member of the population is updated using three operations: mutation, crossover, and selection. The DE parameters, (i) population size, (ii) mutation factor and (iii) cross-over frequency, are chosen suitably after some trial runs. The objective function of the updated member is also evaluated. This process is continued until the objective function satisfies the convergence criteria.

4.3.3.1 Differential Evolution

The steps of a basic differential evolution technique that minimizes an objective function are presented here.

1) Generate the initial population (G) by randomly selecting the values of the unknown design variables (N) from their respective bounds using uniform distribution. Each set of values for the design variables are tested for feasibility. The feasibility tests are problem dependent.
2) Evaluate the objective function for each member of the population and store it as a (NP) × (N+1) matrix.
3) If the objective function satisfies the convergence criteria, the solution is obtained. Otherwise, update the population using the following steps. Each member of the population is tested whether it must be carried on to the next generation of population (G+1) or not. The testing process is as follows.
   i) Select the first member ($i = 1$) of the current population as the target vector. Select three distinct members (r_1, r_2 and r_3) randomly from the population using uniform distribution. These members must be different from the target vector.
   ii) Form the mutant vector ($V_{i,G+1}$) using the three selected members.

$$V_{i,G+1} = X_{r1,G} + F\left(X_{r2,G} - X_{r3,G}\right) \quad (4.6)$$

where X denotes the vector containing the unknown parameters. The term $'F'$ is called the mutation scale factor and the new vector generated is called the mutant vector. This process is called 'mutation'.

iii) Use the target vector and mutant vector to generate a new vector called the trial vector. A crossover constant, $CR \in [0,1]$ equivalent to the probability that a trial vector element will come from the mutant vector, is used. Select N uniform random numbers $rand(j) \in [0,1], j = 1$ to N and compare with $'CR'$ to determine if each element of the trial vector will come from the target vector or the mutant vector.

If rand(j)>CR, j^{th} element of target vector is j^{th} element of trial vector

If rand(j)<CR, j^{th} element of mutant vector is j^{th} element of trial vector (4.7)

where $j = 1, N$.

After applying the above condition for all elements of the member, a new trial vector is formed. The trial vector is tested for feasibility before accepting it.

iv) Evaluate the objective function of the trial vector. If the objective function of the trial vector is less than the current objective function, the trial vector replaces the current member. Otherwise, the current member is retained.

v) The steps (i) to (iv) are repeated for all members of the population and the next generation of population is generated.

4) Repeat step (3) until the convergence criterion is satisfied.

4.3.4 Algorithm

As discussed earlier, the MCDE technique consists of two loops. In the inner loop, differential evolution is used for the selection of hyperbolic orbital elements and multiconic technique is used for the analytical propagation within the pseudosphere of the target planets. The selected departure hyperbolic orbital elements, on multiconic propagation, achieves the desired V-infinity vector at the pseudosphere. In the outer loop, the transfer trajectory design from the parking orbit of Earth to the parking orbit of the arrival planet is obtained by solving the Lambert problem that connects the departure and arrival position vectors at the respective pseudosphere. In the current problem, the periapsis distance ($r_{P_{\infty D}}$) and inclination (i_{∞_D}) of the departure hyperbolic orbit are fixed. Also, the departure takes place from the periapsis ($\nu_{P_{\infty D}} = 0$). So, the unknowns

at the departure are, (i) semi-major axis (a_{∞_D}), (ii) right ascension of ascending node (RAAN, Ω_{∞_D}) and (iii) argument of periapsis (AoP, ω_{∞_D}). The DE bounds for these variables are fixed in the neighborhood of the corresponding values of the ITR-PS design. The objective function for the departure phase is set as,

$$J = \text{minimize} \left| \boldsymbol{v}_{\infty_{D_{desired}}} - \boldsymbol{v}_{\infty_{D_{achieved}}} \right| \tag{4.8}$$

where $\boldsymbol{v}_{\infty_{D_{desired}}}$ is the desired departure V-infinity vector at the pseudosphere of Earth (obtained on solving the Lambert problem) and $\boldsymbol{v}_{\infty_{D_{achieved}}}$ is the achieved V-infinity vector at the pseudosphere of Earth obtained on multiconic propagation. Similarly, the unknowns at the arrival phase are, (i) semi-major axis (a_{∞_A}), (ii) RAAN (Ω_{∞_A}) and (iii) AoP (ω_{∞_A}). The objective function for the arrival phase is set as,

$$J = \text{minimize} \left| \boldsymbol{v}_{\infty_{A_{desired}}} - \boldsymbol{v}_{\infty_{A_{achieved}}} \right| \tag{4.9}$$

where $\boldsymbol{v}_{\infty_{A_{desired}}}$ is the desired arrival V-infinity vector at the pseudosphere of the arrival planet (obtained on solving the Lambert problem) and $\boldsymbol{v}_{\infty_{A_{achieved}}}$ is the achieved V-infinity vector at the pseudosphere of the arrival planet obtained on multiconic propagation.

The algorithm of the MCDE technique is given below.

The periapsis distance and inclination (i_{∞_D}) *of the departure hyperbolic orbit are fixed. The departure epoch, flight duration* (t_{FD}) *and the durations that represent the pseudosphere of the departure and arrival planets* (t_D *and* t_A *respectively) are fixed. Also, the arrival parameters such as the required closest approach altitude (CAA), time of periapsis* (T_P) *and inclination* (i_{∞_A}) *are fixed.*

1) Obtain the ITR-PS design (cf. section 4.2.1) and the departure and arrival pseudostates (position and velocity vectors). The departure pseudostate is propagated *forward* under the Keplerian two-body force model involving the Sun and the spacecraft for a duration of t_D days. This results in the heliocentric states (position vector, $\boldsymbol{R}_{D_{PS}}$ and velocity vector, $\boldsymbol{V}_{D_{PS}}$) at the departure pseudosphere. The heliocentric states are transformed to geocentric states (position vector, $\boldsymbol{r}_{D_{PS}}$ and velocity vector, $\boldsymbol{v}_{D_{PS}}$). Similarly, the heliocentric position and velocity vectors of the arrival pseudostate point are propagated *backward* for a duration of t_A days to obtain

the heliocentric states (position vector, $\boldsymbol{R}_{A_{PS}}$and velocity vector, $\boldsymbol{V}_{A_{PS}}$) at the arrival pseudosphere. The heliocentric states are transformed to planetocentric states ($\boldsymbol{r}_{A_{PS}}$ and $\boldsymbol{v}_{A_{PS}}$).

2) Determine the Lambert conic by connecting the heliocentric position vectors at the departure $\left(\boldsymbol{R}_{D_{PS}}\right)$ and arrival $\left(\boldsymbol{R}_{A_{PS}}\right)$ pseudospheres for an updated flight duration $(t_{FD} - t_D - t_A)$.

3) Obtain the Lambert velocity vector at the departure pseudosphere and set this value as $\boldsymbol{V}_{D_{PS_{desired}}}$. Compute the desired departure V-infinity vector $\left(\boldsymbol{v}_{\infty D_{desired}}\right)$ as follows,

$$\boldsymbol{v}_{\infty D_{desired}} = \boldsymbol{V}_{D_{PS_{desired}}} - \boldsymbol{V}_{Earth}^{t_D} \tag{4.10}$$

where $\boldsymbol{V}_{Earth}^{t_D}$ is the heliocentric velocity vector of Earth after t_D days from the departure epoch.

Similarly, obtain the Lambert velocity vector at the arrival pseudosphere and set this value as $\boldsymbol{V}_{A_{PS_{desired}}}$. Compute the desired arrival V-infinity vector $\left(\boldsymbol{v}_{\infty A_{desired}}\right)$ as,

$$\boldsymbol{v}_{\infty A_{desired}} = \boldsymbol{V}_{A_{PS_{desired}}} - \boldsymbol{V}_{arrival\ planet}^{t_A} \tag{4.11}$$

where $\boldsymbol{V}_{arrival\ planet}^{t_A}$ is the heliocentric velocity vector of the arrival planet t_A days before the arrival epoch.

The steps for the selection of suitable departure hyperbolic orbital elements that achieves $\boldsymbol{v}_{\infty D_{desired}}$ precisely at the pseudosphere of Earth are given below. In similar steps, suitable arrival hyperbolic orbital elements that achieves $\boldsymbol{v}_{\infty A_{desired}}$ precisely at the pseudosphere of the arrival planet can also be obtained with some modifications. These modifications are discussed later.

4) Generate the members $a_{\infty_D}, \Omega_{\infty_D}, \omega_{\infty_D}$ of the population (first generation).

5) Evaluate the objective function for each member of the population by multiconic forward propagation until the pseudosphere is reached. The geocentric velocity vector obtained at the Earth pseudosphere is termed as the achieved velocity vector at the departure pseudosphere $\left(\boldsymbol{v}_{\infty D_{achieved}}\right)$.

6) Compute the objective function J of the departure phase using Eq. 4.8.

7) Update the population using the steps of differential evolution technique described in section (4.3.3.1) until J is less than a threshold value. The member corresponding to the minimum objective function is considered for further steps. Let the converged departure hyperbolic orbital elements be $(a_{\infty_D}, e_{\infty_D}, i_{\infty_D}, \Omega_{\infty_D}, \omega_{\infty_D}, \nu_{P_{\infty D}} = 0)$.

To generate the arrival hyperbolic orbital elements, the steps (4) to (7) are executed. The steps for the arrival phase are obtained by replacing, (i) subscript 'D' by 'A', (ii) the terms 'departure' by 'arrival', 'geocentric' by 'arrival planetocentric', and 'backward' by 'forward'. The objective function for the arrival phase is given in Eq. 4.9.

8) Propagate the departure hyperbolic orbit $(a_{\infty_D}, e_{\infty_D}, i_{\infty_D}, \Omega_{\infty_D}, \omega_{\infty_D}, \nu_{P_{\infty D}} = 0)$ *forward* up to the departure pseudosphere and obtain the heliocentric states (position vector, $\boldsymbol{R}'_{D_{PS}}$ and velocity vector, $\boldsymbol{V}'_{D_{PS}}$). Similarly, propagate the arrival hyperbolic orbit $(a_{\infty_A}, e_{\infty_A}, i_{\infty_A}, \Omega_{\infty_A}, \omega_{\infty_A}, \nu_{P_{\infty A}} = 0)$ *backward* up to the arrival pseudosphere and obtain the heliocentric states (position vector, $\boldsymbol{R}'_{A_{PS}}$and velocity vector, $\boldsymbol{V}'_{A_{PS}}$).

9) Check if the following condition is satisfied.

$$\begin{cases} \left(\boldsymbol{R}_{D_{PS}} - \boldsymbol{R}'_{D_{PS}}\right) \\ \left(\boldsymbol{R}_{A_{PS}} - \boldsymbol{R}'_{A_{PS}}\right) \end{cases} \leq \epsilon \tag{4.12}$$

where $'\epsilon'$ is a prefixed small threshold value. The choice of the threshold value is made based on an analysis which is presented later. If the condition is not satisfied, set $\boldsymbol{R}_{D_{PS}} = \boldsymbol{R}'_{D_{PS}}$and $\boldsymbol{R}_{A_{PS}} = \boldsymbol{R}'_{A_{PS}}$ and repeat the steps (2) to (9).

The steps (8) and (9) constitute the outer loop that iterates on the position vectors at the departure and arrival pseudosphere points whereas, in the ITR-PS technique, the outer loop iterates on the pseudostate points. The departure orbital elements, thus obtained, forms the MCDE design and are used to determine the TPI and POI velocity impulses. The flowchart illustrating the MCDE technique is given in Fig. 4.2.

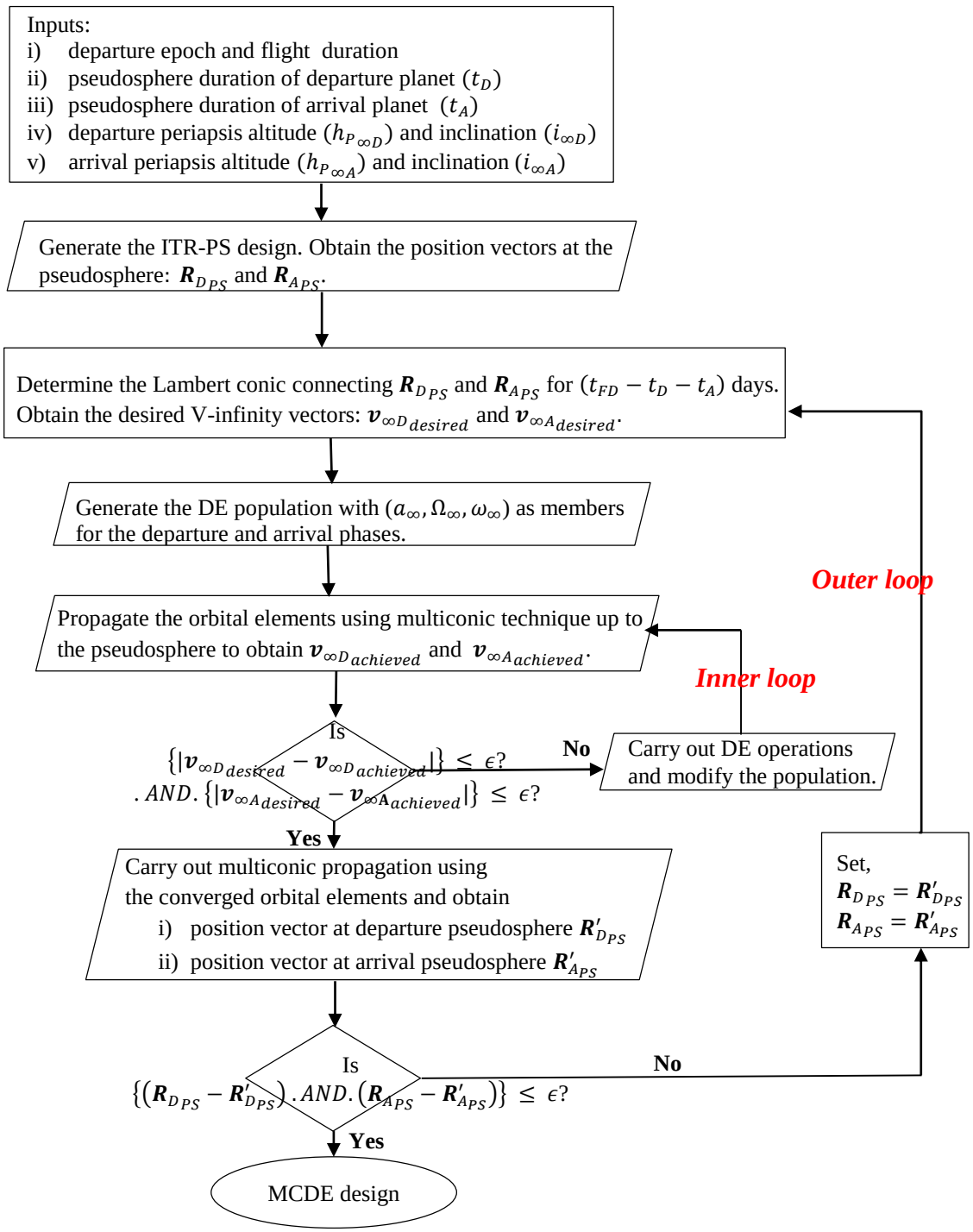

Fig. 4.2. Flowchart illustrating the MCDE technique

4.3.5 Illustrative Results

The performance of the MCDE technique is illustrated for an Earth to Mars orbiter mission for the minimum energy opportunity occurring on 12 May 2018 0 h TDB with a flight duration of 204 days. The periapsis altitude and inclination of the departure hyperbolic orbit are considered as 300 km and 75 deg with respect to Earth equator and Equinox of J2000. The periapsis altitude and inclination of the arrival hyperbolic orbit

are considered as 300 km and 75 deg with respect to Mars equator and IAU vector of J2000. The pseudosphere durations of Earth and Mars are considered as 3 and 2 days respectively.

Initially, the four transfer trajectory design options available for the minimum-energy opportunity are obtained using the ITR-PS technique (cf. Table 4.2). These designs are used to fix bounds for the unknown parameters in the differential evolution technique. The differential evolution parameters are set as follows: population size (NP) =40, cross-over frequency (*CR*) =0.5, mutation factor (*F*) =0.8.

Table 4.7 Effect of velocity threshold values on arrival parameters

(Position threshold value: 10 km)

Threshold values (km/s)	Arr. CAA (km)	% deviation in CAA	Arr. APO inclination (deg)	% deviation in inclination	T_P (UTC)
1	18,964.64	-	12.54	-	2 Dec 2018 03:41:58
0.1	869.42	15.40	91.73	22.30	1 Dec 2018 23:47:06
0.01	342.39	1.14	76.08	1.44	1 Dec 2018 23:58:35
1.0E-05	318.15	0.48	75.28	0.33	1 Dec 2018 23:59:15

Table 4.8 Effect of position threshold values on arrival parameters

(Velocity threshold value: 1E-05 km/s)

Threshold values (km)	Number of iterations/ computation time	Arr. CAA (km)	% deviation in CAA	Arr. APO inclination (deg)	% deviation in inclination	T_P (UTC)
100	1 / 40 s	380.4	2.16	77.6612	3.54	1 Dec 2018 23:56:12
10	2 / 88 s	318.15	0.48	75.2875	0.38	1 Dec 2018 23:59:15
1	3 / 127 s	317.77	0.47	75.3760	0.50	1 Dec 2018 23:58:52

The loops of the MCDE technique terminate based on threshold values (outer loop based on the difference in position vectors of successive iterations and inner loop based on the difference in velocity vectors of successive iterations). First, the implication of these threshold values on the arrival target parameters is analyzed. The desired values of arrival parameters are; (i) closest approach altitude (CAA) 300 km, and (ii) inclination:

75 deg and (iii) time of periapsis (T_P): 2 Dec 2018 00:00:00 UTC. Table 4.7 gives the arrival target parameters obtained on numerical propagation of the MCDE designs, for different velocity thresholds (velocity threshold is the magnitude of difference between the desired and achieved V-infinity vectors at the pseudosphere). It is clear that, for a difference of 1 km/s, there are large deviations in the target arrival parameters (achieved CAA: 18,964 km, inclination: 12 deg and time of periapsis deviates by about 4 h). For a velocity threshold value of 1E-05 km/s, the arrival target parameters are very close to the desired values. Further reduction of threshold value results in increased computation time without significant improvement in the achieved target parameters. So, the velocity threshold is fixed as 1E-05 km/s. The relative improvement in achievable accuracies are better understood from the percentage deviations (computed as the ratio of the difference in the achieved and desired values to the desired value) given in Table 4.7. The MCDE design options are numerically propagated under the design force model and the resulting target parameters are presented in Table 4.8, for different position threshold values. A position threshold of 100 km results in an achieved CAA of 380 km (deviation 2.1%), APO inclination of 77.66 deg (deviation 3.5%) and time of periapsis deviates by about 4 minutes. These deviations are reduced for a position threshold value of 10 km. The achieved CAA is 318 km (1.6%), APO inclination is 75.2 deg (0.3%) and the deviation in the time of periapsis is less than 1 minute. Also, the number of iterations for convergence is only two (computation time: 88 s). Further reduction in position threshold value does not significantly improve the achieved target parameters for the corresponding increase in computation time. Therefore, a position threshold value of 10 km is used in this study.

Table 4.9 presents the performance of the MCDE technique. The MCDE design is obtained after two iterations and the computation time is about 88 seconds in an Intel Core i5-3230 CPU 2.60 GHz processor. Note that, the hyperbolic orbital elements are different even after the first iteration of the MCDE technique. The deviations in the departure/TPI angles (RAAN and AoP) are 0.009 deg and 0.002 deg respectively. Such small deviations in the departure angles result in large deviations in the achieved arrival target parameters on numerical propagation. For example, the inclination of the arrival hyperbola obtained on numerical propagation of the ITR-PS design is 32 deg as compared to that of the MCDE design, 75.28 deg (cf. Table 4.11).

Table 4.9 Performance of MCDE technique

(Thresholds on: position, 10 km; velocity magnitude/angle: 1E-05 km/s/1E-3 deg)

Parameters	ITR-PS design	MCDE design	
		after 1st iteration	after 2nd (final) iteration
a_{∞_D} (km)	-58625.72	-58613.46	-58613.83
e_{∞_D}	1.113911	1.113935	1.113934
Ω_{∞_D} (deg)	333.6273	333.6182	333.6186
ω_{∞_D}(deg)	167.5207	167.5185	167.5183
a_{∞_A}(km)	-4977.42	-4977.42	-4977.43
e_{∞_A}	1.7427944	1.742793	1.742792
Ω_{∞_A}(deg)	68.0867	68.0867	68.0868
ω_{∞_A}(deg)	115.1685	115.1685	115.1684

Table 4.10 MCDE design options (i_{∞_D} =75 deg; i_{∞_A}=75 deg)

Parameters	MCDE designs			
	option 11	option 12	option 21	option 22
a_{∞_D} (km)	-58613.8	-58552.8	-58836.9	-58776.5
e_{∞_D}	1.113934	1.114053	1.113502	1.113618
Ω_{∞_D} (deg)	333.6186	333.6763	130.2251	130.2141
ω_{∞_D}(deg)	167.5183	167.4459	64.4509	64.5483
a_{∞_A}(km)	-4977.4	-4978.7	-4973.1	-4974.4
e_{∞_A}	1.742792	1.742594	1.743437	1.743232
Ω_{∞_A}(deg)	68.0868	242.9018	68.0914	243.0627
ω_{∞_A}(deg)	115.1684	314.9007	115.4479	314.5919

The four design options obtained using the MCDE technique are given in Table 4.10. The MCDE design is compared with the numerical design obtained under the design force model (pseudostate force model) for the design option 11 in Table 4.11. It is observed that the MCDE design is very close to the numerical design. The computation time required for numerical refinement of the MCDE design under the design force model is less than 1 s as compared to the ITR-PS design which is about 6 s (cf. Table 4.14). ***So,***

it is clear that the MCDE design serves as a better initial guess for numerical refinement.

Table 4.11 Comparison of MCDE and numerical designs (i_{∞_D} =75 deg; i_{∞_A}=75 deg)

Parameters	MCDE design	Numerical design
a_{∞_D} (km)	-58613.8	-58613.9
e_{∞_D}	1.113934	1.113911
Ω_{∞_D} (deg)	333.6186	333.6176
ω_{∞_D}(deg)	167.5183	167.5163
a_{∞_A}(km)	-4977.4	-4977.4
e_{∞_A}	1.742792	1.742577
Ω_{∞_A}(deg)	68.0868	68.0835
ω_{∞_A}(deg)	115.1684	115.1746

Table 4.12 Achievable accuracies of pseudostate designs under design force model

Parameters		option 11	option 12	option 21	option 22
ITR-PS	CAA (Km)	1,916.3	4,540.2	6,956.8	11,244.9
	APO inclination (deg)	32.32	50.26	10.63	41.35
	T_P (UTC)	2 Dec 2018 01:32:02	2 Dec 2018 01:38:16	2 Dec 2018 02:32:55	2 Dec 2018 02:39:40
MCDE	CAA (km)	318.15	286.25	317.04	308.20
	APO inclination (deg)	75.28	75.31	74.91	75.00
	T_P (UTC)	1 Dec 2018 23:59:15	1 Dec 2018 23:59:06	1 Dec 2018 23:59:30	1 Dec 2018 23:59:25

The arrival target parameters obtained on numerical propagation of the ITR-PS and MCDE designs under the design force model are given in Table 4.12. As mentioned earlier, on numerical propagation under the design force model, the ITR-PS design options result in CAAs varying from about 1,916 km to 11,245 km for the four design options. The deviations in the time of periapsis are around 1 to 2 hours. The deviations in the achieved inclination for all the four ITR-PS design options are significant. These large deviations in the arrival inclinations are corrected by the MCDE designs. The achieved inclinations of the arrival hyperbolic orbit range from 74.91 deg to 75.31 deg (against the desired value: 75 deg) and so, are very close to the desired value. Also, the MCDE design options result in CAAs varying from about 286 km to 318 km. The deviations in the time of periapsis are only few seconds. Thus, the MCDE design achieves all the arrival target

parameters with better accuracy. The computation time required for obtaining the ITR-PS design is about 5 ms while the MCDE design requires 88 s (cf. Table 4.14). Though the computation time for MCDE design is more, there is a significant improvement in the trajectory design in terms of the achieved target parameters (cf. Table 4.12).

Table 4.13 Comparison of velocity impulses from different pseudostate techniques

Velocity impulses	ITR-PS design	MCDE design
TPI (m/s)	1311.68	1311.74
POI (m/s)	2233.94	2233.94
Total (m/s)	3545.62	3545.68

Table 4.14 Comparison of computation time

	ITR-PS design	MCDE design
Design generation	0.005 s	88 s
Numerical refinement	6 s	<1 s

For completion, the velocity impulses, viz. TPI and POI, obtained from the MCDE design is compared with that from ITR-PS design for the design option 11 (cf. Table 4.13. The velocity impulses are almost the same. Similar result follows for the other three design options also and hence, not presented.

4.3.6 Disadvantages

The disadvantages of MCDE techniques are,

1) The MCDE technique requires a large computation time for generating the design.
2) The use of DE makes the technique semi-analytical.
3) Even within the pseudosphere, the transfer trajectory is heliocentric.

4.4 Conclusions

The iterative pseudostate (ITR-PS) technique identifies the four distinct design options for an opportunity by iterating on the pseudostates. This technique captures the small differences in departure angles, viz. RAAN and AoP which result in the completely different arrival geometries. The computation time required for generating the ITR-PS design is only 6 ms. However, the use of the one-step pseudostate technique for analytical propagation causes small deviation in the departure V-infinity vector achieved at the boundary of the pseudosphere. So, the arrival target parameters are largely deviated from

the desired values especially the arrival inclination. Therefore, ITR-PS design needs further modification in the design process.

This modification of ITR-PS design is done by applying the pseudostate technique in multiple steps (multiconic propagation). A random search method, differential evolution (DE) is employed for the selection of hyperbolic orbital elements that achieves the V-infinity vector at the pseudosphere. The use of multiconic technique for analytical propagation and DE for searching the hyperbolic orbital elements help in targeting the V-infinity vector more accurately. ***This technique, named as multiconic differential evolution (MCDE) technique, reduces the deviations in the arrival target parameters including the arrival inclination.*** The achieved inclinations of the arrival hyperbolic orbit range from 74.91 deg to 75.31 deg (against the desired value, 75 deg). Also, the MCDE design options result in CAAs varying from about 286 km to 318 km. The deviations in the time of periapsis are only few seconds. ***So, the MCDE design can be used as a better initial guess for the numerical refinement process.*** Also, the computation time required for numerical refinement of the MCDE design under the design force model is less than 1 s as compared to the ITR-PS design which is about 6 s. Thus, MCDE technique can be used to analytically refine the ITR-PS design which results in significant improvement in the trajectory design especially in terms of the achieved arrival inclination.

♠♠♠♠♠♠♠♠♠♠♠♠♠♠♠♠♠♠♠

CHAPTER 5
ITERATIVE PATCHED CONIC TECHNIQUE FOR TRANSFER TRAJECTORY DESIGN

5.1 Chapter Summary

The previous chapter discussed analytical techniques that are based on the pseudostate concept wherein the transfer trajectory is heliocentric even in the close vicinity of the target planets. This makes the inclusion of the non-spherical gravity of Earth in the trajectory design process difficult.

To overcome this difficulty, an iterative analytical technique that derives the merit from the simple patched conic assumptions as well as the iterative pseudostate technique is proposed in this chapter. This technique, named as ***iterative patched conic technique*** (ITR-PC) generates quick and improved design. The iterative nature help in identifying the four distinct design options for an opportunity. A sensitivity analysis has been carried out which justifies the need for the improved design using the ITR-PC technique. A comparative analysis of the ITR-PC and conventional patched conic designs is included. The use of the ITR-PC technique as a mission design and analysis tool to analyze the four design options for an Earth to Mars orbiter mission is demonstrated.

5.2 Iterative Patched Conic Technique

The working principle of the iterative patched conic technique is as follows.

Initially, the position vectors of the departure and arrival target planets at the departure and arrival epochs respectively, are connected using the heliocentric Lambert conic. The asymptotic velocity (V-infinity) vectors at departure and arrival are calculated as the difference between the heliocentric velocity vectors at the respective SOI and the target planets. The departure and arrival hyperbolic orbit characteristics are computed and modified using the analytical tuning strategy to achieve the V-infinity vectors at the respective SOI. The modified departure and arrival hyperbolic orbits are propagated under Keplerian force model for the respective SOI-durations and the planetocentric state

vectors are obtained. The locations on the departure and arrival SOIs, thus obtained, are known as **patch points**. The planetocentric position vectors of the patch points are transformed to the heliocentric frame and connected using a heliocentric Lambert conic for the flight duration that excludes the SOI durations. The V-infinity vectors are updated and the hyperbolic orbit characteristics are modified to obtain the updated V-infinity vectors at the respective SOI. Thus, the ITR-PC technique consists of two loops, (i) an inner loop that modifies the departure and arrival hyperbolic orbit characteristics to achieve the V-infinity vector at the respective SOI, and (ii) an outer loop for determining the Lambert conic (that connects the position vectors of the target planets in the first iteration, and the patch points at the departure/arrival phases in the subsequent iterations). This reduces the position discontinuity at the boundary of SOI of the target planets. ***These loops determine the four distinct V-infinity vectors as well as the related hyperbolic orbital elements.*** As an example, the three segments of a typical Earth to Mars transfer based on patched conic assumptions are given in Fig. 5.1a.

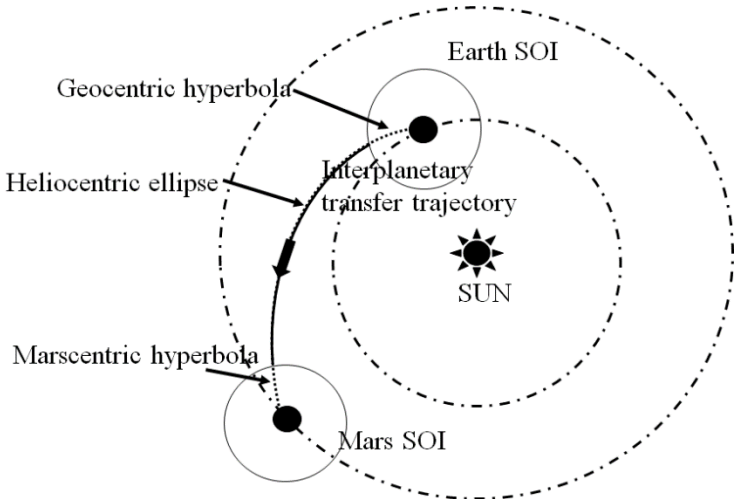

Fig.5.1a. Patched conic approximation for Earth-Mars interplanetary transfer

The steps describing the ITR-PC technique are given below. The hyperbolic orbital elements are computed using the steps (1) to (4). The patch points at the sphere of influence (SOI) are obtained at the departure and arrival phases using the steps (5) to (7). Then, an updated Lambert conic is determined by connecting the patch point position vectors for a different flight duration that excludes the SOI durations.

The departure epoch and flight duration (t_{FD}) are fixed. The periapsis distance and inclination of the departure hyperbolic orbit, and the SOI-durations of the departure and arrival phases (t_D and t_A days respectively) are also fixed.

1) Obtain the heliocentric states of the departure planet on the departure epoch ($\boldsymbol{R_1}, \boldsymbol{V_1}$) and the arrival planet on the arrival epoch ($\boldsymbol{R_2}, \boldsymbol{V_2}$). These heliocentric states are in Earth mean equator and equinox of J2000 frame.
2) Determine the heliocentric Lambert conic connecting the position vectors ($\boldsymbol{R_1}, \boldsymbol{R_2}$) for the prefixed flight duration (t_{FD}). Compute the corresponding heliocentric velocity vectors ($\boldsymbol{V_{D_{PC}}}$ and $\boldsymbol{V_{A_{PC}}}$) in the transfer trajectory.
3) Compute the planetocentric V-infinity vectors at the departure and arrival phases, i.e., $\boldsymbol{v_{\infty_D}}$ and $\boldsymbol{v_{\infty_A}}$ respectively.

$$\boldsymbol{v_{\infty_D}} = \boldsymbol{V_{D_{PC}}} - \boldsymbol{V_1} \tag{5.1}$$

$$\boldsymbol{v_{\infty_A}} = \boldsymbol{V_{A_{PC}}} - \boldsymbol{V_2} \tag{5.2}$$

   The arrival V-infinity vector is transformed to Mars Mean Equator and IAU vector of J2000 (Archinal et al., 2009).
4) From the V-infinity vectors, find the orbital elements ($a_\infty, e_\infty, i_\infty, \Omega_\infty, \omega_\infty, \nu_\infty = \nu_{P_\infty} = 0$) of the departure and arrival hyperbolic orbits using the procedure described in section 3.2.

The steps (1) to (4) constitute the conventional patched conic technique and result in four notional design options which are not distinct. One of the four design options is chosen for further modification.

5) Find the departure planetocentric velocity vector/propagated velocity vector ($\boldsymbol{V_{h_D}}$) from the departure hyperbolic orbital elements by solving the Kepler equation for the prefixed SOI duration (t_D) and. Similarly, find the arrival planetocentric velocity vector ($\boldsymbol{V_{h_A}}$).

   This step involves the numerical solution of Kepler equation. For a threshold value of 1E-15, each solution run takes about 4 to 5 iterations.
6) The desired and propagated V-infinity vectors, i.e. $\boldsymbol{v_{\infty_D}}$ and $\boldsymbol{v_{h_D}}$, are matched at the SOI of the departure planet using the analytical tuning strategy described in section 3.3. The tuning of the desired and propagated V-infinity vectors at the arrival planet is also carried out using the same strategy.
7) Obtain the planetocentric position vectors of the patch points at the departure ($\boldsymbol{r_{h_D}}$) and arrival ($\boldsymbol{r'_{h_A}}$) phases by propagating the respective updated/tuned hyperbolic orbital elements under the two-body (Keplerian) force model. The planetocentric

position vector of the arrival patch point ($\boldsymbol{r'_{h_A}}$) is transformed to Earth equator and Equinox of J2000 frame ($\boldsymbol{r_{h_A}}$).

The steps (1) to (7) constitute the V-infinity tuned patched conic technique. The conventional and the V-infinity tuned patched conic techniques gives only notional design options and fails to distinguish between them.

The following steps of the ITR-PC technique make the departure hyperbolic orbital elements distinct from the other options.

8) The planetocentric position vectors of the patch points at SOI are transformed into heliocentric position vectors.

$$\boldsymbol{R_D^{SOI}} = \boldsymbol{R_D^{t_D}} + \boldsymbol{r_{h_D}} \tag{5.3}$$

$$\boldsymbol{R_A^{SOI}} = \boldsymbol{R_A^{t_A}} + \boldsymbol{r_{h_A}} \tag{5.4}$$

where $\boldsymbol{R_D^{t_D}}$ is the heliocentric position vector of the departure planet after t_D days from the departure epoch and $\boldsymbol{R_D^{SOI}}$ is the heliocentric position vector of the departure patch point. Similarly in Eq. 5.4, $\boldsymbol{R_A^{t_A}}$ is the heliocentric position vector of the arrival planet before t_A days from the arrival epoch and $\boldsymbol{R_A^{SOI}}$ is the heliocentric position vector of the arrival patch point.

9) Determine the Lambert conic connecting the heliocentric position vectors of the patch points ($\boldsymbol{R_D^{SOI}}$, $\boldsymbol{R_A^{SOI}}$) for a flight duration defined by ($t_{FD} - t_D - t_A$). The corresponding heliocentric velocity vectors are $\boldsymbol{V_{D_{PC}}^{SOI}}$ and $\boldsymbol{V_{A_{PC}}^{SOI}}$.

10) Compute the planetocentric V-infinity vectors at the patch points, i.e. $\boldsymbol{v_{\infty_D}}$ and $\boldsymbol{v_{\infty_A}}$,

$$\boldsymbol{v_{\infty_D}} = \boldsymbol{V_{D_{PC}}^{SOI}} - \boldsymbol{V_D^{t_D}} \tag{5.5}$$

$$\boldsymbol{v_{\infty_A}} = \boldsymbol{V_{A_{PC}}^{SOI}} - \boldsymbol{V_A^{t_A}} \tag{5.6}$$

where $\boldsymbol{V_D^{t_D}}$ is the heliocentric velocity vector of the departure planet after t_D days from the departure epoch and $\boldsymbol{V_A^{t_A}}$ is the heliocentric velocity vector at the SOI of the arrival planet before $\boldsymbol{t_A}$ days from the arrival epoch. These velocity vectors are with respect to Earth Equator and Equinox of J2000 frame. The arrival V-infinity vector is transformed to Mars Equator and IAU vector of J2000 frame.

11) From the V-infinity vectors, find the orbital elements ($a_\infty, e_\infty, i_\infty, \Omega_\infty, \omega_\infty, \nu_\infty = \nu_{P_\infty} = 0$) of departure and arrival hyperbolic orbits.

12) Propagate the hyperbolic orbital elements for the SOI-durations. Tune the hyperbolic orbital elements to achieve the desired V-infinity vector at the SOI using the analytical tuning strategy.
13) Find the planetocentric position vectors of the patch points at the departure ($\boldsymbol{r'}_{\boldsymbol{h_D}}$) and arrival phases. The planetocentric position vector of the arrival patch point is transformed to Earth Equator and Equinox of J2000 frame ($\boldsymbol{r'}_{\boldsymbol{h_A}}$).
14) Transform the planetocentric position vectors to heliocentric position vectors ($\boldsymbol{R'}_{\boldsymbol{D}}^{\boldsymbol{SOI}}$ and $\boldsymbol{R'}_{\boldsymbol{A}}^{\boldsymbol{SOI}}$) and find the difference between successive position vectors of the patch points.
15) If the differences are less than the predefined small values, then the transfer trajectory design is obtained. Otherwise the heliocentric position vectors of the patch points are reset as ($\boldsymbol{R'}_{\boldsymbol{D}}^{\boldsymbol{SOI}}$ and $\boldsymbol{R'}_{\boldsymbol{A}}^{\boldsymbol{SOI}}$) and the steps (9) to (15) are repeated.

At the end of these steps, the transfer trajectory design for one of the options is obtained. We can apply these steps for the other three design options as well. The hyperbolic orbital elements, thus obtained, are used to determine the TPI and POI velocity impulses. The flowchart of the ITR-PC technique is presented in Fig. 5.1b.

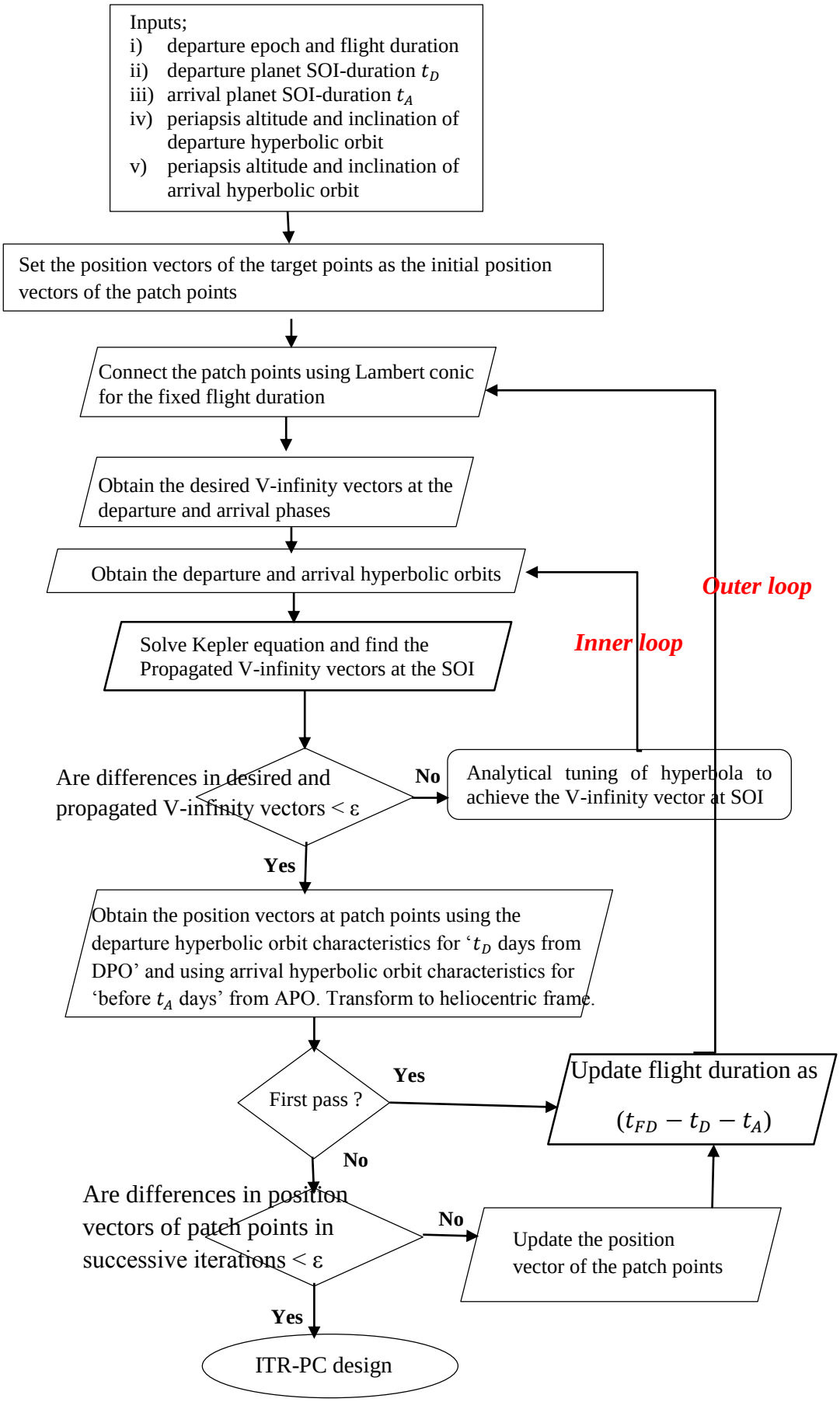

Fig.5.1b. Flowchart of the ITR-PC technique

5.3 Illustrative Results

The ITR-PC technique is used to obtain the distinct design options for a typical Earth to Mars orbiter mission. The minimum energy opportunity of 2018 is used here. However, for completion, it is repeated here. The departure epoch is on 12 May 2018 0 h TDB and the flight duration is 204 days. The Earth parking orbit is 300 x 25,000 km and inclination of 75 deg with respect to Earth equator and Equinox of J2000. The Mars parking orbit is 300 km circular and inclination of 75 deg with respect to Mars equator and IAU vector of J2000. The SOI duration of Earth and Mars are fixed as 3 and 2 days respectively.

Table 5.1a Illustration of iterative process on heliocentric patch points (outer loop)

Parameters	Outer loop iterations (iterations on heliocentric patch points)						
	1*	**1****	**2**	**3**	**4**	**5**	**6**
x_{PC_D}(km)	-88622845	-88646825	-88648536	-88648646	-88648654	-88648655	-88648655
y_{PC_D}(km)	-112491471	-112472620	-112468234	-112468111	-112468067	-112468063	-112468062
z_{PC_D}(km)	49111210	-49089131	-49091490	-49092057	-49092124	-49092133	-49092134
x_{PC_A}(km)	196451122	195789253	195789620	195789592	195789590	195789590	195789590
y_{PC_A}(km)	75677142	76523208	76524043	76524168	76524182	76524184	76524185
z_{PC_A}(km)	29099505	29831022	29828870	29828625	29828591	29828586	29828585
Δr_{PC_D} (km)	-	8387633	5266	590	79	11	1.4
Δr_{PC_A} (km)	-	3937777	2337	276	37	5	0.7

1*: initial value of patch point (position of target planets)
1:** patch point after analytical tuning
Position threshold: 10 km
$\{x_{PC_D}, y_{PC_D}, z_{PC_D}\}$ position vector of the departure patch point
$\{x_{PC_A}, y_{PC_A}, z_{PC_A}\}$ position vector of the arrival patch point
Δr_{PC_D} difference in departure patch point position vectors
Δr_{PC_A} difference in arrival patch point position vectors

As discussed earlier, the ITR-PC technique has two loops, an inner loop for analytical tuning (cf. Table 3.2) and an outer loop for lambert conic determination. Tables 5.1a and 5.1b illustrate the outer loop iterations. It can be noted that the outer loop converges in six iterations. For each of the outer loop iteration, there is an inner loop (4 to 5 iterations) for analytically tuning the departure and arrival hyperbolic orbital elements. For completion, the inner loop iterations for the 6th outer loop is given in Table 5.1c. Table 5.1a shows the change in the departure and arrival patch points with each outer loop iteration. From Table 5.1b, it can be noted that the departure and arrival hyperbolic orbital elements (design) significantly changes over each iteration. The outer loop iteration converges on achieving the condition set on the position threshold value.

Thus, with the two loops, the ITR-PC technique reduces the discontinuities in the position and velocity vectors at the SOI.

Table 5.1b Illustration of iterative process on departure/arrival hyperbola (outer loop)

Outer loop iterations	Design parameters							
	a_{∞_D} (km)	e_{∞_D}	Ω_{∞_D} (deg)	ω_{∞_D}(deg)	a_{∞_A}(km)	e_{∞_A}	Ω_{∞_A}(deg)	ω_{∞_A}(deg)
1*	-51239.9	1.130330	333.0131	169.3999	-4881.1	1.755807	68.1673	115.1321
1**	-58640.4	1.113882	333.0131	167.8129	-4973.4	1.741783	68.1673	115.4488
2	-59021.2	1.113147	333.3635	167.4153	-4980.2	1.740769	68.0909	115.2498
3	-58970.0	1.113246	333.3833	167.3836	-4979.9	1.740804	68.0883	115.2197
4	-58966.4	1.113253	333.3883	167.3788	-4980.0	1.740798	68.0879	115.2159
5	-58965.7	1.113254	333.3888	167.3782	-4980.0	1.740798	68.0878	115.2154
6	-58965.6	1.113254	333.3889	167.3781	-4980.0	1.740798	68.0878	115.2153

1* : Conventional patched conic design
1:** V-infinity tuned patched conic design

Table 5.1c Illustration of iterative process in the inner loop (outer loop iteration: 6th)
(Thresholds on velocity vector: direction (deg, ϵ): 1E-3, magnitude: 1E-6 km/s)

Iteration no.	Departure phase		Arrival phase	
	Difference between desired and propagated V-infinity vectors			
	angle (ϵ,deg)	magnitude (km/s)	angle (ϵ,deg)	magnitude (km/s)
1	0.049418	0.164042	0.003445	0.027158
2	1.469073	0.071832	0.311127	0.016076
3	0.072526	0.003540	0.002734	0.000141
4	0.003443	0.000168	0.000023	0.000001
5	0.000163	0.000007	0.000023	0.000001

For comparison, the departure and arrival V-infinity vectors obtained using the conventional/V-infinity tuned patched conic technique and the ITR-PC technique are given in Table 5.2. While the conventional/V-infinity tuned patched conic technique generates only one set of departure and arrival V-infinity vector, the ITR-PC technique generates four distinct sets of V-infinity vectors. For the transfer to be feasible, in the conventional PC technique, the DPO inclination can vary from 36.8 deg to 143.2 deg as the value of declination of the departure V-infinity for the 2018 minimum energy opportunity is -36.8 deg (cf. Table 5.2). The feasible range of inclination can be fixed more accurately from the ITR-PC design options. While, with the ITR-PC technique, the

feasible range for option 11 is between 37.21 deg and 143.79 deg. ***This indicates that, we cannot generate the design for a coplanar transfer with a DPO inclination of 36.8 deg.***

The four distinct design options of the ITR-PC technique in terms of hyperbolic orbital elements are given in Table 5.3. Note that although the differences in the departure/TPI angles between the design options are very small (design options 11 and 12: RAAN, 0.06 deg and AoP, 0.07 deg), the resulting arrival hyperbolas are completely different. This indicates the high sensitivity of the arrival geometry to the departure angles. Similar trend is observed for the design options 21 and 22. The different analytical designs for the trajectory design option 11 are compared with the numerical design generated under the design force model (PCFM) in Table 5.4. It can be noted that the ITR-PC design is very close to the numerical design.

Table 5.2 Departure and arrival V-infinity vectors

Parameters	Conventional PC/VPC technique	ITR-PC technique			
		option 11	option 12	option 21	option 22
v_{∞_D}(km/s)	2.7891	2.7826	2.7839	2.7779	2.7791
α_{∞_D}(deg)	321.42	321.65	321.68	321.53	321.55
δ_{∞_D}(deg)	-36.85	-37.21	-37.29	-36.84	-36.92
v_{∞_A}(km/s)	2.9621	2.9602	2.9598	2.9614	2.9610
α_{∞_A}(deg)	245.66	245.51	245.49	245.60	245.56
δ_{∞_A}(deg)	9.25	9.50	9.54	9.22	9.26

Table 5.3 Design options using ITR-PC technique (i_{∞_D} =75 deg; i_{∞_A}=75 deg)

Parameters	option 11	option 12	option 21	option 22
a_{∞_D} (km)	-58965.7	-58904.1	-59206.2	-59145.1
e_{∞_D}	1.113254	1.113371	1.11279	1.112912
Ω_{∞_D} (deg)	333.3889	333.4465	129.9454	129.9341
ω_{∞_D}(deg)	167.3782	167.3057	64.4571	64.5547
a_{∞_A}(km)	-4980.0	-4981.3	-4975.7	-4977.1
e_{∞_A}	1.742402	1.742202	1.743048	1.742842
Ω_{∞_A}(deg)	68.0878	242.9041	68.0925	243.0652
ω_{∞_A}(deg)	115.1783	314.9085	115.4581	314.5994

The conventional patched conic, VPC and ITR-PC designs are used as the initial guess for numerical refinement under the design force model PCFM and the computation time required for the process are given in Table 5.5. *When the ITR-PC design is used as the initial guess, the numerical refinement needs only about 6 s whereas the VPC design needs 780 s. The numerical refinement of the conventional patched conic design needs a computation time of more than a day.* ***This clearly brings out the fact that the ITR-PC design serves as a good initial guess for numerical refinement.***

Table 5.4 Comparison of analytical designs with numerical design
($i_{\infty D}$=75 deg; $i_{\infty A}$=75 deg)

Parameters	Conventional PC design	VPC design	ITR-PC design	Numerical design (PCFM)
a_{∞_D} (km)	-51239.9	-58640.5	-58965.7	58966.9
e_{∞_D}	1.130332	1.113882	1.113254	1.11325
Ω_{∞_D} (deg)	333.0131	333.0131	333.3889	333.3881
ω_{∞_D}(deg)	169.3999	167.8129	167.3782	167.3788
a_{∞_A}(km)	-4881.1	-4973.4	-4980.0	-4980.0
e_{∞_A}	1.757441	1.743391	1.742402	1.742170
Ω_{∞_A}(deg)	68.1673	68.1673	68.0878	68.0824
ω_{∞_A}(deg)	115.0951	115.4118	115.1783	115.1852

The achievable accuracies of the analytical designs on numerical propagation under the design force model PCFM are given in Table 5.6. The design obtained from the conventional and V-infinity tuned patched conic technique result in very large deviations in the achieved target parameters as pointed out in chapter 3. In the case of ITR-PC designs, the achieved CAA values range from 220 km to 330 km for the four design options. The achieved arrival inclination is very close to the desired value. Also, the deviation in time of periapsis is 2 to 3 minutes only. The TCM required for the aforementioned designs to achieve the arrival target parameters are also presented in Table 5.6. ***It can be noted that the TCM value is very high (>150 m/s) for the conventional and VPC designs while the ITR-PC design requires less than 0.1 m/s.***

The TPI and POI velocity impulses required for the interplanetary transfer (Earth to Mars orbiter mission, 2018) for different patched conic design techniques are given in Table 5.7. The difference between the conventional patched conic design and the ITR-PC design is high (about 58 m/s). Thus, the ITR-PC design allows considerable saving in

fuel, roughly 20 kg. The difference between the VPC and ITR-PC designs is very small (< 2 m/s). The total velocity impulse for the distinct ITR-PC design options are also almost same. ***This brings out the fact that no additional velocity impulse is incurred for achieving the different arrival geometries.***

Table 5.5 Computation time for numerical refinement

Parameters	initial guess used		
	Conventional PC design	VPC design	ITR-PC design
Computation time	> 1 day	780 s	6 s

Table 5.6 Achievable accuracies on numerical propagation under PCFM

Designs		Achieved CAA (km)	Arrival inclination (deg)	T_P (UTC) DD/MM/YYYY HH:MM:SS	TCM (m/s)
Conventional patched conic design		3,011,712	156.32	05/11/2018 22:16:50	>200
VPC design		1,107,535	141.01	29/11/2018 17:22:58	~ 165
ITR-PC design	option 11	330	75.39	01/12/2018 23:58:19	< 0.1
	option 12	233	75.44	01/12/2018 23:58:17	< 0.1
	option 21	226	73.47	01/12/2018 23:57:40	< 0.1
	option 22	220	73.39	01/12/2018 23:56:52	< 0.1

Table 5.7 Velocity impulses from different patched conic techniques

Design		Velocity impulses (m/s)		
		TPI	POI	Total
Conventional PC design		1355.22	2248.21	3603.43
VPC design		1311.61	2223.38	3545.41
ITR-PC design	option 11	1309.93	2233.54	3543.48
	option 12	1310.25	2233.57	3543.82
	option 21	1308.71	2233.44	3542.15
	option 22	1309.02	2233.23	3542.25

In Table 5.8, the conventional patched conic design and the ITR-PC design (option 11) are given for a **DPO/APO inclination of 90 deg**. In this case, Eqs. (3.6) and (3.7) have singularities. As discussed earlier, this situation is handled by adopting the

values of α_∞ and $(180-\alpha_\infty)$ for RAAN to avoid arithmetic overflow. It is to be noted that even though the differences in departure RAAN (0.02 deg) between the two designs is small and departure AoP (2 deg) is large, there is a large improvement in the achievable accuracies of the arrival target parameters (achieved CAA 320 km, inclination 90.12 deg and the time of periapsis deviates by about 1.5 minutes) on numerical propagation under the force model PCFM (cf. Table 5.9). Similar trend as in Table 5.6 is seen. This clearly brings out the need to improve the conventional patched conic design.

Table 5.8 Conventional patched conic and ITR-PC designs **($i_{\infty_D} = 90$ deg; $i_{\infty_A} = 90$ deg)**

Parameters	Conventional PC design	ITR-PC design
a_{∞_D} (km)	-51239.9	-58875.2
e_{∞_D}	1.130330	1.113428
Ω_{∞_D} (deg)	321.6262	321.6492
ω_{∞_D}(deg)	170.9305	168.9178
a_{∞_A}(km)	-4881.1	-4978.0
e_{∞_A}	1.755807	1.7410
Ω_{∞_A}(deg)	65.6645	65.4988
ω_{∞_A}(deg)	115.4617	115.5243

Table 5.9 Achievable accuracies on numerical propagation under PCFM

Designs	Achieved CAA (km)	Arrival inclination (deg)	T_P (UTC)
Desired value	300	90.0	2 Dec 2018 00:00:00
Conventional PC design	3,054,598	156.4	6 Nov 2018 16:37:54
ITR-PC design	320.11	90.12	1 Dec 2018 23:58:31

5.3.1 Sensitivity Analysis

To bring out the sensitivity of the achievable accuracies to the departure hyperbolic orbital elements, an analysis is carried out. Each of the departure design parameters (cf. Table 5.3, option 11) viz. semi-major axis, eccentricity, inclination, RAAN and AoP are perturbed one-at-a-time and the design is numerically propagated under the design force model PCFM.

The deviations in the achievable accuracies give an indication of the sensitivity of the design parameters. Table 5.10 presents the achievable accuracies on perturbing the departure RAAN of the ITR-PC design. The target parameters undergo considerable deviations if the perturbation is greater than ± 0.001 deg. The deviation in the departure

RAAN deviates T_P significantly (1 deg change deviates T_P by 3 days). If the departure RAAN is perturbed by about 0.01 deg, it results in impact. Table 5.11 gives the achievable accuracies on perturbing the departure AoP of the ITR-PC design. Note that the target parameters undergo considerable deviations if the perturbation is greater than ± 0.0001 deg. The deviation in the departure AoP deviates the arrival/APO inclination significantly (0.001 deg change deviates APO inclination by about 3 deg).

Table 5.10 Sensitivity of achievable accuracies to departure RAAN

Perturbation (deg)	CAA (km)	Arr. Inc. (deg)	T_P (UTC)
-1	112,305	128.9	29 Nov 2018 03:00:16
-0.1	10,280	116.3	1 Dec 2018 17:15:56
-0.01	937	84.1	1 Dec 2018 23:18:04
-0.001	382	76.3	1 Dec 2018 23:54:36
-0.0001	334	75.4	1 Dec 2018 23:58:16
0.0001	324	75.3	1 Dec 2018 23:59:05
0.001	278	74.4	2 Dec 2018 00:02:46
0.01	-91 (impact)	64.9	2 Dec 2018 00:39:43
0.1	5,037	14.7	2 Dec 2018 07:17:00
1	151,819	37.3	5 Dec 2018 01:23:47

Table 5.11 Sensitivity of achievable accuracies to departure AoP

Perturbation (deg)	CAA (km)	Arr. Inc. (deg)	T_P (UTC)
-1	409,597	38.4	2 Dec 2018 05:51:16
-0.1	30,709	30.3	2 Dec 2018 01:01:39
-0.01	-80 (impact)	41.6	1 Dec 2018 23:59:16
-0.001	201	72.3	1 Dec 2018 23:58:27
-0.0001	316	75.1	1 Dec 2018 23:58:39
0.0001	343	75.6	1 Dec 2018 23:58:42
0.001	474	78.2	1 Dec 2018 23:58:56
0.01	2,410	98.1	2 Dec 2018 00:02:45
0.1	36,161	132.0	2 Dec 2018 00:25:15
1	392,413	139.0	1 Dec 2018 23:10:49

Table 5.12 depicts the achievable accuracies on perturbing the inclination of the departure hyperbolic orbit (ITR-PC design). Here, the target parameters undergo

considerable deviations if the perturbation is greater than ± 0.001 deg. Table 5.13 presents the achievable accuracies on perturbing the eccentricity of the departure hyperbolic orbit (ITR-PC design). The eccentricity is a highly sensitive parameter and so the target parameters undergo considerable deviations if the perturbation is > ± 0.00001. Table 5.14 gives the achievable accuracies on perturbing the semi-major axis of the departure hyperbolic orbit (ITR-PC design). Here, the target parameters undergo considerable deviations if the perturbation is greater than ± 1 km. ***Thus, it can be concluded that the arrival parameters are extremely sensitive to even a small change in any one of the characteristics of the departure hyperbolic orbit. So, the departure design parameters must be obtained with a reasonably good accuracy.***

Table 5.12 Sensitivity of achievable accuracies to departure inclination

Perturbation (deg)	CAA (km)	Arr. Inc. (deg)	T_P (UTC)
-1	185,788	134.4	29 Nov 2018 13:31:19
-0.1	16,464	123.5	1 Dec 2018 18:18:10
-0.01	1319	88.8	1 Dec 2018 23:16:14
-0.001	466	78.0	1 Dec 2018 23:55:27
-0.0001	395	76.7	1 Dec 2018 23:58:27
0.0001	380	76.4	1 Dec 2018 23:59:08
0.001	314	75.1	2 Dec 2018 00:02:09
0.01	-146 (impact)	60.6	2 Dec 2018 00:32:49
0.1	10,775	21.9	2 Dec 2018 06:21:10
1	208,618	37.6	4 Dec 2018 14:00:47

Table 5.13 Sensitivity of achievable accuracies to eccentricity of departure hyperbolic orbit

Perturbation	CAA (km)	Arr. Inc. (deg)	T_P (UTC)
-0.001	38,141	132.3	2 Dec 2018 00:28:31
-0.0001	2516	98.3	1 Dec 2018 23:45:03
-0.00001	503	77.9	1 Dec 2018 23:40:56
0.00001	223	71.8	1 Dec 2018 23:40:23
0.0001	-84	41.6	1 Dec 2018 23:58:58
0.001	32,119	30.7	2 Dec 2018 01:00:30

It is to be noted that the ***high sensitivity of the arrival parameters to the initial departure conditions indicate that the perturbations in the departure phase must be included in the trajectory design process***. In other words, an interplanetary mission would miss its target entirely if the perturbing forces in the departure phase were not taken into account in the trajectory design.

5.3.2 Comparison of Conventional Patched conic and ITR-PC Techniques

From section 5.3, it is clear that the conventional PC design must be improved. Also, the high sensititvity of the arrival target parameters to the departure design parameters are brought out in section 5.3.1. This section presents a comparative analysis of the conventional PC and ITR-PC designs generated for a range of departure epochs and flight durations.

Table 5.14 Sensitivity of achievable accuracies to semi-major axis of departure hyperbolic orbit

Perturbation (km)	CAA (km)	Arr. Inc. (deg)	T_P (UTC)
-1000	510,389	21.0	4 Dec 2018 22:22:40
-100	42,005	14.6	2 Dec 2018 07:48:39
-10	1,377	39.4	2 Dec 2018 00:44:03
-1	303	71.2	2 Dec 2018 00:02:49
1	366	79.1	1 Dec 2018 23:54:35
10	1,924	108.3	1 Dec 2018 23:21:18
100	42,754	151.1	1 Dec 2018 17:46:21
1000	469,412	158.1	29 Nov 2018 00:46:08

Initially, the conventional patched conic (PC) and ITR-PC designs are generated for a range of departure epochs (1 April 2018 to 30 June 2018). The differences in the departure/TPI angles (RAAN and AoP) between the conventional patched conic and ITR-PC designs are depicted in Fig.5.2a. For this range of departure epochs, the difference in departure RAAN varies from -0.8 deg to 0.2 deg. There are three random departure epochs for which the difference becomes almost zero. Note that, the corresponding designs are generated from different V-infinity vectors obtained using the conventional PC and ITR-PC techniques, even though for the same opportunity. Furthermore, the difference in departure AoP vary from 0.5 to 2.05 deg. Figure 5.2b shows the differences

in the arrival angles (RAAN and AoP) between the conventional patched conic (PC) and ITR-PC designs. The maximum difference in the arrival RAAN is about 0.13 deg and arrival AoP is about 0.27 deg. Figure 5.3 shows the differences in the TPI and POI velocity impulses between the PC and ITR-PC designs. The maximum difference in TPI is 45 m/s and POI is 15 m/s. Note that the total velocity impulse of the ITR-PC design is significantly smaller than that of the conventional patched conic design.

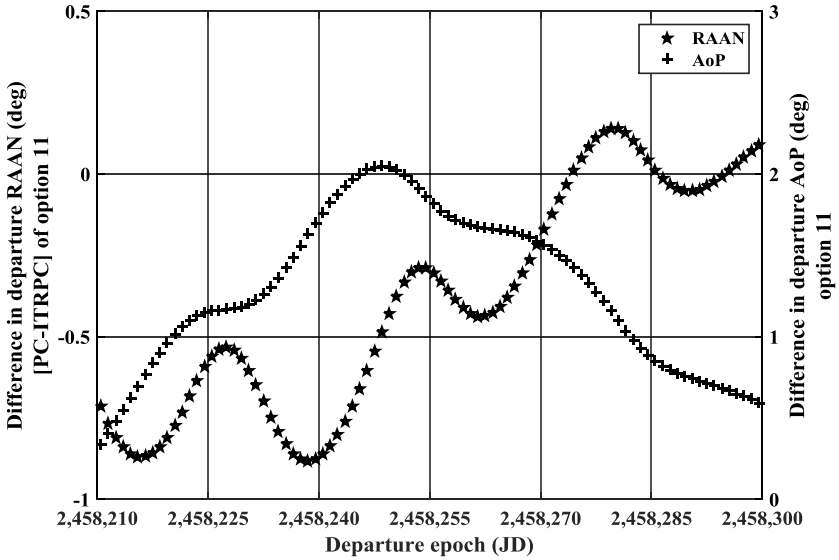

(a)

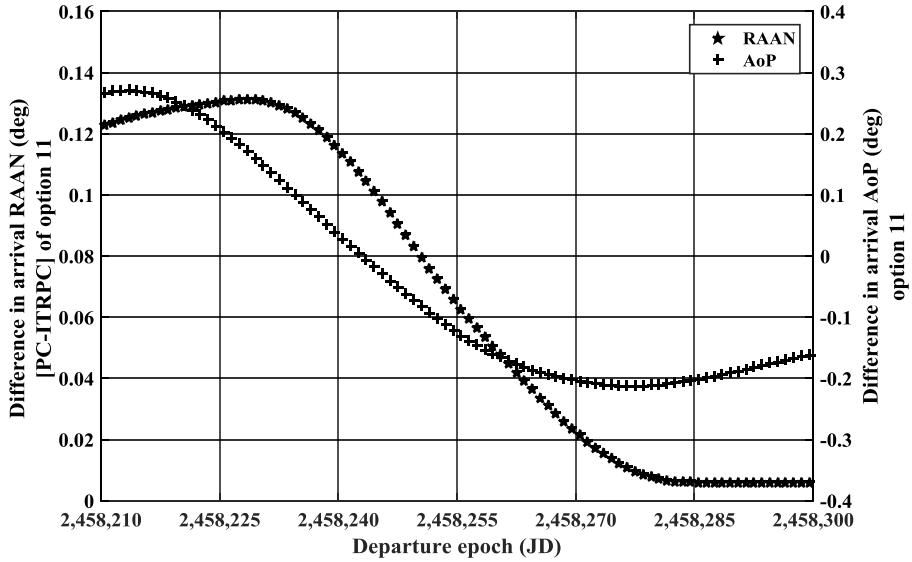

(b)

Fig.5.2. Difference in (a) departure angles (b) arrival angles between the PC and ITRPC designs (option 11) for different departure epochs

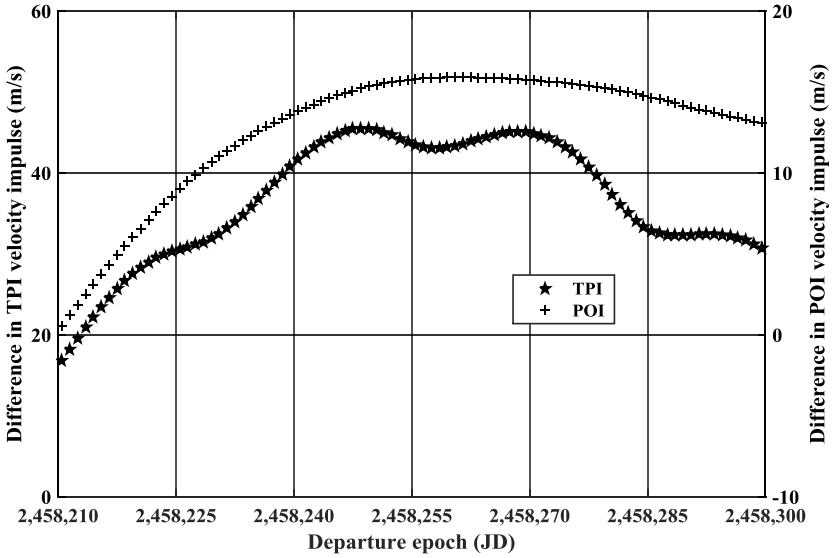

Fig.5.3. Difference in TPI and POI velocity impulses between the PC and ITRPC designs (option 11) for different departure epochs

The conventional and ITR-PC designs are generated for a range of flight durations (150 to 250 days). The differences in the departure/TPI angles; RAAN and AoP (deg) between the conventional patched conic and ITR-PC designs are depicted in Fig.5.4a. For this range of flight duration, the difference in the departure RAAN varies from 0 deg to about 0.4 deg. The difference in the departure AoP varies between -0.2 to 1.2 deg. From figure 5.4b, the differences in the arrival angles are vary from 0 deg to 0.2 deg. The difference is very large for the 180 deg transfer case. Figure 5.4c shows the differences in the TPI and POI velocity impulses between the PC and ITR-PC designs. The maximum difference is 45.5 m/s for TPI and 15.6 m/s for POI in the range of flight durations for which the transfer angles are less than 180 deg. The total velocity impulse of the ITR-PC design is significantly smaller than that of the conventional patched conic design. The difference increases in the neighbourhood of 250 days which corresponds to the 180 deg transfer regime. ***Thus, it can be concluded that the differences between the conventional PC and ITR-PC designs vary randomly for different mission scenarios. Hence, it is necessary to carry out the design analysis using the ITR-PC technique to comprehend the trends and tradeoffs for an actual mission.***

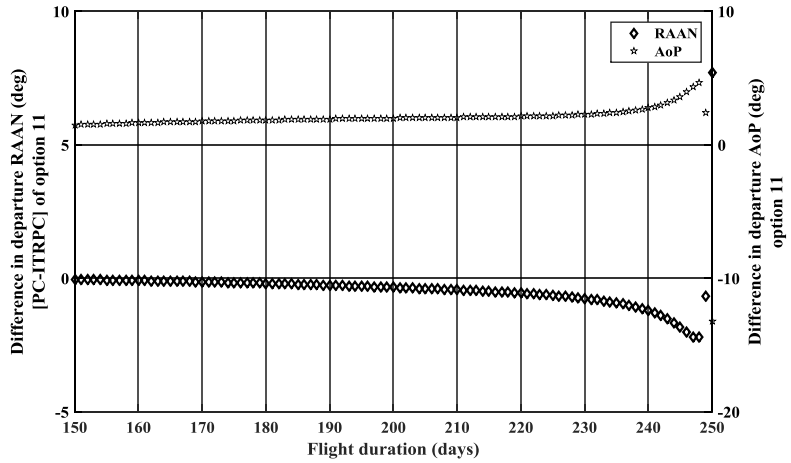

(a)

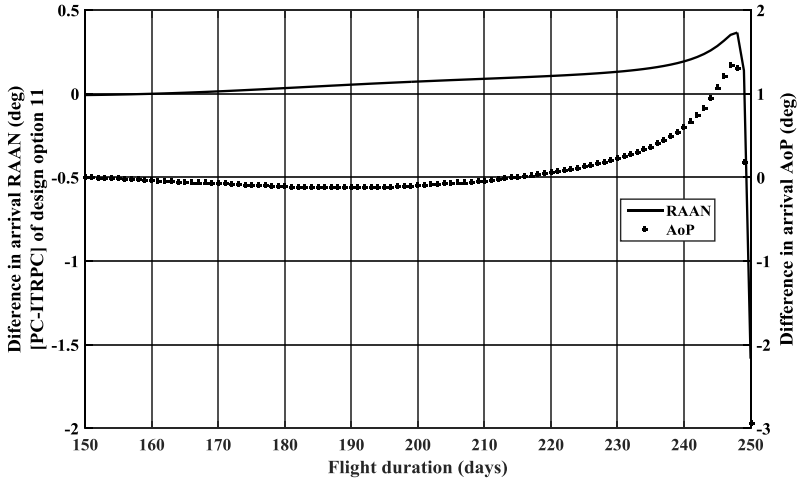

(b)

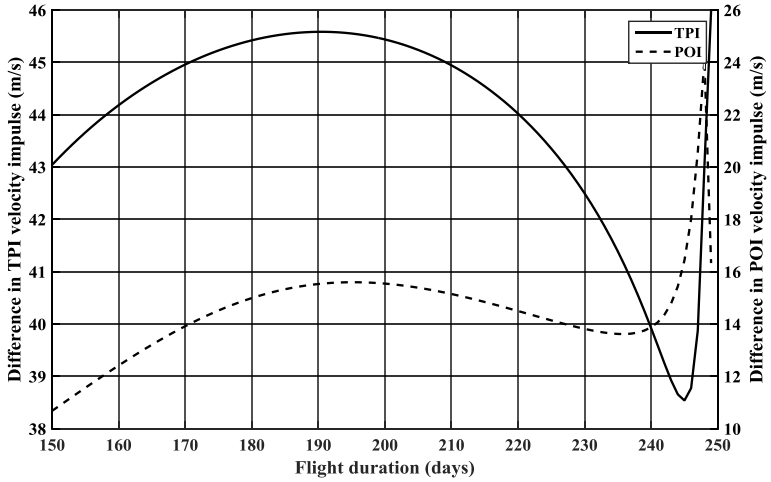

(c)

Fig.5.4. Difference in (a) departure angles (b) arrival angles (c) TPI and POI velocity impulses between the PC and ITRPC designs (option 11) for different flight durations

5.4 Design Analysis

An analysis of all the four design options for different mission scenarios is carried out using ITR-PC technique. The significance of identifying the four design options available for any opportunity and some inferences drawn from the design analysis using the four design options are presented towards the end of this section (section 5.4.6). The inputs for the analysis are; (i) departure epoch 12 May 2018 0 h TDB and flight duration/time of flight 204 days, (ii) DPO periapsis altitude 300 km and apoapsis altitude 25000 km, (iii) DPO inclination 75 deg with respect to Earth equator and equinox of J2000, (iv) APO 300 km circular, (v) APO inclination 75 deg with respect to Mars equator and equinox of J2000, and (vi) SOI-duration of the departure and arrival phases 3 and 2 days respectively.

5.4.1 Different departure epochs

The departure epoch is varied from 1 April 2018 to 30 June 2018 which is around the minimum energy opportunity. To understand the pattern in which the V-infinity vector (magnitude and the orientation angles: right ascension and declination) changes over this duration, the variation for the departure and arrival phases are shown in Figs. 5.5 and 5.6 respectively for **option 11**. Similar trend follows for the other three design options and hence, not presented. Note that the minimum energy opportunity is computed as the opportunity wherein the value of V-infinity is minimum. Figure 5,5c gives the variation of declination of the V-infinity vector for different opportunities. For feasible transfer, the inclination for the corresponding opportunities much be chosen such that it is greater than the declination value.

The net variation of departure angles for the **design options 11 and 21** are shown in Fig.5.7a. The departure angles are largely different between these two design options. Note that the departure RAAN varies by nearly 80 deg for option 11 and 25 deg for option 21. Also, the departure AoP varies by nearly 50 deg for both the options 11 and 21 (cf. Fig.5.7b). Because, the departure angles vary by a small value between the **design options 11 and 12**, Fig.5.8a presents the differences in the departure RAAN and AoP. The differences are small (maximum difference: RAAN, 0.11 deg and AoP, 0.075 deg) yet significant as the corresponding arrival angles have large differences (Fig.5.8b). Similar trend is seen between options 21 and 22 and hence, not presented.

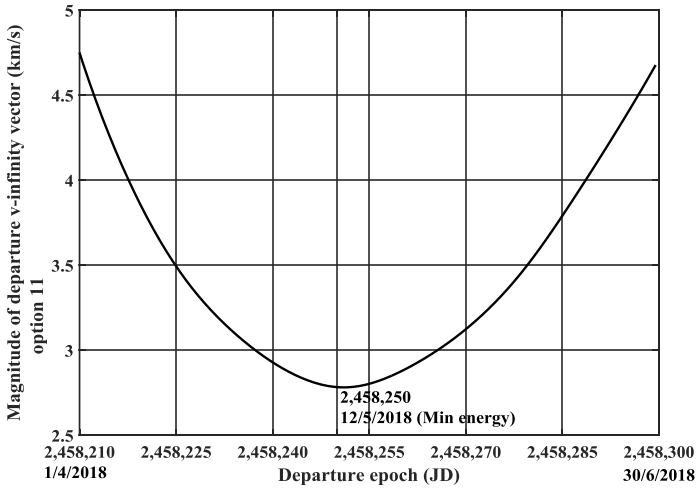

(a)

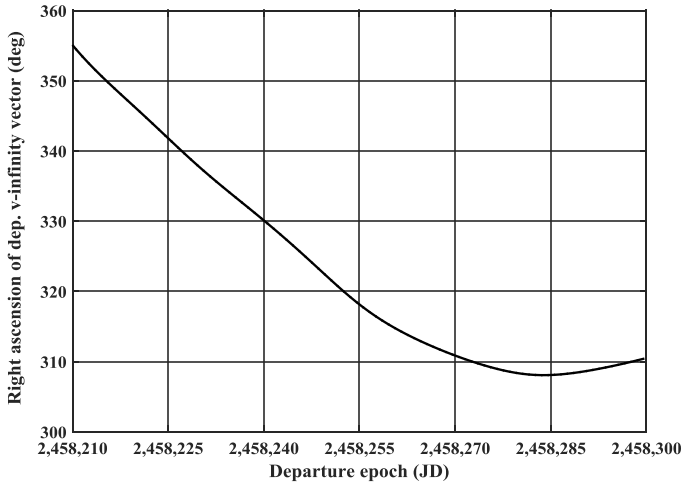

(b)

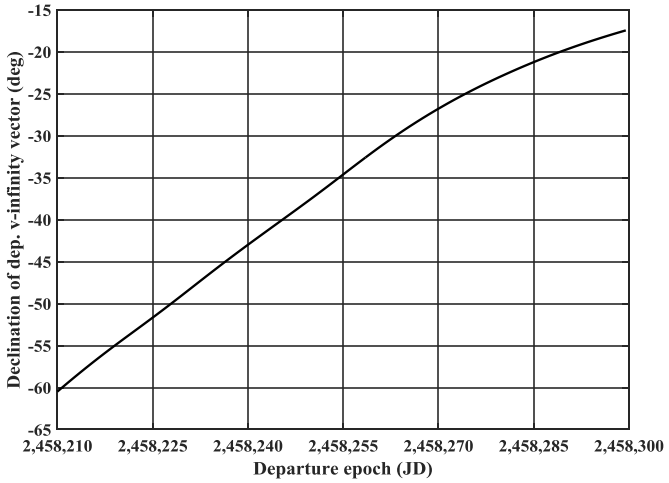

(c)

Fig.5.5.Variation of departure V-infinity vector of options 11 (from ITR-PC) for different departure epochs (a) magnitude (b) right ascension and (c) declination

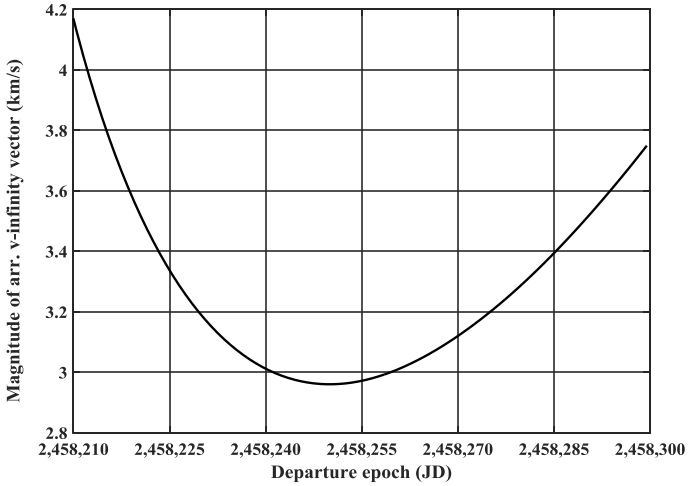

(a)

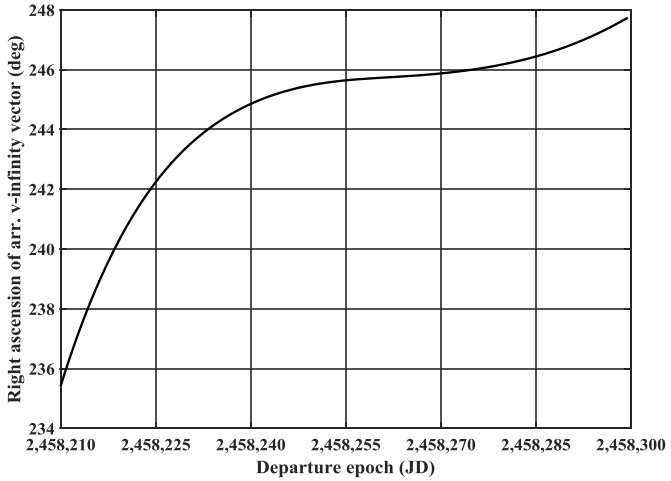

(b)

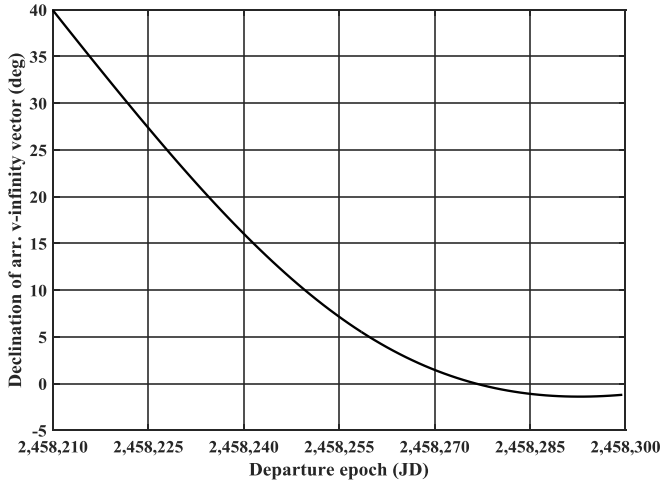

(c)

Fig.5.6.Variation of arrival V-infinity vector of options 11 (from ITR-PC) for different departure epochs (a) magnitude (b) right ascension and (c) declination

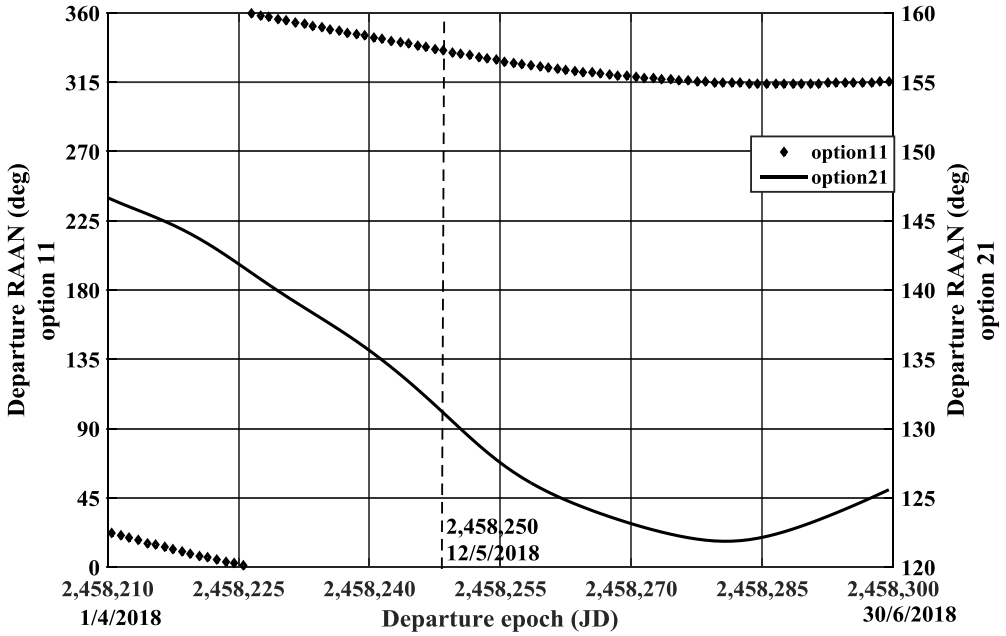

(a)

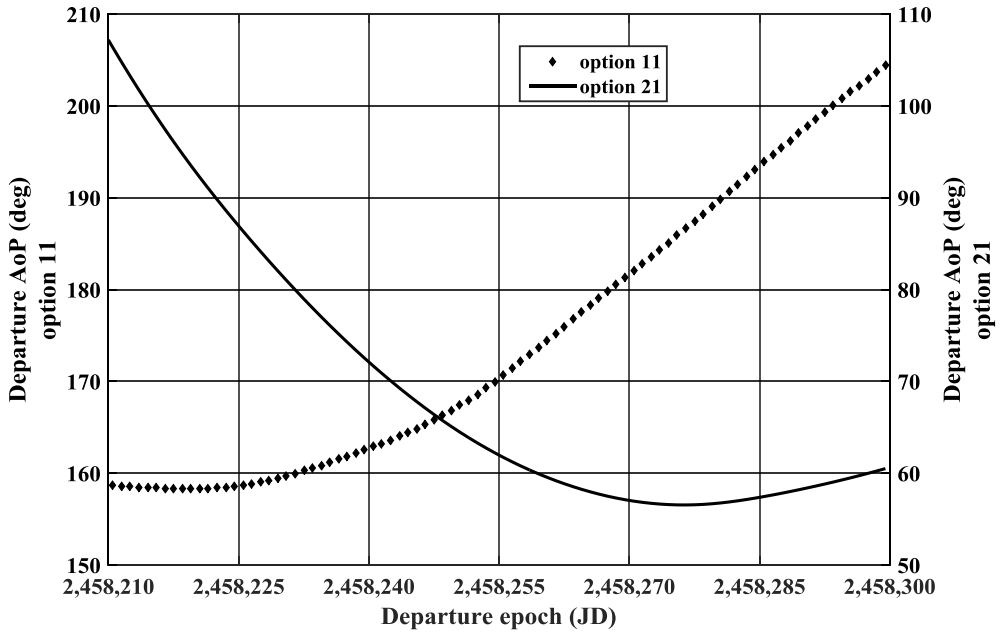

(b)

Fig.5.7.Variation of departure angles of options 11 and 21 (from ITR-PC) for different departure epochs (a) departure RAAN (b) departure AoP

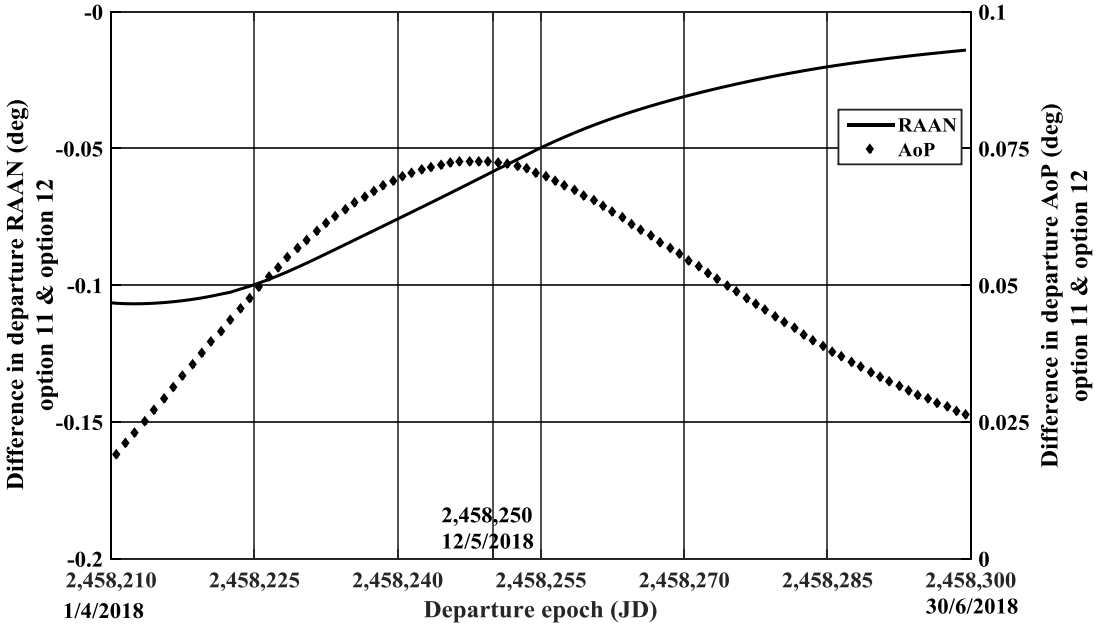

(a)

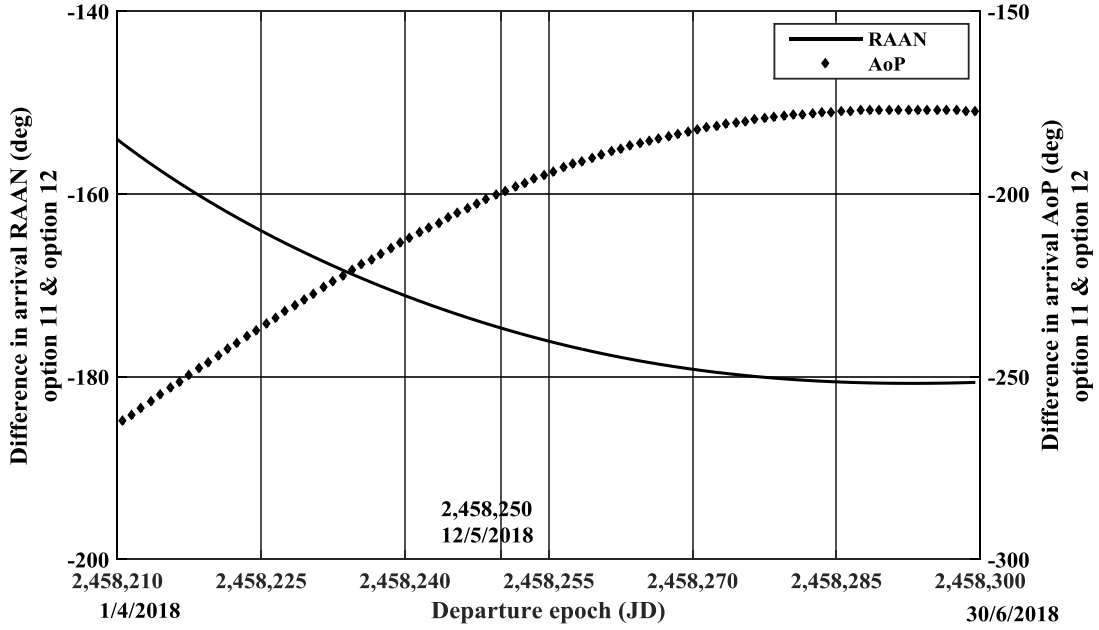

(b)

Fig.5.8. Difference in (a) departure angles, (b) arrival angles between options 11 and 12 (from ITR-PC) for different departure epochs.

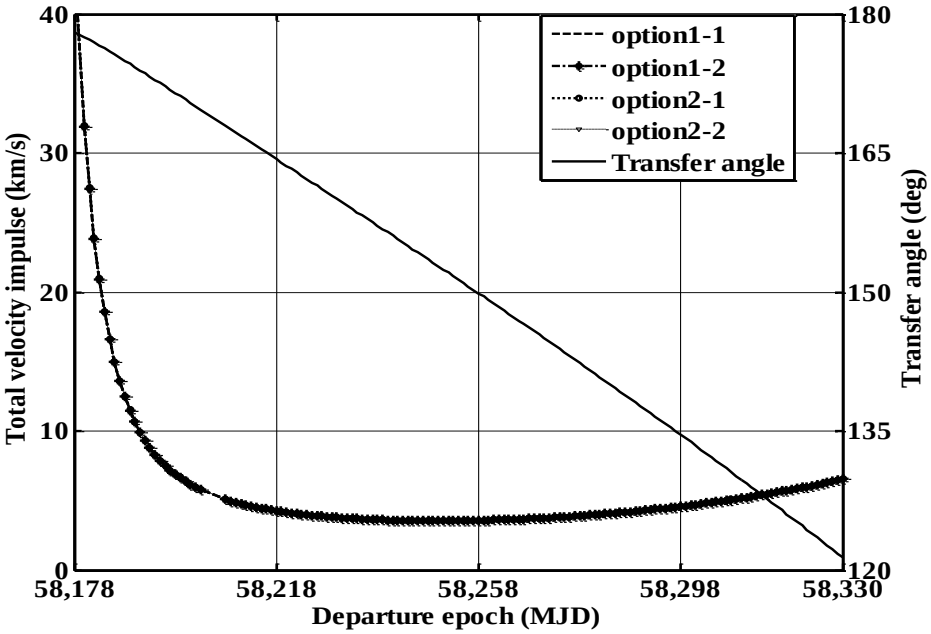

(a)

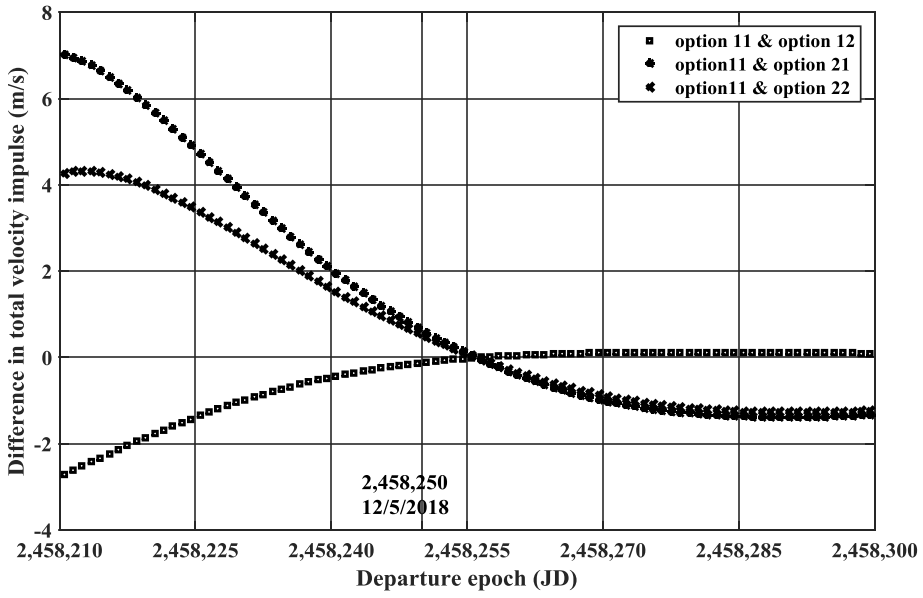

(b)

Fig.5.9. (a) Variation of total velocity impulse and transfer angle, (b) difference in magnitude of total velocity impulse between option 11 and the other three options, for different departure epochs

Figure 5.9a gives the total velocity impulse required for the interplanetary transfer for all the four design options. The range of departure epochs is extended to include the 180 deg transfer cases also. Note that the total velocity impulse is extremely high, about 40 km/s for the 180 deg transfer case. This is because when the departure planet Sun and the target planet are roughly lined up, the dynamics of a single plane transfer forces the transfer trajectory to go over the Sun. This situation is due to the relative inclinations of the planets. To perform out of plane maneuver, huge velocity impulse is required. When the transfer angle is not in the neighborhood of 180 deg, the total velocity impulse required for the interplanetary transfer comes down to about 4 to 7 km/s. Similar trend is seen for all options. Figure 5.9b shows the differences in the total velocity impulse between the design option 11 and the other three design options (21, 12 and 22) for the range of departure epochs excluding the 180 deg transfer regime and is about 3 to 7 m/s only (cf. Fig.5.9b*).* Similar trend is expected for the differences between other options as well. *It can be concluded that, for different departure epochs excluding the 180 deg transfer regime, the total velocity impulses between different design options are almost the same.* ***Thus, any arrival condition can be achieved without incurring significant change in the total velocity impulse.*** The computation time required to generate the ITR-PC designs for this range of departure epochs (5 months; step size, 24 h) and fixed flight duration is only 242 ms with an Intel core i5 2.5GHz processor. *It is evident that the ITR-PC technique generates data for design analysis very quickly.*

5.4.2 Different periapsis altitudes of departure hyperbolic orbit/ DPO

The DPO periapsis altitude is varied from 200 km to 2000 km. The variation of the departure RAAN of design options 11 and 21 for different DPO periapsis altitudes are shown in Fig.5.10a. The variation for this range of DPO periapsis altitudes is only about 0.02 deg for option 11 and 0.002 deg for option 21. The variation of the departure AoP of design options 11 and 21 is about 3 deg for different DPO periapsis altitudes and are shown in Fig.5.10b. The differences in departure angles between design options 11 and 12 are shown in Fig.5.11a. These differences are negligibly small but result in large difference in arrival angles (RAAN, 174 deg and AoP, 199 deg; cf. Fig.5.11b). The total velocity impulse required for the interplanetary transfer with different DPO periapsis altitudes for option 11 is shown in Fig.5.12a and the variation is about 120 m/s. ***For interplanetary transfer, lower periapsis altitude is preferable for the departure parking***

orbit because the total velocity impulse is less. It is well known that the launch vehicle can achieve more payload for lower altitudes. The differences in the total velocity impulse between the design option 11 and the other three design options are shown in Fig.5.12b. It can be noted that the differences are less than 1 m/s.

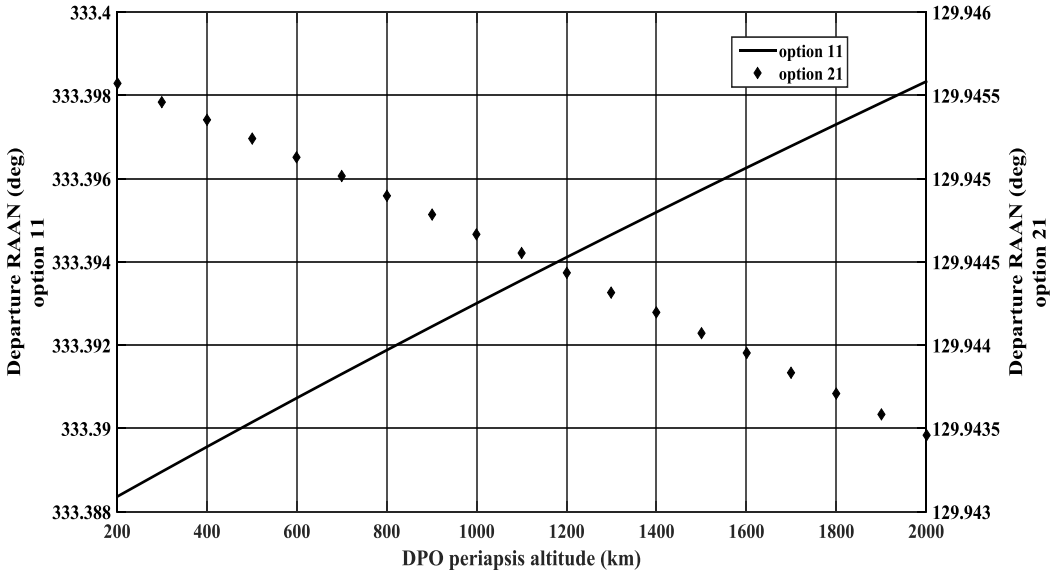

(a)

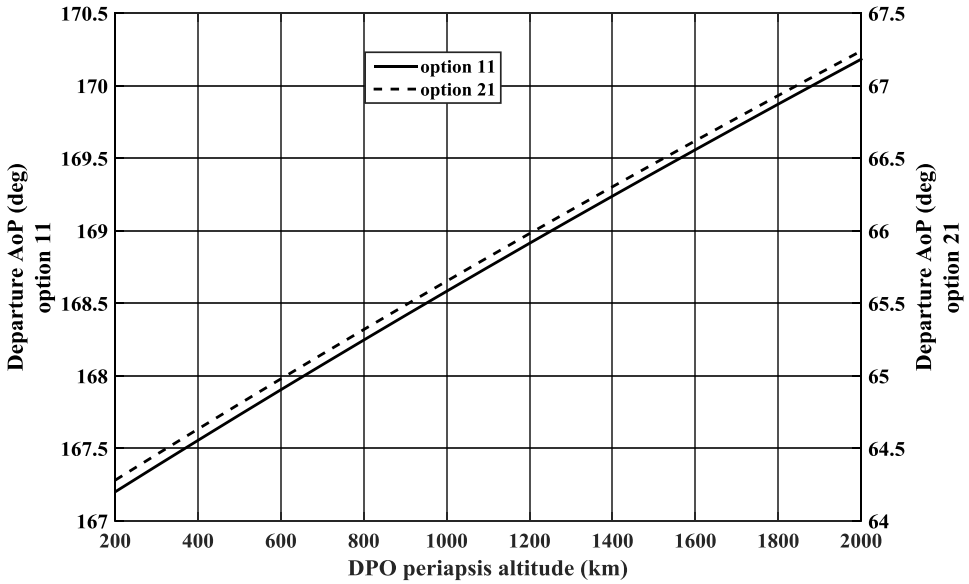

(b)

Fig.5.10.Variation of (a) departure RAAN, (b) departure AoP of options 11 and 21 (from ITR-PC) for different DPO periapsis altitudes

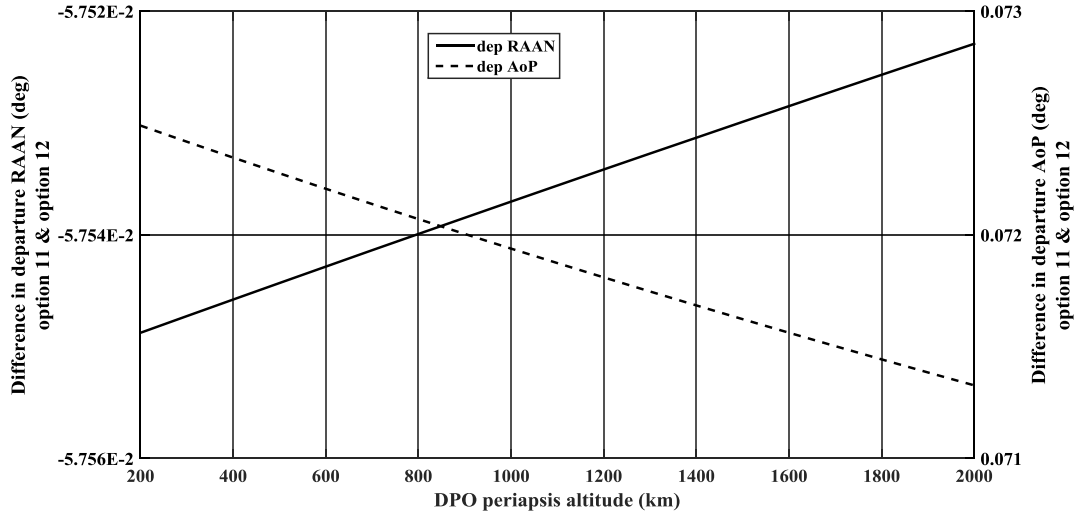

(a)

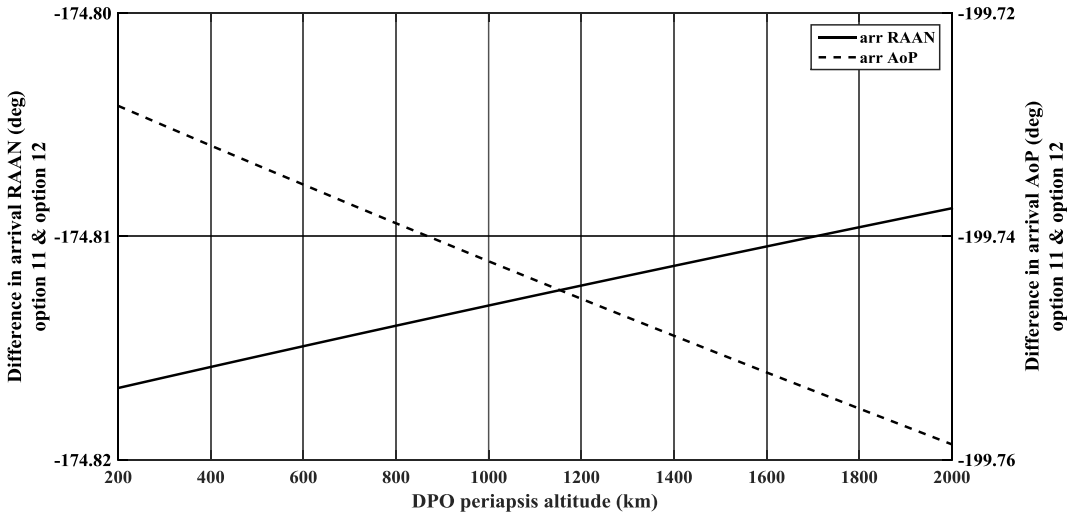

(b)

Fig.5.11. Difference in (a) departure angles, (b) arrival angles between options 11 and 12 (from ITR-PC) for different departure epochs.

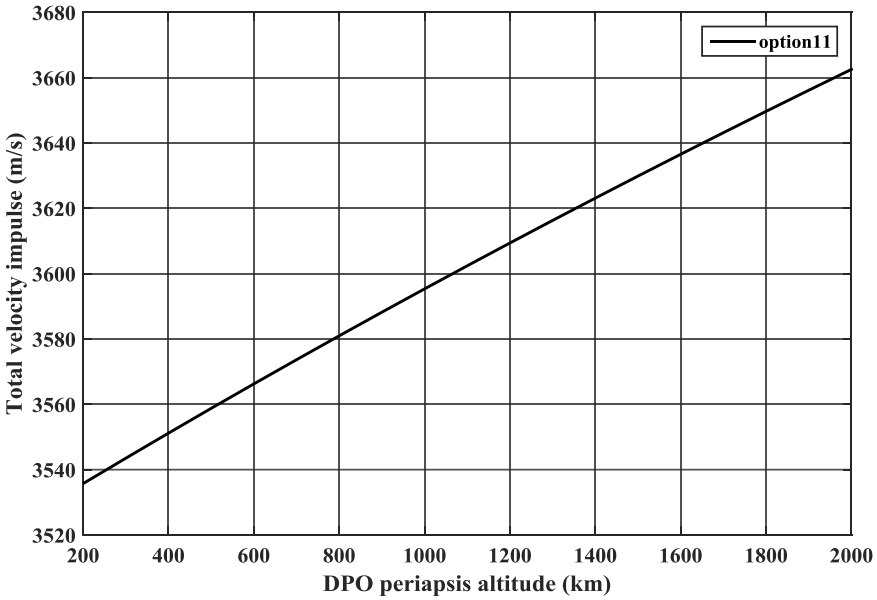

(a)

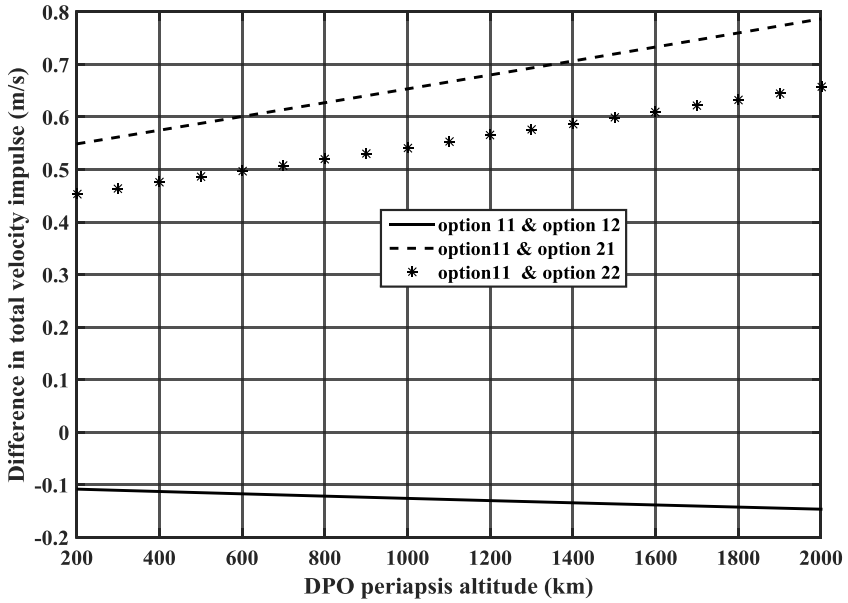

(b)

Fig.5.12. (a) Variation of total velocity impulse of option 11, (b) difference in the magnitude of total velocity impulse between option 11 and the other three options, for different DPO periapsis altitudes

5.4.3 Different inclinations of departure hyperbolic orbit/DPO

As pointed out earlier, the feasible inclination for the design option 11 starts from –37.2 deg to 142.8 deg (cf. Table 5.2). The variation of the departure RAAN of all the four distinct design options for different DPO inclinations are shown in Fig.5.13a. Note that the variation is symmetric about 90 deg. The net variation in departure RAAN are about 170 deg for the design options 11 and option 12, and 150 deg for the design options 21 and 22 for this range of DPO inclinations. The net variation in departure AoP is about 42 deg for all the four distinct departure design options and are shown in Fig.5.13b. The differences in departure angles between the design options 11 and 12 are shown in Fig.5.14a.The maximum difference in departure RAAN is about 0.6 deg and AoP is about 0.5 deg. These result in large differences in the arrival angles, 174 deg for RAAN and 199 deg for AoP (cf. Fig.5.14b).

The total velocity impulse required for the interplanetary transfer for different DPO inclinations is shown in Fig.5.15a and the net variation is about 4 m/s. ***This brings out the fact that all feasible DPO inclinations can be used for interplanetary transfer with a penalty of less than 4 m/s in total velocity impulse.*** The differences in the total velocity impulse between the design option 11 and the other three design options are shown in Fig.5.15b. It can be noted that the differences are less than 1 m/s. ***It can be concluded that any design option can be chosen with a marginal penalty which is less than 1 m/s.***

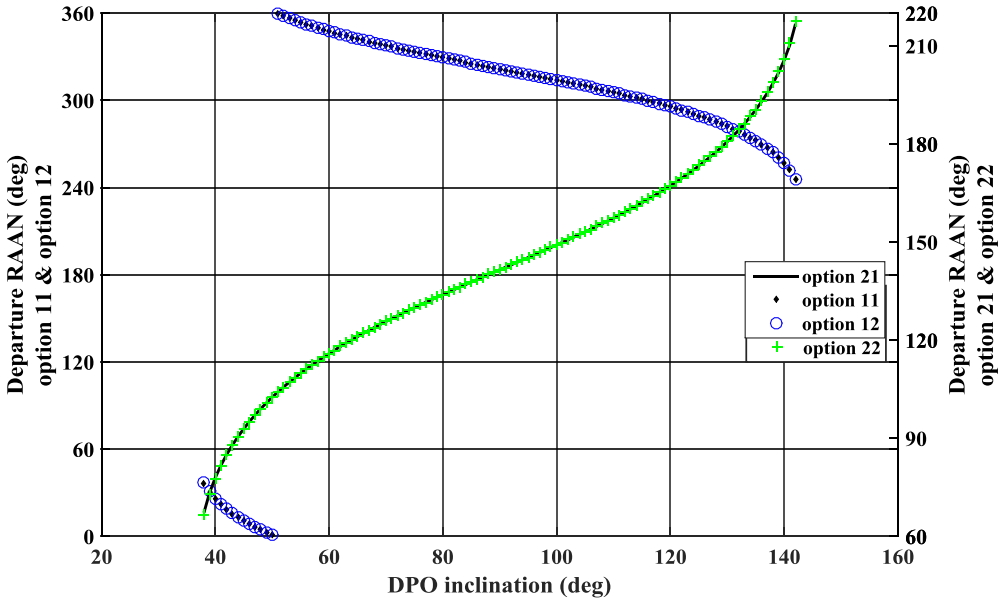

(a)

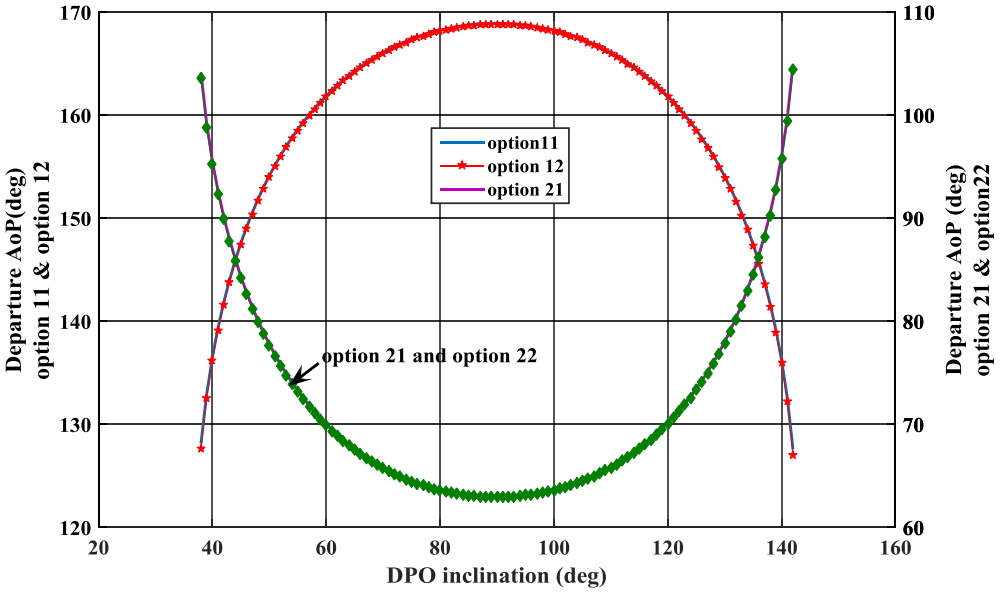

(b)

Fig.5.13.Variation of (a) departure RAAN, (b) departure AoP of options 11 and 21 (from ITR-PC) for different DPO inclinations

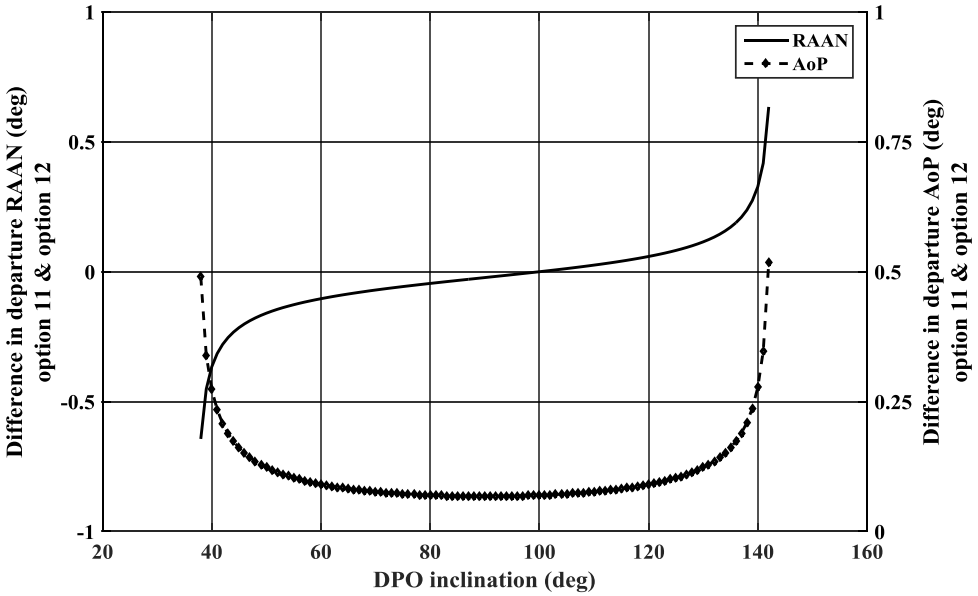

(a)

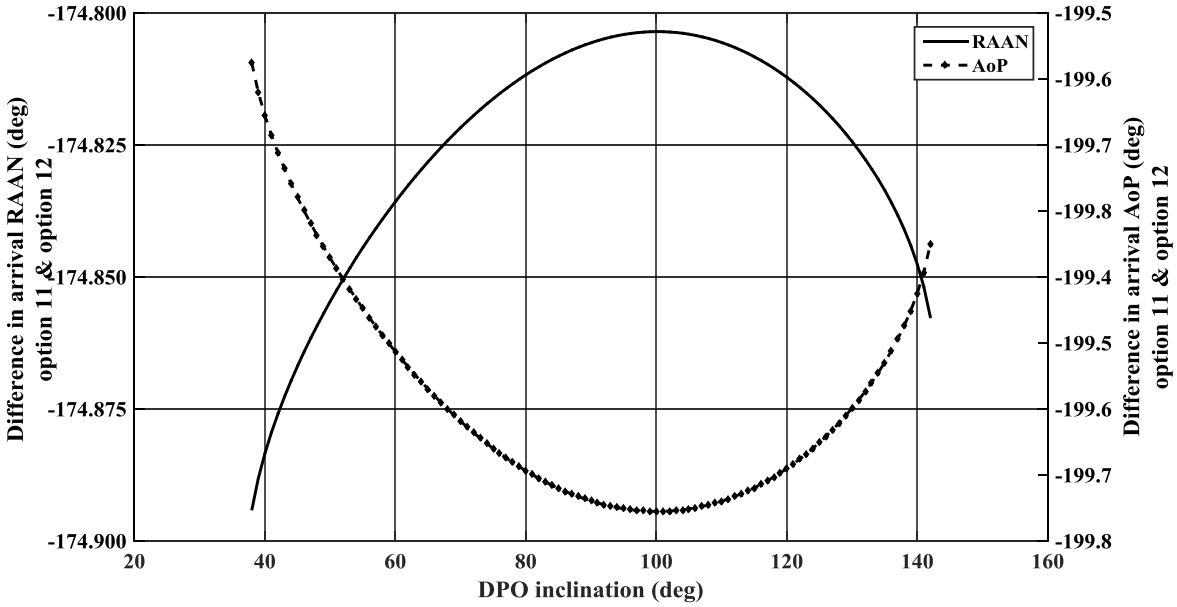

(b)

Fig.5.14. Difference in (a) departure angles, (b) arrival angles between options 11 and 12 (from ITR-PC) for different DPO inclinations.

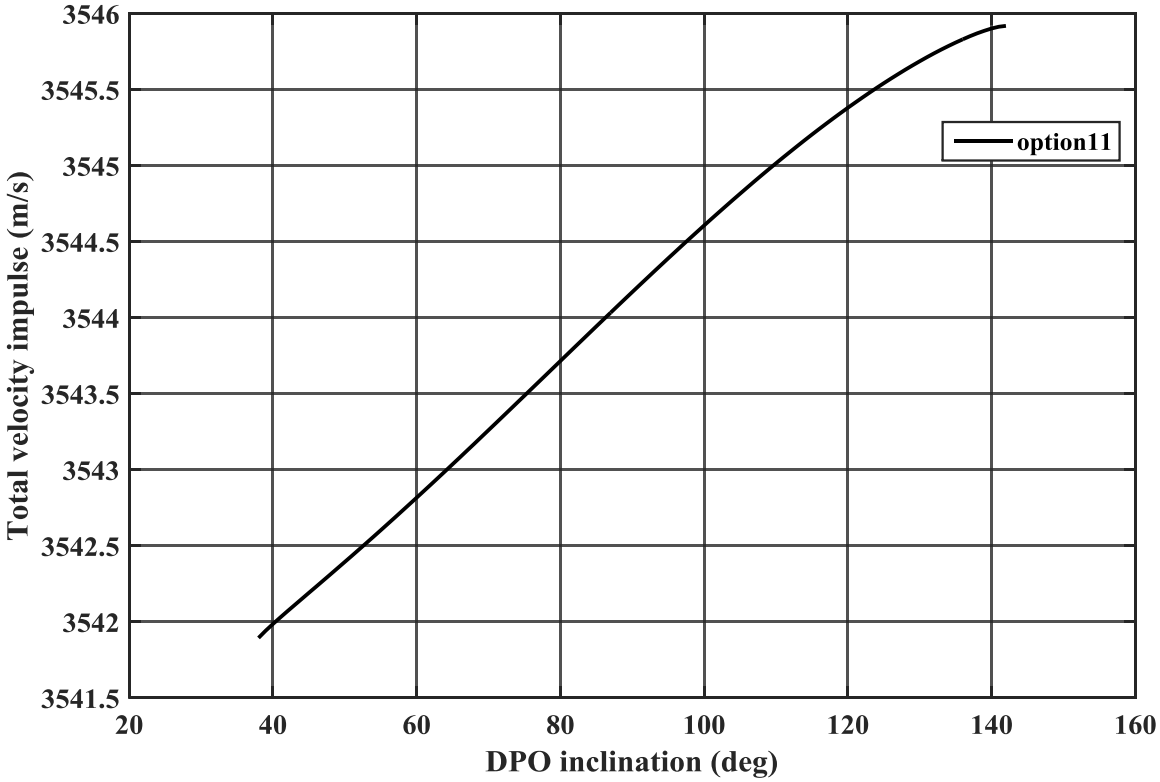

(a)

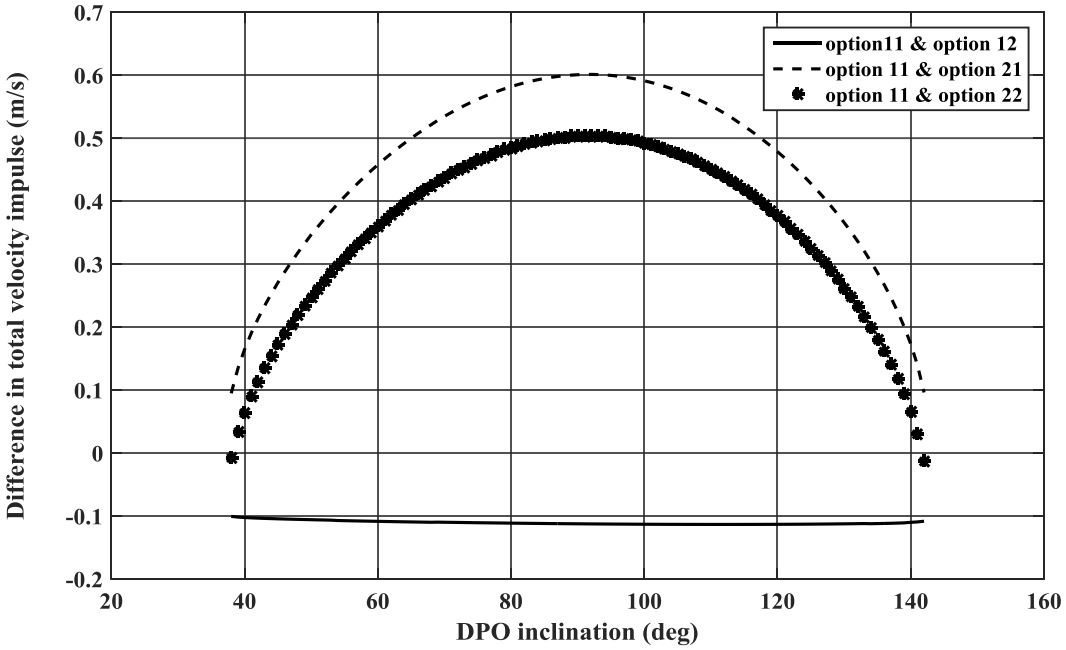

(b)

Fig.5.15. (a) Variation of total velocity impulse of option 11, (b) difference in the magnitude of total velocity impulse between option 11 and the other three options, for different DPO inclinations

5.4.4 Different periapsis altitudes of arrival hyperbolic orbit/ APO

The APO periapsis altitude is varied from 200 km to 2000 km. The variation of the departure RAAN of design options 11 and 21 for different APO periapsis altitudes are shown in Fig.5.16a. The net variation in departure RAAN is only about 0.012 deg for option 11 and 0.0012 deg for option 21. The net variation of the departure AoP of design options 11 and 21 for different APO periapsis altitudes are shown in Fig.5.16b and the net variation is about 0.015 deg for the design option 11, and about 0.02 deg for the design option 21. The differences in departure angles between design options 11 and 12 are shown in Fig.5.17a. The maximum difference in departure RAAN for this range of APO periapsis altitudes is 0.074 deg and about 0.092 deg in departure AoP. These result in large differences in the arrival angles (RAAN, 174 deg and AoP, 199 deg; cf. Fig.5.17b).

The total velocity impulse required for the interplanetary transfer with different APO periapsis altitudes for option 11 is shown in Fig.5.18a and the variation is about 115 m/s. ***It is to be noted that directly targeting lower APO periapsis altitudes is beneficial compared to the strategy of targeting higher APO periapsis altitudes and then reducing to lower APO periapsis altitudes.*** For example, to achieve 200 km circular orbit around

Mars, the total velocity required is 3555 m/s and for 400 km is 3535 m/s. The difference is only 20 m/s whereas if the initial target is 400 km and later circularized to 200 km, the total velocity required is 92 m/s which is larger. The differences in the total velocity impulse between the design option 11 and the other three design options are shown in Fig.5.18b. It can be noted that the differences are less than 1 m/s.

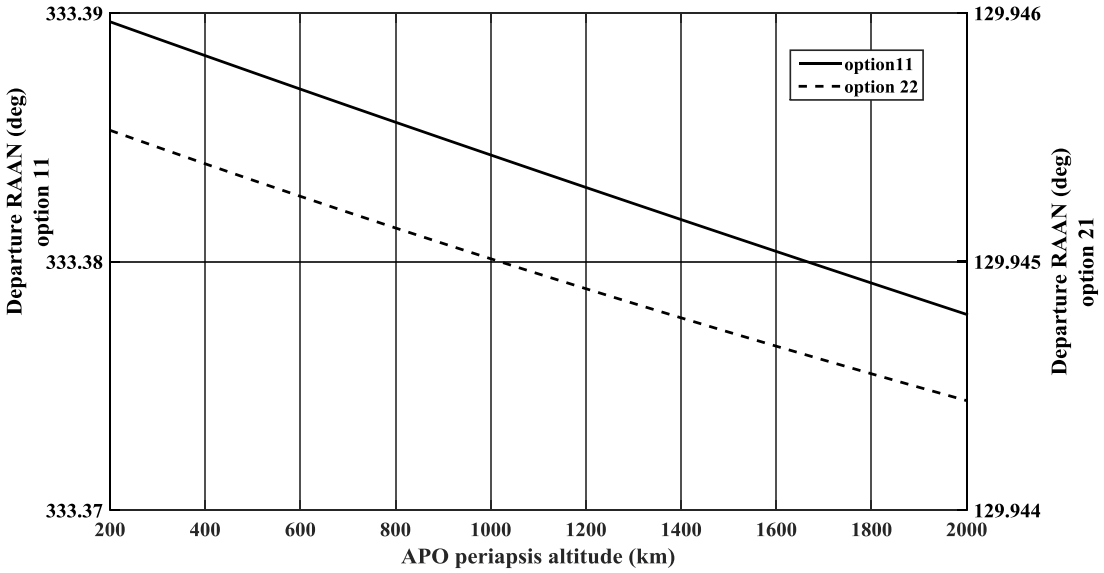

(a)

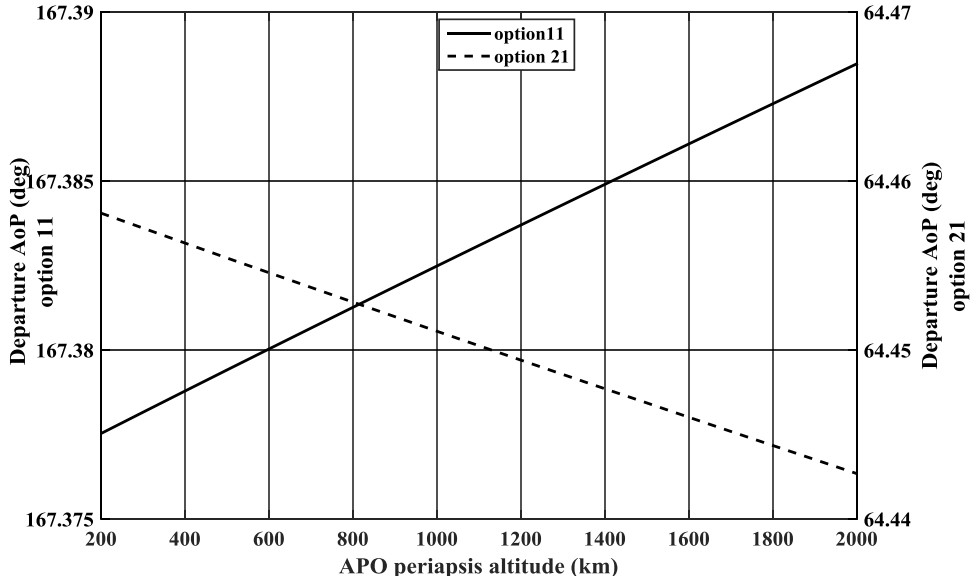

(b)

Fig.5.16.Variation of (a) departure RAAN, (b) departure AoP of options 11 and 21 (from ITR-PC) for different APO periapsis altitudes

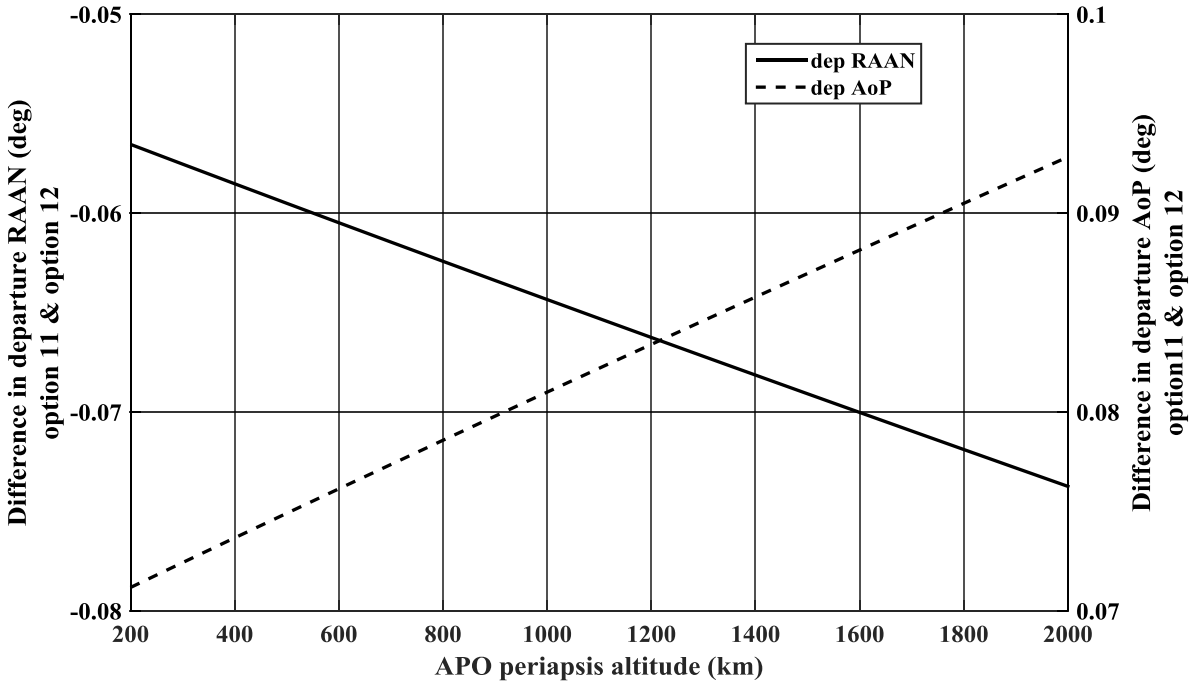

(a)

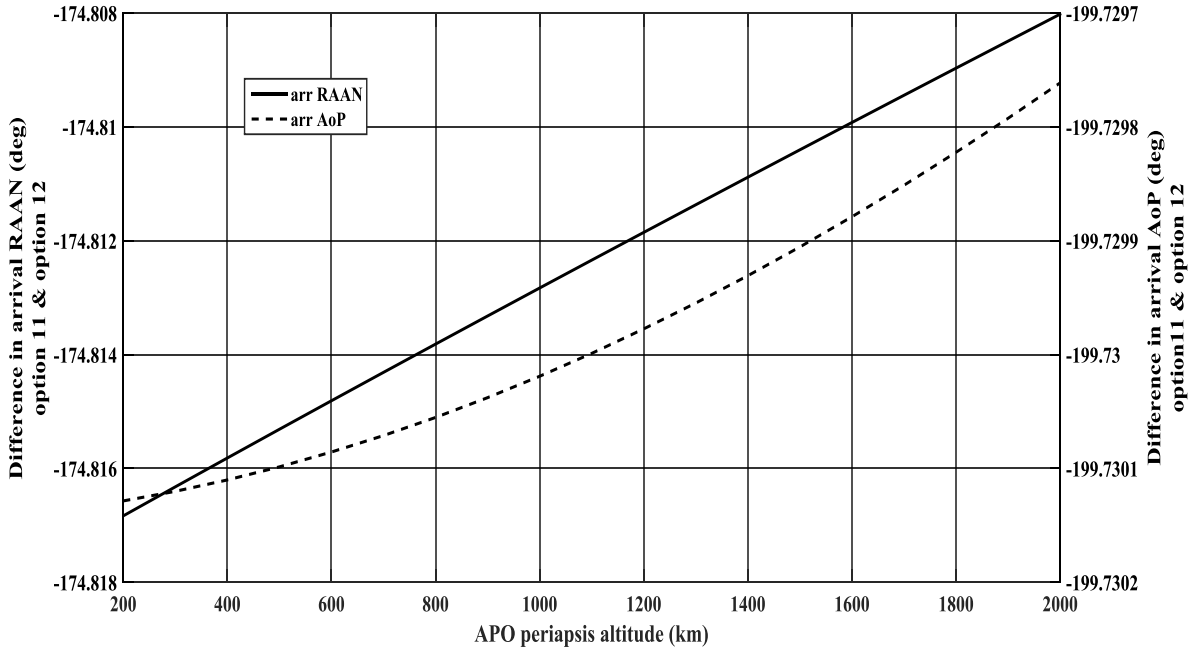

(b)

Fig.5.17. Difference in (a) departure angles, (b) arrival angles between options 11 and 12 (from ITR-PC) for different APO periapsis altitudes

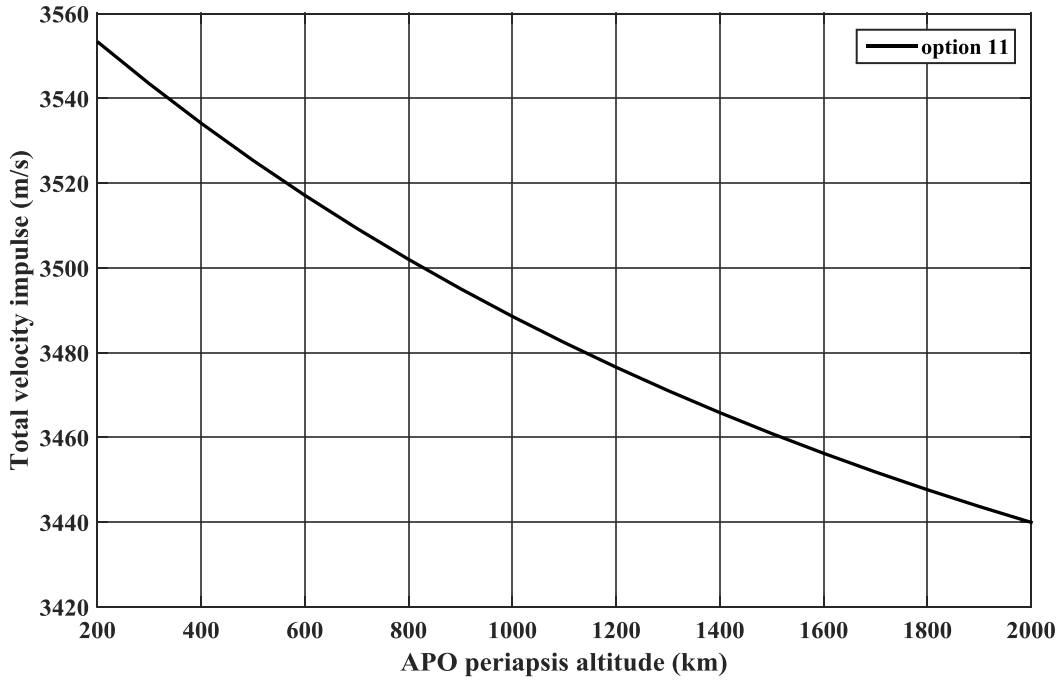

(a)

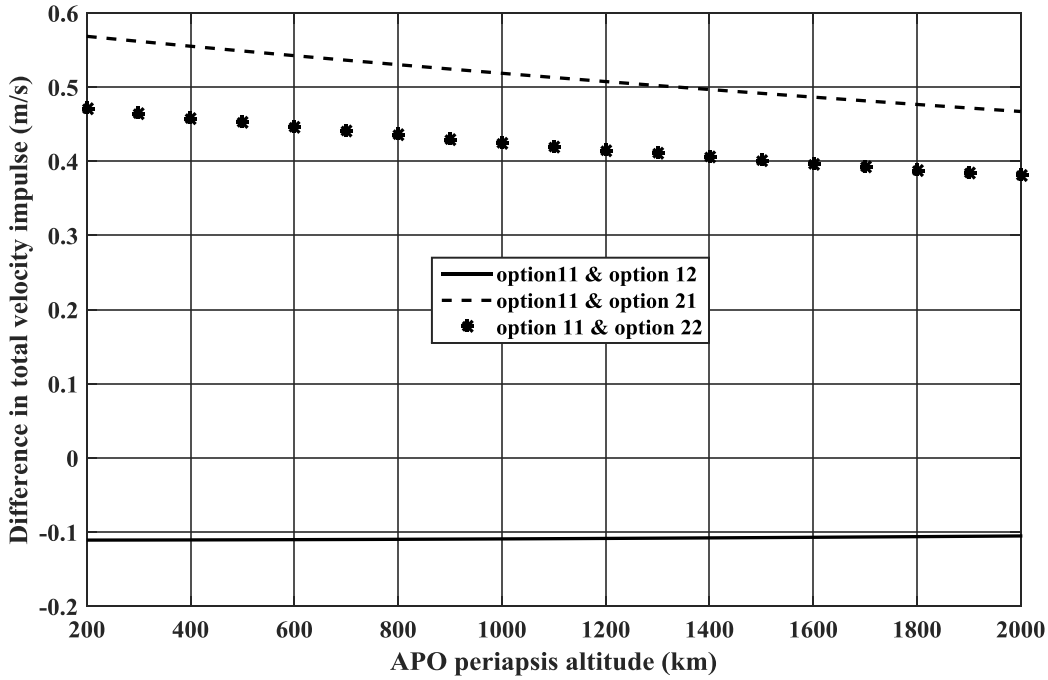

(b)

Fig.5.18. (a) Variation of total velocity impulse of option 11, (b) difference in the magnitude of total velocity impulse between option 11 and the other three options, for different APO periapsis altitudes

5.4.5 Different inclinations of arrival hyperbolic orbit/APO

For the 2018 minimum energy opportunity, the declination of arrival V-infinity vector is 9.25 deg. Hence, the APO inclination is varied from 10 deg to 170 deg for feasible transfer. The variation of the departure RAAN of the design options 11 and 21 for different APO inclinations are shown in Fig.5.19a. Note that the variation is symmetric about an inclination of 90 deg. The net variation is only about 0.065 deg for the design option 11 and 0.035 deg for design option 21. The variation of the departure AoP of the distinct departure design options 11 and 21 for different APO inclinations are shown in Fig.5.19b. The net variation is only about 0.05 deg for the design option 11 and 0.07 deg for design option 21. Thus, for different APO inclinations, the variation in departure angles are very small. The differences in departure angles between design options 11 and 12 are shown in Fig.5.20a.The maximum difference in departure RAAN is about 0.06 deg and AoP is about 0.08 deg. These result in large differences in the arrival angles (cf. Fig.5.20b).

The total velocity impulse required for the interplanetary transfer with different APO inclinations for the design option 11 is shown in Fig.5.21a and the variation is less than 1 m/s. ***This clearly indicates that any feasible APO inclination can be achieved without incurring significant additional velocity impulse.*** The differences in the total velocity impulse between the design option 11 and the other three design options are shown in Fig.5.21b. It can be noted that the differences are less than 1 m/s.

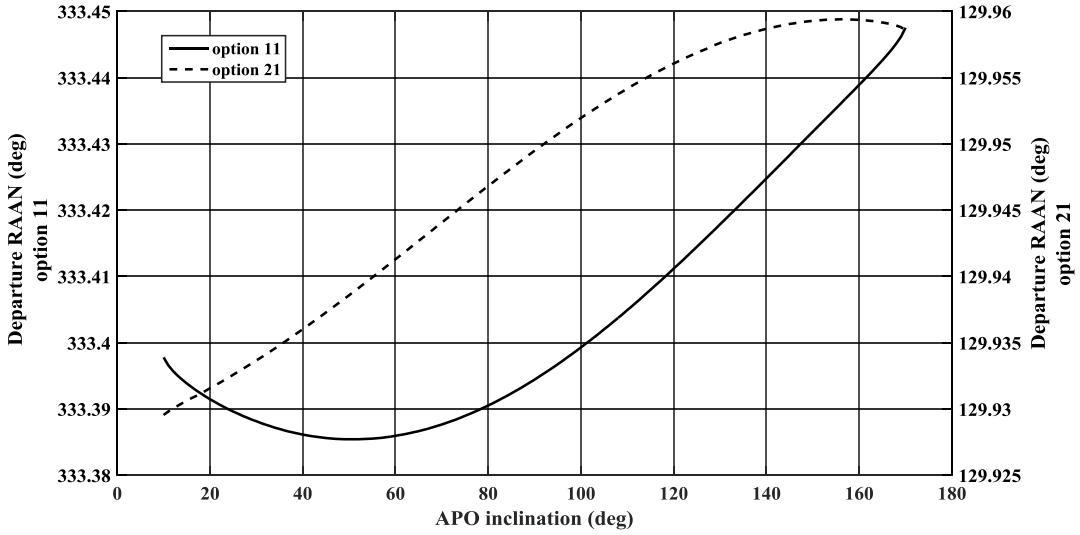

(a)

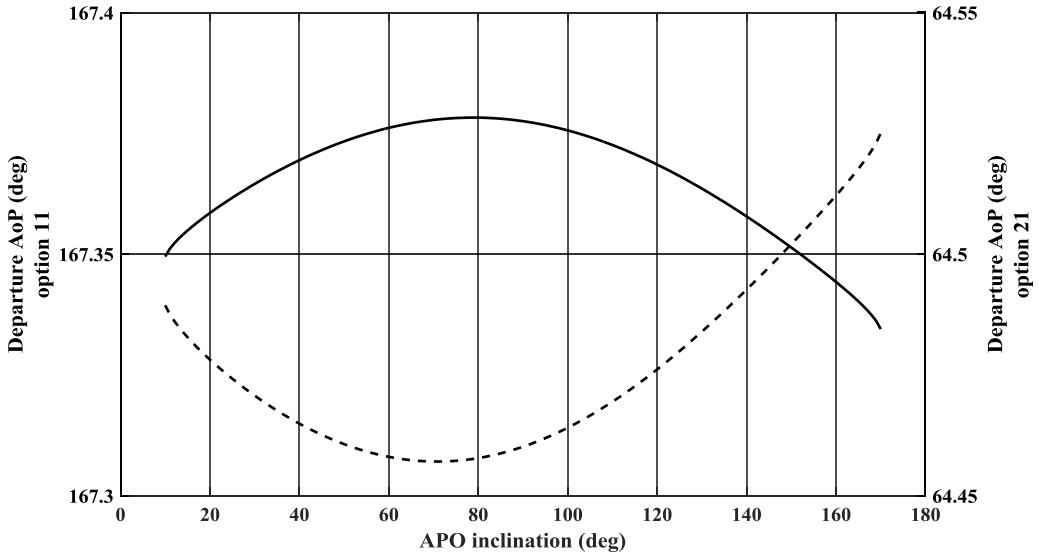

(b)

Fig.5.19.Variation of (a) departure RAAN, (b) departure AoP of options 11 and 21 (from ITR-PC) for different APO inclinations

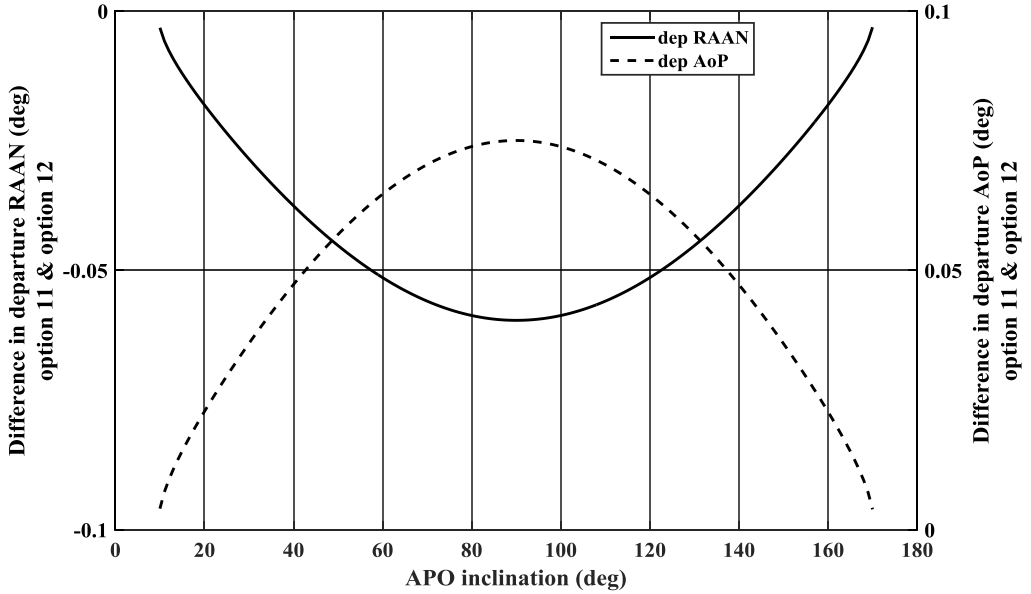

(a)

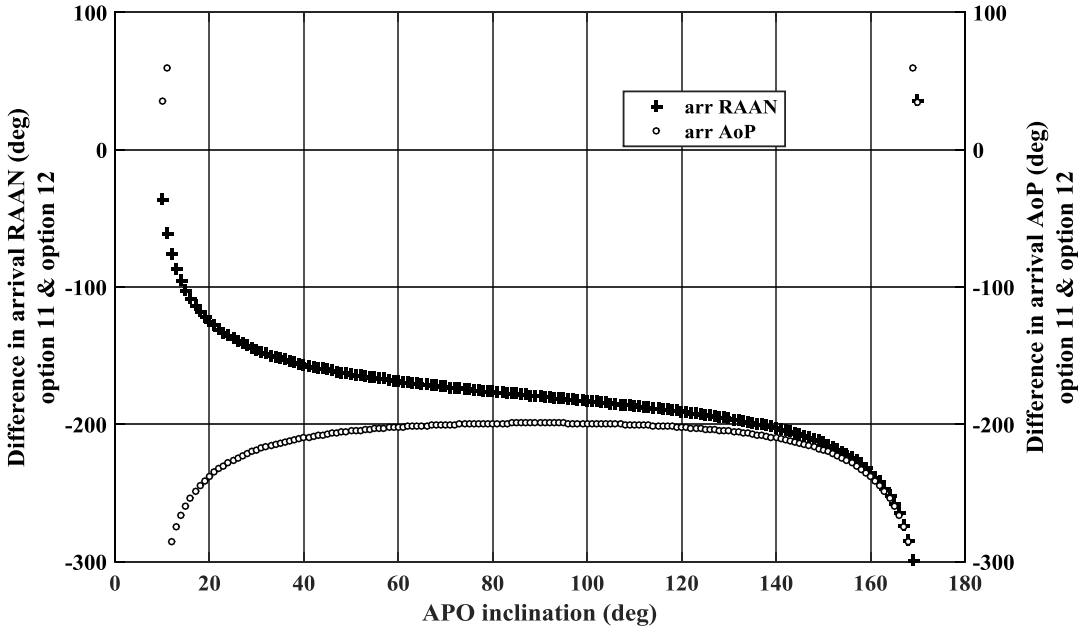

(b)

Fig.5.20. Difference in (a) departure angles, (b) arrival angles between options 11 and 12 (from ITR-PC) for different APO inclinations

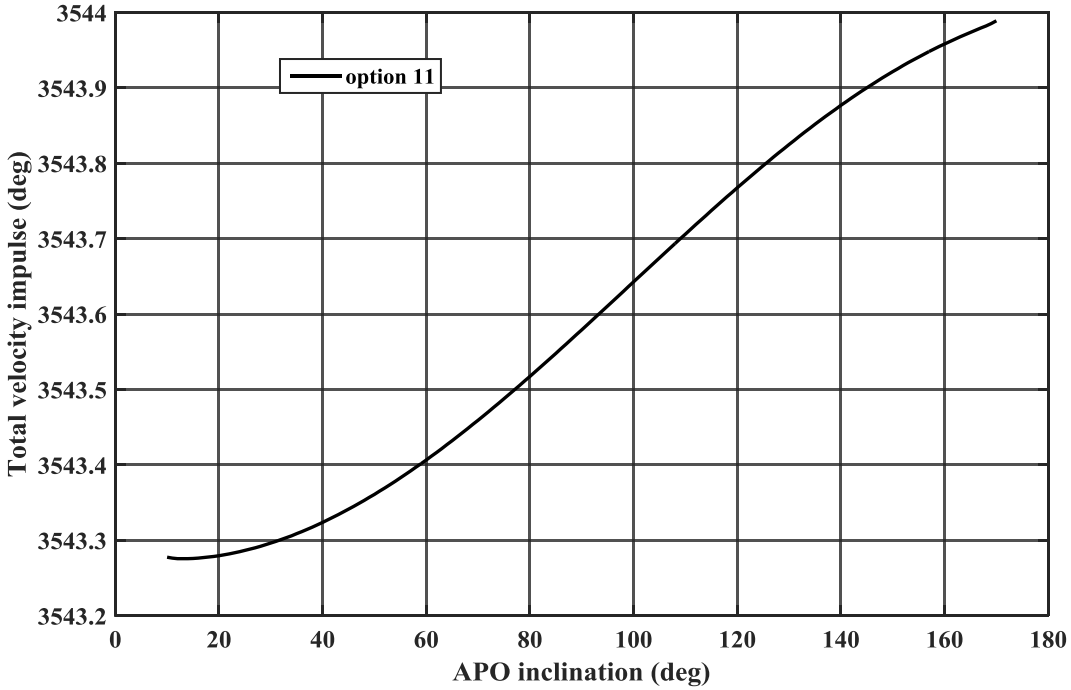

(a)

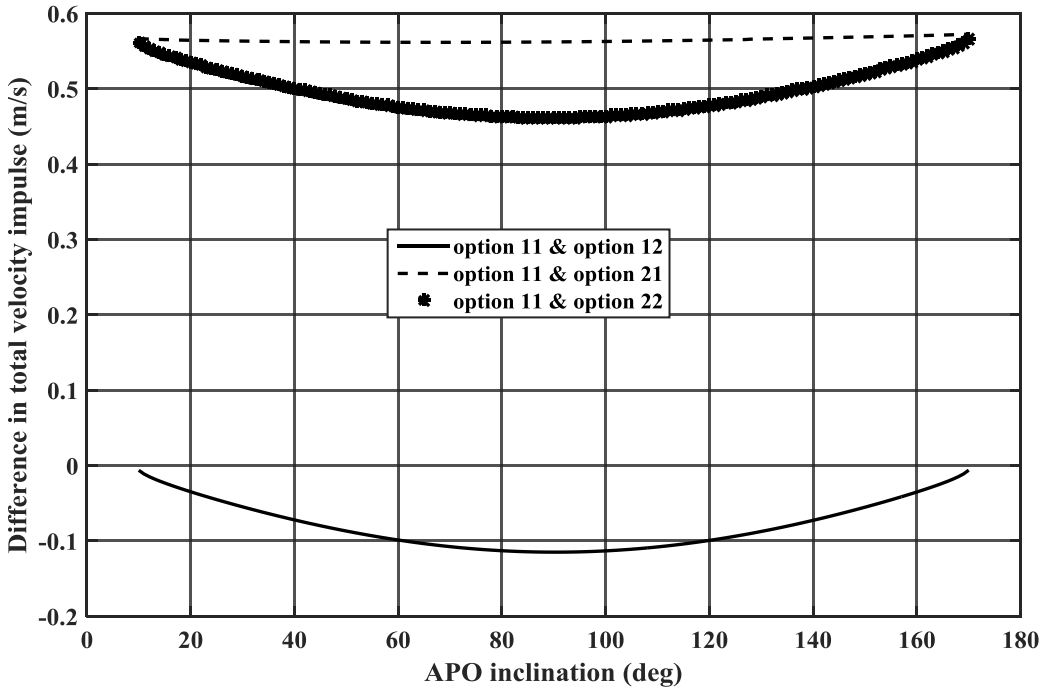

(b)

Fig.5.21. (a) Variation of total velocity impulse of option 11, (b) difference in the magnitude of total velocity impulse between option 11 and the other three options, for different APO inclinations

5.4.6 Some Important Inferences from Design Analysis

The ***design analysis of all the four distinct options*** for different mission scenarios have been carried out and many important inferences are drawn such as,

1) Any arrival geometry (corresponding to option 11 or option 12) can be achieved without incurring significant change in the total velocity impulse.
2) For interplanetary transfer, lower periapsis altitude is preferable for the departure parking orbit, for a fixed apoapsis altitude, because the total velocity impulse required is less. Also, the launch vehicle can achieve more payload in this scenario.
3) For the whole range of feasible DPO inclinations, the interplanetary transfer incurs a penalty of less than 4 m/s only.
4) Any of the four design options can be chosen depending upon the mission requirement, for a given DPO inclination, with only a marginal penalty in total velocity impulse (less than 1 m/s).

5) Directly targeting lower APO periapsis altitudes is beneficial compared to the strategy of targeting higher APO periapsis altitudes and then reducing to lower APO periapsis altitudes.
6) Any feasible APO inclination can be achieved without incurring significant additional velocity impulse.
7) The feasible range of DPO inclinations for coplanar transfer are obtained more accurately.

5.5 Conclusions

The iterative patched conic technique generates analytical designs whose departure angles have only small differences from the corresponding values of the conventional patched conic designs. Yet, the achievable accuracies of the arrival target parameters on numerical propagation of the ITR-PC designs show huge improvement over that of the conventional patched conic designs. This is showcased through ***the sensitivity analysis which points out that the achievable accuracies of the arrival parameters undergo significant deviation for even a small perturbation in the departure hyperbolic orbit characteristics***. ***The sensitivity analysis also brings out the fact that the perturbations in the departure phase have to be included in the trajectory design process.***

While the conventional and the V-infinity tuned patched conic techniques generate four notional design options for an opportunity, ***the ITR-PC technique generates four distinct transfer trajectory design options.*** The ITR-PC technique generates improved designs which can be used as initial guess for numerical refinement. The trajectory correction maneuver (TCM) required for the ITR-PC designs under the design force model to meet the desired target conditions is less than 1 m/s whereas the TCM required for the conventional design is more than 200 m/s. Also, the computation time for the generating the ITR-PC design is only about 6 ms. ***So, this technique can be used to generate quick analytical designs with improved accuracies compared to the conventional analytical techniques.*** The FORTRAN 95 code, developed based on this technique, is used as a design analysis tool to understand the trends and tradeoffs of various mission scenarios. ***The design analysis of all the four distinct options*** for different mission scenarios have been carried out and many important inferences are drawn.

The ITR-PC technique, while maintaining the simplicity of the patched conic approach, generates better initial guess for numerical refinement and also distinctly identifies the four design options for a given opportunity. The use of this technique for mission planning and analysis provides in-depth insight into the realistic trends and tradeoffs of various mission scenarios.

♠♠♠♠♠♠♠♠♠♠♠♠♠♠♠♠♠♠♠

CHAPTER 6
BIASED-ITERATIVE PATCHED CONIC TECHNIQUE FOR TRANSFER TRAJECTORY DESIGN

6.1 Chapter Summary

The iterative patched conic technique achieves the target parameters with reasonably good accuracy under the design force model (cf. Chapter 5). However, on numerical propagation under a force model that includes perturbations, there are significant deviations in the arrival target parameters. Further, the numerical refinement of the ITR-PC design, under the force model including perturbations, converges to any of the design options in the absence of additional information on the arrival parameters. So, the ITR-PC design needs to be improved under a force model that includes perturbations. This chapter includes the major perturbing forces in the analytical design process and generates an improved trajectory design. The proposed technique, named as ***biased-iterative patched conic technique*** (B-ITRPC), modifies the ITR-PC design to include the major perturbing forces in the departure phase of the interplanetary trajectory design process. This technique generate analytical designs that are close to the numerical designs and hence, is used to develop a quick mission design and analysis tool to understand the realistic trends with improved accuracy. The current chapter begins with a study which identifies the major perturbing forces that influences the interplanetary transfer trajectory and proceeds to present the new technique.

6.2 Introduction

There are many perturbing forces apart from the primary body that influence the trajectory of the spacecraft. Considering perturbing forces in the departure phase is critical because the accuracy with which the V-infinity vector is determined influences the achieved target parameters on arrival. The perturbations are classified into two types:

1) Gravitational perturbation, such as oblateness of Earth and the third-body attraction.

2) Non-gravitational perturbation, such as solar radiation pressure and atmospheric drag.

A study to identify the major perturbing forces that influences the interplanetary transfer trajectory during the departure phase is carried out. The current chapter focuses on an analytical trajectory design technique that includes the identified perturbations in the design process. The proposed analytical technique, named as biased-iterative patched conic technique (B-ITRPC), generates improved trajectory design.

In the B-ITRPC design process, the initial design is obtained using the iterative patched conic technique (ITR-PC) for the prefixed departure design parameters such as the periapsis altitude, inclination and the SOI-duration. The state vector of the patch point of the current ITR-PC design is propagated backward including the perturbations which results in different departure design parameters. The backward propagation of the state vector at the SOI is carried out analytically using linear approximation technique (Zhang et al., 2014). The differences in the departure design parameters are computed and used to bias the input parameters at the departure epoch. These input parameters are used to obtain the ITR-PC design in the subsequent iterations. In this technique, the equations of motion are linearized about an initial point and the solutions of the linearized equations of motion are obtained from the closed form expressions using the generalized spectral decomposition theorem. Thus, ***the B-ITRPC technique includes two loops, (i) an inner loop that obtains the ITR-PC design and (ii) an outer loop that obtains the biased input parameters/departure design parameters.*** The B-ITRPC design, thus obtained, is very close to the numerical design. Also, the B-ITRPC design is an excellent initial guess for numerical refinement even under a realistic force model that includes the perturbations. It does not require additional information on the arrival geometry unlike the ITR-PC design.

The current chapter is organized as follows. Section 6.3 identifies the major perturbations that are to be included in the B-ITRPC technique. The equations of motion that include the perturbations and the linear approximation technique are explained in section 6.4. The solutions of the linearized equations of motion using the generalized spectral decomposition theorem are discussed in section 6.5. The detailed algorithm of the B-ITRPC technique is provided in section 6.6. In section 6.7, the performance of the proposed design technique is illustrated using an Earth to Mars orbit mission for the minimum energy opportunity of 2018. The FORTRAN 95 code developed based on the B-ITRPC technique is used as a quick mission design and analysis tool in section 6.8.

The proposed technique is used to analyze the trajectory design of India's maiden interplanetary transfer, the Mars Orbiter Mission (MOM) in section 6.9. The trajectory design for the MAVEN mission which utilized the same opportunity is also generated using the B-ITRPC technique. The B-ITRPC trajectory designs are generated for Earth to Jupiter and Earth to Venus direct transfers for the upcoming minimum energy opportunities of 2022 and 2023 respectively and presented (cf. section 6.10). In section 6.11, the performance of different analytical techniques is consolidated. Section 6.12 presents the chapter conclusions.

6.3 Major Perturbations

To identify the major perturbing forces that influence the interplanetary transfer trajectory, the ITR-PC design for an Earth to Mars transfer (minimum energy opportunity: 2018) is numerically propagated under different forces models. In the force models, different perturbing forces are included in the departure phase. The achieved arrival parameters on numerical propagation under different force models are given in Table 6.1. It can be seen that the deviations in the arrival parameters are maximum (achieved CAA 2,16,733 km, inclination 19.76 deg and the time of periapsis deviates by about 7.3 h) due to the non-spherical gravity of Earth. Also, the deviations are significantly large for the perturbations due to the third body gravity effects of the Moon and the Sun. Note that, the inclusion of the third body effects of the other bodies such as Jupiter, Saturn, Venus, Mars, and Mercury etc. in the departure phase does not cause significant deviations in the arrival target parameters (achieved CAA 329 km, inclination 75.41 deg and the time of periapsis deviates by about 2 minutes). Also, the non-gravitational perturbations such as the solar radiation pressure and atmospheric drag are modelled for a spacecraft assuming a dry mass of 1000 kg and a cross-sectional area of 10 m^2. These forces cause small deviations in the arrival parameters and so, are not considered in the trajectory design process.

The trajectory correction maneuvers (TCM) required for the ITR-PC design to achieve the desired target conditions under different force models are presented in Table 6.1. The largest TCM correction is required to compensate for the non-spherical gravity perturbation of the Earth (15.3 m/s). The TCM requirement for the perturbations due to the Moon and the Sun are also significantly high (about 4 to 5 m/s). So, these perturbing forces are included in the departure phase of the B-ITRPC design process. Also note that, the TCM requirement to compensate for the third body gravity effects of the planets such

as Jupiter, Saturn, Venus, Mars, and Mercury etc. and the non-gravitational perturbations are less than 1 m/s. Based on the above analysis, it is concluded that the major perturbations such as the non-spherical gravity of the Earth and the third body gravity effects of the Sun and the Moon are to be essentially included in the trajectory design process.

Table 6.1a Achievable accuracies on numerical propagation of ITR-PC design under different force models

Index	Perturbing forces in departure phase	Arrival CAA (km)	Arr. Inc. (deg)	T_P (UTC)	TCM (m/s)
A	Spherical Earth	330	75.40	1 Dec 2018 23:58:40	< 1
B	A + all planets	329	75.41	1 Dec 2018 23:58:41	<1
C	A + SRP	325	75.56	1 Dec 2018 23:57:42	< 1
D	A + atmospheric drag	308	73.31	2 Dec 2018 00:00:37	<1
E	A + Moon	1,14,852	20.03	2 Dec 2018 10:38:01	5.2
F	A + Sun	1,05,317	19.88	2 Dec 2018 11:15:33	4.6
G	Non-spherical Earth	2,16,733	19.76	3 Dec 2018 07:29:00	15.3
H	G + Moon + Sun	4,62,978	21.52	4 Dec 2018 02:50:42	18.1
I	H + all planets	4,62,979	21.52	4 Dec 2018 02:50:42	18.0
*Cruise phase: Sun; Arrival phase: Mars Desired values: CAA, 300 km; Inc., 75.00 deg and T_P, 2 Dec 2018 00:00:00 UTC					

6.4 Linear Approximation Technique

The linear approximation technique (LA) is used to linearize the equations of motion about an initial point and the solutions of the linearized equations of motion are obtained in closed form using the generalized spectral decomposition theorem. This as an effective alternative to numerical propagation. From Table 6.1b, it is found that the LA technique is faster than the numerical integration of the equations of motion by about nine times for the same step size. A set of initial state vector (cf. Table 6.1b) is propagated using the LA technique and the numerical integration for the same duration (3 days) using a step size of 1 s. All major perturbing forces mentioned in section 6.3 are included in the force model. The state vector obtained from the numerical technique i.e. the numerical

integration of the equations of motion is taken as the reference. It is to be noted that the LA technique resulted in a state vector with marginal errors in the position and velocity vectors i.e. 2 km and 0.014 m/s respectively. The computation time required for the LA technique is only 4.7 s while the numerical technique required 41.8 s. So, it can be concluded that the LA propagation is a good alternative to obtain a reasonably accurate and quick result.

Table 6.1b Comparison of analytical and numerical state vector propagation techniques

Parameters	*Initial	LA propagation	Numerical propagation
x(km)	-5657.28	487072.49	487070.82
y(km)	3256.55	-396779.29	-396779.01
z(km)	1409.76	-507557.97	-507555.25
$\dot{x}$(km/s)	-3.4650	1.725662	1.725655
$\dot{y}$(km/s)	-1.4367	-1.372006	-1.372004
$\dot{z}$(km/s)	-10.5860	-1.670202	-1.670190
Δr (km)	-	**2.84**	-
Δv (m/s)	-	**0.014**	-
Computation time (s)	**-**	***4.7***	***41.8***
*corresponding initial departure hyperbolic orbital elements: a_{∞_D}= -58963.7 km; e_{∞_D}=1.113258; i_{∞_D}= 75 deg; Ω_{∞_D}=333.3910 deg; ω_{∞_D}=167.3762 deg; $\nu_{P\infty_D}$=0 deg step size = 1 s			

6.4.1 Linearization of Equations of Motion

The four-body geometry is shown in Fig.6.1. The geocentric equations of motion of the spacecraft in the EME2000 inertial frame are,

$$\dot{\boldsymbol{r}} = \boldsymbol{v} \tag{6.1}$$

$$\boldsymbol{a} = \dot{\boldsymbol{v}} = -\mu_e\left(\frac{\boldsymbol{r}}{r^3}\right) - \mu_m\left(\frac{\boldsymbol{r_{md}}}{{r_{md}}^3} + \frac{\boldsymbol{r_m}}{{r_m}^3}\right) - \mu_s\left(\frac{\boldsymbol{r_{sd}}}{{r_{sd}}^3} + \frac{\boldsymbol{r_s}}{{r_s}^3}\right) + \boldsymbol{F} \tag{6.2}$$

where $\boldsymbol{r}$, $\boldsymbol{v}$ and $\boldsymbol{a}$ are the geocentric position, velocity and acceleration vectors of the spacecraft respectively, $\boldsymbol{r_{md}}$ is the selenocentric position vector of the spacecraft, $\boldsymbol{r_m}$ is the geocentric position vector of the Moon, $\boldsymbol{r_{sd}}$ is the heliocentric position vector of the spacecraft, $\boldsymbol{r_s}$ is the geocentric position vector of Sun. The disturbing function $'\boldsymbol{F}'$ includes the non-spherical perturbations due to Earth and its components [Schaub, 2009] are as follows.

$$F_x = -\mu_e\left(\frac{x}{r^3}\right)\left[\frac{3}{2}J_2\frac{{R_e}^2}{r^2}\left(1-5\frac{z^2}{r^2}\right)+\frac{5}{2}J_3\frac{{R_e}^3}{r^3}\left(3-7\frac{z^2}{r^2}\right)\frac{z}{r}-\frac{5}{8}J_4\frac{{R_e}^4}{r^4}\left(3-42\frac{z^2}{r^2}+63\frac{z^4}{r^4}\right)-\frac{3}{8}J_5\frac{{R_e}^5}{r^5}\left(35-210\frac{z^2}{r^2}+231\frac{z^4}{r^4}\right)\frac{z}{r}+\frac{1}{16}J_6\frac{{R_e}^6}{r^6}\left(35-945\frac{z^2}{r^2}+3465\frac{z^4}{r^4}-3003\frac{z^6}{r^6}\right)\right] \quad (6.3a)$$

$$F_y = -\mu_e\left(\frac{y}{r^3}\right)\left[\frac{3}{2}J_2\frac{{R_e}^2}{r^2}\left(1-5\frac{z^2}{r^2}\right)+\frac{5}{2}J_3\frac{{R_e}^3}{r^3}\left(3-7\frac{z^2}{r^2}\right)\frac{z}{r}-\frac{5}{8}J_4\frac{{R_e}^4}{r^4}\left(3-42\frac{z^2}{r^2}+63\frac{z^4}{r^4}\right)-\frac{3}{8}J_5\frac{{R_e}^5}{r^5}\left(35-210\frac{z^2}{r^2}+231\frac{z^4}{r^4}\right)\frac{z}{r}+\frac{1}{16}J_6\frac{{R_e}^6}{r^6}\left(35-945\frac{z^2}{r^2}+3465\frac{z^4}{r^4}-3003\frac{z^6}{r^6}\right)\right] \quad (6.3b)$$

$$F_z = -\mu_e\left(\frac{z}{r^3}\right)\left[\frac{3}{2}J_2\frac{{R_e}^2}{r^2}\left(3-5\frac{z^2}{r^2}\right)+\frac{5}{2}J_3\frac{{R_e}^3}{r^3}\left(6-7\frac{z^2}{r^2}\right)\frac{z}{r}-\frac{5}{8}J_4\frac{{R_e}^4}{r^4}\left(15-70\frac{z^2}{r^2}+63\frac{z^4}{r^4}\right)-\frac{3}{8}J_5\frac{{R_e}^5}{r^5}\left(105-315\frac{z^2}{r^2}+231\frac{z^4}{r^4}\right)\frac{z}{r}+\frac{1}{16}J_6\frac{{R_e}^6}{r^6}\left(245-2205\frac{z^2}{r^2}+4851\frac{z^4}{r^4}-3003\frac{z^6}{r^6}\right)\right]+\frac{\mu_e}{r^2}\left(\frac{3}{2}J_3\frac{{R_e}^3}{r^3}-\frac{15}{8}J_5\frac{{R_e}^5}{r^5}\right) \quad (6.3c)$$

where R_e is the equatorial radius of Earth and J_2 to J_6 are the zonal harmonic coefficients of the non-spherical Earth. Let $\boldsymbol{r_0}$ and $\boldsymbol{v_0}$ be the position and velocity vectors of the spacecraft at the initial time, t_0. Equation 6.2 models the acceleration ($\boldsymbol{a} = \dot{\boldsymbol{v}}$) experienced by the spacecraft due to the primary and perturbing gravitational forces at any time, t. This acceleration is expressed as a Taylor series expansion around the initial point ($\boldsymbol{r_0}$) with the radius vector ($\boldsymbol{r}$) as the independent variable.

$$\boldsymbol{a} = \boldsymbol{a_0} + \left\{\left(\left.\frac{\partial \boldsymbol{a}}{\partial \boldsymbol{r}}\right|_{\boldsymbol{r_0}}\delta\boldsymbol{r}\right)+\left(\left.\frac{\partial \boldsymbol{a}}{\partial \boldsymbol{r_m}}\right|_{\boldsymbol{r_{m_0}}}\delta\boldsymbol{r_m}\right)+\left(\left.\frac{\partial \boldsymbol{a}}{\partial \boldsymbol{r_s}}\right|_{\boldsymbol{r_{s_0}}}\delta\boldsymbol{r_s}\right)\right\}+\left\{\left(\frac{1}{2!}\left.\frac{\partial^2 \boldsymbol{a}}{\partial \boldsymbol{r}^2}\right|_{\boldsymbol{r_0}}(\delta\boldsymbol{r})^2\right)+\cdots\right. \quad (6.4)$$

where the term '$\delta\boldsymbol{r}$'is defined as,

$$\delta\boldsymbol{r} = \boldsymbol{r}(t) - \boldsymbol{r}(t_0) \quad (6.5a)$$

$$\delta\boldsymbol{r_m} = \boldsymbol{r_m}(t) - \boldsymbol{r_m}(t_0) \quad (6.5b)$$

$$\delta\boldsymbol{r_s} = \boldsymbol{r_s}(t) - \boldsymbol{r_s}(t_0) \quad (6.5c)$$

Eq. 6.5a is obtained by solving

$$\delta\dot{\boldsymbol{r}} = \boldsymbol{v} \quad (6.6)$$

Eq. 6.5b is solved in the next section. Because the heliocentric position vector of the spacecraft varies very slowly for the prefixed step size (1 s) used for LA propagation, the

value of $\delta \boldsymbol{r_s}$ is very small and so, can be neglected. The current research considers the linearized equations of motion and so only the first order term of Eq. 6.4 is considered. Through linear expansion about the initial point during a finite time span from t_0 to t, Eq. 6.2 can be approximated as,

$$\dot{\boldsymbol{v}} = \boldsymbol{M}\delta\boldsymbol{r} + \boldsymbol{M}'\delta\boldsymbol{r_m} + \boldsymbol{C} \tag{6.7}$$

where $\boldsymbol{C}$ includes the terms corresponding to the perturbations which do not change over a finite duration ($\delta t = t_0 - t$). Note that the terms in $\boldsymbol{C}$ are different from the one given in Zhang et al. (2014) wherein the formulation for LA technique is in the context of lunar transfer and so it considers only the third body perturbation due to the Moon. The formulation in the current research is in the context of interplanetary transfer wherein the third-body perturbations of due to the Sun and the non-spherical gravity of Earth are also considered in addition to the perturbation due to the Moon. The matrices $\boldsymbol{M}$, $\boldsymbol{M}'$ and $\boldsymbol{M}''$ in Eq. (6.7) are given as,

$$\boldsymbol{M} = \boldsymbol{M_1} + \boldsymbol{M_2} + \boldsymbol{M_4} \tag{6.8}$$

$$\boldsymbol{M}' = \boldsymbol{M_3} - \boldsymbol{M_2} \tag{6.9}$$

where

$$\boldsymbol{M_1} = -\frac{\mu_e}{{r_0}^3}\left(I - 3\hat{\boldsymbol{r}}_{\boldsymbol{0}}\hat{\boldsymbol{r}}_{\boldsymbol{0}}{}^T\right) \tag{6.10}$$

$$\boldsymbol{M_2} = -\frac{\mu_m}{{r_{md0}}^3}\left(I - 3\hat{\boldsymbol{r}}_{\boldsymbol{md0}}\hat{\boldsymbol{r}}_{\boldsymbol{md0}}{}^T\right) \tag{6.11}$$

$$\boldsymbol{M_3} = -\frac{\mu_m}{{r_{m0}}^3}\left(I - 3\hat{\boldsymbol{r}}_{\boldsymbol{m0}}\hat{\boldsymbol{r}}_{\boldsymbol{m0}}{}^T\right) \tag{6.12}$$

$$\boldsymbol{M_4} = -\frac{\mu_s}{{r_{sd0}}^3}\left(I - 3\hat{\boldsymbol{r}}_{\boldsymbol{sd0}}\hat{\boldsymbol{r}}_{\boldsymbol{sd0}}{}^T\right) \tag{6.13}$$

where μ_e, μ_m and μ_s are the gravitational constants of Earth, Moon and Sun respectively. The notation '^' refers to unit vector and the subscript '0' indicates the initial condition. The components of $\boldsymbol{C}$ that includes the perturbations due to the non-spherical gravity of Earth upto six zonal harmonics and the lunisolar perturbations are,

$$C_x = F_x + \left\{-\mu_m\left[\frac{x_{md_0}}{{r_{md}}_0{}^3} + \frac{x_{m_0}}{{r_{m}}_0{}^3}\right] - \mu_s\left[\frac{x_{sd_0}}{{r_{sd}}_0{}^3} + \frac{x_{s_0}}{{r_{s}}_0{}^3}\right]\right\} \tag{6.14}$$

$$C_y = F_y + \left\{-\mu_m\left[\frac{y_{md_0}}{{r_{md}}_0{}^3} + \frac{y_{m_0}}{{r_{m}}_0{}^3}\right] - \mu_s\left[\frac{y_{sd_0}}{{r_{sd}}_0{}^3} + \frac{y_{s_0}}{{r_{s}}_0{}^3}\right]\right\} \tag{6.15}$$

$$C_z = F_z + \left\{-\mu_m\left[\frac{z_{md_0}}{{r_{md}}_0{}^3} + \frac{z_{m_0}}{{r_{m}}_0{}^3}\right] - \mu_s\left[\frac{z_{sd_0}}{{r_{sd}}_0{}^3} + \frac{z_{s_0}}{{r_{s}}_0{}^3}\right]\right\} \tag{6.16}$$

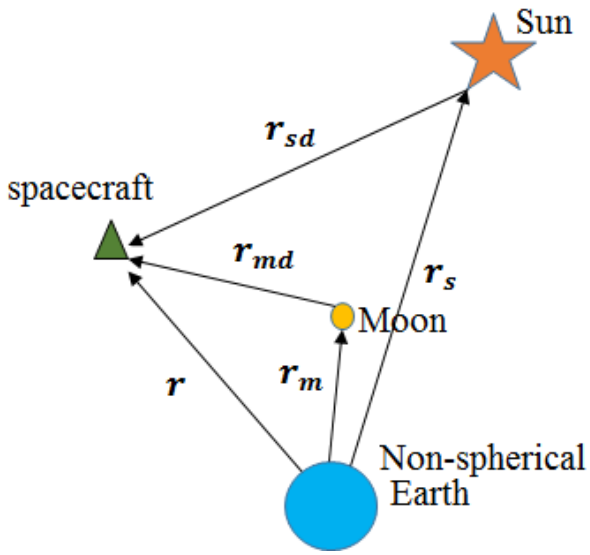

Fig.6.1. Four-body geometry

The solutions of Eqs. (6.2) and (6.6) are obtained in closed form using the generalized spectral decomposition theorem which is discussed in the following section.

6.4.2 Solution Method

From the previous section, Eqs. 6.6 and 6.7 are expressed as,

$$\begin{bmatrix} \delta\dot{\boldsymbol{r}} \\ \dot{\boldsymbol{v}} \end{bmatrix} = \begin{bmatrix} \mathbf{0} & \boldsymbol{I} \\ \boldsymbol{M} & \mathbf{0} \end{bmatrix} \begin{bmatrix} \delta\boldsymbol{r} \\ \boldsymbol{v} \end{bmatrix} + \begin{bmatrix} \mathbf{0} \\ \boldsymbol{M}'\delta\boldsymbol{r}_{\boldsymbol{m}} + \boldsymbol{C} \end{bmatrix} \tag{6.17}$$

Equation 6.17 can be rewritten in the following form,

$$\boldsymbol{X}(\boldsymbol{t}) = \boldsymbol{A}\boldsymbol{X}(\boldsymbol{t_0}) + \boldsymbol{f}(\boldsymbol{t}) \tag{6.18}$$

where

$$\boldsymbol{A} = \begin{bmatrix} \mathbf{0} & \boldsymbol{I} \\ \boldsymbol{M} & \mathbf{0} \end{bmatrix}$$

$$\boldsymbol{X}(\boldsymbol{t_0}) = \begin{bmatrix} \delta\boldsymbol{r} \\ \boldsymbol{v} \end{bmatrix}$$

$$\boldsymbol{f}(\boldsymbol{t}) = \begin{bmatrix} \mathbf{0} \\ \boldsymbol{M}'\delta\boldsymbol{r}_{\boldsymbol{m}} + \boldsymbol{C} \end{bmatrix}$$

The solution of Eq. 6.18 can be written as,

$$\boldsymbol{X} = e^{\boldsymbol{A}t}\boldsymbol{X_0} + \int_0^t e^{\boldsymbol{A}(t-\tau)}\boldsymbol{f}(\tau)\, d\tau \tag{6.19a}$$

which is

$$\boldsymbol{X} = e^{\boldsymbol{A}t}\boldsymbol{X_0} + e^{\boldsymbol{A}t}\int_0^t e^{\boldsymbol{A}(-\tau)}\boldsymbol{f}(\tau)\, d\tau \tag{6.19b}$$

According to the generalized spectral decomposition theorem, $e^{\boldsymbol{A}t} = \sum_{i=1}^{3} \frac{\boldsymbol{G_i P_i}(t)}{H_i}$

The derivation of the variables $\boldsymbol{G}, \boldsymbol{P}$ and H is given below.

Eq. 6.8 is rewritten as,

$$\boldsymbol{M} = k_e\left(I - 3\hat{\boldsymbol{r}}_{\boldsymbol{0}}\hat{\boldsymbol{r}}_{\boldsymbol{0}}{}^T\right) + k_m\left(I - 3\hat{\boldsymbol{r}}_{\boldsymbol{md0}}\hat{\boldsymbol{r}}_{\boldsymbol{md0}}{}^T\right) \tag{6.20}$$

The eigenvalues of $\boldsymbol{M}$ are denoted by s_1, s_2 and s_3 and they are,

$$s_1 = k_e + k_m \tag{6.21a}$$

$$s_2 = -\frac{1}{2}(k_e + k_m) + \frac{3}{2}((k_e - k_m)^2 + 4k_e k_m(\hat{\boldsymbol{r}}_{\boldsymbol{0}} \cdot \hat{\boldsymbol{r}}_{\boldsymbol{m0}})^2)^{\frac{1}{2}} \tag{6.21b}$$

$$s_3 = -\frac{1}{2}(k_e + k_m) - \frac{3}{2}((k_e - k_m)^2 + 4k_e k_m(\hat{\boldsymbol{r}}_{\boldsymbol{0}} \cdot \hat{\boldsymbol{r}}_{\boldsymbol{m0}})^2)^{\frac{1}{2}} \tag{6.21c}$$

Let $\lambda_1 = \sqrt{|s_1|}$, $\lambda_2 = \sqrt{|s_2|}$, $\lambda_3 = \sqrt{|s_3|}$. The eigenvalues of $\boldsymbol{A}$ in Eq. 6.19 are denoted by $\lambda(\boldsymbol{A})$.

$$\lambda(\boldsymbol{A}) = \begin{cases} \{\lambda_1 i, -\lambda_1 i, \lambda_2, -\lambda_2, \lambda_3, -\lambda_3\}, s_3 > 0 \\ \{\lambda_1 i, -\lambda_1 i, \lambda_2, -\lambda_2, \lambda_3 i, -\lambda_3 i\}, s_3 < 0 \end{cases} \tag{6.22}$$

Now, the variables $\boldsymbol{G}, \boldsymbol{P}$ and H are obtained as,

$$H_1 = \begin{cases} \lambda_1(\lambda_1{}^2 + \lambda_2{}^2)(\lambda_1{}^2 + \lambda_3{}^2), s_3 > 0 \\ \lambda_1(\lambda_1{}^2 + \lambda_2{}^2)(\lambda_1{}^2 - \lambda_3{}^2), s_3 < 0 \end{cases} \tag{6.23a}$$

$$H_2 = \begin{cases} \lambda_2(\lambda_1{}^2 + \lambda_2{}^2)(\lambda_2{}^2 - \lambda_3{}^2), s_3 > 0 \\ \lambda_2(\lambda_1{}^2 + \lambda_2{}^2)(\lambda_1{}^2 + \lambda_3{}^2), s_3 < 0 \end{cases} \tag{6.23b}$$

$$H_3 = \begin{cases} \lambda_3(\lambda_1{}^2 + \lambda_3{}^2)(\lambda_3{}^2 - \lambda_2{}^2), s_3 > 0 \\ \lambda_3(\lambda_2{}^2 + \lambda_3{}^2)(\lambda_3{}^2 - \lambda_1{}^2), s_3 < 0 \end{cases} \tag{6.23c}$$

$$\boldsymbol{G}_1 = \begin{cases} \boldsymbol{A}^4 - \left(\lambda_2{}^2 + \lambda_3{}^2\right)\boldsymbol{A}^2 + \lambda_2{}^2\lambda_3{}^2\boldsymbol{I}, s_3 > 0 \\ \boldsymbol{A}^4 - \left(\lambda_2{}^2 - \lambda_3{}^2\right)\boldsymbol{A}^2 - \lambda_2{}^2\lambda_3{}^2\boldsymbol{I}, s_3 < 0 \end{cases} \tag{6.24a}$$

$$\boldsymbol{G}_2 = \begin{cases} \boldsymbol{A}^4 - \left(\lambda_3{}^2 - \lambda_1{}^2\right)\boldsymbol{A}^2 - \lambda_1{}^2\lambda_3{}^2\boldsymbol{I}, s_3 > 0 \\ \boldsymbol{A}^4 + \left(\lambda_3{}^2 + \lambda_1{}^2\right)\boldsymbol{A}^2 + \lambda_1{}^2\lambda_3{}^2\boldsymbol{I}, s_3 < 0 \end{cases} \tag{6.24b}$$

$$\boldsymbol{G}_3 = \boldsymbol{A}^4 + \left(\lambda_1{}^2 - \lambda_2{}^2\right)\boldsymbol{A}^2 - \lambda_1{}^2\lambda_2{}^2\boldsymbol{I} \tag{6.24c}$$

$$\boldsymbol{P}_1(t) = \sin(\lambda_1 t)\boldsymbol{A} + \lambda_1 \cos(\lambda_1 t)\,\boldsymbol{I} \tag{6.25a}$$

$$\boldsymbol{P}_2(t) = \sin\mathrm{h}(\lambda_2 t)\boldsymbol{A} + \lambda_2 \cos\mathrm{h}(\lambda_2 t)\,\boldsymbol{I} \tag{6.25b}$$

$$\boldsymbol{P}_3 = \begin{cases} \sin\mathrm{h}(\lambda_3 t)\boldsymbol{A} + \lambda_3 \cos\mathrm{h}(\lambda_3 t)\,\boldsymbol{I}, s_3 > 0 \\ \sin(\lambda_3 t)\boldsymbol{A} + \lambda_3 \cos(\lambda_3 t)\,\boldsymbol{I}, s_3 < 0 \end{cases} \tag{6.25c}$$

Because the Moon's orbit around Earth is nearly circular, the position of the Moon is approximated as follows,

$$\boldsymbol{r}_m = r_{m0}\,(\cos(\omega\tau)\,\hat{\boldsymbol{r}}_{m0} + \sin(\omega\tau)\,\hat{\boldsymbol{r}}_{m\perp 0}) \tag{6.26}$$

$$\Rightarrow \delta\boldsymbol{r}_m = r_{m0}\,(\cos(\omega\tau)\,\hat{\boldsymbol{r}}_{m0} + \sin(\omega\tau)\,\hat{\boldsymbol{r}}_{m\perp 0}) - \boldsymbol{r}_{m0}$$

where $\hat{\boldsymbol{r}}_{m\perp 0}$ is the unit vector perpendicular to $\hat{\boldsymbol{r}}_{m0}$ which is nothing but the direction of the velocity vector in this case and ω is the angular velocity of the Moon around Earth. Thus, Eq. 6.5b is obtained. Let

$$\boldsymbol{f}(\tau) = \begin{bmatrix} \boldsymbol{0} \\ r_{m0}\boldsymbol{M}'\hat{\boldsymbol{r}}_{m\perp 0} \end{bmatrix} \cos(\omega\tau) + \begin{bmatrix} \boldsymbol{0} \\ r_{m0}\boldsymbol{M}'\hat{\boldsymbol{r}}_{m\perp 0} \end{bmatrix} \sin(\omega\tau) + \begin{bmatrix} \boldsymbol{0} \\ \boldsymbol{C} - \boldsymbol{M}'\hat{\boldsymbol{r}}_{m0} \end{bmatrix} \tag{6.27}$$

$$\boldsymbol{f}(\tau) = \boldsymbol{C_1}\cos(\omega\tau) + \boldsymbol{C_2}\sin(\omega\tau) + \boldsymbol{C_3} \tag{6.28}$$

Then

$$e^{-\boldsymbol{A}\tau}\boldsymbol{f}(\tau) = \sum_{i=1}^{3} \frac{\boldsymbol{G}_i\boldsymbol{Q}_i(\tau)}{H_i} \tag{6.29}$$

and

$$\int_0^t e^{-\boldsymbol{A}\tau}\boldsymbol{f}(\tau)d\tau = \sum_{i=1}^{3} \frac{\boldsymbol{G}_i\boldsymbol{R}_i(t)}{H_i} \tag{6.30}$$

where

$$\boldsymbol{Q}_1(\tau) = (\lambda_1 \cos(\lambda_1\tau)\,\boldsymbol{I} - \sin(\lambda_1\tau)\,\boldsymbol{A})(\cos(\omega\tau)\,\boldsymbol{C_1} + \sin(\omega\tau)\,\boldsymbol{C_2} + \boldsymbol{C_3}) \tag{6.31a}$$

$$\boldsymbol{Q}_2(\tau) = (\lambda_2 \cosh(\lambda_2\tau)\,\boldsymbol{I} - \sinh(\lambda_2\tau)\,\boldsymbol{A})(\cos(\omega\tau)\,\boldsymbol{C_1} + \sin(\omega\tau)\,\boldsymbol{C_2} + \boldsymbol{C_3}) \tag{6.31b}$$

$$\boldsymbol{Q}_3(\tau) = \begin{cases} (\lambda_3 \cosh(\lambda_3\tau)\,\boldsymbol{I} - \sinh(\lambda_3\tau)\,\boldsymbol{A})(\cos(\omega\tau)\,\boldsymbol{C_1} + \sin(\omega\tau)\,\boldsymbol{C_2} + \boldsymbol{C_3}), s_3 > 0 \\ (\lambda_3 \cos(\lambda_3\tau)\,\boldsymbol{I} - \sin(\lambda_3\tau)\,\boldsymbol{A})(\cos(\omega\tau)\,\boldsymbol{C_1} + \sin(\omega\tau)\,\boldsymbol{C_2} + \boldsymbol{C_3}), s_3 < 0 \end{cases} \tag{6.31c}$$

$$\begin{aligned} \boldsymbol{R}_1(t) = {} & -\boldsymbol{AC_1}\int_0^t sin(\lambda_1\tau)\cos(\omega\tau)\,d\tau + \lambda_1\boldsymbol{C_1}\int_0^t \cos(\lambda_1\tau)\cos(\omega\tau)\,d\tau - \\ & \boldsymbol{AC_2}\int_0^t sin(\lambda_1\tau)\sin(\omega\tau)\,d\tau + \lambda_1\boldsymbol{C_2}\int_0^t sin(\omega\tau)\cos(\lambda_1\tau)d\tau - \\ & \boldsymbol{AC_3}\int_0^t sin(\lambda_1\tau)d\tau + \lambda_1\boldsymbol{C_3}\int_0^t cos(\lambda_1\tau)d\tau \end{aligned} \tag{6.32a}$$

$$\boldsymbol{R}_2(t) = -\boldsymbol{AC_1}\int_0^t sinh(\lambda_2\tau)\cos(\omega\tau)\,d\tau + \lambda_2\boldsymbol{C_1}\int_0^t \cosh(\lambda_2\tau)\cos(\omega\tau)\,d\tau - \boldsymbol{AC_2}\int_0^t sinh(\lambda_2\tau)\sin(\omega\tau)\,d\tau + \lambda_2\boldsymbol{C_2}\int_0^t sinh(\lambda_2\tau)\cos(\omega\tau)d\tau - \boldsymbol{AC_3}\int_0^t sinh(\lambda_2\tau)d\tau + \lambda_2\boldsymbol{C_3}\int_0^t cosh(\lambda_2\tau)d\tau \quad (6.32b)$$

$$\boldsymbol{R}_3(t) = \begin{cases}\boldsymbol{R}_{31}(t), s_3 > 0\\ \boldsymbol{R}_{32}(t), s_3 < 0\end{cases} \quad (6.32c)$$

where

$$\boldsymbol{R}_{31}(t) = -\boldsymbol{AC_1}\int_0^t sinh(\lambda_3\tau)\cos(\omega\tau)\,d\tau + \lambda_3\boldsymbol{C_1}\int_0^t \cosh(\lambda_3\tau)\cos(\omega\tau)\,d\tau - \boldsymbol{AC_2}\int_0^t sinh(\lambda_3\tau)\sin(\omega\tau)\,d\tau + \lambda_3\boldsymbol{C_2}\int_0^t sinh(\lambda_3\tau)\cos(\omega\tau)d\tau - \boldsymbol{AC_3}\int_0^t sinh(\lambda_3\tau)d\tau + \lambda_3\boldsymbol{C_3}\int_0^t cosh(\lambda_3\tau)d\tau \quad (6.32d)$$

$$\boldsymbol{R}_{32}(t) = -\boldsymbol{AC_1}\int_0^t sin(\lambda_3\tau)\cos(\omega\tau)\,d\tau + \lambda_3\boldsymbol{C_1}\int_0^t \cos(\lambda_3\tau)\cos(\omega\tau)\,d\tau - \boldsymbol{AC_2}\int_0^t sin(\lambda_3\tau)\sin(\omega\tau)\,d\tau + \lambda_3\boldsymbol{C_2}\int_0^t sin(\omega\tau)\cos(\lambda_3\tau)d\tau - \boldsymbol{AC_3}\int_0^t sin(\lambda_3\tau)d\tau + \lambda_3\boldsymbol{C_3}\int_0^t cos(\lambda_3\tau)d\tau \quad (6.32e)$$

Thus, the states are obtained as,

$$\boldsymbol{X} = \left(\sum_{i=1}^{3}\frac{\boldsymbol{G_i P}_i(t)}{H_i}\right)\left(\boldsymbol{X_0} + \sum_{i=1}^{3}\frac{\boldsymbol{G_i R}_i(t)}{H_i}\right) \quad (6.33)$$

The position vector is updated as,

$$\boldsymbol{r} = \boldsymbol{r_0} + \boldsymbol{\delta r} \quad (6.34)$$

and the velocity vector ($\boldsymbol{v}$) is directly obtained.

6.5 Biased-Iterative Patched Conic Technique

The biased iterative patched conic technique (B-ITRPC) generates improved analytical trajectory design by including the perturbations in the departure phase (within the SOI of Earth) in the trajectory design process. The perturbations within the SOI of the arrival planet are not considered as their influence on the trajectory design process is only marginal (discussed later). The proposed technique is applicable for direct transfer to all planets.

For a fixed epoch and flight duration, the steps of the B-ITRPC technique which biases the input parameters at the departure to account for the perturbations is given below. The input design parameters are, (i) Earth-SOI duration (t_D), (ii) DPO periapsis altitude ($h_{P_{\infty D}}$), and (iii) DPO inclination ($i_{P_{\infty D}}$).

The periapsis altitude $\left(h_{P_{\infty D_{desired}}}\right)$ *and inclination* $\left(i_{P_{\infty D_{desired}}}\right)$ *of the departure hyperbolic orbit are fixed. Also, the desired values for the departure and arrival SOI durations i.e.,* $t_{D_{desired}}$ *and* t_A *respectively, are fixed.*

1) Set the initial values of the input design as the desired values,

$$h_{P_{\infty D}} = h_{P_{\infty D_{desired}}} \tag{6.35}$$

$$i_{P_{\infty D}} = i_{P_{\infty D_{desired}}} \tag{6.36}$$

$$t_D = t_{D_{desired}} \tag{6.37}$$

2) Obtain the iterative patched conic design (cf. chapter 5) that achieves the desired arrival target conditions viz. periapsis altitude and inclination of the arrival hyperbolic orbit expressed with respect to Mars equator and IAU vector of J2000 frame [Archinal et al., 2009]. Let the departure hyperbolic orbit characteristics at the perigee, thus obtained be ($a_{\infty_D}, e_{\infty_D}, i_{\infty_D}, \Omega_{\infty_D}, \omega_{\infty_D}, \nu_{\infty_D} = \nu_{P_{\infty_D}} = 0$).
3) Propagate the departure hyperbolic orbit characteristics forward for a duration of t_D days by solving the Kepler equation and obtain the true anomaly at the SOI of Earth $\left(\nu_{h_{\infty D}}\right)$.
4) Obtain the state vector of the patch point at the departure SOI from the departure hyperbolic orbit characteristics and backward by including the perturbations till the perigee is reached.

   The analytical propagation is carried out using the LA technique by including the gravity perturbations of the Sun, Moon and the non-spherical Earth.

Let the duration required to reach the perigee be $t_{D_{perturbed}}$ which is different from the prefixed Earth-SOI duration $\left(t_{D_{desired}}\right)$ due to the perturbing forces. Further, the perigee altitude and inclination of the departure hyperbolic orbit are also different from the desired values. First, the difference in Earth-SOI duration is removed (step 5), followed by that of the periapsis altitude and inclination of the departure hyperbolic orbit (step 6).

5) The difference in Earth-SOI duration (t_ε) is removed using the following procedure.
   i) Compute the difference in Earth-SOI duration.

$$t_\varepsilon = t_{D_{desired}} - t_{D_{perturbed}} \tag{6.38}$$

If t_ε is less than a prefixed small threshold value, execute step (8).

ii) Otherwise, bias the Earth-SOI duration as,

$$t_{D_{biased}} = t_D + t_\varepsilon \tag{6.39}$$

and repeat the steps (2) to (5) with the updated Earth-SOI duration by setting $t_D = t_{D_{biased}}$. Note that the perigee altitude and inclination is retained as the desired values.

Let the time-biased departure hyperbolic orbit characteristics, thus obtained at the perigee, be $(a_{\infty_D}, e_{\infty_D}, i_{\infty_D}, \Omega_{\infty_D}, \omega_{\infty_D}, \nu_{P_{\infty_D}} = 0)\Big|_{time-biased}$.

6) The process that introduces bias in the periapsis altitude and inclination of the departure hyperbolic orbit at perigee is as follows.

i) Compute the perigee altitude of the time-biased departure hyperbolic orbit $\left(h_{PD_{time-biased}}\right)$.

$$h_{PD_{time-biased}} = a_{\infty D\,time-biased}\left(1 - e_{\infty D\,time-biased}\right) - R_e \tag{6.40}$$

ii) Compute the deviations in the periapsis altitude and inclination at t_0, as follows.

$$h_\varepsilon = \left(h_{P_{\infty D\,desired}} - h_{PD\,time-biased}\right) \tag{6.41}$$

$$i_\varepsilon = \left(i_{P_{\infty D\,desired}} - i_{\infty D\,time-biased}\right) \tag{6.42}$$

Now, the biased perigee altitude $\left(h_{P_{\infty D\,biased}}\right)$ and inclination $\left(i_{P_{\infty D\,biased}}\right)$ of the departure hyperbolic orbit at the SOI of Earth are,

$$h_{P_{\infty D\,biased}}\Big|_{SOI} = h_{P_{\infty D}} + h_\varepsilon \tag{6.43}$$

$$i_{P_{\infty D\,biased}}\Big|_{SOI} = i_{P_{\infty D}} + i_\varepsilon \tag{6.44}$$

These values are used as the input design parameters to generate the subsequent iterative patched conic design.

iii) Set the values of periapsis altitude and inclination of the departure hyperbolic orbit,

$$h_{p_{\infty D}} = h_{P_{\infty D}biased}\Big|_{SOI} \tag{6.45}$$

$$i_{P_{\infty D}} = i_{P_{\infty D}biased}\Big|_{SOI} \tag{6.46}$$

Determine the iterative patched conic design by repeating the steps (4) to (8) till the values of h_ε and i_ε are less than the prefixed threshold values.

The design thus obtained is the required B-ITRPC design. The B-ITRPC hyperbolic orbital elements are used to determine the TPI and POI velocity impulses. The flowchart of the B-ITRPC algorithm is given in Fig. 6.2.

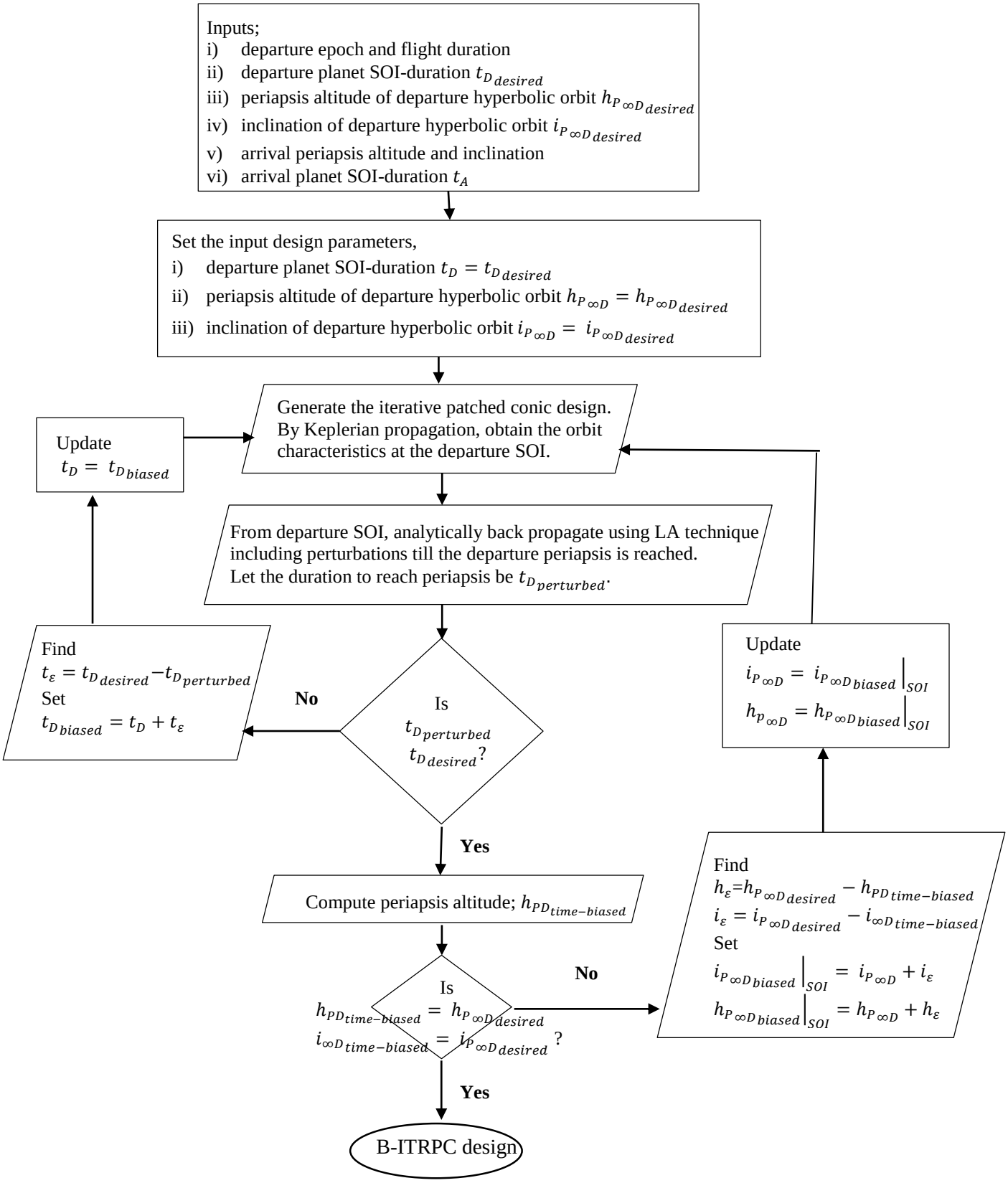

Fig.6.2. Flowchart illustrating the B-ITRPC design technique

6.6 Illustrative Results

To illustrate the proposed biased iterative patched conic (B-ITRPC) technique, the transfer trajectory design of an orbiter mission from Earth to Mars is considered. The force model included in this technique, called the B-ITRPC Force Model (BFM), includes (i) Spherical Earth, Earth J_2 to J_6, Moon and Sun for t_D days, (ii) Sun for $(t_{FD} - t_D - t_A)$ days and (iii) arrival planet for t_A days. Both type I and type II minimum energy opportunities are used for demonstration. The type I opportunity occurs on 12 May 2018 0 h TDB with a flight duration of 204 days and the type II opportunity occurs on 30 Aug 2022 0 h TDB with a flight duration of 348 days. The DPO and APO are 300 x 25,000 km and 300 km circular respectively. The DPO/APO inclinations are considered as 75 deg with respect to the planet Equator.

Table 6.2a Biased input parameters used in a typical outer loop (2018)

Iteration no.	Iteration 1	Iteration 2	Iteration 3	Iteration 4
Earth SOI-duration	3 days 0 minutes	3 days 3.38 minutes	3 days 3.37 minutes	3 days 3.24 minutes
Periapsis radius (km)	6,678.00	6,305.46	6,306.71	6,305.26
Inclination (deg)	75.0000	76.9464	76.9449	76.9447

Table 6.2b Illustration of the outer loop iterations of B-ITRPC technique (2018)

Iteration no.	Iteration 1*		Iteration 2		Iteration 3		Iteration 4	
Locations	at Perigee	at SOI	at Perigee	at SOI	at Perigee	at SOI	at Perigee	at SOI
a_{∞_D} (km)	-58193.0	-58965.6	-58105.4	-58946.1	-58105.5	-58946.1	-58105.5	-58946.1
e_{∞_D}	1.121748	1.113254	1.114918	1.106956	1.114931	1.106969	1.114931	1.106968
i_{∞_D} (deg)	73.1778	75.0000	75.0015	76.9464	75.0001	76.9449	74.9999	76.9447
Ω_{∞_D} (deg)	335.0848	333.3889	333.5513	331.7888	333.5524	331.7900	333.5526	331.7901
ω_{∞_D} (deg)	167.7805	167.3781	167.4880	167.0887	167.4892	167.0898	167.4891	167.0897
ν_{∞_D} (deg)	0.0000	151.9609	0.0000	152.6967	0.0000	152.6952	0.0000	152.6953
a_{∞_A} (km)	-4980.0	-4980.0	-4979.7	-4979.7	-4979.7	-4979.7	-4979.7	-4979.7
e_{∞_A}	1.740798	1.740798	1.740842	1.740842	1.740842	1.740842	1.740842	1.740842
i_{∞_A} (deg)	75.0000	75.0000	75.0000	75.0000	75.0000	75.0000	75.0000	75.0000
Ω_{∞_A} (deg)	68.0878	68.0878	68.0851	68.0851	68.0851	68.0851	68.0851	68.0851
ω_{∞_A} (deg)	115.2153	115.2153	115.2142	115.2142	115.2142	115.2142	115.2142	115.2142
ν_{∞_A} (deg)	0.0000	122.1109	0.0000	122.1000	0.0000	122.1002	0.0000	122.1100
1*: ITR-PC design								

The position and velocity vectors of the planets are obtained using JPL ephemeris DE405. The ITR-PC design for the Earth to Mars minimum energy opportunities are analytically refined by including the perturbations using the proposed technique.

The tolerances for the departure design parameters/ biased input parameters are as follows: Earth-SOI duration 0.1 s, perigee altitude 1 km and inclination 1E-5 deg. The outer loop is illustrated in Tables 6.2a and 6.2b. The biased input parameters that are used to generate the ITR-PC design are presented in Table 6.2a and the departure and arrival design parameters at the perigee and SOI for all the outer loop iterations are given in Table 6.2b.

Table 6.3a V-infinity vectors from B-ITRPC technique

Parameters	2018				2022			
	option 11	option 12	option 21	option 22	option 11	option 12	option 21	option 22
v_{∞_D}(km/s)	2.7828	2.7840	2.7781	2.7793	3.8794	3.8786	3.8845	3.8837
α_{∞_D}(deg)	321.65	321.67	321.52	321.54	80.39	80.3940	80.4345	80.42
δ_{∞_D}(deg)	-37.20	-37.28	-36.84	-36.92	3.46	3.50	3.28	3.32
v_{∞_A}(km/s)	2.9603	2.9599	2.9615	2.9611	2.6005	2.5996	2.6055	2.6045
α_{∞_A}(deg)	245.51	245.48	245.59	245.56	39.55	39.56	39.64	39.65
δ_{∞_A}(deg)	9.50	9.54	9.21	9.25	31.63	31.60	31.78	31.76

Table 6.3b B-ITRPC design options: 2018 opportunity

Parameters	At perigee				At SOI			
	option 11	option 12	option 21	option 22	option 11	option 12	option 21	option 22
a_{∞_D} (km)	-58105.5	-58046.3	-59433.8	-59374.1	-58946.1	-58884.6	-59186.4	-59125.5
e_{∞_D}	1.114931	1.115048	1.112362	1.112475	1.106968	1.107070	1.112584	1.112699
i_{∞_D} (deg)	75.0000	75.0000	75.0000	75.0000	76.9447	76.9430	77.2952	77.2946
Ω_{∞_D} (deg)	333.5526	333.6102	130.1202	130.1091	331.7901	331.8443	131.7993	131.7932
ω_{∞_D}(deg)	167.4891	167.4166	64.5445	64.6418	167.0897	167.0168	63.9902	64.0863
ν_{∞_D}(deg)	0.0000	0.0000	0.0000	0.0000	152.6953	152.6858	152.0303	152.0198
a_{∞_A}(km)	-4979.7	-4981.0	-4975.4	-4976.8	-4979.7	-4981.0	-4975.4	-4976.8
e_{∞_A}	1.740842	1.740644	1.741483	1.741277	1.740842	1.740644	1.741483	1.741277
i_{∞_A} (deg)	75.0000	75.0000	75.0000	75.0000	75.0000	75.0000	75.0000	75.0000
Ω_{∞_A}(deg)	68.0851	242.9014	68.0902	243.0631	68.0851	242.9014	68.0902	243.0631
ω_{∞_A}(deg)	115.2142	314.9445	115.4944	314.6351	115.2142	314.9445	115.4944	314.6351

For 2018 and 2022 opportunities, the V-infinity vectors at the departure and arrival phases are given in Table 6.3a. The four distinct design options of the trajectory for 2018 and 2022 opportunities are given in Tables 6.3b and 6.3c. The designs are generated for Earth-SOI and Mars-SOI durations of 3 and 2 days respectively. Note that, the B-ITRPC design at the perigee and departure SOI are different for the departure phase and same for the arrival phase. This is because the effect of perturbations are considered for the departure phase only. It is well known that the orbital elements undergo changes due to perturbations. For example, in design option 11 of the 2018 opportunity, the inclination of the departure hyperbolic orbit at perigee is 75 deg and that at SOI is 76.9447 deg. The difference is due to the perturbing effects of the non-spherical Earth and the lunisolar effects within the Earth SOI. The arrival phase is considered Keplerian and so the orbital characteristics does not change within the Mars SOI.

Table 6.3c B-ITRPC design options: 2022 opportunity

Parameters	At perigee				At SOI			
	option 11	option 12	option 21	option 22	option 11	option 12	option 21	option 22
a_{∞_D} (km)	-27851.1	-27863.5	-27737.1	-27749.1	-27866.0	-27878.2	-27787.6	-27799.8
e_{∞_D}	1.239779	1.239672	1.240765	1.240661	1.244053	1.243933	1.233694	1.233605
i_{∞_D} (deg)	75.0000	75.0000	75.0000	75.0000	76.0000	75.9994	75.5598	75.5601
Ω_{∞_D} (deg)	79.5315	79.5162	261.3631	261.3689	79.5344	79.5199	261.2806	261.2860
ω_{∞_D}(deg)	219.8641	219.8982	32.9624	32.9153	220.0849	220.1180	32.4721	32.4261
ν_{∞_D}(deg)	0.0000	0.0000	0.0000	0.0000	142.4054	142.4125	143.0906	143.0959
a_{∞_A}(km)	-6509.4	-6514.5	-6483.6	-6488.6	-6509.4	-6514.5	-6483.6	-6488.6
e_{∞_A}	1.566745	1.566303	1.569000	1.568558	1.566745	1.566303	1.569000	1.568558
i_{∞_A} (deg)	75.0000	75.0000	75.0000	75.0000	75.0000	75.0000	75.0000	75.0000
Ω_{∞_A}(deg)	229.0592	30.0705	229.2085	30.1057	229.0592	30.0705	229.2085	30.1057
ω_{∞_A}(deg)	96.7659	342.5300	96.5381	342.6216	96.7659	342.5300	96.5381	342.6216

For comparison, the B-ITRPC, ITR-PC and the numerical designs that are generated under the BFM force model for the design option 11 are shown in Table 6.4a. It can be noted that the deviations in the design parameters between the B-ITRPC design and the numerical design are small compared to that between the ITR-PC and numerical designs. Clearly, the B-ITRPC design is close to the numerical design. The computation time required for the numerical refinement of the ITR-PC and B-ITRPC designs (option 11) under the BFM force model are given in Table 6.4b. The B-ITRPC design takes very

less computation time (5 s for 2018 design, 3 s for 2022 design) compared to the ITR-PC design. Also, numerical refinement under a realistic force model A is attempted. The force model A includes; (i) departure phase/non-spherical Earth, Sun and Moon for a fixed Earth-SOI duration, (ii) cruise phase/all bodies including Earth in the heliocentric phase, and (iii) arrival phase/Mars within the Mars-SOI duration. The computation time for numerical refinement of 2018 designs are 246 s (initial guess: ITR-PC design option 11) and 32 s (initial guess: B-ITRPC design option 11). The difference in computation time is significant considering that we need to repeat similar process for several cases in a design analysis. The numerical refinement takes very less computation time with the B-ITRPC design because it is very close to the numerical design. Also, if the ITR-PC design is used as the initial guess, additional information on the arrival angles must be given as constraints in the numerical refinement process as it may otherwise converge to any one of the similar departure design options. ***The use of B-ITRPC design as the initial guess do not require any such additional information. So, it is very clear that the B-ITRPC design serves as a good initial guess for numerical refinement.***

Table 6.4a Comparison of ITR-PC, B-ITRPC and numerical designs (option 11)

(i_{∞_D} =75 deg; i_{∞_A}=75 deg)

Parameters	2018			2022		
	ITR-PC	B-ITRPC	Numerical	ITR-PC	B-ITRPC	Numerical
a_{∞_D} (km)	-58965.7	-58105.5	-58104.7	-27866.3	-27851.1	-27852.1
e_{∞_D}	1.113254	1.114931	1.114934	1.239648	1.239779	1.239761
Ω_{∞_D} (deg)	333.3889	333.5526	333.5557	79.4710	79.5315	79.5325
ω_{∞_D}(deg)	167.3782	167.4891	167.4882	219.8234	219.8641	219.8643
a_{∞_A}(km)	-4980.0	-4979.7	-4979.7	-6509.3	-6509.4	-6509.4
e_{∞_A}	1.742402	1.740842	1.742243	1.566754	1.566745	1.566732
Ω_{∞_A}(deg)	68.0878	68.0851	68.0846	229.0607	229.0592	229.0582
ω_{∞_A}(deg)	115.1783	115.2142	115.1809	96.7644	96.7659	96.7643

Table 6.4b Computation time for numerical refinement under force model BFM

Design option 11	Computation time (s)		TCM (m/s)
	2018	2022	2018
ITR-PC	125	110	18
B-ITRPC	5	3	<1

Table 6.5a Achievable accuracies (2018) on numerical propagation under force model BFM (with perturbations)

Parameters		Arrival CAA (km)	Arrival inclination (deg)	T_P (UTC)
Desired values		300	75.00	02 Dec 2018 00:00:00
ITR-PC design Options	option 11	462,975	21.52	04 Dec 2018 02:50:41
	option 12	466,863	22.89	04 Dec 2018 02:43:09
	option 21	207,543	146.33	30 Nov 2018 12:37:16
	option 22	202,089	149.48	30 Nov 2018 12:24:57
B-ITRPC design Options	option 11	543	75.41	01 Dec 2018 23:51:45
	option 12	51	74.18	01 Dec 2018 23:49:42
	option 21	605	74.32	01 Dec 2018 23:47:52
	option 22	45	73.95	01 Dec 2018 23:45:34

Table 6.5b Achievable accuracies (2022) on numerical propagation under force model BFM (with perturbations)

Parameters		Arrival CAA (km)	Arrival inclination (deg)	T_P (UTC)
Desired values		300	75.00	12 Aug 2023 00:00:00
B-ITRPC design options	option 11	-161	74.70	11 Aug 2023 23:49:54
	option 12	798	77.51	11 Aug 2023 23:53:17
	option 21	-165	76.11	11 Aug 2023 23:53:26
	option 22	525	76.66	11 Aug 2023 23:57:31

Table 6.6 Total velocity impulse requirement of B-ITRPC design options

Design options	2018			2022		
	TPI (m/s)	POI (m/s)	Total (m/s)	TPI (m/s)	POI (m/s)	Total (m/s)
option 11	1314.3	2233.5	3547.9	1641.2	2051.5	3692.7
option 12	1314.7	2233.3	3548.1	1640.9	2051.0	3692.0
option 21	1307.56	2234.25	3541.82	1643.8	2053.9	3697.7
option 22	1307.86	2234.04	3541.91	1643.5	2053.4	3696.9

The achievable accuracies on numerical propagation of the ITR-PC and B-ITRPC designs (2018 opportunity) under the force model BFM are given in Table 6.5a. The ITR-PC designs result in large deviations in the achieved arrival parameters. For example, for 2018 design option 11, the achieved CAA is 462,975 km, inclination is 21.52 deg and the time of periapsis (T_P) deviates by about 2 days. These large deviations in the achieved target parameters are because of not accounting the perturbations in the design process.

The numerical propagation of the B-ITRPC designs results in achieved target parameters with reasonably good accuracies For example, for 2018 design option 11, the achieved CAA is 543 km, inclination is 75.41 deg the time of periapsis deviates by about 8 minutes only. For the other design options also, the deviations in achieved target parameters are: on CAA, $\pm$ 250 km; on APO inclination, $\pm$1 deg, on T_P, 9 to 15 minutes. Note that, the B-ITRPC design has significantly improved the achievable accuracies as compared to that of the ITR-PC design. The achievable accuracies on numerical propagation of the B-ITRPC designs of 2022 opportunity under the force model BFM are given in Table 6.5b. The deviations in achieved target parameters are more: on CAA, $\pm$ 225 km to $\pm$ 500 km; on APO inclination, $\pm$ 0.3 deg to $\pm$ 2.5 deg; on T_P , 7 to 11 minutes. The larger deviations are due to the larger flight duration for the type II transfer.

The total velocity impulse required for the interplanetary transfer obtained using the B-ITRPC technique is given in Table 6.6. There is only marginal increase in the total velocity impulse i.e. 1 to 2 m/s, between the ITR-PC and B-ITRPC design options (cf. Tables 5.7 and 6.6). ***Note that the difference in total velocity impulse between the four B-ITRPC design options vary from 1 to 7 m/s.***

Table 6.7 Influence of perturbations in arrival phase on achievable accuracies (2022)

Parameters	BFM force model	BFM + perturbations within Mars-SOI
CAA (km)	984.22	990.43
APO inclination (deg)	84.68	84.98
T_P (UTC)	13 Aug 2023 00:03:55	13 Aug 2023 00:03:46

To illustrate the effect of inclusion of perturbations within the SOI of the arrival phase, the B-ITRPC design 11 (2022 opportunity) is numerically propagated under two force models, (i) BFM, and (ii) BFM + perturbations of Sun and Earth within the SOI of Mars. The achieved accuracies are presented in Table 6.7. It can be seen that the achieved arrival parameters do not vary significantly. ***This brings out the fact that the inclusion of perturbations within the arrival SOI does not contribute much to the trajectory design.***

The computation time required to generate the ITR-PC and B-ITRPC designs for 2190 sample cases, by an Intel core i5 2.5GHz processor, are as follows: ITR-PC designs, 592 ms [Parvathi and Ramanan, 2017] and B-ITRPC designs, 2254 ms. The B-ITRPC

technique requires more computation time, however it results in significant improvement in the achievable accuracies of the arrival target parameters.

6.7 Impact of SOI duration

The implication of SOI durations on the trajectory design is studied by varying the Earth and Mars SOI durations. Table 6.8a presents the B-ITRPC design option 11 for different Earth-SOI durations (2018 opportunity). The achieved target/arrival parameters on numerical propagation of these designs under the force model A are presented in Table 6.8b. Note that, the accuracy of the achieved target parameters improves as the Earth-SOI duration is increased. The B-ITRPC design with an Earth-SOI duration of 3 days results in the achieved target parameters with maximum accuracy. However, on increasing the SOI-duration further, the deviations of the target parameters increases. This is because the linearization of the equations of motion for larger SOI duration does not represent the non-linear dynamics well.

Table 6.8a B-ITRPC design option 11 (2018 opportunity) for different Earth-SOI durations (Mars-SOI duration = 2 days)

Parameters	B-ITRPC design			
	t_D = 1 days	t_D = 2 days	t_D = 3 days	t_D = 4 days
$a_{\infty D}$(km)	-77710.8	-62223.5	-58105.5	-56181.2
$e_{\infty D}$	1.08593	1.107324	1.114931	1.118867
$i_{\infty D}$(deg)	74.9999	75.0000	74.9999	74.9999
$\Omega_{\infty D}$(deg)	333.3966	333.4853	333.5526	333.6053
$\omega_{\infty D}$(deg)	164.7520	166.7829	167.4891	167.8477
$a_{\infty A}$(km)	-4979.4	-4979.6	-4979.7	-4979.7
$e_{\infty A}$	1.740877	1.740854	1.740842	1.7408
$i_{\infty A}$(deg)	75.0000	75.0000	75.0000	75.0000
$\Omega_{\infty A}$(deg)	68.1169	68.0977	68.0851	68.0756
$\omega_{\infty A}$(deg)	115.2767	115.2388	115.2142	115.1958
TPI	1237.1	1294.1	1314.3	1324.8
POI	2233.6	2233.6	2233.5	2233.5
Total (m/s)	3470.7	3527.7	3547.9	3558.4

The perturbing effect of the Moon and the Sun cannot be linearized beyond 3 days as their effect is significantly high in this region. Hence, from the computation point of view, the linear approximation technique imposes a restriction on the maximum Earth-SOI duration. Moreover, an Earth-SOI duration of 8 days results in a negative perigee altitude on biasing the departure design parameters, thereby resulting in infeasible solution. So, the maximum Earth-SOI duration that can be considered for B-ITRPC technique is 7

days***. Note that, as the Earth-SOI duration is increased, the total velocity impulse required for the transfer also increases.*** For all these analysis, the Mars-SOI duration is fixed as 2 days. Hence, for best results, the Earth-SOI duration considered in the current research is 3 days.

Table 6.8c presents the B-ITRPC design option 11 for different Mars-SOI durations (2018 opportunity). The achieved target/arrival parameters upon numerical propagation of these designs under the force model A is presented in Table 6.8d. It can be seen that there is no significant improvement in the achieved target parameters on increasing the Mars-SOI duration.

Table 6.8b Achieved accuracies on numerical propagation under force model A

Parameters	Desired values	t_D = 1 day	t_D = 2 days	t_D = 3 days	t_D = 4 days
CAA (km)	300	2,27,447	905	560	1333
APO inclination (deg)	75.00	19.63	90.49	75.41	93.29
T_P (UTC)	2 Dec 2018 00:00:00	3 Dec 2018 07:09:03	1 Dec 2018 22:04:09	01 Dec 2018 23:51:45	1 Dec 2018 21:52:44

Table 6.8c B-ITRPC design option 11 (2018 opportunity) for different Mars-SOI durations (Earth-SOI duration = 3 days)

Parameters	B-ITRPC design		
	t_A = 1 days	t_A = 2 days	t_A =3 days
$a_{\infty D}$(km)	-58105.3	-58105.5	-58105.6
$e_{\infty D}$	1.114931	1.11493	1.114930
$i_{\infty D}$(deg)	74.9999	74.9999	74.9999
$\Omega_{\infty D}$(deg)	333.5489	333.5526	333.5547
$\omega_{\infty D}$(deg)	167.4875	167.4891	167.4900
$a_{\infty A}$(km)	-5071.1	-4979.7	-4951.5
$e_{\infty A}$	1.727491	1.74084	1.745055
$i_{\infty A}$(deg)	75.00000	75.0000	75.00000
$\Omega_{\infty A}$(deg)	68.0910	68.0851	68.0802
$\omega_{\infty A}$(deg)	115.5128	115.2142	115.1210
TPI	1314.3	1314.3	1314.3
POI	2219.8	2233.5	2237.9
Total (m/s)	3534.2	3547.9	3552.3

Table 6.8d Achieved accuracies on numerical propagation under force model A

Parameters	Desired values	t_A = 1 day	t_A = 2 days	t_A =3 days
CAA (km)	300	520	560	570
APO inclination (deg)	75.0000	75.32	75.41	75.80
T_P (UTC)	2 Dec 2018 00:00:00	01 Dec 2018 22:51:45	01 Dec 2018 23:51:45	01 Dec 2018 23:52:45

6.8 Design Analysis

The FORTRAN 95 code developed based on the B-ITRPC design technique is used as a quick mission design and analysis tool for orbiter missions. Because the B-ITRPC design is very close to the numerical design, the inferences drawn from the analysis will also be applicable to the numerical designs. In the previous chapter, note that ITR-PC technique is used for design analysis. Therein, the main focus is the analysis of four design options for an opportunity. Here, a large number of cases have been analyzed for the design option 11 to examine the reliability and efficiency of this design technique. The results indicate that this design technique has a good balance between the accuracy and computational speed. ***Similar analysis by numerical technique will require enormous computation time and effort. To demonstrate, a type-II 2022 minimum energy opportunity has been considered. The advantage of this opportunity is the low value of the declination of V-infinity vector which allows wide range of the parking orbit inclination for analysis purpose.*** The DPO and APO are 300 x 25,000 km and 300 km circular respectively. The DPO/APO inclinations are considered as 45 deg and 90 deg respectively with respect to the planet Equator and Equinox/IAU vector of J2000 respectively. The Earth and Mars SOI durations are fixed as 3 and 2 days respectively. Of the four design options, option 11 is used for analysis purposes. The observations made for option 1-1 is valid for other options too.

6.8.1 Different departure epochs

The departure epoch is varied from 59,806 MJD (15 Aug 2022) to 59,836 MJD (14 Sep 2022). For different departure epochs, the departure and arrival hyperbolic/parking orbit angles (RAAN and AOP) are given in Figs. 6.3 and 6.4. For the range of departure epochs considered, the departure angles vary by about 6 and 12 deg respectively. The arrival angles vary by about 8 and 6 deg respectively. Note that the variation of arrival angles is

nearly linear. Figure 6.5 depicts the differences in the departure angles (RAAN and AOP) obtained from the ITR PC and B-ITRPC techniques. The maximum absolute difference in the departure RAAN is about 0.25 deg and departure AOP is 0.18 deg. These differences are substantial considering that the arrival parameters are highly sensitive to the departure angles. The differences in the arrival angles (cf. Fig.6.6) are marginal.

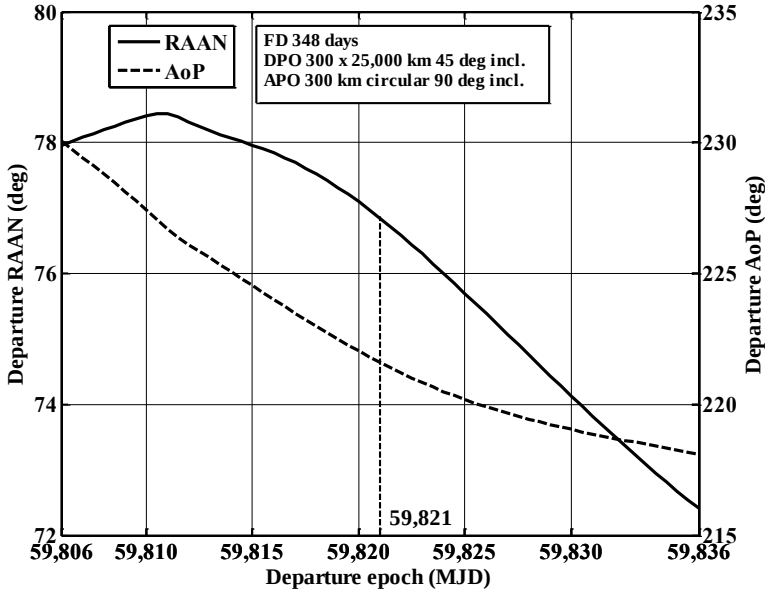

Fig. 6.3. Variation of departure/TPI angles (B-ITRPC technique) for different departure epochs.

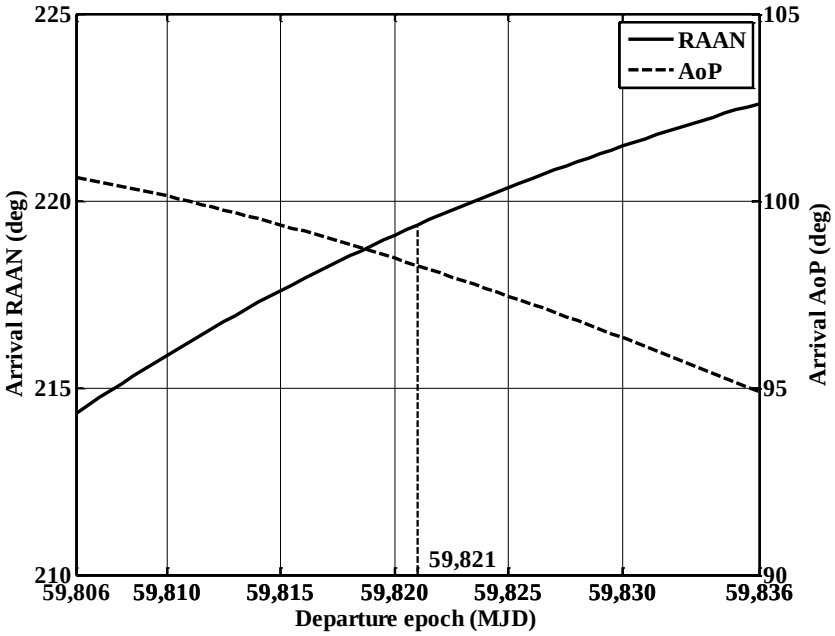

Fig. 6.4. Variation of arrival/POI angles (B-ITRPC technique) for different departure epochs.

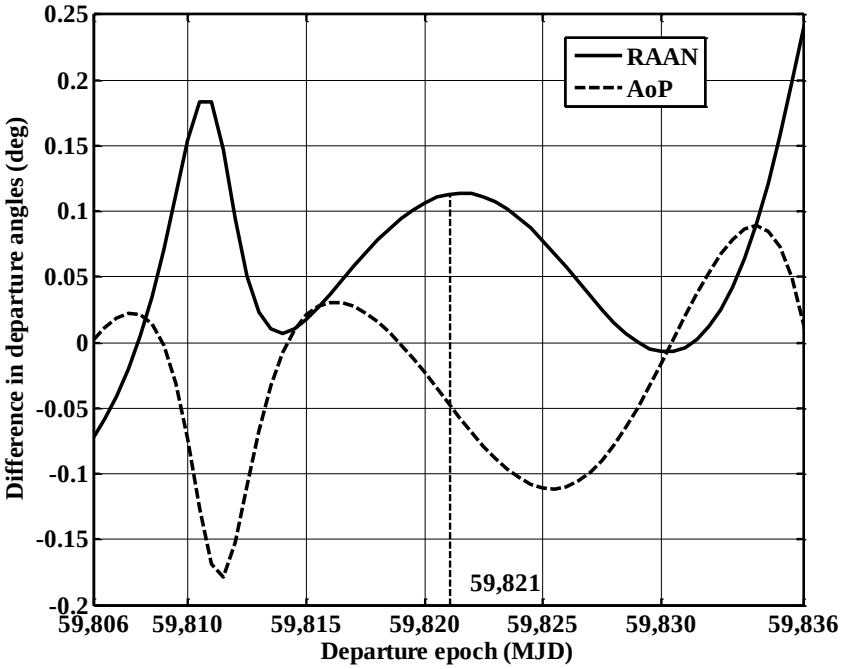

Fig. 6.5. Differences [B ITRPC-ITR PC] in departure angles for different departure epochs.

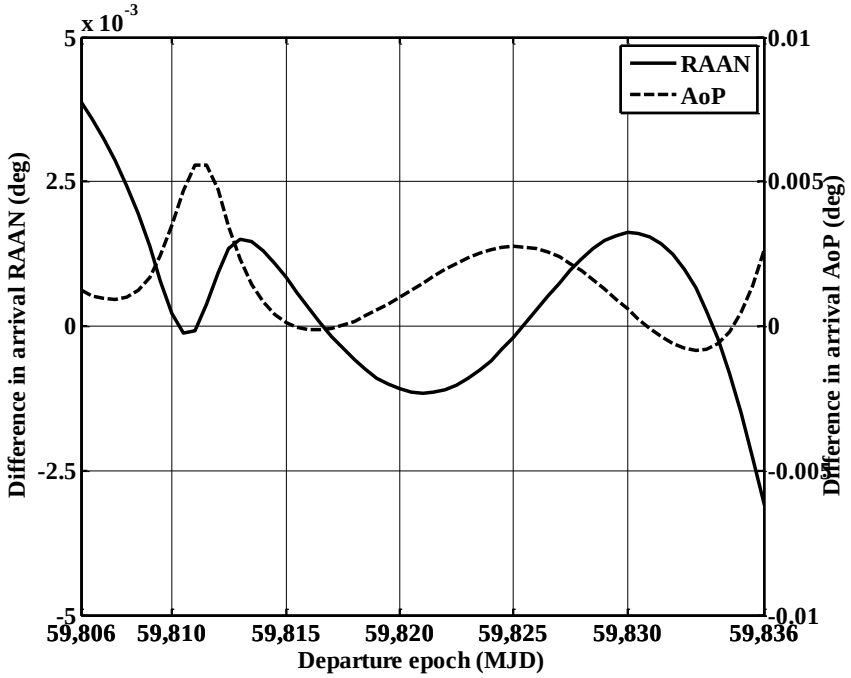

Fig. 6.6. Differences [B ITRPC-ITR PC] in arrival angles for different departure epochs.

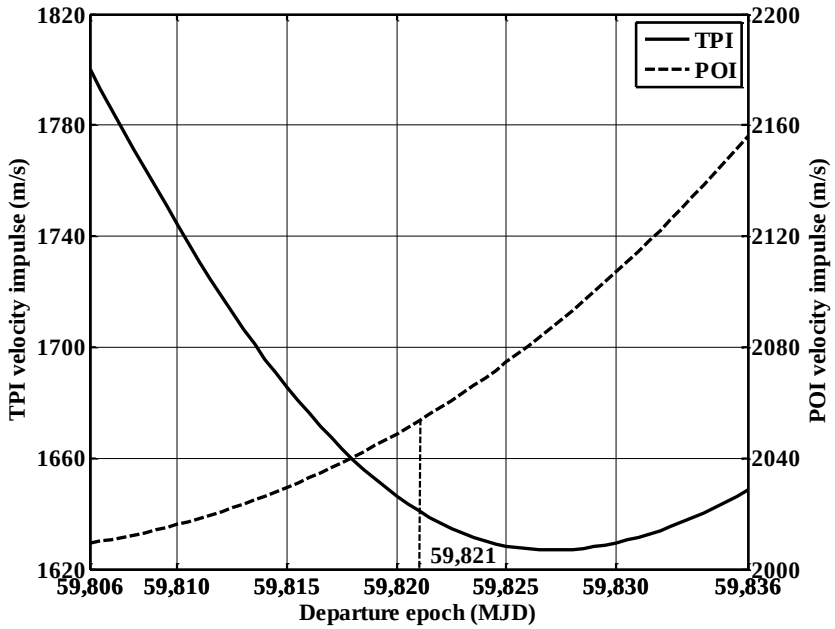

Fig. 6.7. Variation of TPI and POI velocity impulses (B-ITRPC technique) for different departure epochs.

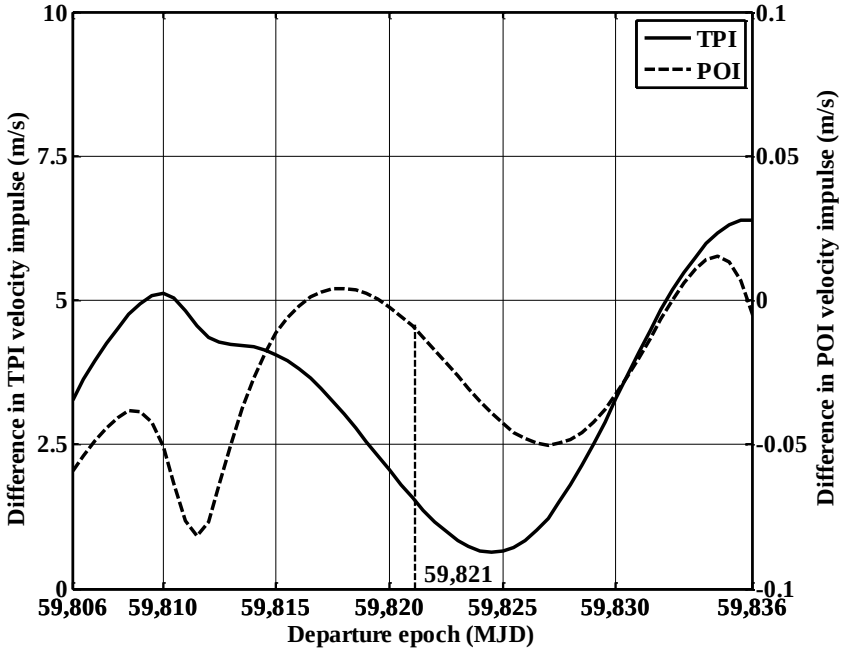

Fig. 6.8. Differences [B ITRPC-ITR PC] in TPI and POI velocity impulses for different departure epochs.

Figs. 6.7 and 6.8 give the details about the velocity impulses. The transplanetary injection (TPI) velocity impulse vary from 1630 to 1800 m/s. The parking orbit insertion (POI) velocity impulse varies from 2010 to 2160 m/s for this range of departure epochs. The maximum difference in TPI velocity impulse between the ITR PC and B-ITRPC

designs is about 6 m/s. The difference in the POI velocity impulse between the designs is negligible.

6.8.2 Different flight durations

The flight duration is varied from 320 days to 420 days. The departure epoch is 30 August 2022 0 hours TDB (59,821 MJD). The minimum energy opportunity occurs for a flight duration of 348 days. For different flight durations, the variation of departure and arrival hyperbolic/parking orbit angles (RAAN and AOP) are given in Figs. 6.9 and 6.10 respectively. There is a wide variation in the departure angles. The departure RAAN varies by about 15 deg and the departure AOP varies by about 50 deg. The arrival RAAN and AoP vary by about 14 deg and 19 deg respectively. Figure 6.11 depicts the differences in the departure angles obtained from the ITR PC and B-ITR PC design techniques. The maximum absolute difference in the departure RAAN is about 0.14 deg and departure AOP is 0.06 deg. The differences in arrival angles (c.f. Fig.6.12) are negligible. There is a large variation (1620 to 1790 m/s) in the TPI velocity impulse (c.f. Fig.6.13). The POI velocity impulse varies from 2050 to 2600 m/s for different flight durations and this is shown in Fig.6.13. The difference in the TPI and POI velocity impulses between the designs obtained from the ITR PC and B-ITRPC techniques are marginal and shown in Fig.6.14. Although the velocity impulses are same for both the designs, the direction of the velocity impulses are different.

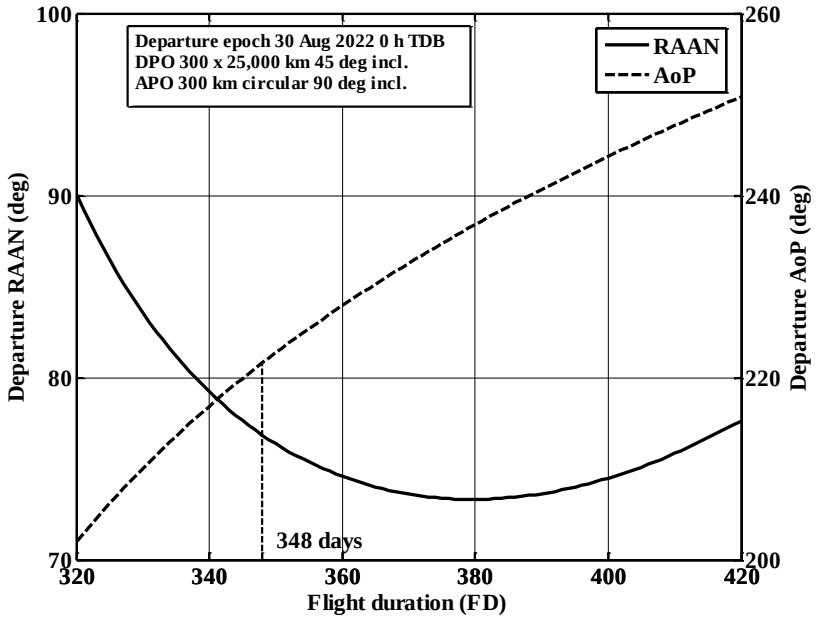

Fig. 6.9. Variation of departure/TPI angles (B-ITRPC technique) for different flight durations.

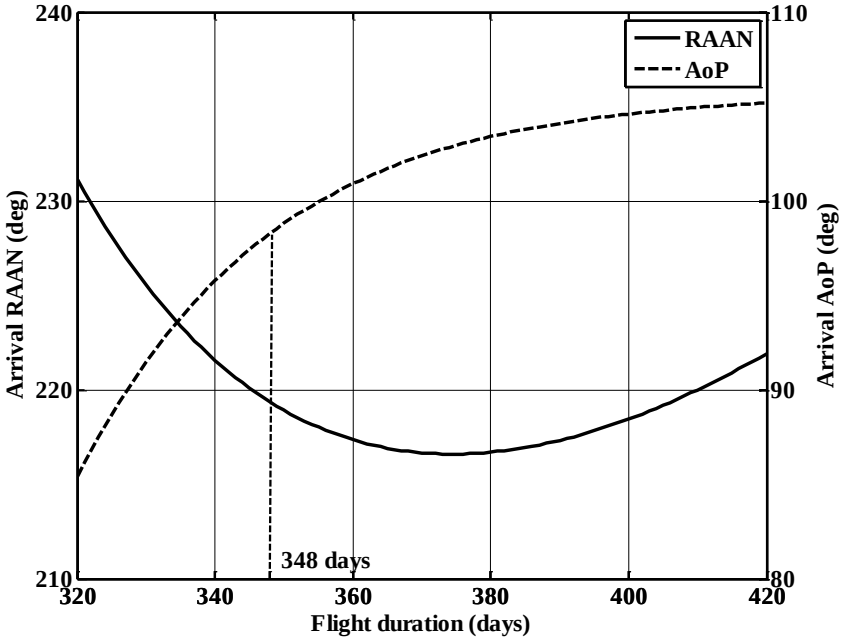

Fig. 6.10. Variation of arrival/POI angles (B-ITRPC technique) for different flight durations.

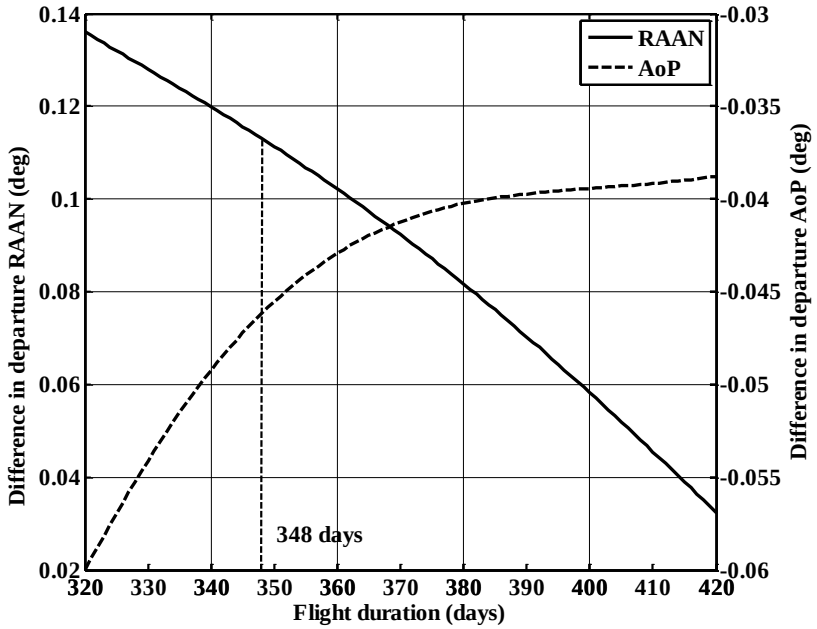

Fig. 6.11. Differences [B ITRPC- ITR PC] in departure angles for different flight durations.

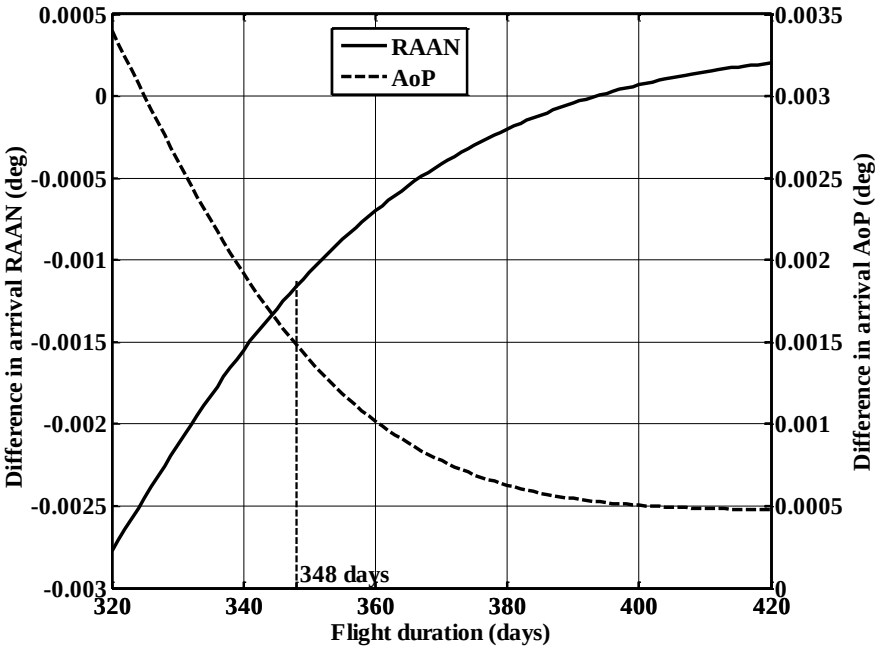

Fig. 6.12. Differences [B ITRPC- ITR PC] in arrival angles for different flight durations.

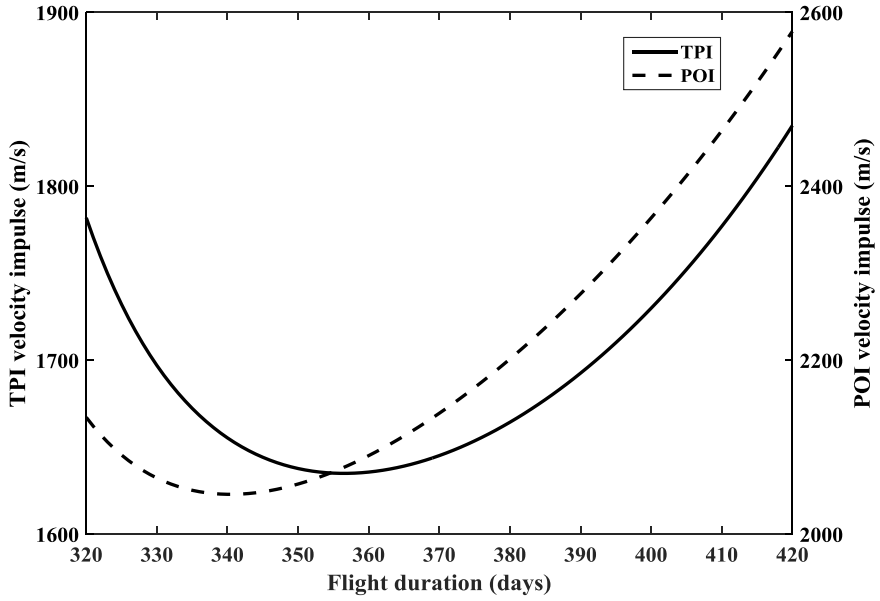

Fig. 6.13. Variation of TPI and POI velocity impulses (B-ITRPC technique) for different flight durations.

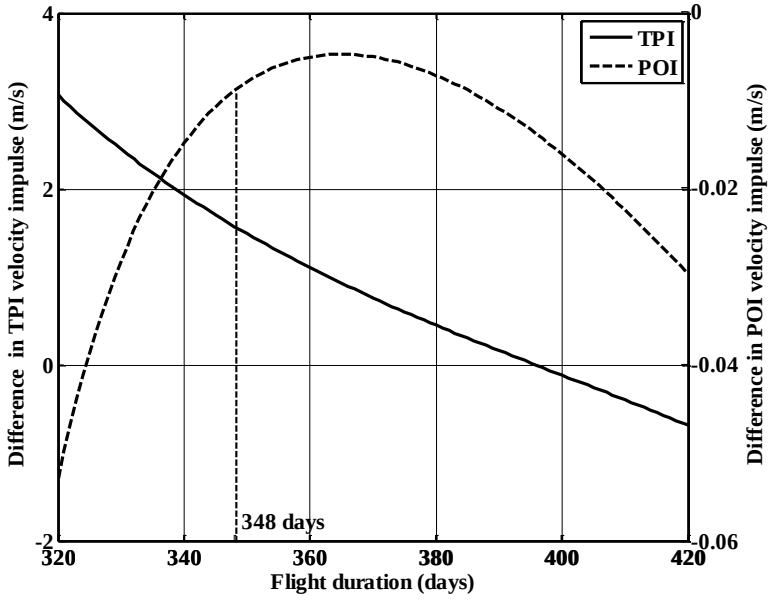

Fig. 6.14. Differences [B ITRPC-ITR PC] in TPI and POI velocity impulses for different flight durations.

6.8.3 Different inclinations of DPO/departure hyperbolic orbit

The departure parking orbit/hyperbolic orbit inclination is varied from 5 deg to 175 deg. This range of inclinations is chosen to satisfy the condition: $i_{\infty_D} \geq \delta_{\infty_D}$. Figure 6.15 gives the variation of TPI and POI velocity impulses with the DPO inclination. The TPI velocity impulse vary from 1640 to 1645 m/s, and the POI velocity impulse vary from 2053 to 2055 m/s. The TPI velocity impulse variation of about 5 m/s is due to the non-spherical gravity effect of Earth. In other words, if non-spherical Earth is ignored, the variation in TPI velocity impulse will be less than 1 m/s. Figure 6.16 depicts the difference in the TPI and POI velocity impulses between the ITR-PC and B-ITRPC designs. The TPI velocity impulse has a maximum difference of about 3.2 m/s for a posigrade DPO of inclination 10 deg and retrograde DPO of inclination 170 deg. For a DPO inclination of 90 deg, the effect of non-spherical Earth is minimum. The difference in POI velocity impulse between the designs is marginal. Figure 6.17 gives the variation of departure angles with DPO inclination. The variation of departure RAAN is anti-symmetric about the DPO inclination of 90 deg. The departure AoP varies from 220 deg to 265 deg. The variation of AoP is symmetric about the DPO inclination of 90 deg. That means, for any departure AoP, there are two possible DPO inclinations. For inclinations less than 20 deg and greater than 160 deg, the change in departure angles is large. It is well known that any launch error in DPO inclination will result in large trajectory correction maneuvers.

The variation of arrival angles with DPO inclination (cf. Fig.6.18) is marginal. Figures 6.19 and 6.20 show the differences in departure and arrival angles respectively between the ITR-PC and B-ITRPC designs.

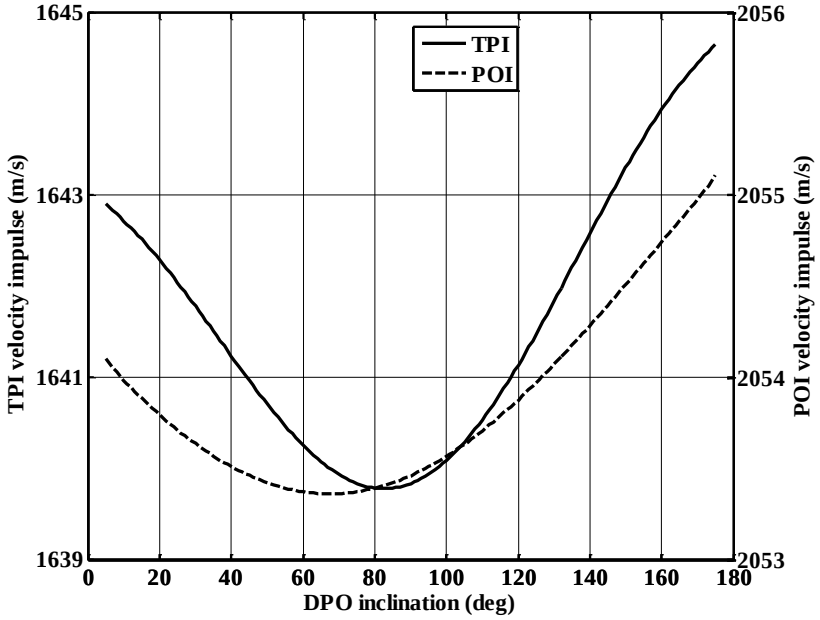

Fig. 6.15. Variation of TPI and POI velocity impulses (B-ITRPC technique) for different DPO inclinations.

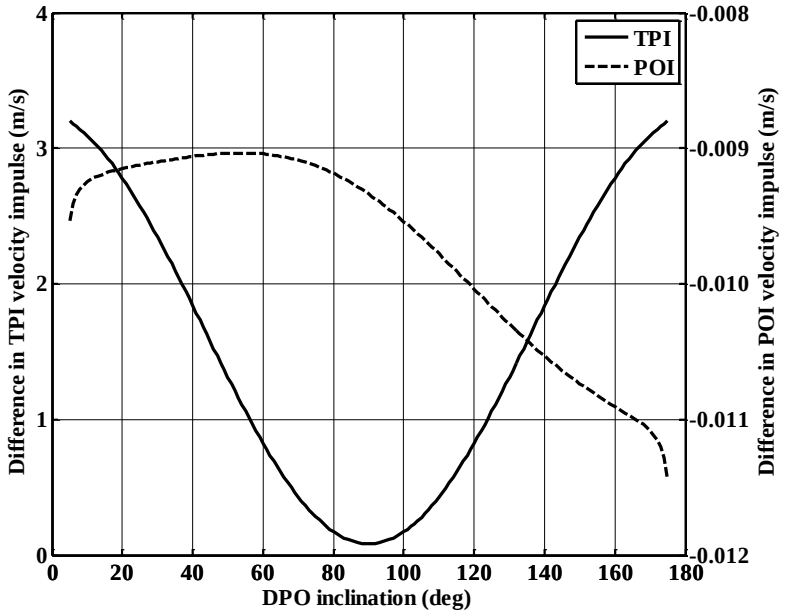

Fig. 6.16. Differences [B ITRPC-ITR PC] in TPI and POI velocity impulses for different DPO inclinations.

The differences in the departure angles between the designs is due to the non-spherical earth because it was found that the changes in the departure angles due to the Sun and the

Moon balance each other for the 2022 opportunity. It can be seen that the differences are minimum for polar DPOs and very large for equatorial DPOs.

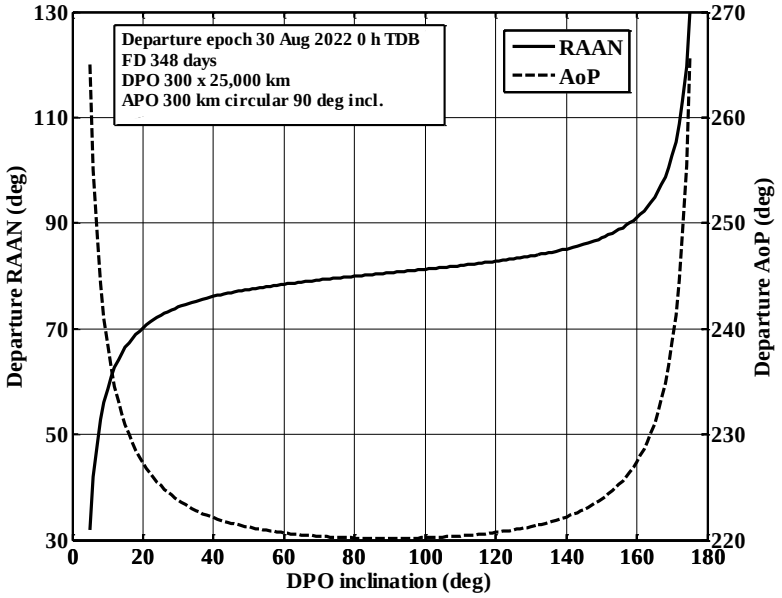

Fig. 6.17. Variation of departure/TPI angles for different DPO inclinations.

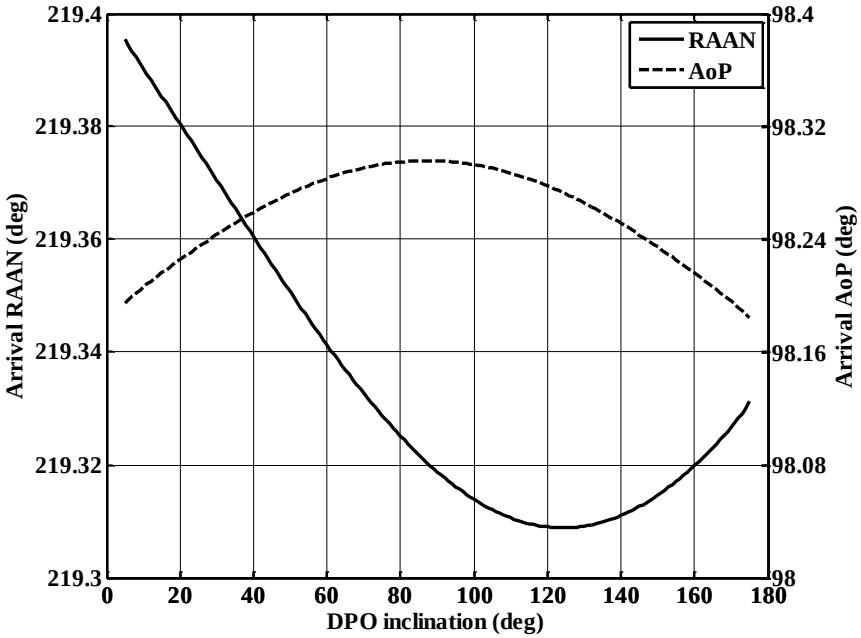

Fig. 6.18. Variation of arrival/POI angles (B-ITRPC technique) for different DPO inclinations.

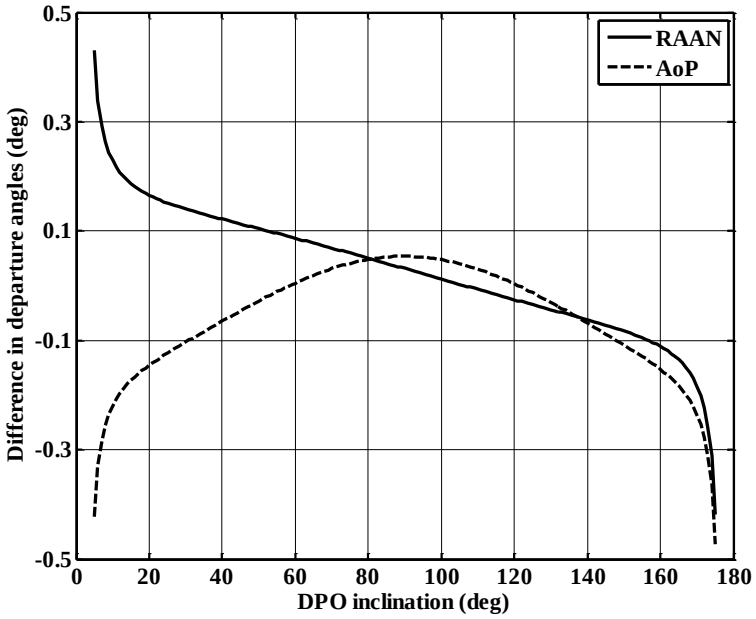

Fig. 6.19. Differences [B ITRPC-ITR PC] in departure angles for different DPO inclinations.

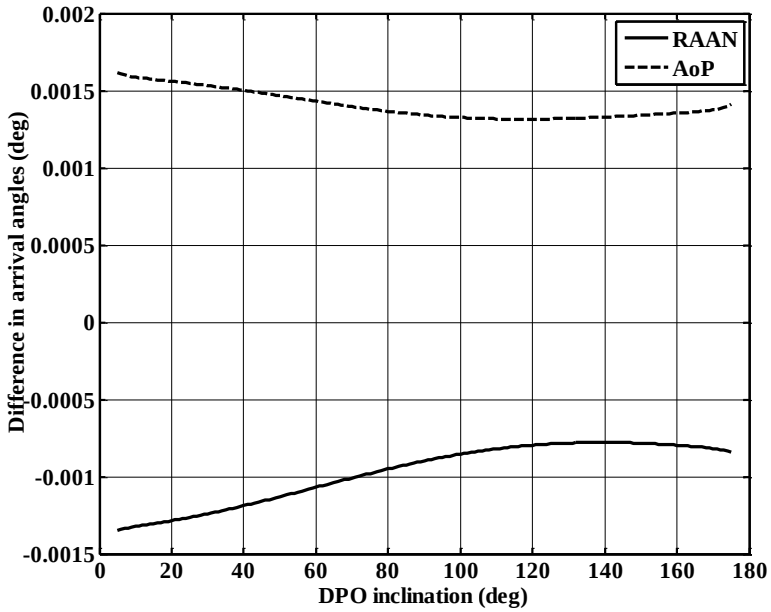

Fig. 6.20. Differences [B ITRPC-ITR PC] in arrival angles for different DPO inclinations.

6.8.4 Different periapsis altitudes of DPO/departure hyperbolic orbit

The DPO periapsis altitude is varied from 100 to 1000 km. The variation of departure and arrival angles for different DPO periapsis altitude are given in Figs. 6.21 and 6.22 respectively. The departure RAAN has marginal variation while the departure AoP has a variation of about 2 deg for this range of DPO periapsis altitudes. The differences in

departure and arrival angles between the ITR-PC and B-ITRPC designs are given in Figs. 6.23 and 6.24 respectively. While the maximum difference in departure angles is about 0.12 and 0.067 deg respectively, the arrival angles differ marginally. Figure 6.25 shows that the TPI velocity impulse vary by about 80 m/s for the whole range of DPO periapsis altitudes. The TPI requirement increases for large values of DPO periapsis altitude. The POI velocity impulse varies marginally. Figure 6.26 shows that the difference in TPI velocity impulse between the ITR-PC and B-ITRPC designs is less than 1 m/s while the difference in POI velocity impulse is negligible.

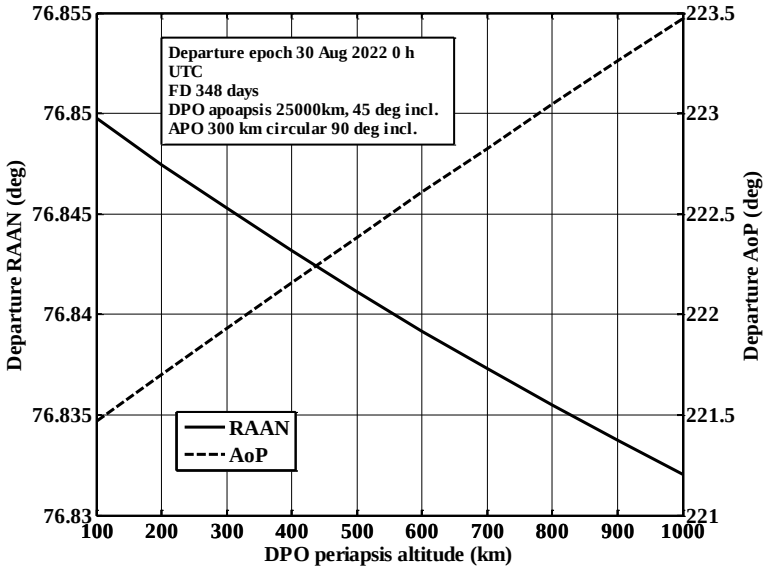

Fig. 6.21. Variation of departure/TPI angles (B-ITRPC technique) for different DPO periapsis altitudes.

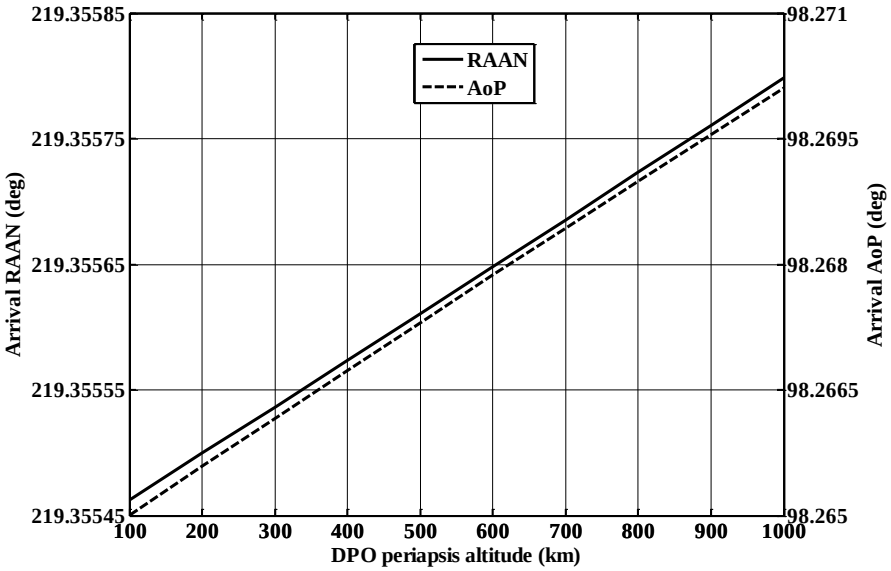

Fig. 6.22. Variation of arrival/POI angles (B-ITRPC technique) for different DPO periapsis altitudes.

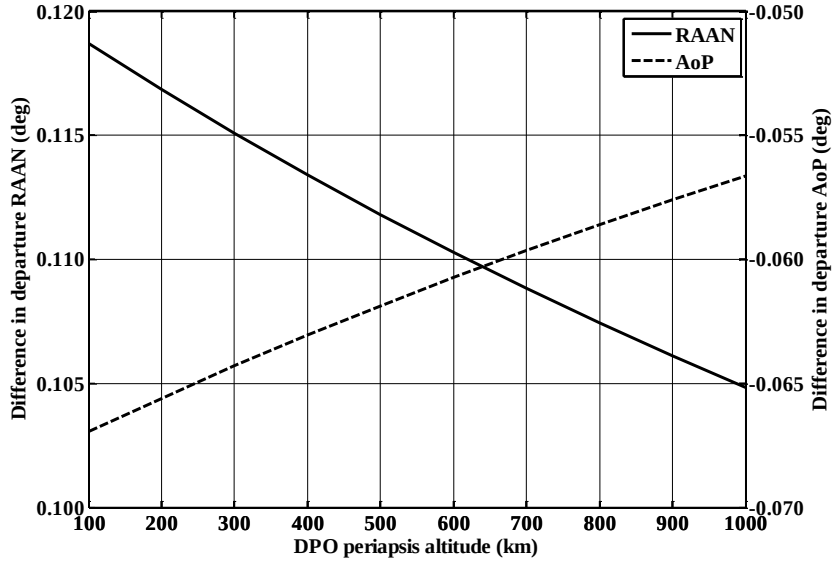

Fig. 6.23. Differences [B ITRPC-ITR PC] in departure angles for different DPO periapsis altitudes.

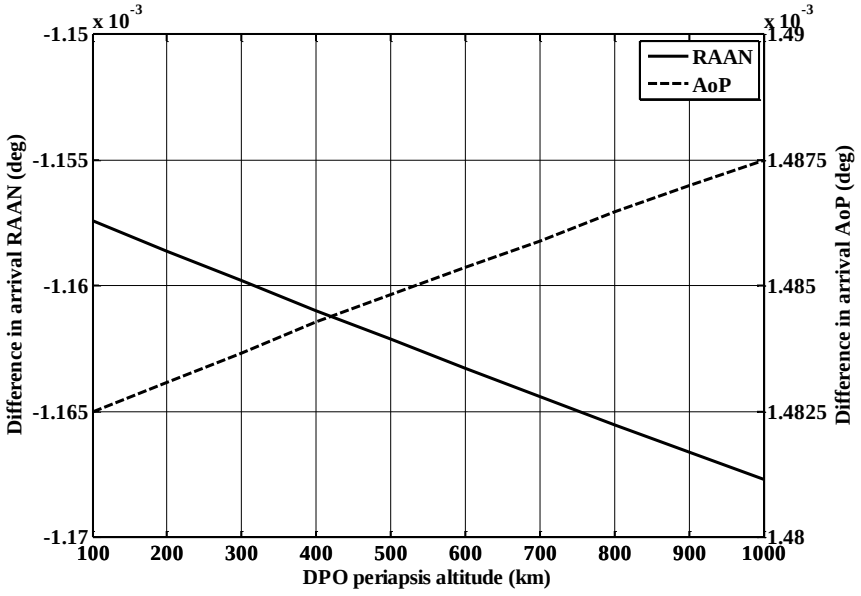

Fig. 6.24. Differences [B ITRPC-ITR PC] in arrival angles for different DPO periapsis altitudes.

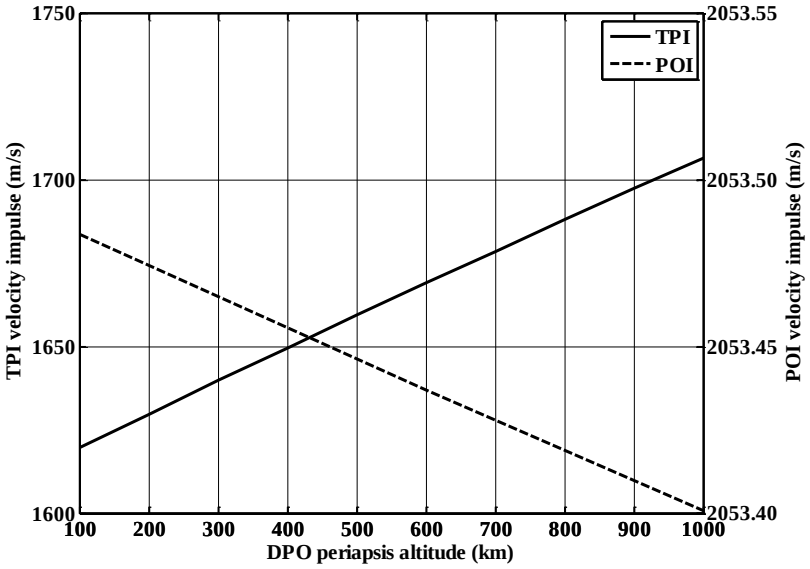

Fig. 6.25. Variation of TPI and POI velocity impulses (B-ITRPC technique) for different DPO periapsis altitudes.

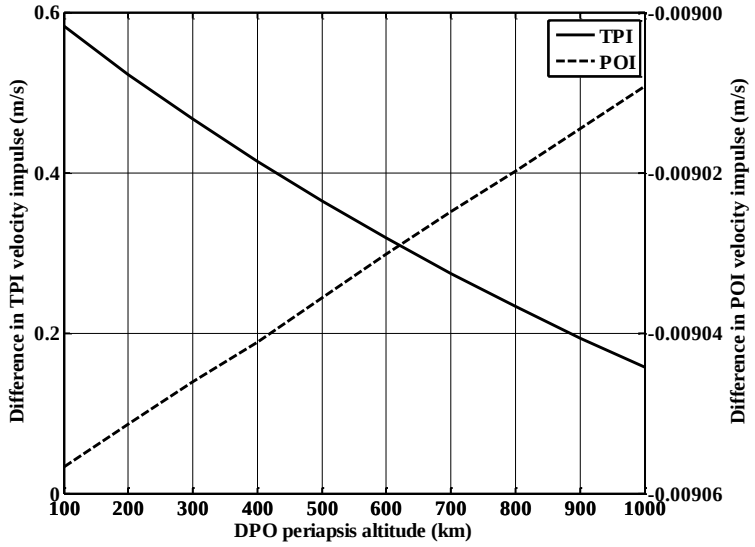

Fig. 6.26. Differences [B ITRPC-ITR PC] in TPI and POI velocity impulses for different DPO periapsis altitudes.

6.8.5 Different inclinations of arrival hyperbolic orbit/APO

The APO/ arrival hyperbolic orbit inclination is varied from 40 deg to 140 deg. This value is chosen to satisfy the condition: $i_{\infty_A} \geq \delta_{\infty_A}$. Figures 6.27 and 6.28 show the variation of departure and arrival angles with different APO inclinations. The variation in departure angles is marginal. The variation of arrival RAAN is anti-symmetric about an APO inclination of 90 deg. The variation in arrival AoP is about 22 deg, symmetric about the APO inclination of 90 deg. Figures 6.29 and 6.30 show the differences in these angles

between the ITR-PC and B-ITRPC designs. The maximum difference in departure angles is about 0.11 and 0.05 deg respectively. Note that, these variations in departure angles lead to huge improvement in the achieved CAA due to the B-ITRPC designs. The differences in the arrival angles between the designs are marginal.

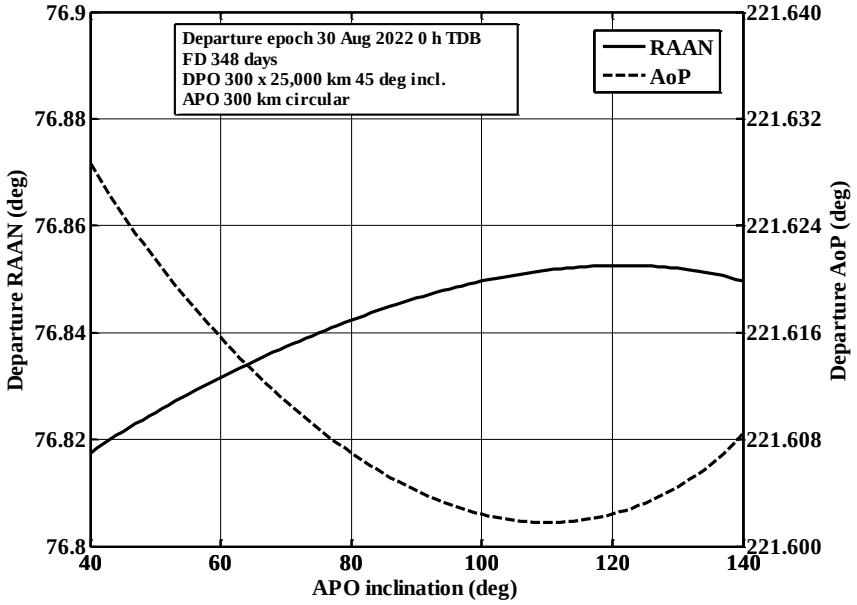

Fig. 6.27. Variation of departure/TPI angles (B-ITRPC technique) for different APO inclinations.

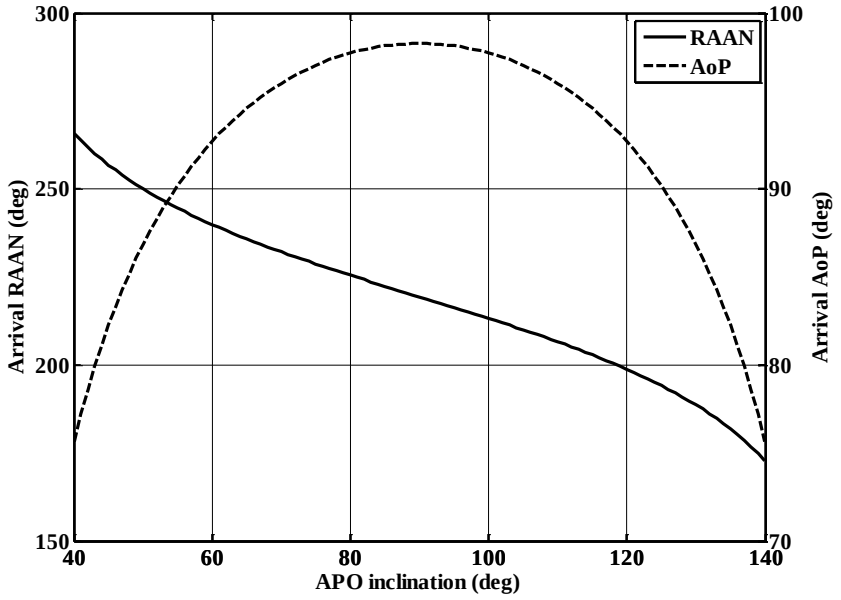

Fig. 6.28. Variation of arrival/POI angles (B-ITRPC technique) for different APO inclinations.

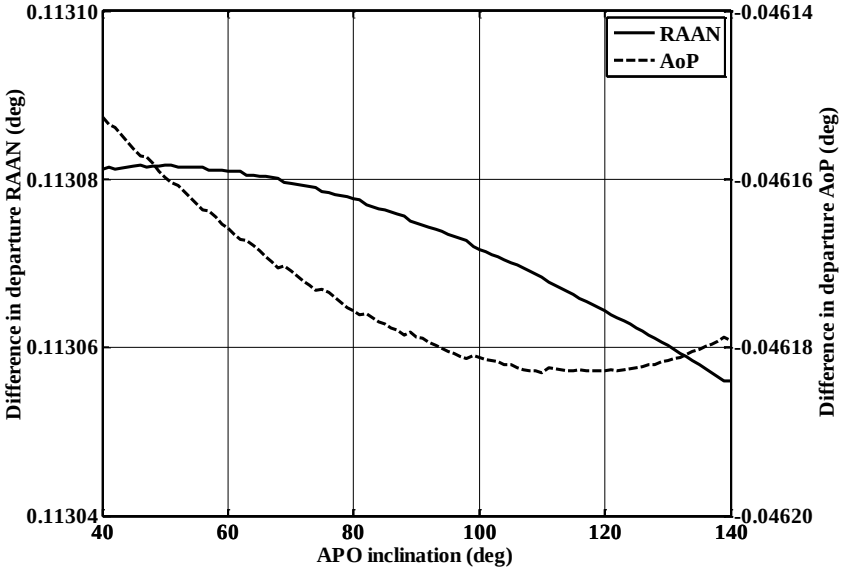

Fig. 6.29. Differences [B ITRPC-ITR PC] in departure angles for different APO inclinations

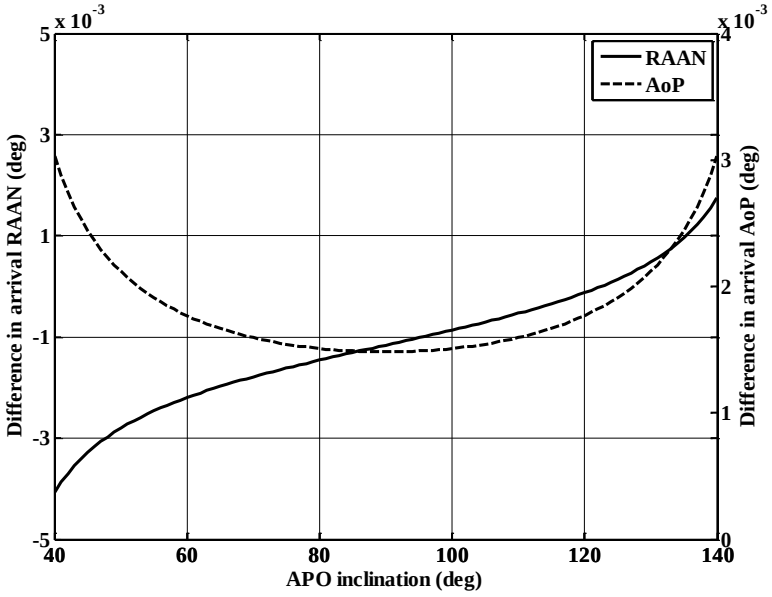

Fig. 6.30. Differences [B ITRPC-ITR PC] in arrival angles for different APO inclinations.

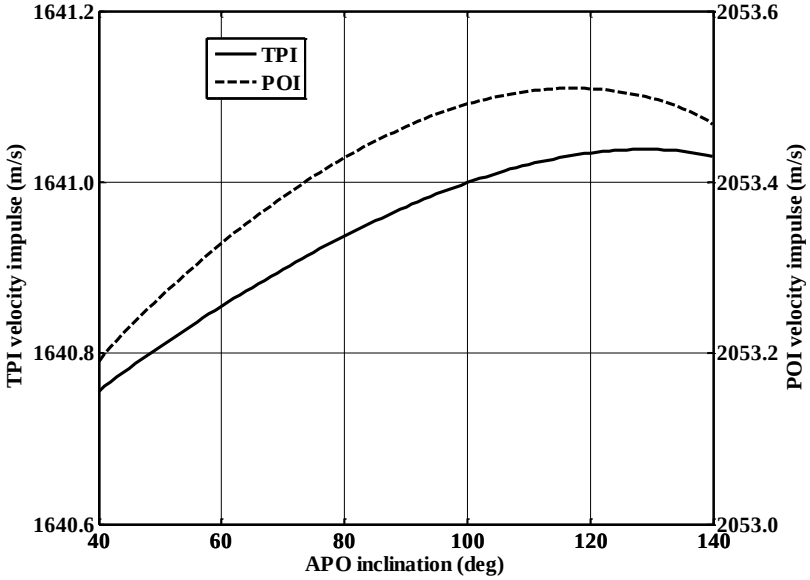

Fig. 6.31. Variation of TPI and POI velocity impulses (B-ITRPC technique) for different APO inclinations.

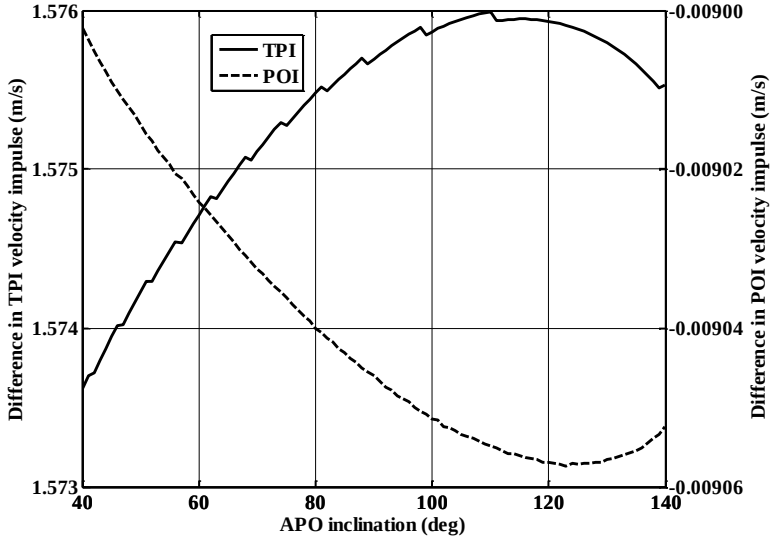

Fig. 6.32. Differences [B ITRPC-ITR PC] in TPI and POI velocity impulses for different APO inclinations

Figure 6.31 shows the variation in TPI and POI velocity impulses for different APO inclinations. The TPI variation for this range of APO inclinations is less than 1 m/s. So, any feasible APO inclination can be achieved without spending excess fuel by properly selecting the departure angles. The variation in POI velocity impulse is negligible. The difference in these velocity impulses between the ITR PC and B-ITRPC designs are negligible and given in fig.6.32.

6.8.6 Different periapsis altitudes of arrival hyperbolic orbit/APO

The APO altitude is varied from 100 km to 1000 km circular orbit. The variation in departure RAAN is marginal while the departure AoP varies by about 4 deg and is shown in Fig.6.33. Figure 6.34 shows that the variations in arrival angles are marginal. The differences in the departure and arrival angles between the ITR PC and B-ITRPC designs are shown in Figs. 6.35 and 6.36. The maximum difference in departure RAAN is about 0.11 deg and departure AoP is 0.05 deg. These differences are due to the non-spherical gravity perturbation effect of the Earth on the departure conditions. The differences in arrival angles are marginal.

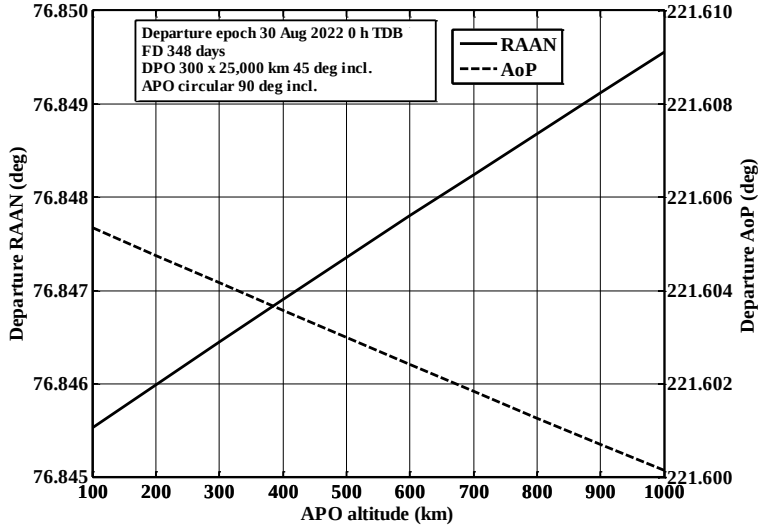

Fig. 6.33. Variation of departure/TPI angles (B-ITRPC technique) for different APO altitudes.

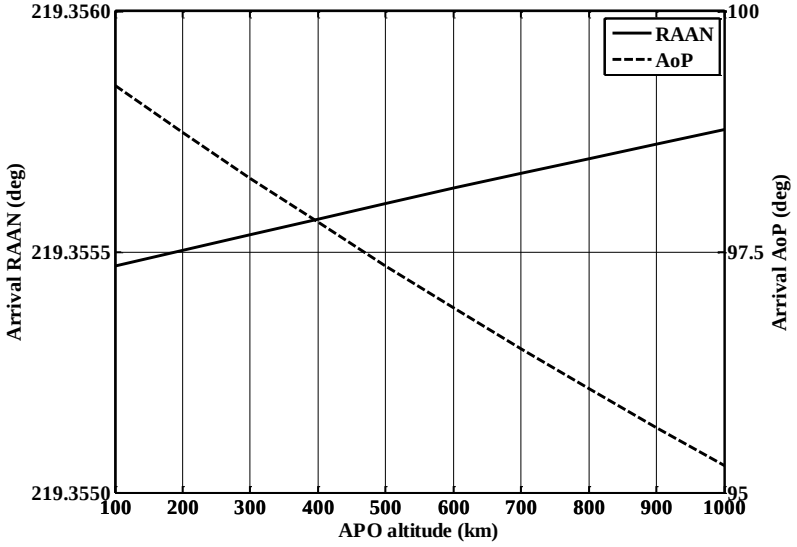

Fig. 6.34. Variation of arrival/POI angles (B-ITRPC technique) for different APO altitudes.

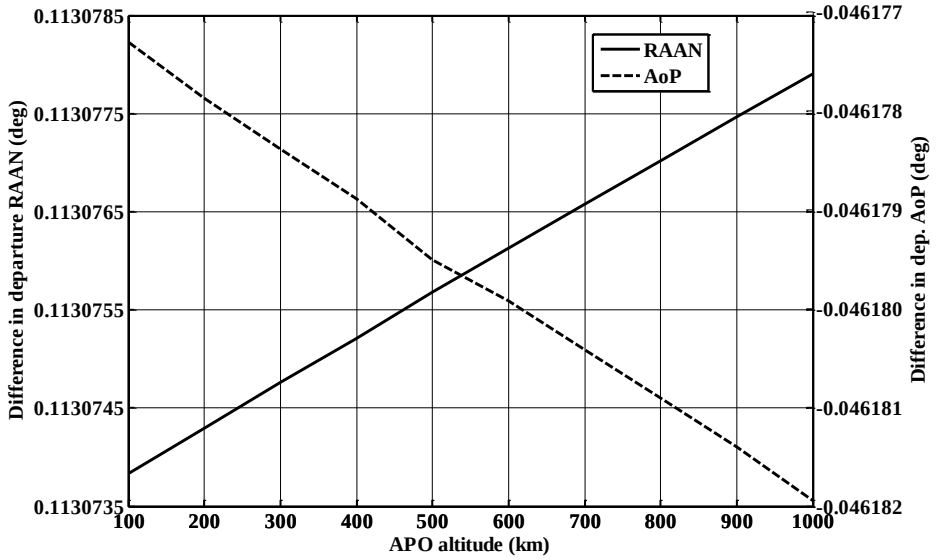

Fig. 6.35. Differences [B ITRPC-ITR PC] in departure angles for different APO altitudes

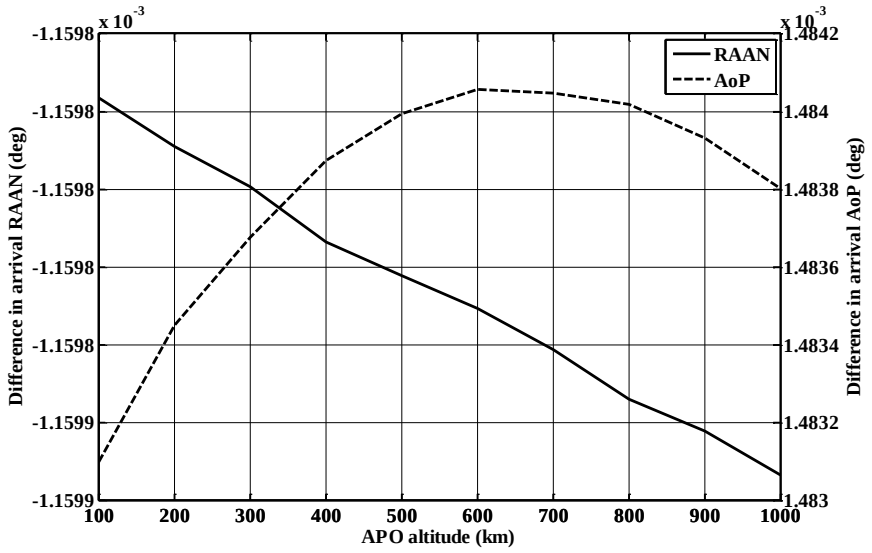

Fig. 6.36. Differences [B ITRPC-ITR PC] in arrival angles for different APO altitudes.

Figure 6.37 gives the TPI and POI velocity impulses for different APO altitudes. The variation in TPI velocity impulse is negligible and POI velocity impulse is about 110 m/s over this range of APO altitudes. The differences in TPI and POI velocity impulses between the ITR-PC and B-ITRPC designs are negligible (cf. Fig.6.38).

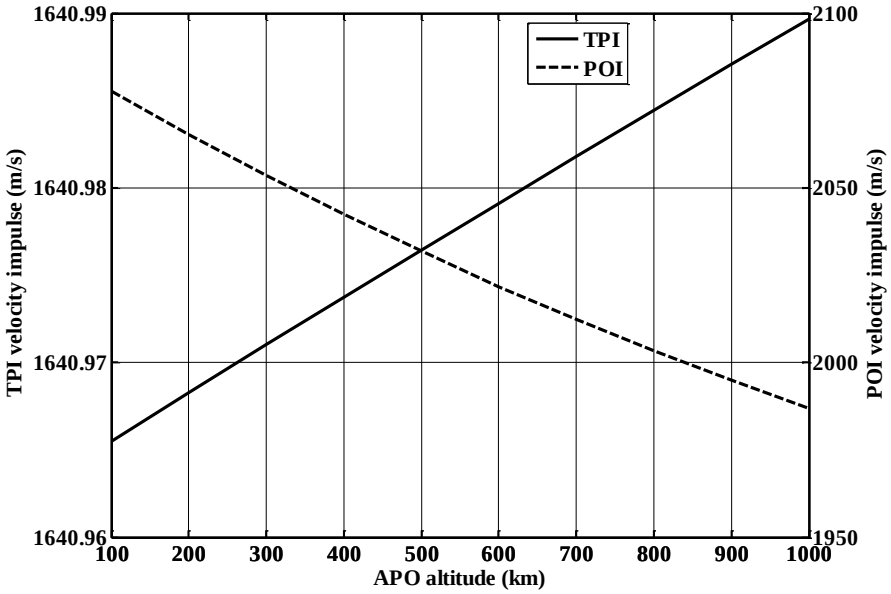

Fig. 6.37. Variation of TPI and POI velocity impulses (B-ITRPC technique) for different APO altitudes.

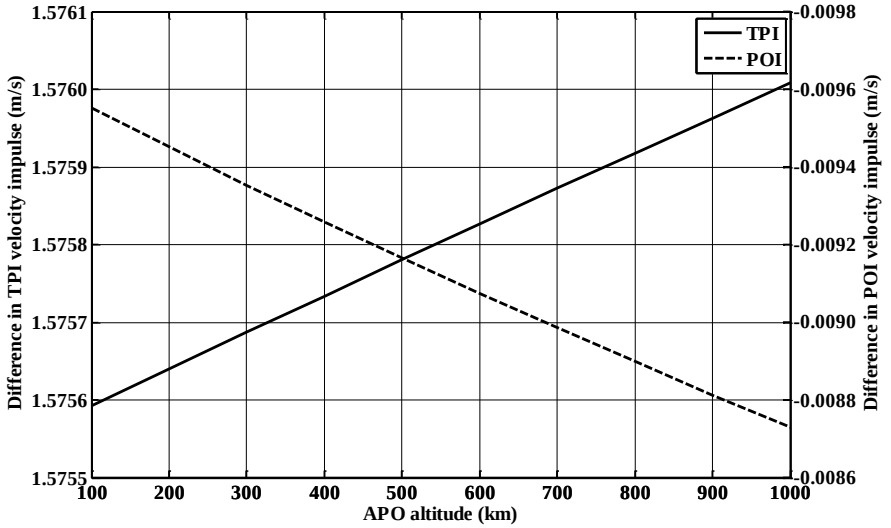

Fig. 6.38. Differences [B ITRPC-ITR PC] in TPI and POI velocity impulses for different APO altitudes.

6.9 B-ITRPC Design for MOM/MAVEN

The B-ITRPC designs are generated for the Mars Orbiter Mission (MOM) and Mars Atmosphere and Volatile Evolution (MAVEN) missions. Both of these orbiter missions were direct transfers from Earth to Mars utilizing the minimum energy opportunity of the year 2013. The MOM is India's first venture into deep space. NASA's Mars Atmosphere and Volatile Evolution (MAVEN) mission was to study the Martian atmosphere while orbiting Mars.

For the MOM mission, the departure epoch was on 30 November 2013 19:30:00 TDB and flight duration was 298 days. The Earth parking orbit and Mars parking orbit are 250 x 23,500 km and 300 x 80,000 km respectively. The inclinations of the departure and arrival parking orbits are same as the declination of the departure and arrival V-infinity vectors respectively. That means, the declination is the naturally occurring value of inclination for the departure and arrival hyperbolic orbits. For any inclination lesser than the declination of the V-infinity vector, a minimum-energy transfer is infeasible. So, the inclination of the departure parking orbit is fixed as 20.8 deg with respect to Earth equator and Equinox of J2000. The inclination of the arrival parking orbit is considered same as the arrival V-infinity vector, i.e. 149.7 deg with respect to Mars equator and IAU vector of J2000. The departure and arrival V-infinity vectors obtained from the B-ITRPC technique and are presented in Table 6.9a.

Table 6.9a V-infinity vector (option 11) for MOM opportunity

v_{∞_D} = 3.1212 m/s	α_{∞_D} = 200.7496 deg	$\boldsymbol{\delta_{\infty_D}}$ = **20.5416 deg**
v_{∞_A} = 3.1581 m/s	α_{∞_A} = 157.5918 deg	$\boldsymbol{\delta_{\infty_A}}$ = **149.7603 deg**

Table 6.9b B-ITRPC designs (option 11) for different arrival inclinations

Parameters	$i_{\infty_A} = \delta_{\infty_A}$	i_{∞_A} = 90 deg
a_{∞_D} (km)	-44570.4	-44567.8
e_{∞_D}	1.148711	1.148720
i_{∞_D} (deg)	21.10	21.10
Ω_{∞_D} (deg)	123.81	123.4712
ω_{∞_D}(deg)	287.13	287.4538
a_{∞_A}(km)	-4361.1	-4362.8965
e_{∞_A}	1.845929	1.84558502
i_{∞_A} (deg)	**149.70**	**90.0000**
Ω_{∞_A}(deg)	73.78	157.5847
ω_{∞_A}(deg)	218.15	272.6374
Velocity impulses (m/s)		
TPI	1461.13	1461.15
POI	1032.57	1032.23
Total	2493.70	2493.38

Using the B-ITRPC technique, analytical trajectory designs are generated for the MOM opportunity for different arrival inclinations and presented in Table 6.9b. For comparison, the velocity impulses, viz. TPI and POI, for these designs from the B-ITRPC technique are also given. The velocity impulses required for both the designs are almost

the same. As discussed earlier, this indicates that ***any APO inclination (say for Polar orbits, i_{∞_A} = 90 deg) can be achieved without incurring additional velocity impulse by precisely generating the design of the initial/departure parameters***

Table 6.9c V-infinity vector (option 11) for MAVEN opportunity

v_{∞_D} = 3.4903 m/s	α_{∞_D} = 198.5335 deg	δ_{∞_D}= 12.8512 deg
v_{∞_A} = 3.1886 m/s	α_{∞_A} = 153.1707 deg	δ_{∞_A} = -25.9133 deg

Table 6.9d B-ITRPC design option 11 for MAVEN opportunity

Parameters	**B-ITRPC design**	**Horizon data at 19:22 UTC**
a_{∞_D} (km)	-35108.22	-32588.45
e_{∞_D}	1.187225	1.2016476
i_{∞_D} (deg)	27.696	27.694
Ω_{∞_D} (deg)	172.119	172.681
ω_{∞_D}(deg)	241.610	242.069
ν_{∞_D}(deg)	0.0	45.54
a_{∞_A}(km)	-4288.26	47825.60
e_{∞_A}	1.881054	0.853755
i_{∞_A} (deg)	74.216	74.218
Ω_{∞_A}(deg)	325.652	325.45
ω_{∞_A}(deg)	149.096	150.68
ν_{∞_A}(deg)	0.0	360.9

Table 6.9e Design at perigee

Parameters	**At Perigee 19:12:20.7 UTC**
a_{∞_D} (km)	-32546.51
e_{∞_D}	1.201893
i_{∞_D} (deg)	27.69628
Ω_{∞_D} (deg)	172.7310
ω_{∞_D}(deg)	242.006
ν_{∞_D}(deg)	0.033

For the MAVEN mission, the departure epoch was on 18 November 2013 19:12:20 UTC and the arrival epoch was 22 September 2014 02:24 UTC (flight duration: 307.29375 days). The Earth parking orbit and Mars parking orbit considered for the design analysis are 195 km circular and 382 x 44430 km respectively. The inclinations of the DPO and APO are 27.696 deg w.r.t Earth equator and Equinox of J2000, and 74.218 deg w.r.t Mars equator and IAU vector of J2000 respectively. The departure and arrival

V-infinity vectors obtained from the B-ITRPC technique are presented in Table 6.9c. For the mission, the design parameters are available in the JPL HORIZON from 18/11/2013 19:22 UTC onwards (cf. Table 6.9d). This data is obtained and numerically propagated backward to reach the perigee using the BFM force model (cf. Table 6.9e). The B-ITRPC trajectory design generated for the MAVEN opportunity for the design option 11 is presented in Table 6.9d. *The difference in design is probably because the B-ITRPC design does not include Earth in the heliocentric (cruise) phase of the trajectory design process.*

6.10 Direct Transfers to Venus and Jupiter

6.10.1 Earth-Venus 2023 opportunity

For an Earth to Venus minimum energy transfer, the analytical trajectory designs are generated and analyzed using the conventional patched conic, ITR-PC and B-ITRPC techniques. The 2023 minimum energy opportunity with a departure epoch on 6 June 2023 0 h TDB and flight duration of 129 days is considered. The Earth parking orbit and Venus parking orbit are 300 x 25,000 km and 500 x 60,000 km respectively. The inclinations of the departure and arrival parking orbits are assumed as 20 deg and 90 deg with respect to the planet equator and equinox of J2000. The orbit sizes and inclinations used in this study do not consider the launch vehicle capabilities. The SOI durations of both Earth and Venus are considered as 3 days.

Table 6.10 V-infinity vectors for Earth-Venus 2023 opportunity

Parameters	Conventional patched conic design	B-ITRPC designs			
		option 11	option 12	option 21	option 22
v_{∞_D}(km/s)	3.4741	3.4743	3.4958	3.4699	3.4915
α_{∞_D}(deg)	122.3117	122.3218	122.2095	122.3439	122.2307
δ_{∞_D}(deg)	-10.9582	-11.1263	-11.6364	-11.0704	-11.5843
v_{∞_A}(km/s)	2.8814	2.8679	2.8723	2.8668	2.8712
α_{∞_A}(deg)	143.0099	142.7750	142.7920	142.7867	142.8029
δ_{∞_A}(deg)	7.1608	7.5728	8.5643	7.4091	8.4075

The V-infinity vectors at the departure and arrival phases obtained using the conventional patched conic technique and the B-ITRPC technique are given in Table 6.10. The four notional design options of the trajectory obtained using the conventional patched conic technique are given in Table 6.11a. The four distinct design options of the trajectory obtained using the ITR-PC and B-ITRPC techniques are given in Tables 6.11b

and 6.11c respectively. Note that the differences in the departure angles (RAAN and AoP) between the design options 11 and 12 are 1.6 deg and 1.1 deg respectively. The total velocity impulse for the ITR-PC designs is about 75 to 78 m/s less than that for the conventional patched conic designs which allows significant saving in terms of fuel requirement, roughly 25 kg (cf. Tables 6.11a and 6.11b). The difference in total velocity impulse between the ITR-PC and B-ITRPC designs is only about 1.5 to 2 m/s (cf. Tables 6.11 b and 6.11c).

Table 6.11a Conventional patched conic designs for Earth-Venus 2023 opportunity

Parameters	option 11	option 12	option 21	option 22
a_{∞_D} (km)	-33024.0	-33024.0	-33024.0	-33024.0
e_{∞_D}	1.202220	1.202220	1.202220	1.202220
i_{∞_D}(deg)	20.0000	20.0000	20.0000	20.0000
Ω_{∞_D} (deg)	154.4508	154.4508	270.1726	270.1726
ω_{∞_D}(deg)	179.9510	179.9510	67.4819	67.4819
a_{∞_A}(km)	-39126.9	-39126.9	-39126.9	-39126.9
e_{∞_A}	1.167449	1.162338	1.167449	1.162338
i_{∞_A}(deg)	90.0000	90.0000	90.0000	90.0000
Ω_{∞_A}(deg)	323.0099	143.0099	323.0099	143.0099
ω_{∞_A}(deg)	141.7725	336.5150	141.7725	336.5150
ΔV (m/s)	2412.3	2412.3	2412.3	2412.3

Table 6.11b ITR-PC designs for Earth-Venus 2023 opportunity

Parameters	option 11	option 12	option 21	option 22
a_{∞_D} (km)	-35441.0	-34960.5	-35540.7	-35056.1
e_{∞_D}	1.188429	1.191019	1.187900	1.190498
i_{∞_D}(deg)	20.0000	20.0000	20.0000	20.0000
Ω_{∞_D} (deg)	155.0091	156.6479	269.8584	267.9865
ω_{∞_D}(deg)	178.4038	176.8057	66.8124	68.8057
a_{∞_A}(km)	-43719.4	-43563.8	-43757.2	-43604.9
e_{∞_A}	1.149860	1.150395	1.149730	1.150253
i_{∞_A}(deg)	90.0000	90.0000	90.0000	90.0000
Ω_{∞_A}(deg)	322.7787	142.7957	322.7904	142.8065
ω_{∞_A}(deg)	142.8243	338.8780	143.0036	338.7288
ΔV (m/s)	2334.2	2342.2	2332.5	2340.5

Table 6.11c B-ITRPC designs for Earth-Venus 2023 opportunity

Parameters	option 11	option 12	option 21	option 22
a_{∞_D} (km)	-35352.82	-34873.09	-35511.69	-35027.37
e_{∞_D}	1.188899	1.191498	1.188054	1.190654
i_{∞_D}(deg)	20.0000	20.0000	20.0000	20.0000
Ω_{∞_D} (deg)	155.6646	157.3156	269.5085	267.6217
ω_{∞_D}(deg)	177.7369	176.1282	67.1821	69.1888
a_{∞_A}(km)	-43713.77	-43557.67	-43751.46	-43598.51
e_{∞_A}	1.149879	1.150416	1.149750	1.150275
i_{∞_A}(deg)	90.0000	90.0000	90.0000	90.0000
Ω_{∞_A}(deg)	322.7750	142.7920	322.7867	142.8029
ω_{∞_A}(deg)	142.8040	338.8944	142.9789	338.7498
ΔV (m/s)	2335.51	2343.58	2332.99	2341.04

Table 6.12 Achievable accuracies of analytical designs on numerical propagation under force model BFM

Parameters		Arrival CAA (km)	APO inc. (deg)	T_P((UTC)	TCM (m/s)
Desired values		500	90.00	13 Oct 2023 00:00:00	-
Conventional PC design		421,826	132.96	1 Oct 2023 03:34:10	170
ITR-PC design options	option 11	15,750	138.37	12 Oct 2023 15:00:16	14
	option 12	11,736	151.51	12 Oct 2023 14:22:17	13.8
	option 21	4,203	122.04	12 Oct 2023 18:18:11	7
	option 22	3,568	126.73	12 Oct 2023 17:50:47	6.4
B-ITRPC design options	option 11	529	87.72	13 Oct 2023 00:20:45	<1
	option 12	459	87.66	13 Oct 2023 00:20:03	<1
	option 21	514	86.29	13 Oct 2023 00:30:03	<1
	option 22	494	86.23	13 Oct 2023 00:29:26	<1

The achievable accuracies on numerical propagation of the analytical designs under the force model BFM are given in Table 6.12. The deviations in the achieved target parameters are significantly large for the conventional patched conic design (achieved CAA: 421,826 km; APO inclination: 132.96 deg and time of periapsis deviates by about 13 days). For ITR-PC designs, the achieved CAA and time of periapsis have significantly improved however the APO inclination has large deviation. The B-ITRPC design improved the achieved accuracies and the deviation in the arrival target parameters are: on CAA, $\pm$ 40 km; on APO inclination, -3 deg to -4 deg; on T_P, 20 to 30 minutes. The TCM required to achieve the desired target parameters are: (i) 170 m/s for conventional

patched conic design, (ii) about 7 to 14 m/s for the ITR-PC design options, and (iii) less than 1 m/s for the B-ITRPC design options (cf. Table 6.12).

6.10.2 Earth-Jupiter 2022 opportunity

For an Earth to Jupiter minimum energy transfer, the analytical trajectory designs are generated and analyzed using the conventional patched conic, ITR-PC and B-ITRPC techniques. The 2022 minimum energy opportunity with a departure epoch on 15 June 2022 0 h TDB and flight duration of 866 days is considered. The Earth parking orbit and Jupiter parking orbit are 300 x 25,000 km and 500 x 60,000 km. The inclinations of the departure and arrival parking orbits are considered as 20 deg and 90 deg with respect to the planet equator and Equinox of J2000. The SOI durations of Earth and Jupiter are considered as 3 and 12 days respectively. The SOI duration of Jupiter is large as Jupiter has a strong gravitational field.

Table 6.13 V-infinity vectors for Earth-Jupiter 2022 opportunity

Parameters	Conventional patched conic design	B-ITRPC designs			
		option 11	option 12	option 21	option 22
v_{∞_D}(km/s)	9.1302	9.0804	9.1513	9.0799	9.1510
α_{∞_D}(deg)	350.8361	350.7814	351.7859	350.7709	351.7818
δ_{∞_D}(deg)	-18.3302	-17.4129	-19.6304	-17.3877	-19.6207
v_{∞_A}(km/s)	5.8344	5.8168	5.8240	5.8167	5.8240
α_{∞_A}(deg)	352.6967	352.3852	352.4400	352.3845	352.4397
δ_{∞_A}(deg)	0.7931	0.5550	1.2760	0.5463	1.2727

The V-infinity vectors at the departure and arrival phases obtained using the conventional patched conic technique and the B-ITRPC technique are given in Table 6.13. The four notional design options of the trajectory obtained using the conventional patched conic technique are given in Table 6.14a. The four distinct design options of the trajectory obtained using the ITR-PC and B-ITRPC techniques are given in Tables 6.14b and 6.14c respectively. It is to be noted that, unlike the Earth-Mars and Earth-Venus mission scenarios, the difference in the departure angles between the design options are significantly large (for option 11 and 12: ΔRAAN, 20 deg; ΔAoP, 18 deg). ***The identification of distinct design options in this case is very important as the different departure RAAN values among the four design options lead to largely different launch windows.*** Also, the total velocity impulse between the four design options vary upto 46

m/s. The total velocity impulse for the ITR-PC designs is about 230 to 277 m/s less than that for the conventional patched conic designs which allows significant saving in terms of fuel requirement, roughly 90 kg (cf. Tables 6.14a and 6.14b). The difference in total velocity impulse between the ITR-PC and B-ITRPC designs is also significant, about 13 to 15 m/s (cf. Tables 6.14 b and 6.14c).

Table 6.14a Conventional patched conic designs for Earth-Jupiter 2022 opportunity

Parameters	option 11	option 12	option 21	option 22
a_{∞_D} (km)	-4781.5	-4781.5	-4781.5	-4781.5
e_{∞_D}	2.396634	2.396634	2.396634	2.396634
i_{∞_D}(deg)	20.0000	20.0000	20.0000	20.0000
Ω_{∞_D} (deg)	56.3759	56.3759	105.2963	105.2963
ω_{∞_D}(deg)	178.4833	178.4833	132.1942	132.1942
a_{∞_A}(km)	-3721653.3	-3721653.3	-3721653.3	-3721653.3
e_{∞_A}	1.019344	1.019344	1.019344	1.019344
i_{∞_A}(deg)	90.0000	90.0000	90.0000	90.0000
Ω_{∞_A}(deg)	172.6967	352.6967	172.6967	352.6967
ω_{∞_A}(deg)	168.0268	349.6132	168.0268	349.6132
ΔV (m/s)	16239.2	16239.2	16239.2	16239.2

Table 6.14b ITR-PC designs for Earth-Jupiter 2022 opportunity

Parameters	option 11	option 12	option 21	option 22
a_{∞_D} (km)	-4853.9	-4778.6	-4854.5	-4778.9
e_{∞_D}	2.375822	2.397500	2.375658	2.397419
i_{∞_D}(deg)	20.0000	20.0000	20.0000	20.0000
Ω_{∞_D} (deg)	50.2898	70.3070	111.4117	93.4091
ω_{∞_D}(deg)	184.0657	166.1519	126.0045	144.4041
a_{∞_A}(km)	-27184640.4	-26592543.6	-27187653.1	-26594309.2
e_{∞_A}	1.002648	1.002707	1.002647	1.002707
i_{∞_A}(deg)	90.0000	90.0000	90.0000	90.0000
Ω_{∞_A}(deg)	172.3853	352.4401	172.3846	352.4399
ω_{∞_A}(deg)	173.0527	354.8609	173.0615	354.8576
ΔV (m/s)	15948.6	15995.0	15948.3	15994.8

The achievable accuracies on numerical propagation of the analytical designs under the force model BFM are given in Table 6.15. Incidentally, the deviations in

achieved target parameters are larger for the ITR-PC designs than that of the conventional patched conic design. However, the deviations are less for the B-ITRPC design options: on CAA, − 105 km to 618 km; on APO inclination, −1 to 2 deg; on T_P, 1 to 2 hours. The TCM required to achieve the desired target parameters are more than 200 m/s for the conventional and ITR-PC design options while that for B-ITRPC design options is less than 1 m/s (cf. Table 6.15).

Table 6.14c B-ITRPC designs for Earth-Jupiter 2022 opportunity

Parameters	option 11	option 12	option 21	option 22
a_{∞_D} (km)	-4831.2	-4756.4	-4832.6	-4757.1
e_{∞_D}	2.382285	2.404003	2.381892	2.403822
i_{∞_D}(deg)	20.0000	20.0000	19.9999	19.9999
Ω_{∞_D} (deg)	50.3255	70.2992	111.4855	93.5245
ω_{∞_D}(deg)	184.0829	166.2070	125.9819	144.3416
a_{∞_A}(km)	-27184075.7	-26592060.7	-27187099.9	-26593841.8
e_{∞_A}	1.002648	1.002707	1.002648	1.002707
i_{∞_A}(deg)	90.0000	90.0000	90.0000	90.0000
Ω_{∞_A}(deg)	172.3852	352.4400	172.3845	352.4397
ω_{∞_A}(deg)	173.0527	354.8608	173.0615	354.8575
ΔV (m/s)	15962.2	16008.6	15961.4	16008.2

Table 6.15 Achieved accuracies of analytical designs on numerical propagation under force model BFM

Parameters		Arrival CAA (km)	Arrival inclination (deg)	T_P((UTC) DD/MM/YYYY HH:MM:SS	TCM (m/s)
Desired values		500	90.00	28 Oct 2024 00:00:00	-
Conventional PC design		920,802	170.95	21 Oct 2024 19:01:07	>200
ITR-PC design options	option 11	1,568,183	19.52	8 Nov 2024 13:41:49	>200
	option 12	1,413,791	2.28	8 Nov 2024 07:15:15	>200
	option 21	1,581,037	19.16	8 Nov 2024 12:07:56	>200
	option 22	1,426,949	2.35	8 Nov 2024 07:25:48	>200
B-ITRPC design options	option 11	395	91.02	27 Oct 2024 22:33:58	<1
	option 12	1188	91.82	27 Oct 2024 22:02:12	<1
	option 21	521	90.62	27 Oct 2024 22:51:09	<1
	option 22	624	90.72	27 Oct 2024 22:47:53	<1

6.11 Performance of Different Patched conic Techniques

This section consolidates the performance of different analytical techniques based on the patched conic concept. The minimum energy opportunity for an ***Earth to Mars transfer occurring on 12 May 2018 0 h TDB and flight duration 204 days*** is considered.

Table 6.16 Analytical designs based on patched conic concept and the computation time

Design parameters	Numerical design	Conventional PC design	VPC design	ITR-PC design	B-ITRPC design
a_{∞_D} (km)	-58103.9	-51239.9	-58640.5	-58965.7	-58105.5
e_{∞_D}	1.114934	1.130332	1.113882	1.113254	1.114931
Ω_{∞_D} (deg)	333.5562	333.0131	333.0131	333.3889	333.5526
ω_{∞_D}(deg)	167.4883	169.3999	167.8129	167.3782	167.4891
a_{∞_A}(km)	-4979.6	-4881.1	-4973.4	-4980.0	-4979.7
e_{∞_A}	1.742253	1.757441	1.743391	1.742402	1.740842
Ω_{∞_A}(deg)	67.9590	68.1673	68.1673	68.0878	68.0851
ω_{∞_A}(deg)	115.2124	115.0951	115.4118	115.1783	115.2142
ΔV (m/s)	-	3603.4	3545.4	3543.4	3547.9
Computation time					
Design generation	-	0.002 s	0.002 s	0.006 s	25 s
Numerical refinement	-	> 1 day	180 s	125 s	5 s
TCM (m/s)	-	high	165	18	<1

For comparison, a comprehensive view of the performance of different analytical designs (for option 11) and the numerical design generated using the BFM force model are presented in Table 6.16. It can be noted that the B-ITRPC design is very close to the numerical design. Also, the total velocity impulse of the B-ITRPC design is less than the conventional patched conic design by about 55 m/s. Also, the difference in total velocity impulse between the ITR-PC and B-ITRPC designs is only 5 m/s. From the computation point of view, the B-ITRPC technique takes about 25 s to generate the design. However, for numerical refinement under the design force model, when B-ITRPC design is used as the initial guess, the computation time is only 4.5 s. The TCM required to meet the arrival target parameters, if B-ITRPC design is used as the initial guess, is less than 1 m/s. This clearly indicates that the B-ITRPC design serves as a good initial guess for numerical refinement. The achievable accuracies of the different analytical designs on numerical

propagation under the BFM force model are given in Table 6.17. It can be noted that the conventional PC design results in very large deviation in the arrival parameters. The VPC and ITR-PC designs result in slight improvement in terms of the achieved closest approach altitude and time of APO periapsis. However, the deviation in APO inclination is significantly large. The B-ITRPC design results in good accuracies in the all the arrival target parameters.

Table 6.17 Achievable accuracies on numerical propagation under force model BFM

Achievable accuracies	Arrival CAA (km)	Arr. Inc. (deg)	T_P (UTC)
Desired	300	75.00	02 Dec 2018 00:00:00
Conventional design	28,48,031	155.84	07 Nov 2018 17:38:01
VPC design	6,95,037	130.72	02 Dec 2018 02:25:30
ITR-PC	4,62,975	21.53	04 Dec 2018 02:13:02
B-ITRPC	560	75.35	01 Dec 2018 23:51:44

6.12 Conclusions

The transfer trajectory design using the biased-iterative patched conic technique provides improved analytical design. The B-ITRPC design reduces the reduction in deviation in the achieved closest approach altitude by about 97%. The arrival inclination deviates only by about 1.3% from the desired value and the time of periapsis by only 3 s. However, the inclusion of the perturbations in the analytical design process results in an additional transplanetary injection (TPI) impulse of about 5 m/s as compared to the ITR-PC design. The computation time taken for numerical refinement using B-ITRPC design as the initial guess is very less (~ 3 to 5 s) as compared to the ITR-PC design (~110 to 125 s), thus demonstrating its ***use as an excellent initial guess for numerical refinement***. ***To arrive at the desired numerical design, if B-ITRPC design is used as the initial guess, the numerical refinement process does not require any additional constraint on the arrival target parameters. The B-ITRPC design is very close to the numerical design and so, can be used for mission design and analysis purpose to understand the realistic trends.***

The total velocity impulse between the four distinct B-ITRPC design options for an opportunity vary upto 7 m/s only. Hence, any arrival geometry can be achieved without incurring high additional velocity impulse. The departure from equatorial parking orbits requires a maximum additional impulse of about 3.2 m/s. If this additional impulse is

ignored, the trajectory correction maneuver (TCM) requirement will be more. ***The B-ITRPC design options result in significantly large improvement in the achievable accuracies of the arrival target parameters and so, it requires very less TCM correction.***

The observations made for direct transfers from Earth to Mars and from Earth to Venus are similar. The situation is very much different for a direct transfer from Earth to Jupiter. The differences in the departure angles between the design options are very large (>18 deg). ***The identification of distinct design options in this case is very important as the different departure RAAN values among the four design options lead to largely different launch windows.*** Also, in this case, the ITR-PC and conventional patched conic designs result in poor achievable accuracies in the target parameters. Furthermore, for an Earth to Jupiter direct transfer, the total velocity impulse between the four B-ITRPC design options vary upto 46 m/s. ***The total velocity impulse for the B-ITRPC designs is about 230 to 277 m/s less than that for the conventional patched conic designs (this range is 57 to 61 m/s for an Earth to Mars transfer) which allows significant saving in terms of fuel requirement, roughly 90 kg.*** The difference in total velocity impulse between the ITR-PC and B-ITRPC designs is about 13 to 15 m/s which also saves about 5 kg of fuel.

Under a realistic force model that includes the major perturbing forces within the departure phase, it is found that the B-ITRPC technique generates the four distinct design options for an opportunity with the highest accuracy as compared to all the other analytical design techniques.

♠♠♠♠♠♠♠♠♠♠♠♠♠♠♠♠♠♠♠

CHAPTER 7

CONCLUSIONS AND FUTURE SCOPE

The current research has developed novel analytical trajectory design techniques for direct interplanetary orbiter missions. The proposed iterative analytical techniques identify the four distinct trajectories possible for an opportunity. The major perturbations have been included in the analytical trajectory design process and the biased-iterative patched conic designs thus generated are close to the numerical designs. The B-ITRPC design can be used as a good initial guess for the numerical refinement process which ensures quick and steady convergence without any additional specification of the arrival target parameters. It is demonstrated that the FORTRAN 95 codes developed based on the proposed techniques can be used as quick mission design and analysis tool for exploring various mission scenarios. All the computations are carried out in an Intel core i5 2.5GHz processor. The important inferences derived from the current research are summarized as follows.

1) The arrival target parameters are extremely sensitive to even a small change in any one of the departure hyperbolic orbit characteristics which is evident from the sensitivity analysis. This brings out the need for improvement of the conventional patched conic design.
2) When analytical tuning is introduced in the patched conic technique, the total velocity impulse is reduced by about 58 m/s. This brings out the necessity of tuning the hyperbolic orbital elements.

3) All the iterative analytical techniques capture the four distinct designs of the transfer trajectory available for an opportunity and they can handle orbiter mission design which requires targeting the arrival conditions. On the other hand, the conventional patched conic and V-infinity tuned patched conic techniques which are non-iterative in nature, can only generate notional designs for orbiter missions.

4) The one-step iterative pseudostate technique (ITR-PS) includes the gravity effect of the Sun within the pseudosphere and thereby improves the achievable accuracies of

the arrival target parameters (CAA and time of arrival periapsis) except the achieved APO inclination. To achieve this specific APO inclination, the multiconic differential evolution technique (MCDE) is proposed which uses the multi-step pseudostate technique for analytical propagation within the pseudosphere and the differential evolution technique for tuning the hyperbolic orbit characteristics. However, the computation time for this technique is very large (88 s) as compared to the ITR-PS design. Further, in the pseudostate concept, the transfer trajectory is heliocentric even within the pseudosphere of the target planets. This complicates the inclusion of perturbations in the design process. So, the pseudostate concept is not recommended.

5) The simplicity of the conventional patched conic technique and the iterative nature of the ITR-PS technique are combined and an iterative patched conic technique (ITR-PC) is proposed. The inferences drawn from the four distinct ITR-PC design options for different interplanetary transfers are as follows.

    a) In a typical Earth to Mars transfer trajectory (2018 opportunity), the departure RAAN values of the four ITR-PC design options are 333.3889 deg, 333.4465 deg, 129.9454 deg, and 129.9341 deg respectively. Although the differences in departure RAAN values between the first two options, and between the other two options are only 0.06 deg and 0.01 deg respectively, the arrival hyperbolic orbits have completely different geometries. Also, the departure designs are completely different for the design options 11 and 21, and options 12 and 22, but they result in similar arrival geometries. This clearly brings out the importance of identifying the distinct design options for an opportunity.
    b) In a typical Earth to Venus transfer trajectory (2023 opportunity), the difference in the departure RAAN between the design options are comparatively higher and vary from 1.6 deg to 2 deg.

    The observations made for direct transfers from Earth to Mars and from Earth to Venus are similar. The situation is very much different for a direct transfer from Earth to Jupiter.

    c) In a typical Earth to Jupiter transfer trajectory (2022 opportunity), the difference in the departure RAAN between the design options are very large and vary from 18 deg to 20 deg. The identification of distinct design options

in this case is very important as the largely different departure RAAN values (of the four design options) lead to largely different launch windows for lift-off.

6) The computation time required to generate designs for 2190 cases is only 592 ms and so, the ITR-PC design technique can be used as a quick mission design and analysis tool to carry out preliminary design analysis. A design analysis for the four design options is done for an Earth to Mars orbiter mission (2018 opportunity) using the ITR-PC technique and some of the salient inferences are listed below.
    a) For an interplanetary transfer, lower periapsis altitude of the departure parking orbit is preferable for a fixed apoapsis altitude because the total velocity impulse, in this case, is less. Also, the launch vehicle can achieve more payload in this scenario.
    b) For the whole range of feasible DPO inclinations for an opportunity, an interplanetary transfer incurs a penalty of less than 4 m/s only.
    c) For a prefixed DPO inclination, any of the four design options can be used for interplanetary transfer with a marginal penalty in the total velocity impulse which is less than 1 m/s.
    d) Directly targeting lower APO periapsis altitudes is beneficial compared to the strategy of targeting higher APO periapsis altitudes and then reducing to lower APO periapsis altitudes.
    e) Any feasible APO inclination can be achieved without incurring significant additional velocity impulse (< 4 m/s).

7) For a co-planar transfer, a realistic estimate of feasible range of DPO inclinations can be obtained with the ITR-PC technique. For example, for 2018 Earth-Mars transfer, the feasible range with the conventional PC technique is from 36.8 deg to 143.2 deg, whereas with the ITR-PC technique, the feasible range for option 11 is between 37.21 deg and 143.79 deg. ***This indicates that, we can generate only a notional design for a coplanar transfer with a DPO inclination of 36.8 deg.***

8) The ITR-PC designs result in improved achievable accuracies in the arrival target parameters on numerical propagation under the design force model (say, for Earth-Mars transfer of 2018 opportunity: achieved CAA is 313 km against 300 km; APO inclination is 75.39 deg against 75.00 deg and time of periapsis deviates by about 2

minutes from the desired value) as compared to the conventional and V-infinity tuned patched conic designs. Note that the numerical propagation of conventional patched conic design results in very large deviations in achieved target parameters (achieved CAA: 30,11,712 km; APO inclination: 156.32 deg; time of periapsis deviates by about 26 days from the desired value).

9) The ITR-PC designs result in poor accuracies in the arrival target parameters on numerical propagation under a force model that includes perturbations (for Earth-Mars transfer of 2018 opportunity: achieved CAA: 4,62,975 km; APO inclination: 21.52 deg and time of periapsis deviates by about 1.5 days from the desired value). Thus, the ITR-PC technique requires further refinement under a realistic force model that includes perturbations.

10) The major perturbations in the departure phase which influence the arrival parameters are the non-spherical Earth and the third-body effects of the Sun and the Moon. The perturbations due to other planets, atmospheric drag and solar radiation pressure can be neglected.

11) The biased-iterative patched conic technique (B-ITRPC) which includes perturbations in the design process, is proposed. The B-ITRPC design options achieve the highest accuracies in the arrival target parameters (for Earth-Mars transfer of 2018 opportunity: achieved CAA: 543 km; APO inclination: 75.41 deg and time of periapsis deviates by about 9 minutes from the desired value).

12) The B-ITRPC design is very close to the numerical design. The trajectory correction maneuvers (TCM) required is less than 1 m/s under the force model that includes major perturbations while the TCM requirement is about 18 m/s if ITR-PC design is adopted for the mission.

13) The design analysis using the B-ITRPC technique provides a realistic insight into various mission aspects. The computation time for generating B-ITRPC design is more than ITR-PC design. Nevertheless, the B-ITRPC technique derives its merit based on the improvement in the trajectory design.

14) For the numerical refinement process under the design force model, if the conventional design is used as the initial guess, the process converges randomly to

any of the design options. In contrast, when the ITR-PC design is used as the initial guess, the numerical refinement process converges to the desired design option. However, under a force model that includes perturbations, the numerical refinement process of ITR-PC design also converges randomly to any of the design options. The B-ITRPC design converges to the desired design option steadily even in the absence of additional information on the arrival parameters.

15) The computation time for numerical refinement, if the conventional patched conic design is used as the initial guess, is more than a day under a force model that includes major perturbations. With the ITR-PC design as initial guess, the process converges in 125 s. The computation time required for the B-ITRPC design to converge is only 5 s (Earth-Mars transfer: 2018 opportunity). Thus, the B-ITRPC technique serves as an excellent initial guess for numerical refinement.

16) The velocity impulse requirement for the analytical designs is less by about 50-75 m/s than velocity impulse requirement for the conventional design (Earth-Mars transfer: 2018 opportunity). This indicates that we get only a conservative estimate of the velocity impulse from the conventional design.

FUTURE SCOPE

The numerical propagation of the analytical trajectory design under a force model that includes the gravity field of Earth also in the heliocentric phase, results in large deviations in the arrival target parameters. So, the trajectory design can be further refined to include Earth in the heliocentric phase.

♠♠♠♠♠♠♠♠♠♠♠♠♠♠♠♠♠♠♠

REFERENCES

1) Archinal, B. A., A'Hearn, M. F., Bowell, E., et al., 2009. "Report of the IAU Working Group on cartographic coordinates and rotational elements". Celestial Mechanics & Dynamical Astronomy, Vol.109, No.2. http://dx.doi.org/10.1007/s10569-010-9320-4.
2) Addis, B., Cassioli, A., Locatelli, M., and Schoen, F., 2009. "A global optimization method for the design of space trajectories". Computational Optimization and Applications, doi: 10.1007/s10589-009-9261-6.
3) Adimurthy, V. and Ramanan, R.V., 2005. "Launch strategy for Indian Lunar mission and precision injection to the Moon using genetic algorithm". Journal of Earth System Sciences, Vol. 114, No.6, December, pp. 711-716.
4) Armellin R., et al, 2011. "Rigorous Global Optimization of Impulsive Planet-to-Planet Transfers in the Patched-Conics Approximation", Engineering Optimization, Taylor Francis, pp.1. <10.1080/0305215X.2011.570757> <hal-00712366>.
5) Avanzini, G., 2008. "A Simple Lambert Algorithm". Journal of Guidance, Control, and Dynamics, Vol. 31, No. 6, pp. 1587–1594, Nov. ISSN 0731-5090. doi:10.2514/1.36426.
6) Bate, R.R., Mueller, D.D., and White, J.E., 1971. "Fundamentals of Astrodynamics". Dover Publications, New York, pp.181-186, Chap 1, pp. 333-341.
7) Battin, R.H., 1987. "Introduction to the Mathematical Methods of Astrodynamics". AIAA Education series, AIAA, New York. doi: 10.2514/4.861543.
8) Battin, R. H. and Vaughan, R. M., 1984. "An elegant Lambert algorithm". Journal of Guidance, Control, and Dynamics, Vol. 7, No. 6, pp. 662–670, Nov. ISSN 0731-5090. doi: 10.2514/3.19910.
9) Bayliss, S. S., 1970. "Precise Targeting for Multiple Swing-by Interplanetary Trajectories". TE-39, Measurement Systems Laboratory, MIT, Cambridge.
10) Becerra, V.M., Myatt, D.R., Nasuto, S.J., Bishop, J.M., Izzo, D., 2005. "An efficient pruning technique for the global optimisation of multiple gravity assist trajectories". In: Proceedings of the Global Optimisation, Acta Futura - Issue 1.
11) Bell, S.C., Ginsburg, M. A. and Rao, P.P., 1995. "Monte Carlo Analysis of the Titan/Transfer Orbit Stage Planetary Mission Guidance System". Journal of

Guidance, Control and Dynamics, Vol.18, No.1, January-February, pp. 121-127.doi: 10.2514/3.56666.

12) Bessette C. R. and Spencer D. B., 2007. “Performance Comparison of Stochastic Search Algorithms on the Interplanetary Gravity-Assist Trajectory Problem", Journal of Spacecraft and Rockets, Vol. 44, No. 3, pp. 722-724.https://doi.org/10.2514/1.25718.

13) Betts, J.T., 1998. “Survey of numerical methods for trajectory optimization”. Journal of Guidance, Control and Dynamics, Vol.21, pp.193-207.

14) Betts, J. T. and Orb, S. O., 2003. “Optimal Low Thrust Trajectories to the Moon”. SIAM Journal on Applied Dynamical Systems, Vol. 2, No. 2, pp. 144–170.

15) Blitzer, L., 1959. “Lunar-Solar Perturbations of an Earth Satellite”. American Journal of Physics, Vol. 27, No. 9, pp. 634-645.

16) Boltz, F. W., 1984. “Second-order p-iterative solution of the Lambert/Gauss problem”. Journal of the Astronautical Sciences, Vol. 32, pp. 475–485.

17) Bradley, N. and Russell, R. P., 2014 “A continuation method for converting trajectories from patched conics to full gravity models”, Journal of Astronautical Sciences, Volume 61, Issue 3, pp 227–254. Doi: 10.1007/s40295-014-0017-x; also in AAS 14-273.

18) Brennan, M.J., 2011. “Patched Conic Interplanetary Trajectory Design Tool”. The University of Texas at Austin, Dec.

19) Brooke, M. Anderson, Park and Henry, Wright, 2007. “Comparison of a simple patched conic trajectory code to commercially available software”. AAS 07-160, 17th AAS/AIAA Space Flight Mechanics Meeting; 28 Jan. - 1 Feb. Sedona, AZ; United States.

20) Brown, C.D., 1992. “Spacecraft Mission Design”. AIAA Education Series, AIM, Washington.

21) Burke L. M. et al., 2010. “Interplanetary Mission Design Handbook: Earth-to-Mars Mission Opportunities 2026 to 2045”, NASA Technical Reports Server (NTRS), NASA/TM-2010-216764, E-17208, Oct 01, 2010, NASA Glenn Research Center; Cleveland, OH, United States.

22) Byrnes, D.V. and Hooper, H.L., 1970. “Multiconic: A Fast and Accurate Method of Computing Space Flight Trajectories”. AIAA paper No.70-1062, AAS/AIAA Astrodynamics Conference, Santa Barbara, California, Aug. 19-21.

23) Byrnes, D.V., 1989. “Application of Pseudostate Theory to the Three-Body Lambert Problem”. Journal of Astronautical Sciences, Vol. 37, No.3, July-Sep., p.p. 221-232.

24) Campagnola, S., Buffington, B. B., Petropoulos, A.E., 2014. “Jovian tour design for orbiter and lander missions to Europa”. Acta Astronautica, Vol. 100, pp. 68-81. doi:10.1016/j.actaastro.2014.02.005.

25) Carlson K. M., 1970. “An analytical solution to patched conic trajectories satisfying initial and final boundary conditions”. Technical Memorandum, Bellcomm, TM-70-2011-1, November 30.

26) Chandrayaan-1, accessed 22 Oct 2008, < https://www.isro.gov.in/Spacecraft/chandrayaan-1>

27) Chobotov, V. A., 2002. “Orbital mechanics”. 3rd edition. Reston, Va.: American Institute of Aeronautics and Astronautics.

28) Clark, S., 2016. “Rosetta mission ends with touchdown on comet 67P-as it happened”. Across the universe Rosetta space probe, The Gaurdian, Sep 30, <https://www.theguardian.com/science/across-the-universe/live/2016/sep/30/rosetta-space-probe-to-end-mission-with-comet-landing-live>.

29) Clarke, Jr., V.C., Bollman, W.E., et al., 1966. “Design parameters for Ballistic Interplanetary trajectories, Part II: One-way transfers to Mercury and Jupiter". NASA Technical report 32-77, Jet Propulsion laboratory, Pasadena, CA, Jan 15.

30) Crain, T., Bishop, R., Fowler, W., and Rock, K., 2000. “Interplanetary Flyby Mission Optimization Using a Hybrid Global-Local Search Method”. Journal of Spacecraft and Rockets, Vol. 37, No. 4, pp. 468–474. doi:10.2514/2.3607.

31) Cornelisse, J.W., 1978. “Trajectory analysis for interplanetary missions". ESA Journal. Vol. 2, No. 2, pp. 131–144.

32) Conway, B.A., 2010. “Spacecraft trajectory optimization”. Cambridge University Press.

33) Cook, G. E., 1962. “Luni-Solar Perturbations of the Orbit of an Earth Satellite”. Geophysical Journal of the Royal Astronomical Society, Vol.6, pp.271–291. doi:10.1111/j.1365-246X.1962.tb00351.x

34) Coverstone-Carroll, V., Hartmann, J. W., and Mason, W. J., 2000. “Optimal Multi-Objective Low-Thrust Spacecraft Trajectories”. Computer Methods in Applied Mechanics and Engineering, Vol. 186, Nos. 2–4, pp. 387–402.

35) Dachwald, B., 2004. “Optimization of Solar Sail Interplanetary Trajectories Using Evolutionary Neurocontrol”. Journal of Guidance, Control, and Dynamics, Vol. 27, No. 1, pp. 66–72.

36) D'Amario, L.A., Byrnes, D.V. and Stanford, R.H., 1982. “Interplanetary Trajectory Optimization with Application to Galileo”. Journal of Guidance, Control and Dynamics, Vol.5, No.5, pp.465-471, September-October.

37) D'Amario, LA, 1989. “Trajectory Optimization Software for Planetary Mission Design”. The Journal of Astronautical Sciences, Vol.37, No.3, pp.213-220, July-September.

38) D'Amario, L.A., Byrnes, D.V., and Stanford, R.H., 1981. “A New Method for Optimizing Multiple-Flyby Trajectories”. Journal of Guidance, Control, and Dynamics, Vol. 4, No. 5, pp. 591-596. https://doi.org/10.2514/3.56115.

39) Domingos, R. C., Vilhena deMoraes, R., and Prado, A. F. Bertachini De Almeida, 2008. “Third-Body Perturbation in the Case of Elliptic Orbits for the Disturbing Body”. Hindawi Publishing Corporation, Mathematical Problems in Engineering, Vol.2, Article ID 763654, doi:10.1155/763654.

40) Englander, J.A., Conway, B.A., Williams, T., 2012. “Automated interplanetary trajectory planning”. In: AIAA 2012-4517, AAS/AIAA Astrodynamics Specialist Conference, Minneapolis, Minnesota, August.

41) Escobal, P.R., 1965. “Methods of Orbit Determination”. John-Wiley & Sons Inc., Newyork.

42) Gage, P. J., et al., 1995. “Interplanetary trajectory optimization using a genetic algorithm”. Journal of Astronautical Science, Vol. 43, No.1, pp. 59–75.

43) Gauss, C. F., 1857. “Theory of the motion of the heavenly bodies moving about the Sun in conic sections”, a translation of Carl Friedrich “Gauss, Theoria motus”, Brown and Co.

44) Giacaglia, G. E. O., 1973. “Lunar Perturbations of Artificial Satellites of the Earth”. Smithsonian Astrophysical Observatory, Special Report 352, Cambridge, MA.

45) Gobetz, F. W. and Doll, J. R, 1969. “A survey of impulsive trajectories". AIAA Journal, Vol. 7, No. 5, pp. 801–834.doi: 10.2514/3.5231.

46) Gooding, R. H., 1990. “A procedure for the solution of Lambert’s orbital boundary-value problem”. Celestial Mechanics and Dynamical Astronomy, Vol. 48, No. 2, pp. 145–165. ISSN 09232958. doi:10.1007/BF00049511.

47) Goodyear, W.H., 1966. “A general method for the computation of cartesian coordinates and partial derivatives of the two-body problem”. NASA CR-522, September.

48) Gurfil, P. and Kasdin, N. J. 2002. “Niching Genetic Algorithms-Based Characterization of Geocentric Orbits in the 3D Elliptic Restricted Three-Body Problem”. Computer Methods in Applied Mechanics and Engineering, Vol. 191, Nos. 49–50, pp. 5683–5706.

49) Hartmann, J., Coverstone-Carroll, V., and Williams, S., 1998. “Generation of Optimal Spacecraft Trajectories via a Pareto Genetic Algorithm”. Journal of the Astronautical Sciences, Vol. 46, pp. 267–282.

50) Heaton, A.F., Stransge, N.J., Longuski, J.M et al., 2002. “Automated design of the Europa orbiter tour”. Journal of Spacecraft and Rockets, Vol. 39, No. 1, pp. 17-22.

51) Hohmann, W., 1960. “The attainability of heavenly bodies”. Technical translation F-44, National Aeronautics and Space Administration, Translation of "Die Erreichbarkeit der Himmelskorper”, R. Oldenbourg (Munich - Berlin), Aug 1925), Washington, November.

52) Hough, M. E., 1981. “Orbits near critical inclination, including lunisolar perturbations”. Celestial Mechanics and Dynamical Astronomy, Vol. 25, No. 2, pp. 111-136.

53) Hughes, G. and McInnes, C. R., 2001. “Solar Sail Hybrid Trajectory Optimization”. Advances in the Astronautical Sciences, Vol. 109, No. 3, pp. 2369–2380.

54) Hughes, S., 2008. “GMAT - generalized mission analysis tool”. Technical report, NASA Goddard Space Flight Center, http://sourceforge.net/projects/gmat.

55) Izzo, D., 2006. “Lambert’s problem for exponential sinusoids”. Journal of Guidance, Control, and Dynamics, Vol. 29, No.5, pp.1242–1245.

56) Izzo, D., Becerra, V.M., Myatt, D.R., Nasuto, S.J., Bishop, J.M., 2006. “Search space pruning and global optimisation of multiple gravity assist spacecraft trajectories”. Journal of Global Optimisation, Vol.38, No.2, pp. 283–296.

57) Izzo, D., 2015. “Revisiting Lambert’s problem”. Celestial Mechanics and Dynamical Astronomy, Vol. 121, No. 1, pp. 1–15, Jan. ISSN 0923-2958, doi:10.1007/s10569-014-9587-y.

58) Jin Li et al., 2018. “A new method of patched conic for interplanetary orbit”, OptiK, Vol. 156, pp.121-127.

59) Jones D. R. and Ocampo C., 2012. “Optimization of impulsive trajectories from a Circular orbit to an Excess Velocity Vector”, Journal of Guidance, Control, and Dynamics, January, Vol. 35, No. 1, pp. 234-244, https://doi.org/10.2514/1.52527.

60) Kaula, M. W., 1962. “Development of the Lunar and Solar Disturbing Functions for a Close Satellite”. Astronautical Journal, Vol. 67, pp. 290-300.

61) Kledron, K. and Sweetser, T.H., 1988. “A Comparison between One step and Other Multiconic Trajectory Propagations Methods”. AIAA/AAS Astrodynamics Conference, AIAA 88-4286-CP, August.

62) Kozai, Y., 1959. “On the Effects of the Sun and the Moon upon the Motion of a Close Earth Satellite”. Smithsonian Astrophysical Observatory, Special Report 22, Cambridge, MA.

63) Kozai, Y., 1962. “Secular Perturbations of Asteroids with High Inclination and Eccentricity”. The Astronomical Journal, Vol. 67, No. 9, pp. 591-598.

64) Kozai, Y., 1963. “The effects of the Sun and Moon upon the motion of a close Earth satellite”. Smithsonian Inst. Astrophysical Observatory Vol. 6, pp. 36-47.

65) Kozai, Y., 1973. “A New Method to Compute Lunisolar Perturbations in Satellite Motions”. Special Report 349, Smithsonian Astrophysical Observatory.

66) Lancaster, E. R., 1969. “Solution for Lambert problem for short arcs”. Technical report, NASA Goddard Space Flight Center, Greenbelt, MD, United States.

67) Lancaster, J.E., 1973. “Application of Matched Asymptotic Expansions to Lunar and Interplanetary Trajectories”. NASA CR-2255, Washington DC, July.

68) Lane, M.T., 1989. “On Analytical Modeling of Lunar Perturbations of Artificial Satellites of the Earth”. Celestial Mechanics and Dynamical Astronomy, Vol.46, No.4, pp.287-305.

69) Luo, Z., Dai, G., & Peng, L., 2011. “A Novel Model for the Optimization of Interplanetary Trajectory Using Evolutionary Algorithm”. JCP, Vol.6, No.10, pp. 2243-2248.

70) Luo, Q., Meng, Z., and Han, C., 2011. “Solution algorithm of a quasi-Lambert’s problem with fixed flight-direction angle constraint”. Celestial Mechanics and Dynamical Astronomy, Vol. 109, No. 4, pp. 409–427. ISSN 09232958, doi:10.1007/s10569-011-9335-5.

71) Mars Orbiter Mission (MOM) completes 4 years in its orbit, accessed 24 Sep, 2018, <https://www.isro.gov.in/update/24-sep-2018/mars-orbiter-mission-mom-completes-4-years-its-orbit>.

72) Marsden, J. E. and Ross, S. D., 2006. “New methods in celestial mechanics and mission design”. Bulletin (new series) of the American Mathematical Society, Vol.43, No.1, pp.43–73.

73) Montenbruck, O. and Gill, E., 2000. “Satellite Orbits - Models, Methods, and Applications”. Springer-Verlag, Heidelberg.

74) Jah, M., n.d. “Derivation of the b-plane (body plane) and its associated parameters”, <https://cbboff.org/UCBoulderCourse/documents/b-plane.PDF>

75) Musen, P., 1961. “On the long-period lunisolar effect in the motion of the artificial satellite”. Journal of Geophysical Research, Vol. 66, pp. 1659–1665.

76) Narumi, Tomohiro and Hanada, Toshiya, 2007. “New Orbit Propagator to Be Used in Orbital Debris Evolutionary Models”. Memoirs of the Faculty of Engineering, Kyushu University, Vol.67, No.4, December.

77) Ocampo, C., 2003. “An architecture for a generalized spacecraft trajectory design and optimization system”. In: Proceedings of the international conference on libration point missions and applications, August.

78) Olds, A., Kluever, C., and Cupples, M., 2007. “Interplanetary Mission Design Using Differential Evolution”. Journal of Spacecraft and Rockets, Vol. 44, No. 5, pp. 1060–1070. doi:10.2514/1.27242.

79) Pamadi, B.N., 1995. “Simple guidance method for single stage to Low Earth Orbit”. Journal of Guidance, Control, and Dynamics, Vol. 18, No.6, pp.1420–1426

80) Penzo, P., 1970. “Computing earth oblateness effects on lunar and interplanetary trajectories”. 8th Aerospace Sciences Meeting, Aerospace Sciences Meetings, doi: http://dx.doi.org/10.2514/6.1970-97.

81) Prussing, J.E., and Conway, B.A., 1993. “Orbital Mechanics”. Oxford University Press, New York, pp 124 -128.

82) Prussing, J. E., 2000. “A Class of Optimal Two-Impulse Rendezvous Using Multiple-Revolution Lambert Solutions”. Journal of the Astronautical Sciences, Vol. 48, No. 2, pp. 131–148.

83) Radice, G. and Olmo, G., 2006. “Ant Colony Algorithms for Two Impulse Interplanetary Trajectory Optimization”. Journal of Guidance, Control, and Dynamics, Vol. 29, No. 6, pp. 1440-1444. https://doi.org/10.2514/1.20828

84) Ramanan, R.V., 2002. “Integrated Algorithm for Lunar Transfer Trajectories using a Pseudostate Technique”. Journal of Guidance, Control and Dynamics, Vol.25, No.5, Sep.-Oct. doi: 10.2514/2.4968.

85) Ramanan, R.V. and Adimurthy, V., 2005. “Nonimpact Lunar Transfer Trajectories Using the Pseudostate Technique”. Journal of Guidance, Control and Dynamics, Vol.28, No.2, March-April, doi: 10.2514/1.7607.

86) Rauwolf, G., and Coverstone-Carroll, V., 1996. “Near-Optimal Low-Thrust Orbit Transfers Generated by a Genetic Algorithm”. Journal of Spacecraft and Rockets, Vol. 33, No. 6, pp. 859–862.

87) Roy, A.E., 1969. “Luni-solar perturbations of an earth satellite”. Astrophysics and Space science, Vol.4, No.4, pp. 375–386.

88) Sauer, C.G., 1989. “MIDAS—mission design and analysis software for the optimization of ballistic interplanetary trajectories”. Journal of Astronautical Sciences, Vol.37, No.3, pp.251–259.

89) Schaub, H., Junkins, J.L., 2009. “Analytical Mechanics of Space Systems”. Second ed. AIAA Education Series.

90) Sentinella, M.R. and Casalino, L., 2009. “Hybrid Evolutionary Algorithm for the Optimization of Interplanetary Trajectories”. Journal of Spacecraft and Rockets, Vol. 46, No. 2, March–April, doi: 10.2514/1.38440.

91) Sergeyevsky, A.B., 1983. “Interplanetary Mission Design Handbook, Vol. 1, part 2-Earth to Mars Ballistic Mission Opportunities 1990-2005”. JPL Publication pp.82-43, Sep. 15.

92) Sergeyevsky, A.B., Byrnes, D.V. and D’Amario, L.A., 1983. “Application of the Rectilinear Impact Pseudostate Method to Modeling of Third Body Effects of Interplanetary Trajectories”. AIAA-83-0015, AIAA 21st Aerospace Sciences Meeting, January 10-13.

93) Solar System Exploration, n.d., <https://solarsystem.nasa.gov/solar-system/our-solar-system>.

94) Solórzano, C. R. H., Prado, A. F. B. de Almeida, 2004. “Third-body perturbation using a single averaged model”. Instituto Nacional Pesquisas Espaciais – INPE, São José dos Campos, SP, Brazil, ISBN 85-17-00012-9.

95) Spreen, C. M., Mueterhies, M. J., Kloster, K. W., 2011. “Preliminary analysis of ballistic trajectories to Uranus using gravity-assists from Venus, Earth, Mars, Jupiter and Saturn”. AAS 11-623, AAS/AIAA Astrodynamics Specialist Conference, Girdwood, Alaska, U.S.A, July 31-August 4.

96) Sweetser, T.H., 1989. “Some Notes on Applying the One-step Multiconic Method of Trajectory Propagation”. The Journal of Astronautical Sciences, Vol.37, No.3, July-September, pp.252-259.

97) Storn and Price, 1997. “Differential Evolution – A Simple and Efficient Heuristic for global Optimization over Continuous Spaces”. Journal of Global Optimization, Vol.11, Issue.4, pp.341-359. doi:10.1023/A:1008202821328.

98) Stumpff, K. and Weiss, E.H., 1968. “Applications of an n-body reference Orbit”. Journal of Astronautical Sciences, Vol.15, No.5, pp.257-261, September-October. Also, “A Fast Method of Orbit Computation”. NASA Technical Note TN D-4470, Washington DC, April.

99) STK/GIS User's Manual (https://books.google.co.in/books?id=L3YJHAAACAAJ), 1997, Analytical Graphics, Inc.

100) Thompson, B. F., 2011. “Enhancing Lambert Targeting Methods to Accommodate 180-Degree Orbital Transfers”. Journal of Guidance, Control, and Dynamics, Vol. 34, No. 6, pp. 1925– 1929. ISSN 0731-5090, doi:10.2514/1.53579.

101) Thorne, J. D. and Bain, R. D., 1995. “Series Reversion/Inversion of Lambert’s Time Function”. Journal of the Astronautical Sciences, Vol. 43, No. 3, pp. 277–287.

102) Tolson, R.H., 1963. “Geometrical Characteristics of Lunar Orbits Established from Earth-Moon Trajectories”. NASA Technical Note D-1780.

103) Vallado, D. A., 1997. “Fundamentals of Astrodynamics and Applications”. McGraw-Hill Companies, ISBN 9780070668348.

104) Vasile, M., Summerer, L., and De Pascale, P., 2005. “Design of Earth-Mars Transfer Trajectories Using Evolutionary-Branching Technique”. Acta Astronautica, Vol. 56, No. 8, pp. 705–720.

105) Vasile, M., DePascale, P., 2006. “Preliminary design of low thrust multiple gravity assist trajectories”. AIAA, Journal of Spacecraft and Rockets, Vol.43, No.5, pp.1065–1076.

106) Vasile, M., Schütze, O., Junge, O., Radice, G., Dellnitz, M., 2006. “Spiral Trajectories in Global Optimisation of Interplanetary and Orbital Transfers”. Ariadna Study Report AO4919 05/4106, ESA.

107) Vasile, M., Minisci, E., Locatelli, M., 2010. “Analysis of some global optimization algorithms for space trajectory design”. Journal of Spacecraft and Rockets, Vol.47, No.2, pp.334–344.

108) Vasile, M., Zuiani, F., 2010. “A hybrid multi-objective optimization algorithm applied to space trajectory optimization”. In: Proceedings of the Special Session on Evolutionary Computation in Aerospace Sciences CEC.

109) Wilson, Jr. S.W., 1970. “A Pseudostate Theory for the Approximation of Three-Body Trajectories”. AIAA Paper No. 70-1061, AAS/AIAA Astrodynamics Conference, Santa Barbara, California, Aug. 19-21.

110) Woo, B., Coverstone-Carroll, V., and Cupples, M., 2006. “Low-Thrust Trajectory Optimization Procedure for Gravity-Assist, Outer-Planet Missions”. Journal of Spacecraft and Rockets, Vol. 43, No. 1, pp. 121–129. doi:10.2514/1.14665

111) Zhang, H., Luo, Q., Han, C., 2014. “Accurate and fast design algorithm for free-return lunar fly-by trajectories”. Acta Astronautica, Vol.102, pp.14-26, https://doi.org/10.1016/j.actaastro.2014.05.015.

♠♠♠♠♠♠♠♠♠♠♠♠♠♠♠♠♠♠♠

APPENDIX A

DESIGN ANALYSIS WITH ITR-PS TECHNIQUE

A FORTRAN 95 code has been developed based on the ITR-PS technique and used as a quick mission design and analysis tool for orbiter mission. The analysis is carried out for various departure and arrival scenarios. A similar analysis by numerical technique will require enormous computation time and effort.

The computation time required for obtaining the ITR-PS design is only 5 ms in an Intel Core i5-3230 CPU 2.60 GHz processor and so, the design analysis takes minimal computer time. For using the ITR-PS technique as a mission analysis tool, the following design data are used; (i) minimum energy opportunity: 12 May 2018 0 h TDB, (ii) flight duration/time of flight: 204 days, (iii) periapsis altitude of DPO: 300 km, (iv) inclination of DPO: 75 deg (with respect to Earth equator and equinox of J2000), (v) periapsis altitude of APO: 300 km, (vi) inclination of APO: 75 deg (with respect to Mars equator and IAU vector of J2000), and (vii) pseudosphere duration at the departure and arrival phases as 3 and 2 days respectively. For the design analysis purpose, the parameter defined in (i) to (vi) are varied one by one. The design analysis is demonstrated for the ITR-PS design option 11. Similar trend is expected for other design options also.

1. Different departure epochs

The influence of the transfer angle on the design analysis is very significant and so, in Fig.A1, the variation of transfer angle for different departure epochs in the neighborhood of the minimum energy epoch is presented. The transfer angle varies from 130 deg to 200 deg over the chosen range of departure epochs (six months starting from 1 January 2018). The flight duration is fixed as 204 days. The sudden jump in the transfer angle happens for a transfer angle of 180 deg and is because of the non-coplanar orbits of the target planets. This occurs by the end of February 2018 (around MJD 58,175).

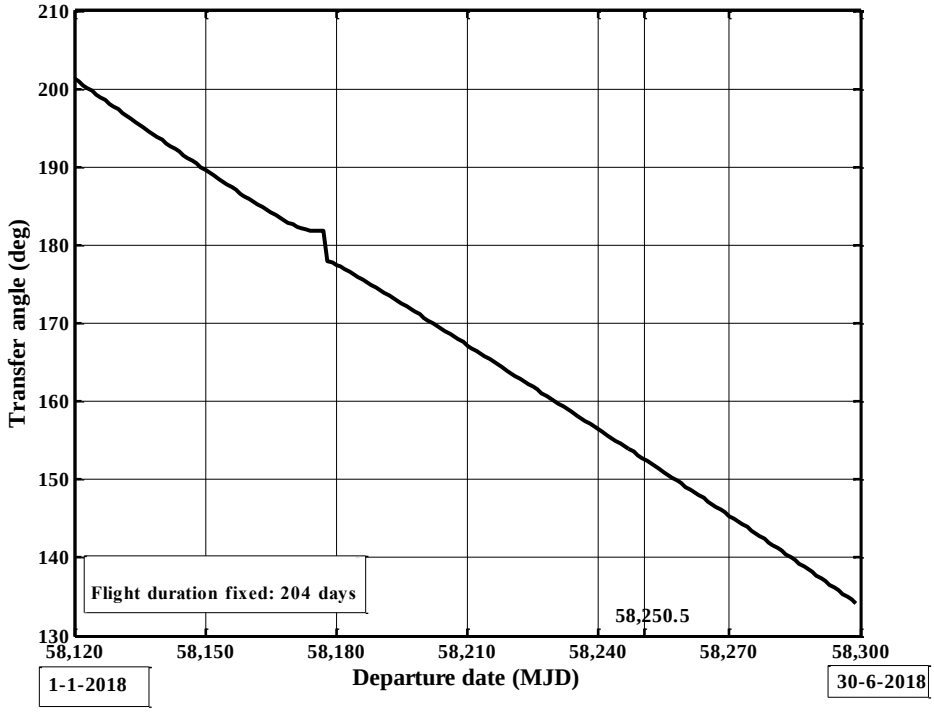

Fig. A1. Variation of transfer angle for different departure epochs

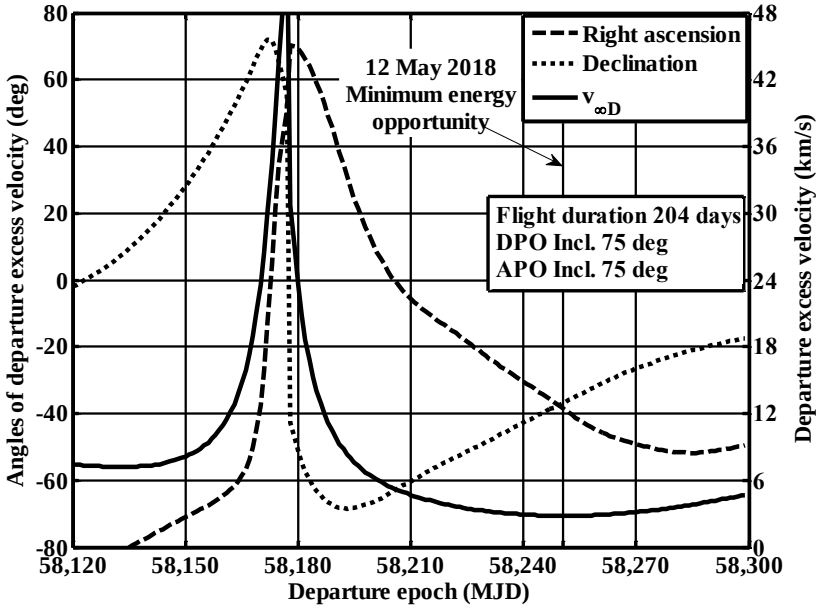

Fig. A2. Variation of departure V-infinity vector (from ITR-PS technique) for different departure epochs

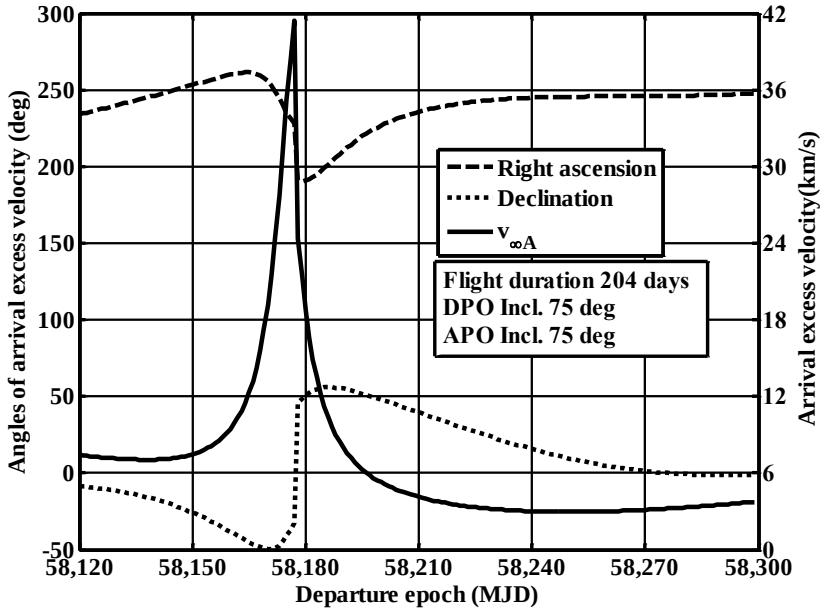

Fig. A3. Variation of arrival V-infinity vector (from ITR-PS technique) for different departure epochs

The departure and arrival V-infinity vectors corresponding to the ITR-PS design option 1-1 are plotted in Figs. A2 and A3 respectively. Note that the magnitude of V-infinity vector steeply goes up in the vicinity of 180 deg transfer angle.

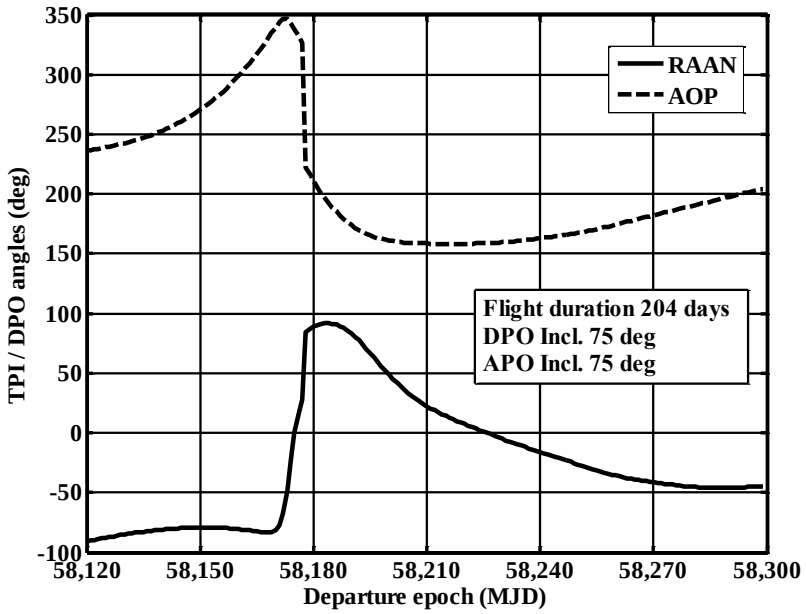

Fig. A4. Variation of DPO angles (from ITR-PS technique) for different departure epochs

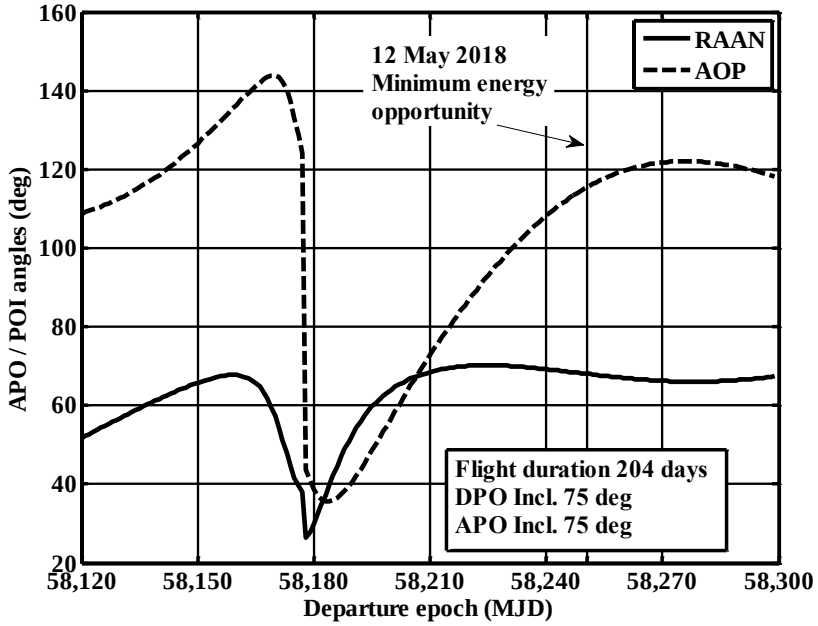

Fig. A5. Variation of APO angles (from ITR-PS technique) for different departure epochs

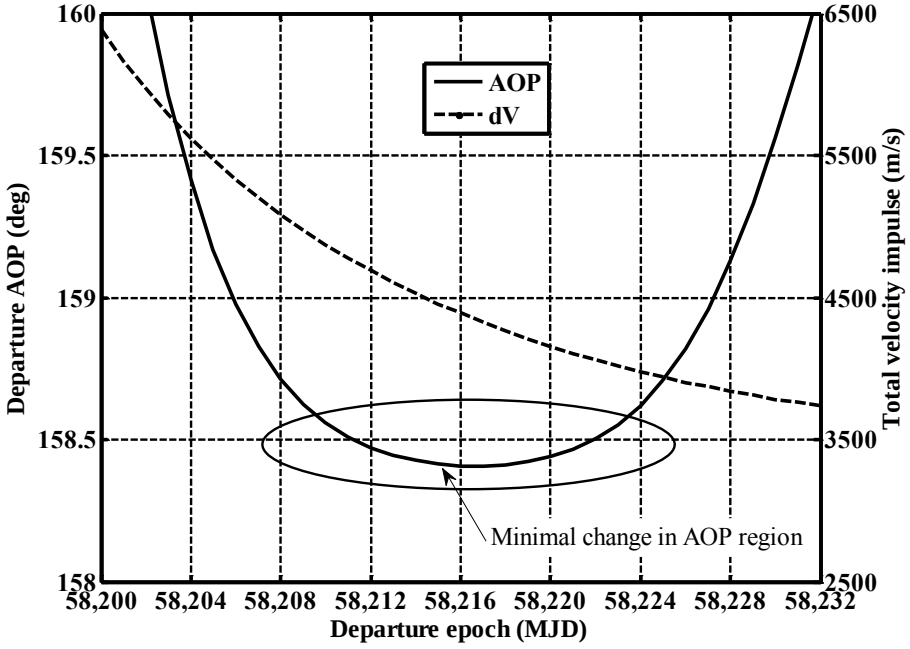

Fig. A6. Minimal variation of departure AOP and corresponding variation of total velocity impulse for different departure epochs

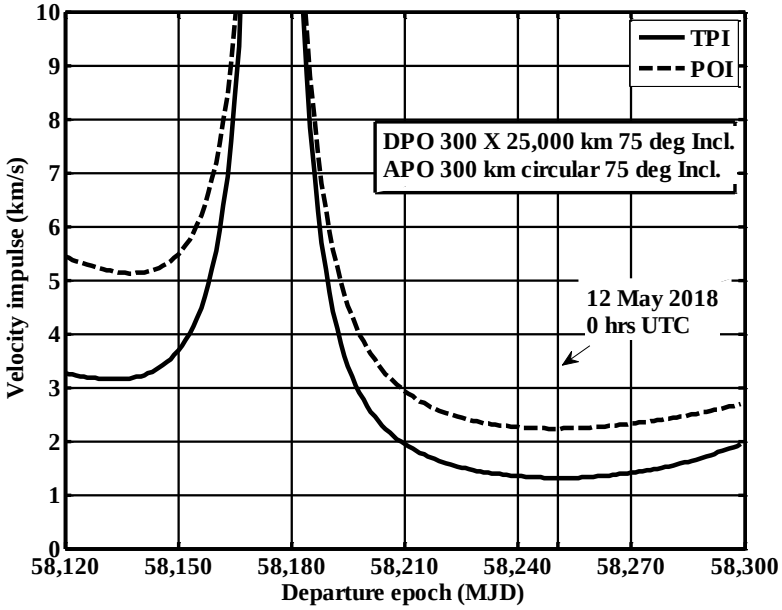

Fig. A7. Variation of TPI and POI velocity impulses (from ITR-PS technique) for different departure epochs

The variation of the DPO (departure RAAN and AOP) and APO (arrival RAAN and AOP) angles, corresponding to the design option 1-1, for different departure epochs are given in Figs. A4 and A5. For a desired departure AOP, the departure epoch can be selected from this figure. The related RAAN to this departure epoch fixes the lift off time of the launch vehicle. For a desired arrival AOP, a similar design analysis can be done. Note that from Fig. A6, for a region of departure epochs (58200-58230), the AOP variation is minimum (~158 deg). This provides a lot of flexibility in the launch date selection with minimum change in the launch vehicle trajectory. However, this launch window flexibility will be available subject to the additional velocity impulse capability of the propulsion system of the spacecraft (cf. Fig. A7). The steep increase in the velocity impulses in Fig. A7 occur in the vicinity of 180 deg transfer angle.

2. Different flight durations

For a fixed departure epoch, the variation in transfer angle for different flight durations is given in Fig. A8. The near linear variation represents the fact that Earth and Mars orbits are near circular. The departure and arrival V-infinity vectors for different flight durations are shown in Figs. A9 and A10. The DPO and APO angles obtained from the ITR-PS technique are given in Figs. A11 and A12. The maximum difference in the TPI and POI angles can be upto 1.5 deg when the transfer angle is in the neighborhood of 180 deg. It can be seen that the arrival velocity impulse for POI is non-linear and varies drastically with flight duration whereas

the departure velocity impulse for TPI varies by about 100 m/s with flight duration (cf. Fig. A13).

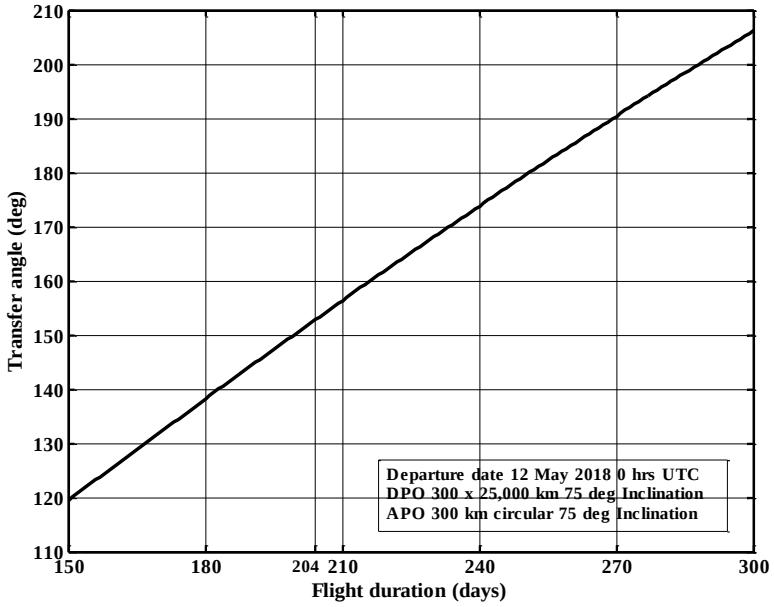

Fig. A8. Variation of transfer angle for different flight durations

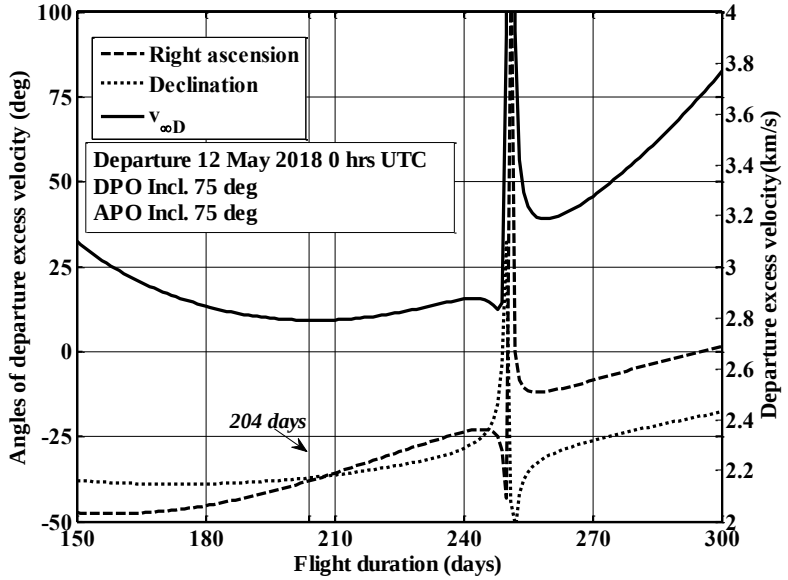

Fig. A9. Variation of departure V-infinity vector (from ITR-PS technique) for different flight durations

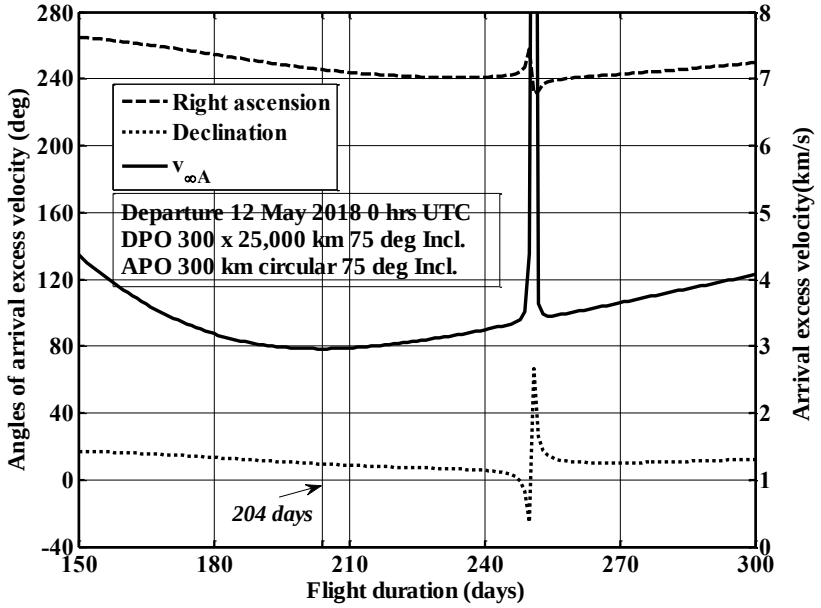

Fig. A10. Variation of arrival V-infinity vector (from ITR-PS technique) for different flight durations

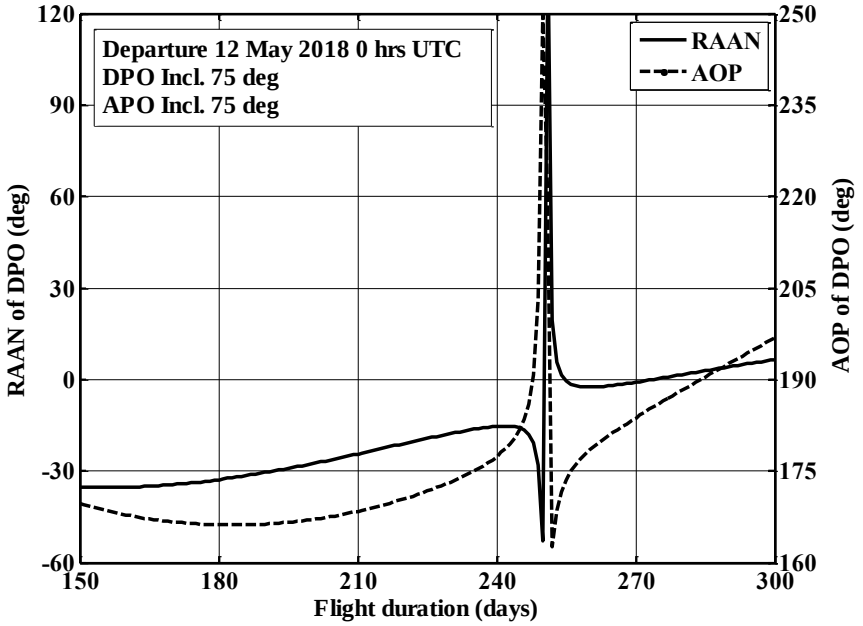

Fig. A11. Variation of TPI angles (from ITR-PS technique) for different flight durations

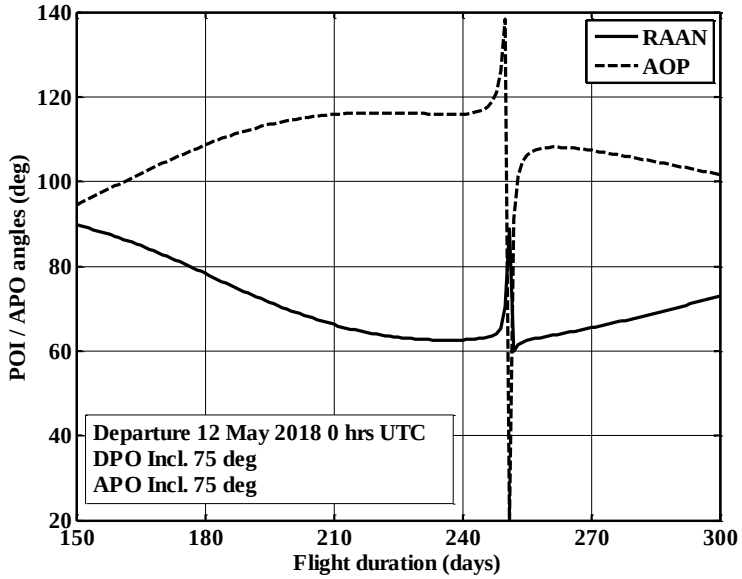

Fig. A12. Variation of POI angles (from ITR-PS technique) for different flight durations

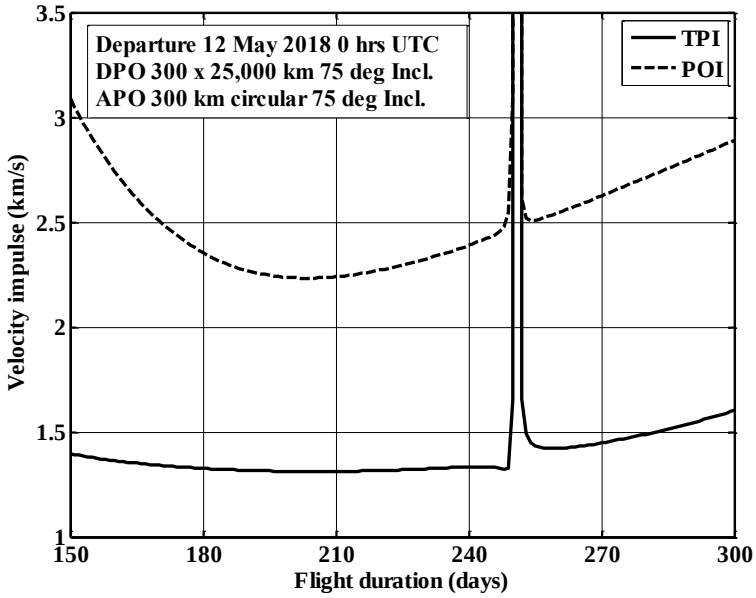

Fig. A13. Variation of TPI and POI velocity impulses (from ITR-PS technique) for different flight durations

3. Different periapsis altitudes of departure hyperbolic orbit/DPO

The periapsis altitude of the departure hyperbolic orbit/DPO is varied from 100 km to 25,000 km. For different DPO periapsis altitudes, the variation of DPO (viz. departure RAAN and AOP) and APO (viz. arrival RAAN and AOP) angles are given in Figs. A14 and A15. The marginal variation observed in departure RAAN implies that there is minimal change in the

departure hyperbolic orbital plane. However, the location of DPO periapsis changes drastically with increase in departure periapsis altitude. The variation in POI angles is insignificant.

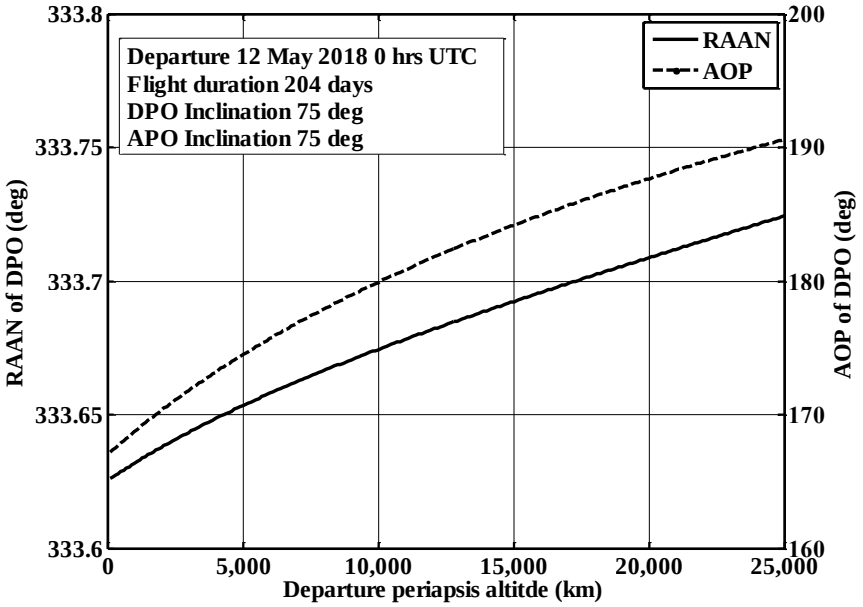

Fig. A14. Variation of DPO angles (from ITR-PS technique) for different departure periapsis altitudes

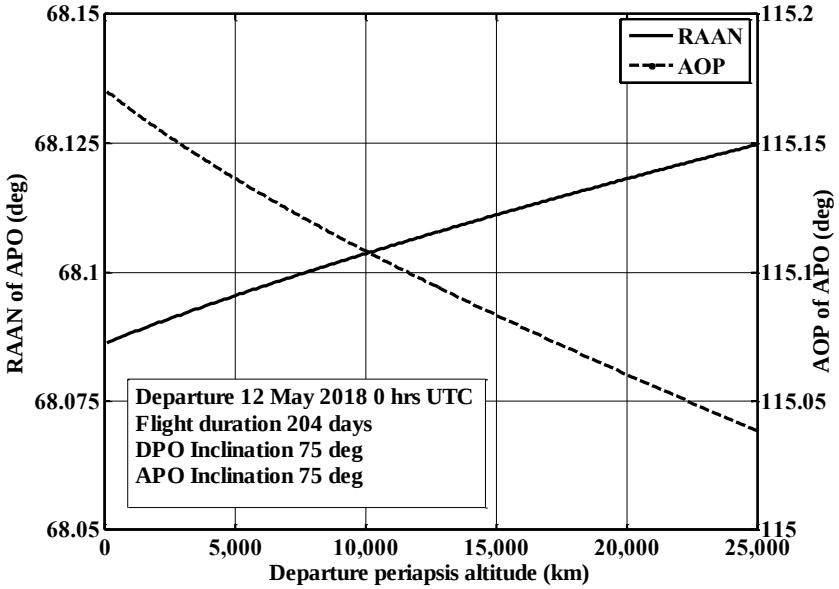

Fig. A15. Variation of APO angles (from ITR-PS technique) for different departure periapsis altitudes

The variation of TPI and POI velocity impulses for different periapsis altitudes are given in Fig. A16. The large variation in TPI impulse is as expected. Note that there is almost no change in the POI impulse for different periapsis altitudes.

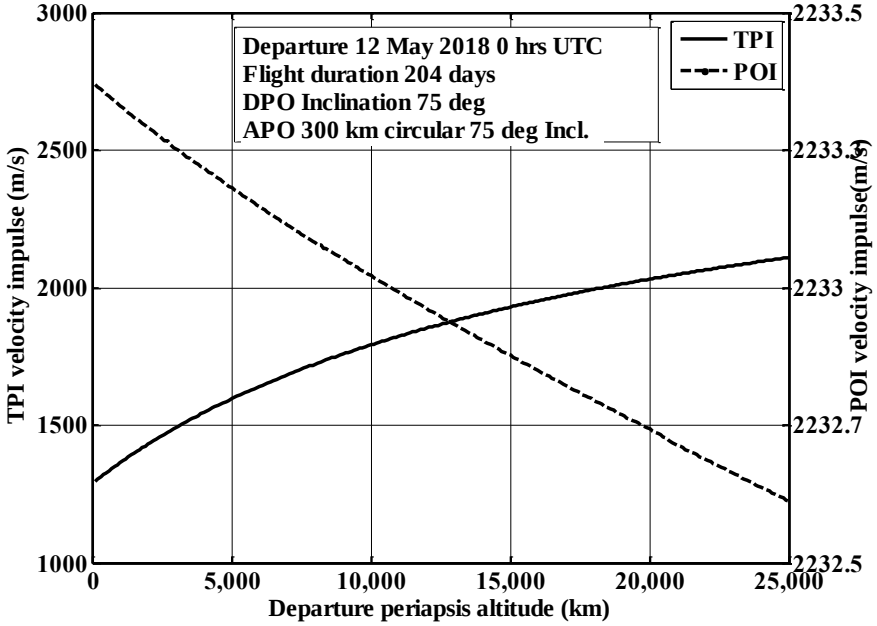

Fig. A16. Variation of TPI and POI impulses (from ITR-PS technique) for different departure periapsis altitudes

4. Different inclinations of departure hyperbolic orbit/DPO

The profiles of the DPO and APO angles for different inclinations of the departure hyperbolic orbit are depicted in Figs. A17 and A18. For coplanar transfer, the range of inclinations between 38 deg and 142 deg only is feasible. The departure AoP is symmetric about 90 deg inclination. The implication of departure hyperbolic orbit inclination on the APO angles is very small. The departure inclination does not contribute to the TPI and POI velocity impulses (cf. Fig. A19).

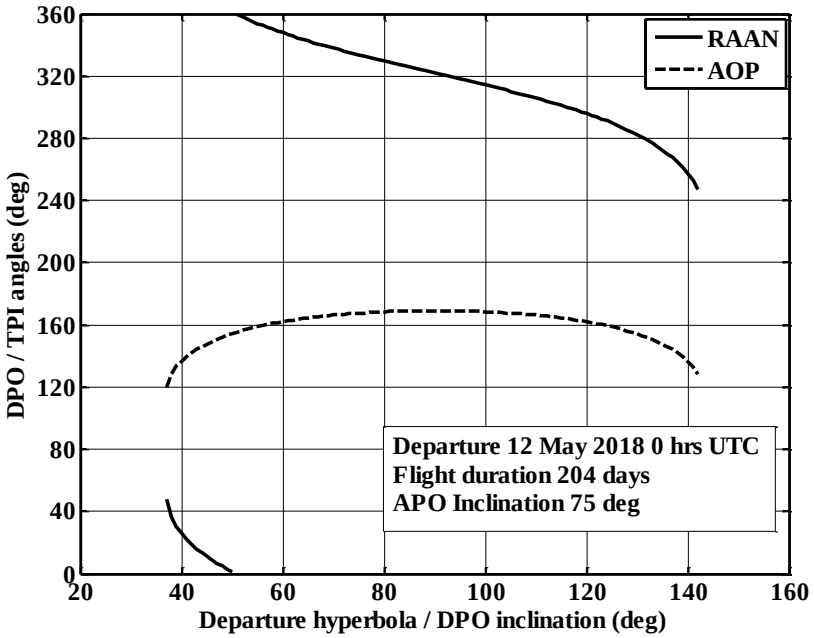

Fig. A17. Variation of DPO angles (from ITR-PS technique) for different departure hyperbola/parking orbit inclinations

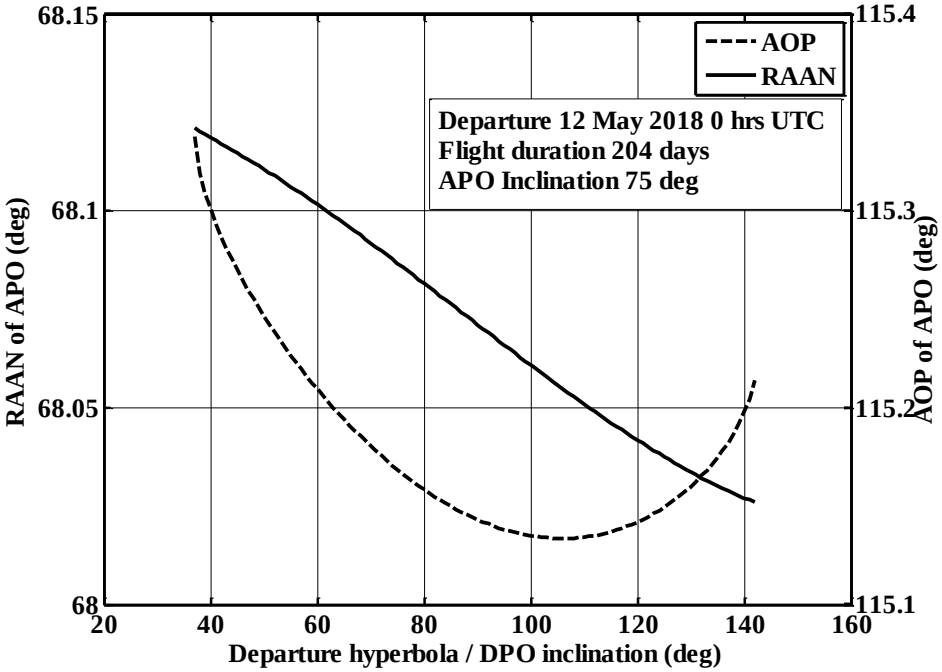

Fig. A18. Variation of APO angles (from ITR-PS technique) for different departure hyperbola/parking orbit inclinations

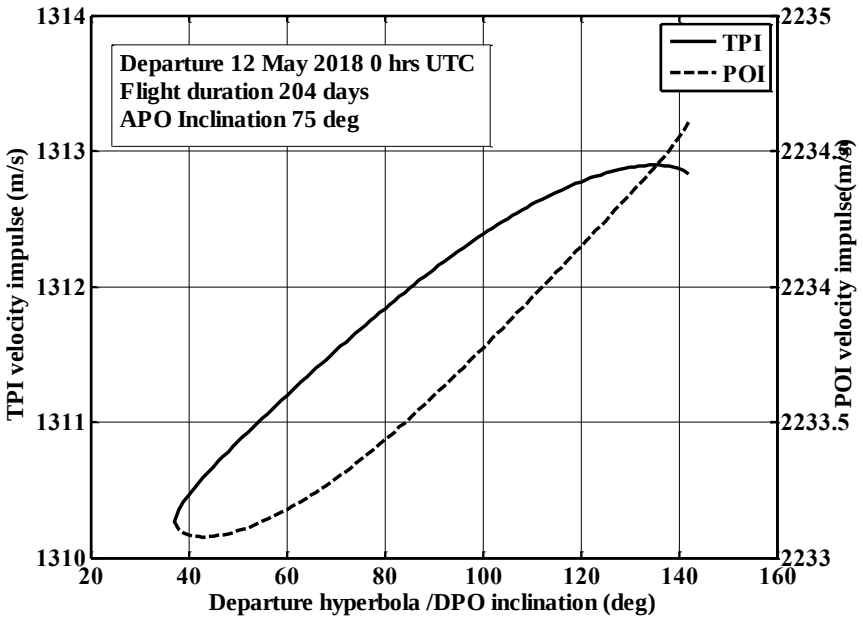

Fig. A19. Variation of TPI and POI velocity impulses (from ITR-PS technique) for different departure parking orbit inclinations

5. Different periapsis altitudes of arrival hyperbolic orbit/APO

The variation in DPO and APO angles to achieve different peripsis altitudes of the arrival hyperbolic orbit is given in Figs. A20 and A21. The change in DPO angles, although very small, results in periapsis altitudes which are entirely different. This brings out the sensitivity of the transfer trajectory design. The resulting APO angles are also given. There is minimal change in the TPI velocity impulse for different target periapsis altitudes and the variation in POI is as about 120 m/s (cf. Fig. A22).

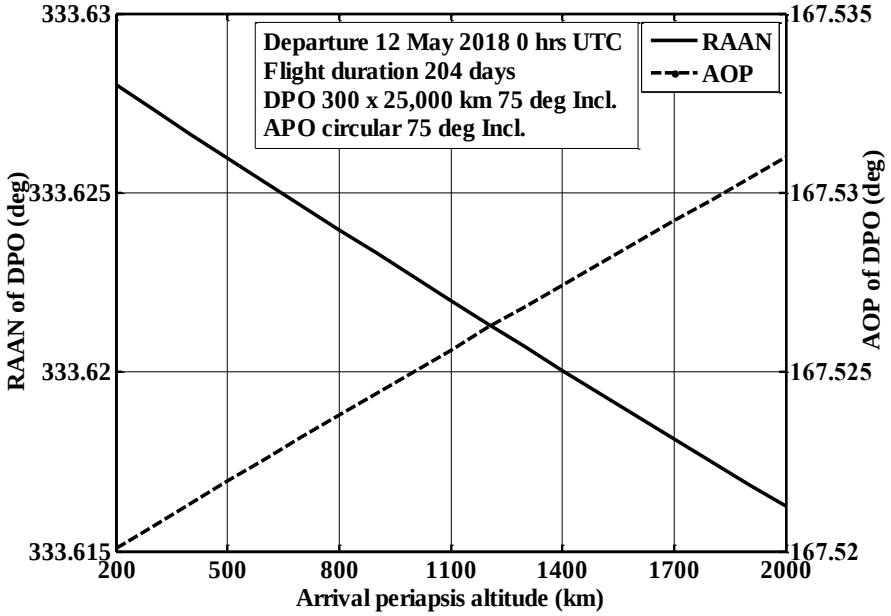

Fig. A20. Variation of DPO angles (ITR-PS technique) for different arrival periapsis altitudes

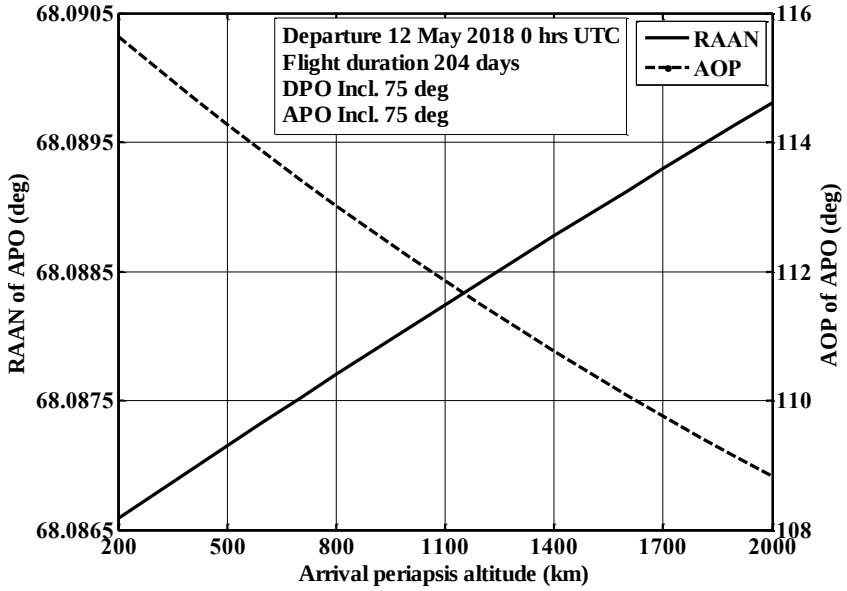

Fig. A21. Variation of APO angles (ITR-PS technique) for different arrival periapsis altitudes

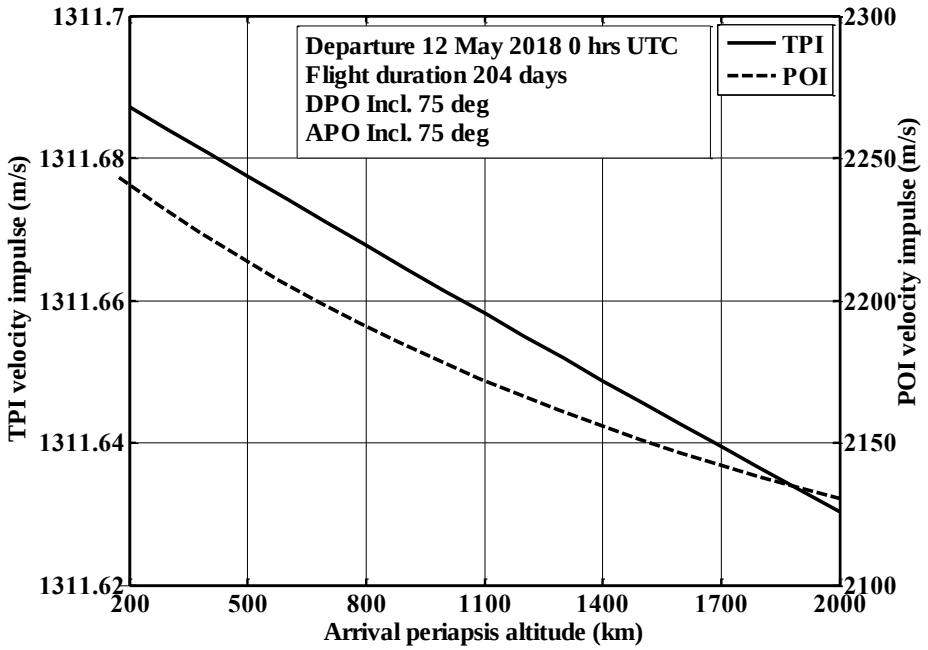

Fig. A22. Variation of TPI and POI velocity impulses (from ITR-PS technique) for different arrival periapsis altitudes

6. Different inclinations of arrival hyperbolic orbit/APO

The profiles of the DPO and APO angles for different inclinations of the arrival hyperbolic orbit are depicted in Figs. A23 and A24. For coplanar transfer, the range of inclination is between 10 deg and 170 deg. The entire range of arrival hyperbolic orbit inclinations can be achieved by a small change in the departure RAAN (0.06 deg) and departure AoP (0.04 deg). This emphasises the high sensitivity of the DPO angles. There are significant variations in the APO angles for different target inclinations. The variation in TPI and POI velocity impulses for different target inclinations are insignificant as seen in Fig. A25.

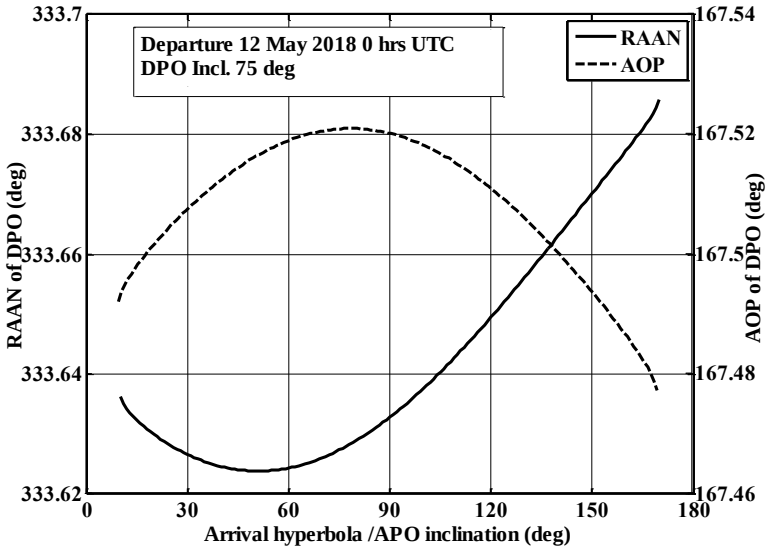

Fig. A23. Variation of TPI angles (ITR-PS technique) for different APO inclinations

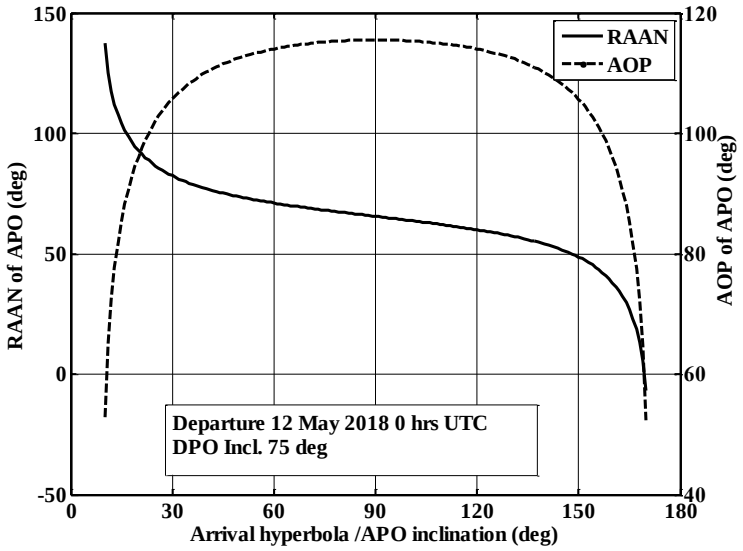

Fig. A24. Variation of POI angles (ITR-PS technique) for different APO inclinations

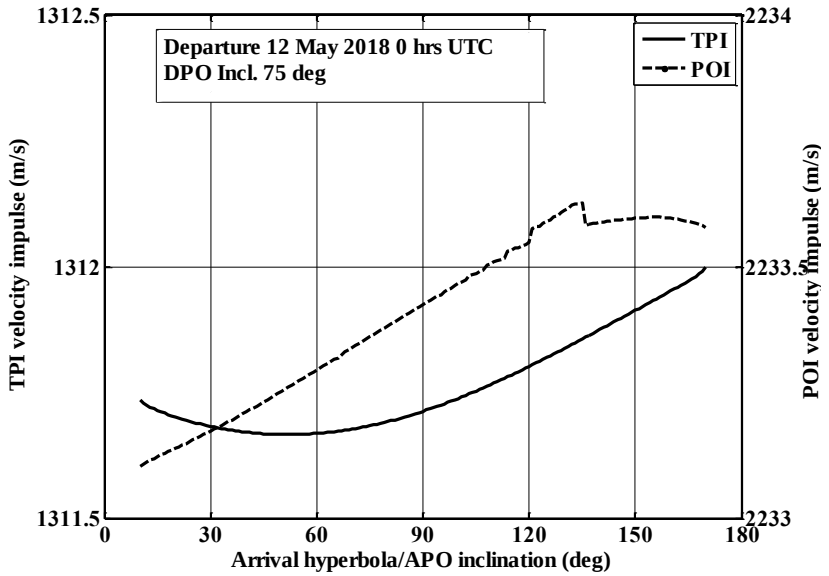

Fig. A25. Variation of TPI and POI velocity impulses (from ITR-PS technique) for different APO inclinations

♠♠♠♠♠♠♠♠♠♠♠♠♠♠♠♠♠♠♠♠